MODELING AND OPTIMIZATION OF MICRO-END MILLING PROCESS FOR MICRO-MANUFACTURING

by

THANONGSAK THEPSONTHI

A dissertation submitted to the

Graduate School-New Brunswick

Rutgers, The State University of New Jersey

In partial fulfillment of the requirements

For the degree of

Doctor of Philosophy

Graduate Program in Interdisciplinary

Industrial and Systems Engineering
Mechanical and Aerospace Engineering

Written under the direction of

Assoc. Prof. Tuğrul ÖZEL

And approved by

_____

_____

_____

_____

_____

New Brunswick, New Jersey

May 2014

ABSTRACT OF THE DISSERTATION

MODELING AND OPTIMIZATION OF MICRO-END MILLING PROCESS FOR MICRO-MANUFACTURING

By THANONGSAK THEPSONTHI

Dissertation Director:

Assoc. Prof. Tuğrul ÖZEL

The miniaturization of devices has been under high demand since they offer added benefits such as high mobility and portability, better accessibility and functionality, and lower energy consumption. Specific applications include energy devices such as heat sinks and exchangers, biomedical devices such as microfluidic devices, microneedles, and implants, automotive and aircraft components, and sensory devices. As the demand to produce such miniature products continue to increase, an imminent need for advanced manufacturing processes that can fabricate very small parts directly, cost effectively, and with high productivity arises. Micro-end milling is one of the most promising manufacturing processes capable of fabricating discrete parts with complex features in micro-scale (feature size < 1000 μm) due to its high flexibility for processing a wide range of materials with a low setup cost. However, micro-end milling process possesses several difficulties in precision fabrication of such products due to size effect, rapid tool wear, burr formation, tool and workpiece deflection, and premature tool breakage. In addition, these micro-products require tighter geometrical tolerances and

better surface quality. These difficulties and requirements make the selection of process parameters for high performance micro-end milling very challenging.

In this research, we conducted experimental and numerical modeling studies and multi-objective process optimization for micro-end milling. An extensive study of process parameters such as tool coatings, cutting velocity, feed rate, and axial depth of cut was performed in order to understand the effects of these parameters on the performance of micro-end milling process. Novel finite element based process models in 2-D and 3-D have been developed. Both experimental models and finite element based process simulations were utilized to construct various predictive models for the process outputs. These predictive models include physics-based outputs such as chip deformations, tool forces and temperatures, tool wear rate and depth, as well as performance related measures such as surface finish, burr formation, and tool life. Furthermore, we developed a comprehensive decision support system by using the predictive models which can facilitate a selection of process parameters and toolpath strategies based on desired performances. Multi-objective optimization studies were conducted by utilizing predictive models for obtaining optimal decision variable sets. Moreover, this research also demonstrates the current capabilities of micro-end milling in fabricating micro-products such as heat sinks in brass and implants in titanium alloys, and micro-needles in polymers.

ACKNOWLEDGEMENTS

First and foremost, I would like to express my deepest gratitude to my advisor, Dr. Tuğrul Özel for his enthusiastic scientific support, insightful guidance, and patient throughout the course of this research. Without his advice, encouragement and faith, the completion of this Ph.D. research would not have been possible.

I would like to thank my committee members, Dr. James T. Luxhøj, Dr. Hae Chang Gea, Dr. Alberto Cuitino and Dr. Adrian Mann for the sound advice and constructive suggestions.

I am deeply indebted to Ministry of Science and Technology of Thailand for their financial support throughout my PhD study.

I appreciate the administrative and technical support I received from Ms. Cindy Ielmini and Mr. Joe Lippencott. I also would like to thank all my friends for their help and support.

Finally, I want to thank my family for having faith in me and motivating me in pursuing my degree.

TABLE OF CONTENTS

LIST OF TABLES

LIST OF ILLUSTRATIONS

LIST OF SYMBOLS

A,B,C	Original J-C material model coefficients
a, b, d, p, r, s	Modified J-C material model coefficients
a_i	Polynomial coefficients
a_p	Axial depth of cut
B, b_0, b_1	Wear depth model constants
B_d	Top-burr widths form down milling side
B_T	Total top-burr width
B_u	Top-burr widths form up milling side
C_p	Specific heat capacity
c_1, c_2	Wear rate model constants
dF_x	Differential force component in X direction
dF_y	Differential force component in Y direction
E	Young's modulus
F_x	Cutting force in X direction
$F_{x_{max}}$	Maximum cutting force in X direction
$F_{x_{\max\_allow}}$	Maximum allowable cutting force in X direction
F_y	Cutting force in Y direction
$F_{y_{max}}$	Maximum cutting force in Y direction
$F_{y_{\max\_allow}}$	Maximum allowable cutting force in Y direction
F_z	Cutting force in Z direction
f_z	Feed per tooth

h	Convection coefficient
h_c	Thermal contact conductance
k	Number of independent variable
k_1, k_2	Acceleration coefficients of particle
L	Maximum linear cutting distance
L_{req}	Required cutting distance
l_c	Tool cutting length
m	Work material shear yield stress
n	Number of micro-end mill tooth
$\boldsymbol{p}_i$	Vector of the personal best position
$\boldsymbol{p}_g$	Vector of the best position found by particles in its neighborhood
p_i	Interface pressure
p_1, p_2, p_3	Penalty values.
R_a	Average surface roughness
$\boldsymbol{R}_1$, $\boldsymbol{R}_2$	Random functions
r_β	Tool edge radius
T	Temperature
T_0	Ambient temperature
T_m	Melting temperature
T_{life}	Maximum tool life
UTS	Ultimate tensile strength
v_i^k	Velocity of particle i at iteration k
v_c	Linear cutting velocity

v_s	Sliding velocity
$\boldsymbol{x}$	Set of independent variables
x_i^k	Position of particle i at iteration k
y	Process response
W	Tool wear depth per pass
W_{max}	Maximum allowable wear depth per tooth
w	Inertia weight
Z_i^U	Utopia points
Z_i^N	Nadir points
α	Thermal expansion coefficient
$\beta_0, \beta_1, \ldots, \beta_k$	Set of response surface coefficients
β	Tool helix angle
ε	True strain
$\dot{\varepsilon}$	True strain rate
$\dot{\varepsilon}_0$	Reference true strain rate
ϵ	Residual error
θ_i	Normalization factors
κ	Thermal conductivity
μ	Coulomb friction factor
ν	Poisson's ratio
σ	Flow stress
σ_n	Normal stress
τ_f	Frictional stress

ϕ	Tool rotation angle
$\varnothing$	Tool diameter
Ω	Spindle speed

CHAPTER 1

INTRODUCTION

1. Introduction

The miniaturization of devices has been under high demand. Miniature products offer several benefits such as high mobility and portability, better accessibility and functionality, lower energy consumption and lesser environmental impact among others. Specific applications include energy applications such as micro-scale fuel cells, micro-scale heat sinks and exchangers; biomedical applications such as microfluidic devices and systems, medical devices and orthodontic and orthopedic implants; automotive applications such as engine fuel delivery components and sensory devices, aerospace applications such as avionics and jet engine components and sensory devices. As demand to produce such miniature products increase rapidly, an imminent need for advanced manufacturing processes that can fabricate very small parts cost effectively and with high productivity increases significantly. The term micro-manufacturing is used to represent processes which are capable of fabricating discrete parts with micro-scale (1-1000 μm) features.

The micro-manufacturing processes consist of several categories including micro-molding, micro-machining, micro-forming, micro-layered manufacturing, etc. Generally, they are a group of processes that are scaled down versions of both conventional and non-conventional macro-manufacturing processes. Micro-manufacturing processes can also be categorized according to the type of energy used in the process, such as mechanical, chemical, electrochemical, electrical, and laser-beam processes. The working principles

behind each process include consideration of mechanical forces, thermal effects, ablation, dissolution, solidification, re-composition, polymerization/lamination, and sintering (Razali & Qin 2013).

Mechanical micro-machining is one process among micro-manufacturing processes. It involves a removal of unwanted material by means of mechanical force applied with a physical cutting tool. The advantages of mechanical micro-machining compared to other processes are; high material removal rate, process flexibility and low setup cost. A 3-D complex shape can be machined out of almost unlimited workpiece materials. Since the process is highly flexible and the setup cost is relatively low, mechanical micro-machining is very suitable for the fabrication of customized products which are also growing in demand.

Mechanical micro-machining is not just simply a scale-down version of tool-based traditional material removal process (mechanical macro-machining). There is a limit to how far the process can be miniaturized (scaled down). Beyond certain dimensions, factors that can be ignored in mechanical macro-machining suddenly take an important role in micro-machining: cutting tool edge geometry, tool-offset and runout, thermal expansion, tool rigidity and stiffness, tool deflections and vibrations, and material microstructure, etc. These factors totally change the way tool and workpiece interact at micro-scale and make mechanical micro-machining much more difficult to pursue. Currently, mechanical micro-machining is capable of fabricating miniature parts as small as ten microns to a few millimeters (Dornfeld et al. 2006). However, there is still room for improvement. Dimensional accuracy, tool life, surface finish and burr formation,

these are the important areas on which researchers and industries are currently paying attention.

1.1 Mechanical micro-machining of metals and polymers

As mentioned before that mechanical micro-machining processes can be applied to every type of material. This advantage makes mechanical micro-machining processes to become highly flexible. However, two major categories of work material which are suitable for mechanical micro-machining are metals and polymers. Also, these materials are widely used in many applications of miniaturized products. Therefore, the main focus of researches and studies are on mechanical micro-machining of metals and polymers.

In general, metals and their alloys have advantages of high strength, high thermal conductivity, and high electrical conductivity. Some metals are also biocompatible. The applications of metals in miniaturized products include micro-die/mold, medical implants, sensory devices, thermal exchange components, and structural components. Due to their importance and application, mechanical micro-machining of metals is extensively studied; a large number of publications can be found in literature (Cardoso & Davim 2010, Chae et al. 2006, Dornfeld et al. 2006, Jin & Altintas 2012, Masuzawa 2000, Saedon et al. 2012, Schueler et al. 2010, Taniguchi 1983). Metals and their alloys which are normally encountered in mechanical micro-machining include steels, aluminum, copper, brass, nickel and titanium and their alloys.

Polymers are another group of materials which find an application in miniaturized products. Polymers have advantages of light weight, translucent or transparent, high chemical passivity, and low cost. The applications of polymers include microfluidic devices, micro-needles, and medical devices and implants. It is true that polymers are

commonly fabricated by extrusion and injection molding processes which offer higher productivity. However, such processes are mostly suitable for mass production since cost of making mold/die tooling is expensive. Mechanical-micro machining offers a solution for low cost fabrication of customized polymer products. Polymers have low strength which makes them easy to be machined; however, machined parts or features can be easily ruined by excessive cutting force or cutting temperature. Therefore, low material removal rate is usually employed to avoid such problems.

1.2 Micro-end milling process

Micro-end milling process is one of the mechanical micro-machining processes. It is a scale down version of the conventional end-milling process. Micro-end milling is typically used to produce a miniature parts that are not axially symmetric and have many features, such as holes, slots, pockets, and even three dimensional surface contours. Micro-end milling is also commonly used as a secondary process to add or refine features on miniature parts that were manufactured using a different process such as molding or casting (Aramcharoen et al. 2008).

1.2.1 Characteristics of micro-end milling

In terms of process characteristics, micro-end milling is almost the same as conventional macro-end milling; the major difference is the size of the tools. Micro-end milling process generally involves material removal by spinning flat-bottom or ball-end tools into the workpiece creating a feature shape. Tools which are called micro-end mills are mostly made of fine grain tungsten carbide in a cobalt matrix (WC/Co). Micro-end mills with a diameter as small as 25 μm are commercially available (Liu et al. 2004). Figure 1.1 shows the image of typical flat micro-end mill. Since, the tool diameter is

extremely small, the machine tool is required to have a very high spindle speed, typically 10,000-100,000 rpm, in order to maintain high cutting velocity and material removal rate. Moreover, the machine tool used for micro-end milling process is required to have higher precision and lower vibration compared to conventional machine tool used for macro-end milling (Bang et al. 2005).

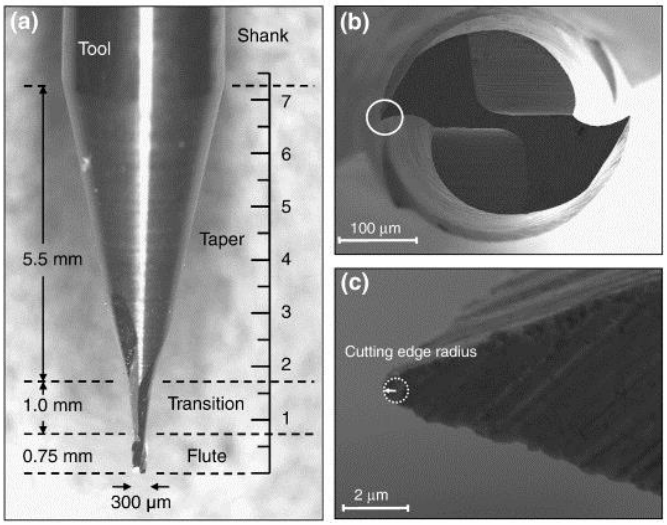

Figure 1.1: (a) Typical flat micro-end mill, (b) The bottom of flat micro-end mill, and (c) SEM image of a corner of the tool with edge radius (Heaney et al. 2008).

Micro-end milling is still a tool-based material removal process; hence it very much relies on the performance of the micro-milling tools. Also this happens to be a barrier limiting the capability of mechanical micro-machining. This problem is encountered when scaling down the tool there are some features of the tool which cannot be reduced further. This problem affects one of the most critical tool geometry, the edge radius. A limitation of grinding technology, grain size and edge strength limits further reduction of the edge radius. Inevitably, the micro-tools are normally fabricated with an edge radius of 1-5 µm (Bissacco et al. 2008).

1.2.2 Capabilities of micro-end milling

Micro-end milling has a high potential to be the major process for customized fabrication of complex miniature parts. Since, it is the most flexible mechanical micro-machining process. It is capable of fabricating 3-D complex shape out of unlimited choice of materials; metals, polymers, glasses and ceramics. Also, it has a high material removal rate compared to other micro-manufacturing processes. In addition, micro-end milling does not require a lot of setup which makes it to become ideal for customized products. Most feature shapes such as groove, cavity, contour and complex surface can be machined using micro-end milling. The feature size, as small as 5-10 μm, can be achieved (Friedrich & Vasile 1996).

1.2.3 Micro-end milling of metals

Micro-end milling of metals are widely implemented, especially in machining of dies/molds. Hence, investigations of micro-end milling of steels are extensively reported. Ding et al. (Ding et al. 2011) studied micro-end milling of hardened H13 tool steels. Tungsten carbide micro-end mills with a diameter of 100 μm were used. The machined surface integrity, geometrical accuracy, size effect, and tool wear progression were experimentally investigated. They reported that the accumulated geometrical error was about 1%; the surface roughness on machined side surface was found to be around 0.5 μm; large burr and built-up edge (BUE) were detected. Saedon et al. (Saedon et al. 2012) conducted the experiment on micro-end milling of AISI D2 hardened steel (62 HRC) by using 4-flute TiAlN coated tungsten carbide end-mills with a diameter of 500 μm. The cutting edge radius was measured to be around 5-7 μm. The experiments were carried out in full immersion slot milling. The results were mainly discussed in terms of tool life.

They found that cutting speed is the main influencing factor on the tool life followed by feed per tooth and axial depth of cut. Also, tool life prediction model was developed based on the experimental results. Komatsu et al. (Komatsu et al. 2012) conducted the micro-end milling tests on stainless steel to investigate the effect of grain size. They reported that burr formation can be controlled by reduction of grain size. Afazov et al. (Afazov et al. 2012) studied micro-end milling of AISI H13 steel. Their results showed that the cutting force and cutting temperature increase by increasing the hardness while the stability of the process decrease by increasing the hardness.

Another material which is normally applied in many miniature products is aluminum and its alloys. Friedrich (Friedrich 2002) has fabricated some prototypes out of aluminum using micro-end milling process. The small capillary channels of 50 μm were machined. He also recommended that mechanical micro-machining is well suited for fabrication of quick and inexpensive prototypes with reasonably good precision. The study by Saptaji et al. (Saptaji et al. 2012) on micro-end milling of aluminum alloy Al-6061 using tungsten carbide tool revealed the effects of side edge angle and effective rake angle on top burr formation. Top burrs can be reduced by both strengthening the side edge and introducing a taper into the milling tool. Kuram and Ozcelik (Kuram and Ozcelik 2013) have investigated micro-end milling of aluminum alloy Al 7075 using ball-end mill. The effects of spindle speed, feed per tooth, and axial depth of cut on tool wear, force components and surface roughness were discussed. Annoni et al. (Annoni et al. 2013) studied the effect of cutting strategy and process parameters on fabrication of aluminum thin wall using micro-end milling. The process parameters and cutting strategy

were chosen to minimize the cutting forces and thus improved thin wall machining accuracy.

Since the applications of miniature products include aerospace and medical applications, machining of super alloys such as nickel alloys and titanium alloy is also investigated. Ucan et al. (Ucan et al. 2013) experimentally investigated the micro-end milling of Inconel 718 super alloy. The effect of tool coating material on tool wear was extensively studied. Their results showed that the micro-end mills coated with TiAlN, TiAlN+AlCrN and AlCrN displayed better performances. Chen et al. (Chen et al. 2012) studied the micro-end milling of titanium alloy Ti-6Al-4V using ball-end mills. The study mainly focused on burr formation in the slot milling process. Similarly, Schueler et al. (Schueler et al. 2010) studied burr formation in micro-end milling of Ti-6Al-4V and Ti-6Al-7Nb. Micro-end mills with 48 μm diameter was developed and used in this study.

1.2.4 Micro-end milling of polymers

Micro-end milling is a promising process for fabricating customized miniature parts out of polymers due to advantages of high material removal rate and low setup cost. Polymers such as polymethyl methacrylate (PMMA) and polydimethylsiloxane (PDMS) provide transparency which is necessary for the applications such as microfluidic devices. Also, many types of polymers are considered biocompatible and can be applied in medical devices and implants.

So far, micro-end milling processes for polymers have not been extensively studied. There is a limited literature on this topic. Rainelli et al. (Rainelli et al. 2003) have fabricated PMMA based miniature flow injection analyzers using micro-end milling with a V-shaped tip engraving tool. Channel cross-sections had a trapezoidal shape of

approximately 150 µm depth and a width from 180 to 360 µm. Filiz et al. (Filiz et al. 2008) introduced the technique of fabrication micro-scale piercing elements (microbarbs). The special V-shaped and T-shaped micro-end mills were utilized to create microbarbs out of PMMA. Kakinuma et al. (Kakinuma et al. 2008) have proposed a cryogenic cooling assisted micro-milling system. The system can be applied to a soft polymer material such as PDMS. The liquid nitrogen was applied to cool the material down to the glassy state which can be easily machined. Ali et al. (Ali et al. 2013) studied the vibration issue in micro-end milling of PMMA. The analysis revealed the optimal parameters which minimize vibrations at a spindle speed of 2500 rpm, a feed rate of 2 mm/min and a depth of cut of 1.5 µm.

1.3 Material removal at micro-scale

As feature size is reduced, the role of material micro-structure becomes much more pronounced. This issue has never arisen in the macro-scale mechanical machining, since the feature size is relatively large compared to the grain size. However, removing material at a micro-scale is done relatively at the same size or smaller than the grain size. As a result, the cutting mechanism at micro-scale and associated process responses may be altered significantly as the cutter engages in different phase and/or grain of the workpiece material.

1.3.1 Cutting with round edge tools

The assumption which is normally used in macro-scale cutting is that the cutting edge is perfectly sharp and there is no contact between the cutting tool and workpiece along the clearance face (Liu et al. 2004). The chip is formed by the mechanical shearing force due to the interaction between sharp tool and workpiece. This assumption, however,

fails to apply in a micro-scale cutting due to the size of cutting edge radius that becomes significantly larger compared to the thickness of material to be removed. Therefore, assuming that the cutting edge is perfectly sharp is not valid in micro-scale cutting. Since, the sharp cutting edge model assumption fails to explain the material removal at micro-scale; Kim and Kim (Kim and Kim 1995) have proposed a round cutting edge model to be applied in micro-scale cutting. The round cutting edge model takes into account the sliding along the clearance face of the tool due to the elastic recovery of the workpiece and the ploughing due to the large negative effective rake angle resulting from the cutting tool edge radius. The difference between the sharp cutting edge model in macro-scale cutting and the round cutting edge model in micro-scale cutting is illustrated in Figure 1.2

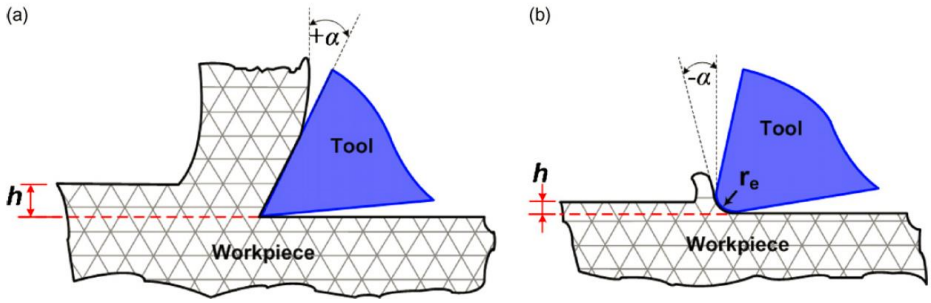

Figure 1.2: (a) macro-scale cutting, (b) micro-scale cutting (Aramcharoen & Mativenga 2009)

1.3.2 Size effect

At small uncut-chip thicknesses, the specific energy required to remove a unit amount of material increases. This phenomenon is referred as “size effect” (Armarego & Brown 1961, Nakayama & Tamura 1968). Mechanical micro-machining experiences size effect due to several reasons. One main reason is due to the fact that all material contain defects (grain boundaries, missing and impurity atoms, etc.), and when the size of the material removed decreases, the probability of encountering a stress-reducing defect

decreases (Shaw 2003). Other reasons include ploughing of the material under the tool due to a large negative effective rake angle; tangential and normal pressure under the flank face of the tool due to elastic recovery of the material; and the strain rate dependency of the material.

1.3.3 Minimum chip thickness

Often, mechanical micro-machining is subjected to a phenomenon, usually referred to as the "minimum chip thickness". The minimum chip thickness is a critical value of uncut-chip thickness where the material removal can be achieved. Machining below this value produces no chip and the entire material is subjected to elastic deformations. Figure 1.3 shows how the chip is formed relative to the minimum chip thickness. If the uncut-chip thickness (h) is smaller than the minimum chip thickness (h_m), chip is not formed; the tool ploughs on the workpiece surface and the material is only subject to the elastic deformations (Figure 1.3a). If the uncut-chip thickness is equivalent to the minimum chip thickness, the material will be subject to both plastic and elastic deformations. Some part of the material will partially form a chip while the rest elastically recovers (Figure 1.3b). The last case is when the uncut-chip thickness is larger than the minimum chip thickness. At this condition, chip is formed without any elastic recovery yielding a favorable cutting condition (Figure 1.3c).

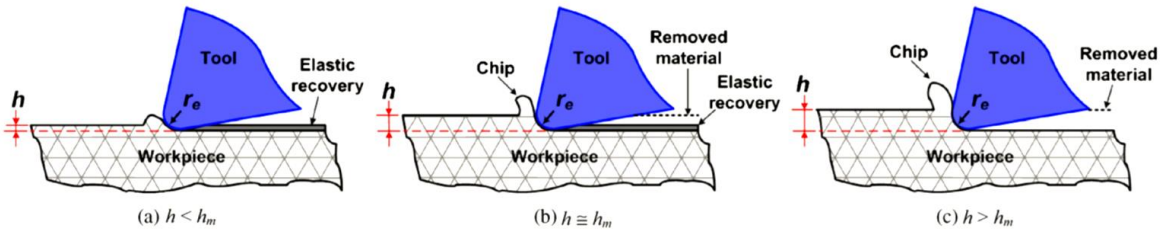

Figure 1.3: Chip formation relative to the minimum chip thickness (Aramcharoen & Mativenga 2009)

Basuray et al. (1977) defined the minimum chip thickness to be a ratio of the uncut-chip thickness to cutting edge radius. Many researchers have attempted to find this critical value using experiment, numerical analysis and simulation (Ikawa et al. 1991, Son et al. 2005, Vogler et al. 2004, Weule et al. 2001, Yuan et al. 1996). However, the value of minimum chip thickness varies depending on a tool-workpiece material, friction between tool-chip interface, workpiece microstructure and size of cutting edge radius. Therefore, determining the minimum chip thickness is very difficult. Based on several studies on determining the value of minimum chip thickness, one would say that the best approach is to employ a value of uncut-chip thickness larger than or equal to the cutting edge radius to ensure the shearing domination. However, the value of uncut-chip thickness is generally limited by the tool and workpiece rigidity. Too large uncut chip thickness may lead to rapid tool wear or sudden tool breakage.

1.4 Process performances in micro-end milling

There are several responses which are used to evaluate the process performance of micro-end milling. Among them, burr formation, surface roughness, tool wear, cutting force and cutting temperature are the key responses determining the success of the process. Especially, burr formation and surface roughness are directly related to the satisfactory level of quality produced.

1.4.1 Burr formation

Burr is the undesirable projection part of a workpiece which is produced through manufacturing processes on an edge or a surface which lies outside the desired geometry (Ko & Dornfeld 1991, Narayanaswami & Dornfeld 1997). Even though burr is not desirable, it is unavoidable. The only solution is to reduce it to an acceptable degree in

which machined part can function properly. Burr in end-milling can be categorized by the position where it occurs as shown in Figure 1.4. Burr formation mechanism is very complicated involving plastic and elastic deformations which are influenced by material properties, tool geometry and machining parameters (Aurich et al. 2009). Burr in micro-end milling of metal alloys such as titanium alloy can be relatively large compared to the feature size as shown in Figure 1.5

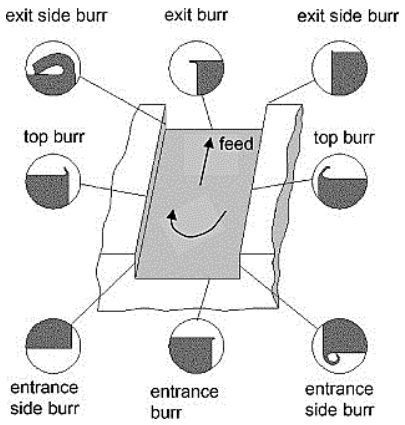

Figure 1.4: Type of end-milling burr (Hashimura et al. 1999)

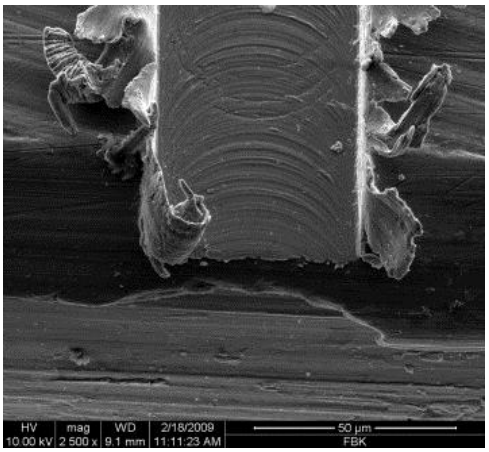

Figure 1.5: Burr of micro-end milling of Ti-6Al-7Nb (Schueler et al. 2010)

There is a large number of burr measuring and detecting methods available. The choice depends on application conditions, requested measuring accuracy and burr values to be measured such as burr height, burr width, burr thickness, burr volume or burr hardness; among those burr height, burr width and burr thickness are the most frequently and easily measured burr values. Some examples of burr measuring method include stylus method, metallographical profile, optical micro scope, scanning electron microscope and confocal microscope.

1.4.2 Surface roughness

One of the most commonly used methods to quantify the quality of machined surface is its surface roughness. Surface roughness is a measure of the texture of a surface. It is quantified by the vertical deviations of a real surface from its ideal form. Surface roughness is normally specified based on the function of the surface. Machine parameters have to be set in order to achieve a desired surface roughness. In macro-machining, it is widely known that surface roughness is majorly affected by the feed rate. Selecting a proper feed rate, most of the time, can yield the desired surface roughness. However, in micro-machining such as micro-end milling there are more factors to be concerned such as minimum chip thickness, size effect, tool deflection, and material properties (Liu et al. 2006a, Liu et al. 2006b, Vogler et al. 2004). Therefore, it is more complicated to select optimal process parameters which result in a desired surface roughness.

1.4.3 Tool wear

Rapid tool wear is a very critical problem in micro-end milling; especially, when it comes to difficult-to-machine materials such as titanium alloys. As tool wear progress,

cutting force, surface roughness and geometrical accuracy will increase. Excessive tool wear may even lead to ultimate tool breakage. The factors that can be attributed to tool wear in micro-end milling are elastic recovery of workpiece, dynamic deflections, tool run-out, and low feed instability (Malekian et al. 2009).

Even though tool wear is undesirable, tool breakage seems to be a more important problem in micro-end milling. Tiny micro-end mills can eventually break when either their cutting edges become dull or a chip clogs. Tansel et al. (Tansel et al. 1998) have found that micro-end mills break quickly as they wear out. This is due to the increase of cutting force of the dull tool causing the stress to exceed the strength of the tiny diameter micro-end mills.

1.4.4 Cutting force

Cutting force in micro-end milling is influenced by several parameters such as feed per tooth, cutting velocity, axial depth of cut, cutting edge radius, helix angle, etc. Cutting force changes dynamically throughout the cutting process due to a variation of uncut-chip thickness at different tool rotational angle. Cutting force in micro-end milling can be measured using dynamometer; however, it requires a very high sampling rate and a capability to suppress the environmental noise. In addition, cutting force can be predicted by analytical models or simulations.

In micro-end milling, the tiny micro-end mills are not rigid enough to sustain a very high cutting force. Tool breakage can be expected if cutting force exceeds a certain limit. Cutting force also determines the degree of tool deflection and the bending stress that limit the feed rate (Chae et al. 2006). Therefore, the ability to predict cutting force prior to executing the cutting process would be greatly beneficial. Well-developed

analytical or simulation models as decision support systems would be helpful for users to choose the right cutting condition for their systems.

1.4.5 Cutting temperature

During a chip formation process, some of energy is released in terms of heat. This heat raises both tool and workpiece temperature. It is generally known that heat has both positive and negative effects on the macro-machining process. It can soften the workpiece and lower the yield strength, making it easy to cut. However, high temperature can promote tool wear. Heat generation depends on the machining parameters and friction between tool and workpiece materials. In case of micro-machining, it is still doubtful about the benefit of heat, since heat may promote even more elastic deformation in the micro-machining process. Unfortunately, there is no information have been reported about this issue.

The determination of temperatures and temperature distribution in the area around the cutting edge and workpiece interface is technically difficult. Some tools and methods that are generally used to measure the cutting temperature are thermocouple method, infrared thermometer and camera and thermographic phosphor thermometry. Due to the difficulty of measurement, analytical models and simulations become an alternative to the direct measurement. It should be noted that cutting temperature measurement has never been conducted in micro-end milling.

1.5 Finite element modeling and simulation

Even though experiment is most reliable way to study a machining process, it sometimes can be costly and very time consuming. Moreover, experiment may not be able to provide the information that the user needs due to the technological limitation.

Modeling and simulation provide an alternative to the experiment. It can help the user to gather desired information at a lower cost. One of the commonly used methods for modeling and simulation of machining process is finite element (FE) method. The FE method is a method of assembling structural elements, which can be separately analyzed, into a global equation of equilibrium for the structure. It has a capability to analyze both mechanics and thermodynamics of the systems, thus it is very suitable for the analysis of machining processes.

1.5.1 FE modeling and simulation of the material removal processes

Material removal processes involve generation of chips by the engagement of tool and workpiece. Plastic deformation plays a major role in material removal processes. The outputs of this process include distributions of stress (von Mises), strain (elastic and plastic), forces, temperature, and wear (rate and depth). FE modeling and simulation has been widely used for analysis and predicting these outputs in the material removal processes for several decades. Thanks to the advancements in computer technology, FE modeling and simulation is now even more powerful than before. Several finite-element techniques are available today for accurate and efficient modeling of the material removal processes: material and geometrical non-linear analysis, mesh rezoning techniques, element-separation for chip formation modeling, element separation criteria, tool wear modeling, residual stress prediction, etc. (Mackerle 1998, Arrazola et al. 2013).

There are two basic models for the FE simulations: orthogonal model (2-D), and oblique (3-D) model. Most machining processes are oblique but the orthogonal model studies are easier to simulate and they can be useful or adequate for understanding the basic mechanics of material removal processes. There are plenty of studies using FE

modeling and simulation to predict cutting force, tool wear, chip formation, stress, strain and cutting temperature (Mackerle 2003, Mackerle 1998, Mamalis et al. 2001, Özel et al. 2010, Özel & Altan 2000, Özel & Zeren 2007, Tay et al. 1974, Umbrello 2008, Yen et al. 2004). In many cases the FEM simulations have also been validated by comparisons with the results of experimental investigations.

1.5.2 FE modeling and simulation of the micro-end milling process

Beside experimental study, FE simulation is another option to study the physical phenomena of the micro-end milling process. Micro-end milling process has also been analyzed by using FE methods which lead to the prediction of chip formation, cutting forces, and stress, strain and temperature distributions. Dhanorker and Özel (Dhanorker and Özel 2008) have conducted one of the pioneering studies on the 2-D FE modeling and simulation of micro-end milling of aluminum and steel. The results showed that the temperature distribution within the tool and the workpiece, cutting forces in terms of normal force and feed force and chip flow can be predicted with reasonable accuracy. Weng et al. (Weng et al. 2009) have studied the chip formation in micro-end milling of aluminum alloy using a 2-D FE simulation approach. In this study, the FE simulation was used to predict the chip velocity, strain rate, contact pressure, cutting force and chip flow. The results from FE simulations were validated with the experiments. Ding et al. (Ding et al. 2011) conducted FE analysis on micro-end milling of hardened H13 tool steel. Their 2-D FE model was developed using ABAQUS software to simulate the continuous chip formation in full immersion slot milling and side cutting conditions. The steady state cutting temperature was investigated. The FE simulation results were discussed in terms of cutting forces, chip formation, stress, temperature, and velocity field. They also

reported that the built-up edge in micro-machining can be predicted with the FE model. Afazov et al. (Afazov et al. 2010, Afazov et al. 2012) modeled the micro-end milling of AISI 4340 steel and AISI H13. The 2-D FE simulations were utilized to predict the cutting forces. The effect of uncut chip thickness, cutting velocity and edge radius were included. Jin and Altintas (Jin and Altintas 2012) have utilized a 2-D FE model for predicting the micro-end milling forces of machining brass. In this case, a series of FE simulations was used to evaluate the cutting force coefficients which were then used to obtain the cutting forces. In short, it can be seen that the use of FE modeling and simulation in micro-end milling is still very limited. Moreover, the applications of FE modeling and simulation are also limited to the orthogonal (2-D) model only, even though the micro-end milling is a form of oblique cutting process.

1.6 Optimization of micro-end milling parameters

The goal of every machining process is to achieve the best performance and reliability. These can be accomplished through optimization of process parameters. In micro-end milling, process parameters include cutting velocity, feed, axial and radial depth of cut, up/down milling, lubrication method, cutting tool geometry, tool path strategy, etc. Unlike the macro-end milling process in which the performance has been extensively studied and optimized, optimization of micro-end milling is still immature; most users still rely on trial and error methods. There are only a few attempts to come up with the decision support system which can facilitate the selection of process parameters. In order to provide decision support system tools researchers have developed several studies. Özel and Liu (Özel and Liu 2009) proposed a mechanics-based process planning approach for micro-end milling of micro-mold cavities. The goal is to facilitate proper

selections of the process parameters for a given workpiece material, cavity geometry, and micro-end mill. Cardoso and Davim (Cardoso and Davim 2010) performed a comprehensive study on the machined surface of micro-end milling of aluminum alloy. The feed rate and machining strategies were optimized to obtain the best surface roughness. Seadon et al. (Seadon et al. 2012) predicted and optimized the tool life in micro-end milling of hardened steel using response surface methodology (RSM). The tool life equations were generated and the tradeoff between tool life and material removal rate (MRR) was analyzed. Kuram and Ozcelik (Kuram and Ozcelik 2013) conducted the multi-objective optimization for micro-end milling of aluminum alloy. The Taguchi based gray relational analysis was utilized for optimization and modeling.

In general, objectives in optimization of machining processes include small surface roughness, small burr formation, high material removal rate, high geometrical accuracy, long tool life, etc. These objectives normally conflict with each other. For example, increasing material removal rate normally results in short tool life. Therefore, optimization in machining process can be very tricky, since there are several objectives to be considered at the same time. Multi-objective optimization can provide a solution to this problem. Nevertheless, it is not yet extensively applied into optimization of micro-end milling processes.

2. Motivation

Miniature products generally require tighter control over geometrical tolerance and surface quality compared to conventional macro-products. However, succeeding these specifications is very difficult. The right choice of process parameters have to be made in order to achieve the desired quality, productivity and reliability. The common

method of optimizing the process parameters is to investigate by experimentation. However, in micro-machining this can be very difficult and time-consuming task. Furthermore, many of process response such as temperature, stress and strain cannot be determined by the experiment alone. Hence, most of the time, the micro-machining are conservatively used under its full capability to avoid excessive tool wear, tool deflection, and tool breakage. This totally reduces the productivity of the micro-end milling process and makes it less competitive.

FE modeling and simulation can be used as an alternative to the experiment or it can even be used to support the experimental results. With advancements in computer technology, FE simulation becomes even more affordable. It can provide good predicted results within a short period of time and at a much lower cost compared to the experimentation. Use of FE simulations in micro-scale cutting would be more beneficial compared to macro-scale cutting, since observation and obtaining any experimental data in micro-scale is much more difficult and costly. FE simulation also allows in depth analysis into process mechanics of material removal at micro-scale which is very beneficial for research and development of micro-machining processes. In spite of its benefits, so far, the implementation of FE modeling and simulation into investigations of micro-end milling processes has not been widely adopted.

Instead of a trial and error approach, it would be very helpful to have the decision support system which can help a user in making choices about process parameters such as cutting velocity, feed rate, depth of cut, tool material and coating, etc. The integration of experimentation, FE modeling and simulation and optimization techniques can provide such a decision support system. The data generated from experiments and FE simulations

can be optimized and used as a resource to make decision based on the user's requirements.

In this study, micro-end milling of metals and polymers were selected as a case study. The traditional experimentation was carried out to study and optimize the process. The 2-D and 3-D FE models of micro-end milling of titanium alloy will be developed to simulate the process responses which will be used to support the experimental results. Then, both experiment and FE simulation results will be integrated and optimized. The final result will be a decision support system which can provide viable choices based on the user's requirements.

3. Objectives

The overall objective of this study is to investigate and optimize the micro-end milling of metals and polymers. The following specific objectives of the proposed approach address the overarching research goal:

Objective 1: To optimize the process parameters such as cutting velocity, feed per tooth, axial depth of cut, and tool coating for micro-end milling of titanium alloy Ti-6Al-4V.

Objective 2: To develop an orthogonal (2-D) FE model for micro-end milling of titanium alloy which can be used to analyze the influence of process parameters such as cutting velocity, feed per tooth, and tool coating. The simulation parameters such as material assumption will be tested to observe its influence over the chip formation in the FE simulation.

Objective 3: To develop an oblique (3-D) FE model to simulate the chip flow in micro-end milling of titanium alloy Ti-6Al-4V. The model will also be used to study the influence of worn cutting edge over the tool wear.

Objective 4: To integrate the results from both experiments and FE simulations and develop a decision support system for micro-end milling of titanium alloy Ti-6Al-4V.

Objective 5: To utilize the obtained knowledge into fabrication of miniature prototypes out of Ti-6Al-4V titanium alloy and polymers such as PMMA.

4. Organization of the Dissertation

The organization of this dissertation can be detailed as follows:

In Chapter 2, the experimental procedure and findings will be reported for micro-end milling tests. The feasibility study of using acoustic emission signal to monitor surface generation in micro-end milling of titanium alloy will be explained in detail. The statistic-based process optimization utilizing the response surface methodology (RSM) will be discussed. Also the multi-objective optimization using particle swarm technique will be presented.

In Chapter 3, the comparison study between cBN coated WC/Co micro-end mill and uncoated WC/Co micro-end mill will be explained in detail. The main focus of this chapter is to investigate the benefit of cBN coated tool in micro-end milling of titanium alloy Ti-6Al-4V. Also, the extensive study on the effects of process parameters such as spindle speed, feed per tooth and axial depth of cut will be presented and discussed. In addition, the multi-objective optimization of the micro-end milling process using cBN coated tool will be presented.

In Chapter 4, 2-D finite element (FE) modeling and simulation of micro-end milling of titanium alloy Ti-6Al-4V will be explained in detail including the material constitution modeling, tool and workpiece geometry, contact and friction determination, meshing technique, material assumption and simulation controls. The simulation results

will be used to support the experimental findings presented in Chapters 2 and 3. Moreover, a comparison of viscoplastic and elasto-viscoplastic models will be presented and discussed.

In Chapter 5, 3-D FE modeling and simulation of micro-end milling of titanium alloy Ti-6Al-4V will be explained. The comparison of 2-D and 3-D FE simulation results will be discussed. The influence of tool wear on the performance of micro-end milling of titanium alloy Ti-6Al-4V will be investigated using 3-D FE simulations.

In Chapter 6, the integration of experiments and FE simulations will be used to construct a decision support system for micro-end milling of titanium alloy Ti-6Al-4V. Several optimization schemes based on multi-objective particle swarm optimization will be utilized to find a set of process parameters which can satisfy the manufacturing requirements and optimize the process performance. The machining validation tests which were guided by the decision support system will be presented.

In Chapter 7, applications of micro-end milling will be presented. The purpose of this chapter is to point out the capability of micro-end milling process. Therefore, various micro-features and micro-products fabricated using micro-end milling process will be presented showing the capability and limitation of the micro-end milling process. Also, the development and investigation of tool path strategy on micro-end milling of micro thin walls and micro-needle arrays will be reported and discussed.

In Chapter 8, contributions and future research directions are discussed.

CHAPTER 2

SENSOR-ASSISTED MONITORING AND OPTIMIZATION OF PROCESS PARAMETERS

1. Introduction

In micro-end milling, obtaining the desired results is much harder than in macro-end milling due to several reasons such as size effect, tool deflection, burr formation and rapid tool wear. The problem is much more pronounced when workpiece material is a difficult-to-process material such as titanium alloys which are widely used as the material of choice for medical devices and implants. Therefore, in order to achieve the desired performance, optimization of process parameters is necessary.

Monitoring of surface generation in micro-machining is proven to be very helpful since the degree of uncertainty in the micro-machining process is relatively high and the small-scale processes make it difficult to be visually observed (Malekian et al. 2009, Tansel et al. 1998a, Tansel et al. 1998b). For instance, tool may be chipped or broken without being noticed resulting in poor surface generation. Therefore, in order to maintain a desired level of surface quality in micro-end milling, it may be necessary to have a capability of direct monitoring so that an adaptive control or correction can be performed.

Although, various sensors such as acoustic emission (AE), accelerometer and force sensors are widely utilized to monitor tool wear and tool breakage in micro-end milling (Malekian et al. 2009), the use of AE sensors for monitoring surface generation is not fully explored. It is also well known that force sensors with limited frequency bandwidth (<1 kHz) are not suitable to monitor micro-end milling process where tooth

passing frequencies are in the order of 1-5 kHz for two-flute end mills rotating between 50,000-150,000 rpm.

Acoustic emission is a class of phenomena whereby transient elastic waves are generated by rapid release of energy from localized sources within a solid material and has been used in monitoring machining processes for more than two decades (Lu 2008). An advantage of using AE for process monitoring over the other approaches is that the frequency bandwidth of AE is much higher (1-104 kHz) than that of machine vibrations and ambient acoustic noise (Beggan et al. 1999). Many research efforts on AE based systems have been directed towards the prediction and monitoring of tool condition in machining processes such as turning (Bhaskaran et al. 2012, Dolinšek & Kopač 1999, Govekar et al. 2000, Jemielniak & Otman 1998, Jemielniak 2001, Kosaraju et al. 2012, Leem & Dornfeld 1996, Li 2002, Ravindra et al. 1997), milling (Ai et al. 2012, Kaya et al. 2012, Prickett & Johns 1999), drilling (König et al. 1992, Neugebauer et al. 2012) and grinding (Inasaki 1998, Lee et al. 2006). Several researchers are interested in the use of AE signal to monitor quality of machined surfaces such as surface roughness (Diniz et al. 1992, Jiang et al. 2013) and surface anomalies (Guo & Ammula 2005). However, it should be noted that such AE signal based systems were well-developed for the conventional macro-machining process.

As previously mentioned that AE signal is capable of monitoring surface generation in macro-milling; however, it has never been deployed in micro-end milling before. Therefore, in this chapter, a feasibility of using AE signal to monitor the surface generation in micro-end milling of Ti-6Al-4V titanium alloy was explored. In addition, the multi-objective optimization of process parameters was also conducted.

This study consists of three phases: experimental, modeling and optimization. The first phase, experimental phase, was where the physical micro-milling experiments were conducted in order to collect all necessary data in terms of AE signal, surface roughness and burr formation. The main method in this phase was a design of experiment (DOE) using Taguchi orthogonal arrays. In the second phase, modeling phase, all data obtained in the experimental phase was used to formulate the predictive models. In this phase the Response Surface Methodology (RSM) was used to construct the predictive models. Finally, the last phase, optimization phase, was carried out in order to obtain the optimal parameters that satisfy the multi-criteria quality requirement. The multi-objective particle swarm optimization (MOPSO) was selected as an optimization method for this phase. The work flow and tools used in each phase is shown in Figure 2.1.

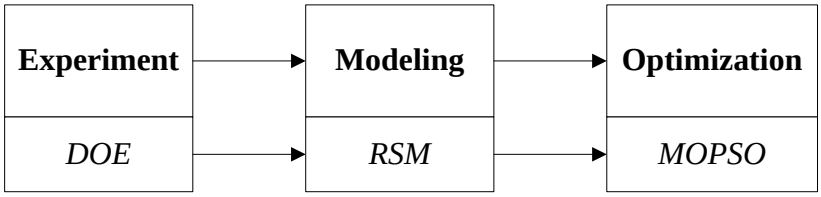

Figure 2.1: Work flow and methods utilized.

2. Experimental Analysis

In this section, the elements of experiments will be explained in detail including experimental setup, tools and workpiece selection and preparation, process responses measurement and experimental methodologies.

2.1 Micro-end milling experiments

The micro-end mills with two-flute, flat-bottom were used throughout this study. The tools were made of fine grain tungsten carbide (grain size of 0.2-0.5 μm) in a cobalt matrix (WC/Co) manufactured by Richards Micro Tools company. The helix angle of the tools is 30° and the effective cutting length is 0.18 mm. The nominal diameter of 635 μm was selected in this study. All fresh micro-tools were inspected with digital microscopy. The mean edge radius of the tool is 3 ±0.5 μm.

In this study the workpiece was selected to be titanium alloy, Ti-6Al-4V, which has a chemical composition as shown in Table 2.1. The mechanical and thermal properties of Ti-6Al-4V are given in Table 2.2.

Table 2.1: Chemical composition of Ti-6Al-4V.

Element	Ti	Al	V	Fe	O	C	N	H	Others
%	Balance	6	4	0.25	0.13	0.08	0.03	0.01	0.4

Table 2.2: Mechanical and thermal properties of Ti-6Al-4V.

Property	Unit	Value
Ultimate Strength	MPa	896
Yield Strength (0.2%)	MPa	827
Hardness	HRC	36
Thermal Expansion	K^{-1}	$9*10^{-6}$
Density	$kg*m^{-3}$	4430
Melting Point	K	1380
Elastic Modulus	GPa	42
Thermal Conductivity	$W*m^{-1}*K^{-1}$	6.6
Specific Heat Capacity	$J*kg^{-1}*K^{-1}$	565

The experimental setup consists of several components as shown in Figure 2.2 and Figure 2.3. The rectangular block of Ti-6Al-4V titanium alloy workpiece was clamped on the fixture mounted on the 3-axis positioning stage. The workpiece surfaces were precisely ground to ensure high flatness and well alignment. The 3-axis positioning stage is controlled by the numerical control software (Unidex 500 MMI W32) with the resolution of 0.1 μm for each axis. The micro-end mill tool was directly mounted to the ceramic bearing-electrically driven precision spindle (NSK ASTRO-E 800) with the tool overhang of 18 mm. The CCD camera connected with the monitor was used to facilitate the zero setting and monitor the process. The acoustic emission (AE) sensor (Kistler piezotron 8152B) with built-in impedance converter was mounted on the fixture. The AE sensor was connected to the coupler with built-in root-mean-square (RMS) converter and limit switch for processing high frequency sound emission signal. The coupler was connected to the computer for data acquisition using Klister-Dynoware software.

2.2 Surface roughness measurement

Surface roughness was measured in terms of average surface roughness (R_a) using a stylus surface roughness tester (Mitutoyo SJ-400) which provide the maximum resolution of 0.000125 μm. JIS 1994 standard was selected. Five measurements were taken from the bottom surface of machined channels then the average was taken to represent the surface roughness of the machined channel. Before taking surface roughness measurement, all burrs were removed from the channel to prevent their interfering with the measurement. Burrs were manually removed under the optical microscope using mechanical tools.

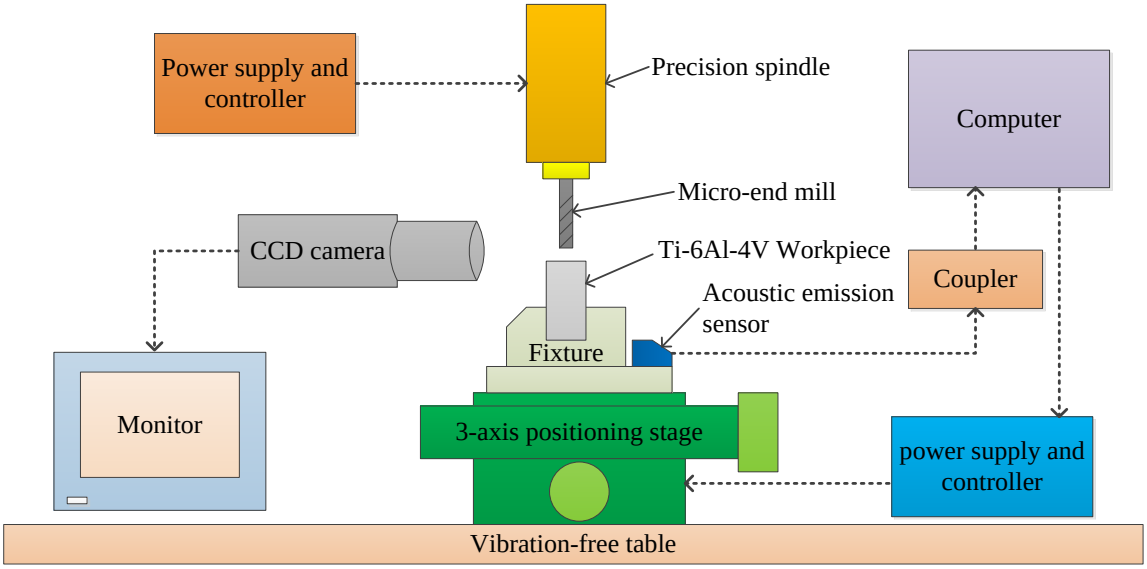

Figure 2.2: Schematic diagram of the experimental setup.

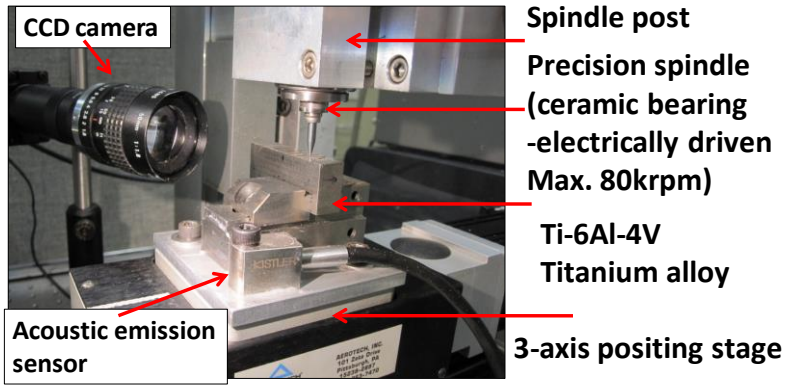

Figure 2.3: Image of experimental setup.

2.3 Burr formation measurement

A degree of burr formation was quantitatively measured in terms of total top-burr width (B_T). The illustration of top-burr width definition is shown in Figure 2.4. Top-burr width was measured using optical microscope. The measurement was taken from both sides of the channel: up-milling side and down-milling side as shown in Figure 2.5. The measurements were taken where the top-burr width is uniform. Three measurement

repetitions were applied and the average values were taken. A total top-burr width (B_T) is an addition of both top-burr widths form down milling side (B_d) and top-burr width from up milling side (B_u) of the channel which can be calculated using Eq. (2.1).

$$B_T = B_d + B_u \qquad \text{Eq. (2.1)}$$

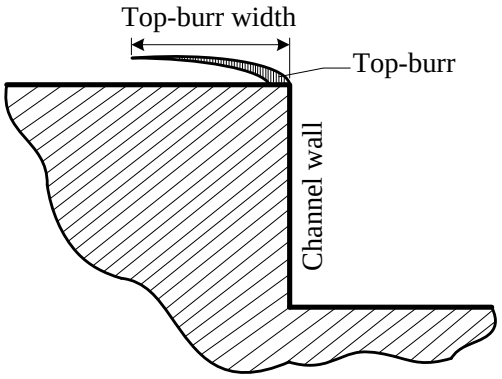

Figure 2.4: Definition of top-burr width.

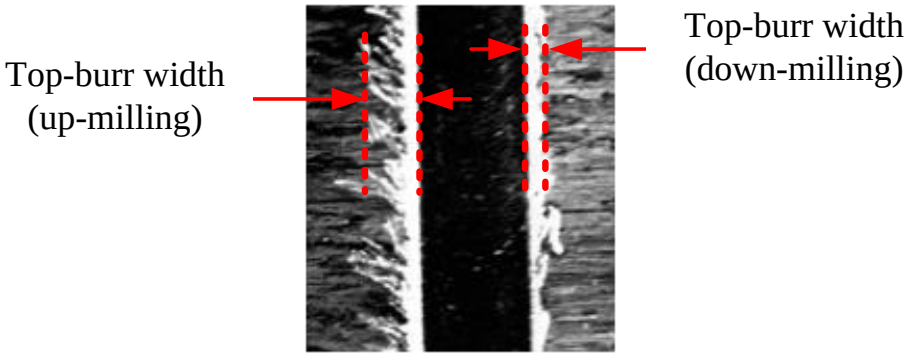

Figure 2.5: Image of top-burr width.

2.4 Acoustic emission signal measurement

AE signal was collected form the whole period of cutting at the sampling frequency of 50 kHz. The raw signal was filtered and calculated into the root mean

square (RMS) value (AE_{RMS}) with the sampling number (n) of 5. Eq. (2.2) shows the general formula for the RMS value. The mean AE_{RMS} was then calculated for the comparison purpose. The signals were also plotted over the time domain for the signal analysis.

$$x_{RMS} = \sqrt{\frac{1}{n}(x_1^2 + x_2^2 + x_3^2 + \ldots + x_n^2)} \qquad \text{Eq. (2.2)}$$

2.5 Experimental designs

The experiment was designed based on L9 Taguchi orthogonal array as shown in Table 2.3. The controlled factors include spindle speed (Ω), feed per tooth (f_z), and axial depth of cut (a_p). Three levels were chosen for each factor based on the literatures and limitation of the machine tool. The results were collected in terms of average surface roughness (R_a), total top-burr width (B_T) and AE_{RMS} signal. The experiment was conducted on the full-immersion slot milling process. The length of cut was 12 mm. Two replications were taken for each experimental condition.

3. Process Modeling

In order to optimize the parameters of micro-milling process, it is necessary to construct relationships between the response and each interested process parameter. One of the well-known methods serving this purpose is Response Surface Methodology (RSM). RSM is a collection of mathematical and statistically based technique useful for the modeling and analysis of problems with several process variables. It also has important applications in the design, development, and formulation of new products, as well as in the improvement of existing product designs (Montgomery 2005). The most extensive applications of RMS are in the situation where several input variables

(independent variables) potentially influencing some performance measure or quality characteristic of the product or process (response). Since the form of the relationship between the response and the independent variable is unknown, the first step in RSM is to find the suitable approximation for the true functional relationship between response (y) and the set of independent variables ($\boldsymbol{x}$).

Table 2.3: Experimental conditions.

Run	Factors			
	Tool	**Ω (krpm)**	**f_z (µm/tooth)**	**a_p (µm)**
1	WC/Co Ø 635 µm	20	0.1	20
2		20	0.3	60
3		20	0.5	100
4		40	0.1	60
5		40	0.3	100
6		40	0.5	20
7		60	0.1	100
8		60	0.3	20
9		60	0.5	60

Usually a low-order polynomial function in some relatively small region of the independent variable space provides a suitable approximation of the true form of the response function. In many cases, either a first-order or a second-order model is sufficient. The general form of the first-order, first-order with interaction and second-order RSM model are shown in Eq. (2.3), Eq. (2.4) and Eq. (2.5), respectively, where β is a RSM coefficient of each term, k is a number of independent variables and ϵ is a residual error.

$$y = \beta_0 + \sum_{i=1}^{k} \beta_i x_i + \epsilon \qquad \text{Eq. (2.3)}$$

$$y = \beta_0 + \sum_{i=1}^{k} \beta_i x_i + \sum_{i<j} \sum \beta_{ij} x_i x_j + \epsilon \qquad \text{Eq. (2.4)}$$

$$y = \beta_0 + \sum_{i=1}^{k} \beta_i x_i + \sum_{i<j} \sum \beta_{ij} x_i x_j + \sum_{i=1}^{k} \beta_{ii} x_i^2 + \epsilon \qquad \text{Eq. (2.5)}$$

The first-order model is sometimes called a main effect model, because it includes only the main effect of the variables. If there is an interaction between these variables, the interaction terms can be easily added as shown in Eq. (2.4). Adding the interaction terms introduces a curvature into the response function. If the curvature in the true response surface is strong enough that the first-order model (even with the interaction terms included) is inadequate. A second-order model will be required.

The second-order model is widely used in RSM for several reasons. First, the second-order model is very flexible; it can take on a wide variety of functional forms. Second, an estimation of the coefficient (β) can be done easily by the method of least squares. Furthermore, there is a considerable practical experience indicating that the second-order works well in solving real response surface problems (Myers & Anderson-Cook 2009).

In this study, surface roughness (R_a) and total top-burr width (B_T) were selected as responses while spindle speed (Ω), feed per tooth (f_z) and axial depth of cut (a_p) were independent variables. The experimental results obtained from the experiments were used to formulate the RMS models for each response. Analysis of variance (ANOVA) was conducted to determine the appropriateness of these models. In addition, the graphical surfaces of the models were plotted to visually observe the effects of individual variables.

4. Process Optimization

Typically, it appears that the relationship between machining parameters and machining responses are non-linear which is sometimes very difficult to optimize analytically. The problem becomes even more difficult when there is a need to optimize

more than one objective at a time (i.e. multi-objective optimization). Multi-objective optimization problems represent an important class of real-world problems. Typically such problems involve trade-offs meaning that their objectives are generally conflicting with each other. For example, mold manufacturers may want to obtain minimum surface roughness, but meanwhile they also want to minimize the machining time. Generally, there is no single optimal solution. Therefore "trade-off" has to be considered before choosing the suitable solution. The curve or surface (for more than two objectives) describing the optimal trade-off solutions between objectives are known as the Pareto front. A multi-objective optimization algorithm is required to find solutions as close as possible to the Pareto front, while maintaining good solution diversity along the Pareto front.

In this study, the Multi-Objective Particle Swarm Optimization (MOPSO) was selected, since it has many advantages over other optimization methods. It works very efficiently to locate the Pareto front of the multi-objective optimization problems. Also it is relatively easy to implement and has a few parameters to adjust.

In general, Particle Swarm Optimization (PSO) is a population-based stochastic optimization technique modeled on the social behaviors observed in animals or insects, e.g., bird flocking, fish schooling, and animal herding. PSO was developed by Kennedy and Eberhart in 1995 (Kennedy & Eberhart 1995). Since its inception, PSO has gained increasing popularity among researchers and practitioners as a robust and efficient technique for solving difficult optimization problems. In PSO, individual particles of a swarm represent potential solutions, which move through the variable space seeking an optimal, or good enough, solution. The particles relay their current positions to

neighboring particles. The position of a particle is modified by using its previous position information and its current velocity (i.e. rate of change). As the model is iterated, the swarm focuses more and more on an area of the search space containing high-quality solutions (Blum & Li 2008).

In PSO, the velocity of each particle is modified iteratively by its personal best position (i.e., the best position found by the particle so far), and the best position found by particles in its neighborhood (Eq.2.6 and 2.7). As a result, each particle searches around a region defined by its personal best position and the best position from its neighborhood.

$$\boldsymbol{v}_i^{k+1} = w\boldsymbol{v}_i^k + k_1\boldsymbol{R}_1\left(\boldsymbol{p}_i - \boldsymbol{x}_i^k\right) + k_2\boldsymbol{R}_2\left(\boldsymbol{p}_g - \boldsymbol{x}_i^k\right) \qquad \text{Eq. (2.6)}$$

$$\boldsymbol{x}_i^{k+1} = \boldsymbol{x}_i^k + \boldsymbol{v}_i^{k+1} \qquad \text{Eq. (2.7)}$$

Where $\boldsymbol{v}_i^k$ denotes the velocity of the i^{th} particle at k^{th} iteration in the swarm, $\boldsymbol{x}_i^k$ denote its current position which can be considered as a set of coordinates describing a point in space, $\boldsymbol{p}_i$ denotes the personal best positions, $\boldsymbol{p}_g$ denotes the best position found by particles in its neighborhood, w denotes a inertia weight, k_1 and k_2 are acceleration coefficients and $\boldsymbol{R}_1$ and $\boldsymbol{R}_2$ are two separate functions each returning a vector comprising random values uniformly generated in the range [0, 1]

Eq. (2.6) shows that the velocity term $\boldsymbol{v}_i^k$ of a particle is determined by three parts, the "momentum", the "cognitive", and the "social" part. The "momentum" term $w\boldsymbol{v}_i^k$ represents the weighted ratio of previous velocity term which is used to carry the particle in the direction it has travelled so far; the "cognitive" part, $k_1\boldsymbol{R}_1\left(\boldsymbol{p}_i - \boldsymbol{x}_i^k\right)$, represents the tendency of the particle to return to the best position it has visited so far; the "social" part, $k_2\boldsymbol{R}_2(\boldsymbol{p}_g - \boldsymbol{x}_i^k)$, represents the tendency of the particle to be attracted

towards the position of the best position found by the entire swarm. The random numbers used in the velocity update step give the PSO a stochastic behavior. It should be noted that the "momentum" term has a tendency to explode to a large value, resulting in particles exceeding the boundaries of the search space. This is more likely to happen especially when a particle is far from $\boldsymbol{p}_g$ or $\boldsymbol{p}_\mathrm{i}$. To overcome this problem, a velocity clamping method can be adopted where the maximum allowed velocity value is set to V_{max} in each dimension of $\boldsymbol{v}_i$.

Position $\boldsymbol{p}_\mathrm{g}$ in the "social" part is the best position found by particles in the neighborhood of the i^{th} particle. Different neighborhood topologies can be used to control information propagation between particles. Constricted information propagation as a result of using small neighborhood topologies has been shown to perform better on complex problems, whereas larger neighborhoods generally perform better on simpler problems (Mendes et al. 2004). Generally speaking, a PSO implementation that chooses $\boldsymbol{p}_g$ from within a restricted local neighborhood is referred to as *lbest* PSO, whereas choosing $\boldsymbol{p}_\mathrm{g}$ without any restriction (hence from the entire swarm) results in a *gbest* PSO.

Algorithm below summarizes a basic PSO algorithm.

- *Initial Step:* Randomly generate an initial swarm position and velocities. The current position of each particle is set as $\boldsymbol{p}_i$. The $\boldsymbol{p}_i$ with best value is set as $\boldsymbol{p}_\mathrm{g}$.
- *Step 1:* For each particle, the objective function value is evaluated. If an agent achieves a better objective value, $\boldsymbol{p}_i$ is replaced by the current position $\boldsymbol{x}_i$.
- *Step 2:* Set $\boldsymbol{p}_\mathrm{g}$ equal to the best collected $\boldsymbol{p}_i$ values.

- *Step 3:* Update the velocity by Eq. (2.6) and update the position by Eq. (2.7).
- *Step 4:* Return to step 1 and repeat until the termination criterion is met.

PSO algorithms have been applied to optimization problems ranging from classical problems such as scheduling, the traveling salesman problem, neural network training, and task assignment, to highly specialized applications. In recent years, PSO has also become a popular choice for many researchers in handling multi-objective optimization problems in manufacturing processes (Ciurana et al. 2009, Karpat & Özel 2007, Vazquez et al. 2011).

In this study, MOPSO methodology proposed by Alvarez-Benitez et al. (Alvarez-Benitez et al. 2005) is adopted. The selection of global guides ($\boldsymbol{p}_g$) is based on Pareto dominance. An external archive is used to store the non-dominated solutions found by the algorithm. When new non-dominated solutions are found, they are entered into the archive and existing members of the archive are deleted if they are dominated by the new solutions. The idea is to select a global guide for a particle from the archive members that dominate the particle. One particle can be dominated by more than one non-dominated solution. The selection can be made randomly or a promotion value can be assigned to each non-dominated solution which increases with the number of iterations. An archive member with high promotion value is more likely to be picked as a global guide. After an archive member is selected, its promotion value is reset to zero. In addition, the archive members in densely populated regions are more likely to dominate more particles than the archive members in sparsely populated regions.

The MOPSO algorithm was implemented in MATLAB, the RSM models formulated from the previous phase served as objective functions, $f(\boldsymbol{x})$ and $g(\boldsymbol{x})$. After completion of the MOPSO algorithm, the Pareto frontier was located indicating a set of solutions in the multi-objective domain. Moreover, all solutions were plotted in a variables domain showing the optimal level of each process parameter.

5. Results and Discussions

5.1 Experimental results

Table 2.4 shows the results obtained from the experiment. The results from the table can be summarized and plotted as main effects plots as shown in Figures 2.6, 2.7 and 2.8. The plots shown in Figures 2.9, 2.10 and 2.11 illustrated the effect of each process parameter on the mean AE_{RMS} and average surface roughness. The comparison of AE_{RMS} signal against surface generation and burr formation over various levels of spindle speed, feed per tooth, and axial depth of cut are shown in Figures 2.12, 2.13 and 2.14, respectively.

Table 2.4: Experimental results.

Run	Factors				Results											
	Tool	Ω (krpm)	f_z (µm/tooth)	a_p (µm)	B_T (mm)				R_a (µm)				AE_{RMS} (v)			
					Rep. 1	Rep. 2	Avg.	Std.	Rep. 1	Rep. 2	Avg.	Std.	Rep. 1	Rep. 2	Avg.	Std.
1	WC/Co Ø 635 µm	20	0.1	20	0.212	0.340	0.276	0.091	0.257	0.263	0.260	0.017	0.14	0.12	0.130	0.014
2		20	0.3	60	0.280	0.396	0.339	0.082	0.140	0.113	0.127	0.016	0.18	0.19	0.185	0.007
3		20	0.5	100	0.225	0.194	0.210	0.022	0.107	0.150	0.128	0.025	0.23	0.29	0.260	0.042
4		40	0.1	60	0.126	0.291	0.209	0.117	0.180	0.163	0.172	0.012	0.28	0.30	0.290	0.014
5		40	0.3	100	0.166	0.227	0.197	0.043	0.153	0.157	0.155	0.012	0.37	0.43	0.400	0.042
6		40	0.5	20	0.364	0.249	0.307	0.081	0.100	0.117	0.108	0.013	0.33	0.30	0.315	0.021
7		60	0.1	100	0.143	0.083	0.113	0.042	0.163	0.150	0.157	0.010	0.54	0.50	0.520	0.028
8		60	0.3	20	0.371	0.142	0.257	0.162	0.153	0.163	0.158	0.010	0.47	0.43	0.450	0.028
9		60	0.5	60	0.185	0.112	0.149	0.052	0.127	0.110	0.118	0.012	0.63	0.70	0.665	0.049

Figure 2.6 and Figure 2.7 illustrate the main effects for total top-burr width and average surface roughness, respectively. Table 2.5 and Table 2.6 show the ANOVA of total-top burr width and average surface roughness, respectively. Based on the ANOVA result, at the significant level of 0.1, the influence of all tested process parameters to top-burr formation are significant. The main effects plot indicates that increase spindle speed (Ω) and axial depth of cut (a_p) reduce top-burr formation; setting the feed per tooth at low level minimize top-burr formation. In addition, it was observed that the top-burr widths from up-milling are larger than those from down-milling. In terms of average surface roughness, it can be seen that the main effect of feed per tooth (f_z) is ranked number one among all three factors; the ANOVA also indicates that it is the only significant factor affecting the surface roughness. The results infer that increasing feed per tooth results in better surface roughness.

In summary, both surface roughness and top-burr formation are parameter dependent. Based on the experimental results; setting spindle speed and feed per tooth at high levels and axial depth of cut at medium level yields the lowest surface roughness; and setting spindle speed and axial depth of cut at high level and feed per tooth at low level yields minimum total top-burr width. However, these settings are not the same meaning that obtaining the best result for both performance measurements is not possible. One process performance has to be sacrificed in order to attain another. Therefore, using the multi-objectives optimization technique would be very helpful for this difficult decision making.

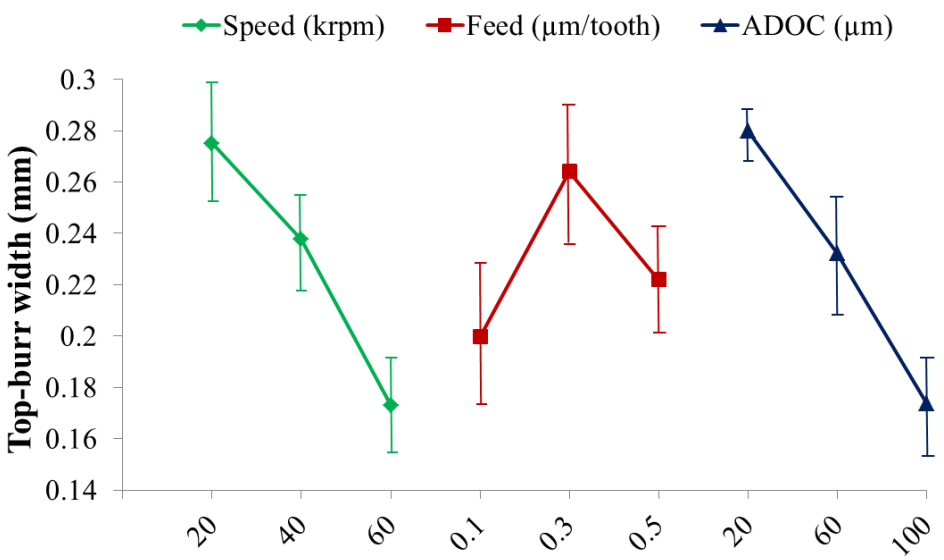

Figure 2.6: Main effects plot for total top-burr width.

Table 2.5: ANOVA table for total top-burr width.

Source	DF	Adj SS	Adj MS	F-value	P-value
Ω	2	2.6667	1.3333	16.00	0.059
f_z	2	2.1667	1.0833	13.00	0.071
a_p	2	6.0000	3.0000	36.00	0.027
Error	2	0.1667	0.0833		
Total	8	11.0000			

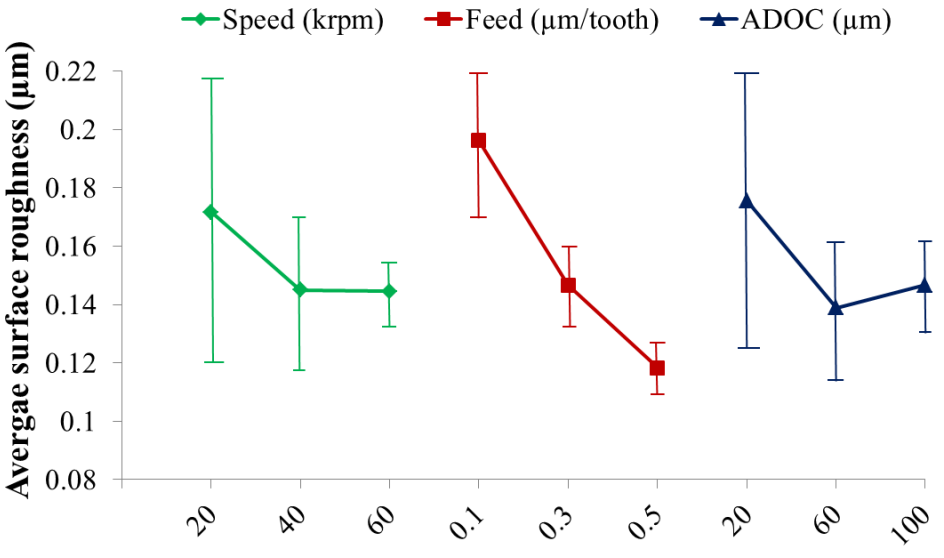

Figure 2.7: Main effects plot for average surface roughness.

Table 2.6: ANOVA table for average surface roughness.

Source	DF	Adj SS	Adj MS	F-value	P-value
Ω	2	0.0002469	0.0001235	0.18	0.849
f_z	2	0.0303136	0.0151568	21.76	0.044
a_p	2	0.0002969	0.0001485	0.21	0.824
Error	2	0.0013932	0.0006966		
Total	8	0.0322506			

The main effects plot in Figure 2.8 suggests that the mean AE_{RMS} increases as spindle speed, feed rate and axial depth cut increase. This implies that the mean AE_{RMS} is related to the material removal rate (MRR). Higher spindle speed, feet rate and axial depth of cut results in higher MRR. As a result of more material being deformed in a unit time, the energy released from deformations would increase, hence RMS value of AE signal increases. The ANOVA table (Table 2.7) shows that, at a significant level of 0.1, the spindle speed significantly affects the mean AE_{RMS}.

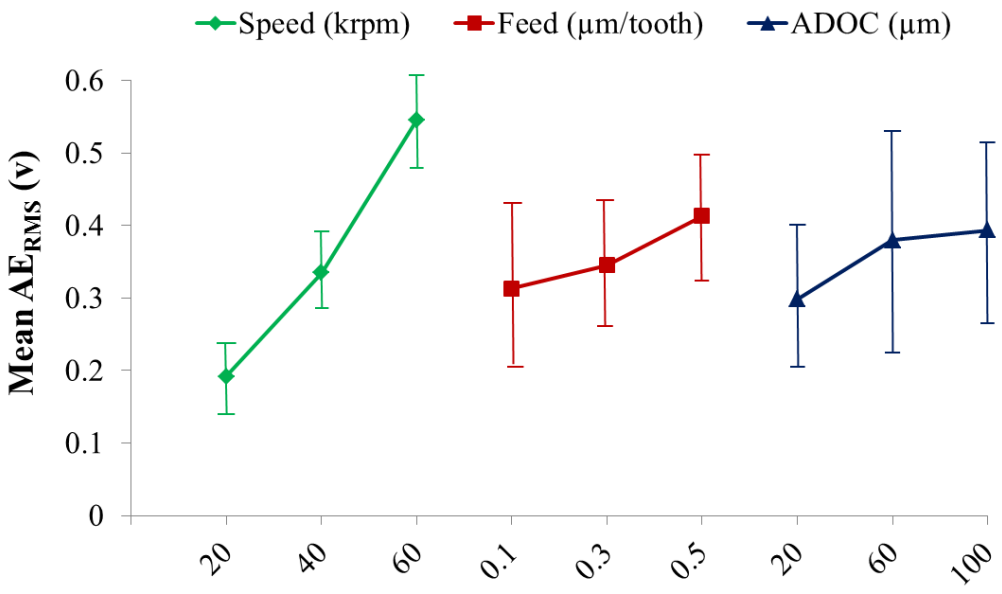

Figure 2.8: Main effects plot for mean AE_{RMS}

Table 2.7: ANOVA table for mean AE_{RMS}

Source	DF	Adj SS	Adj MS	F-value	P-value
Ω	2	0.189489	0.094744	24.70	0.039
f_z	2	0.015672	0.007836	2.04	0.329
a_p	2	0.015872	0.007936	2.07	0.326
Error	2	0.007672	0.003836		
Total	8	0.228706			

Figures 2.9, 2.10 and 2.11 show the relationship between mean AE_{RMS} and average surface roughness (R_a). It can be seen that there is no evidence of strong correlation between the mean AE_{RMS} and average surface roughness. Therefore, it can be concluded that the mean AE_{RMS} is not suitable for determining and monitoring of the surface generation in micro-end milling.

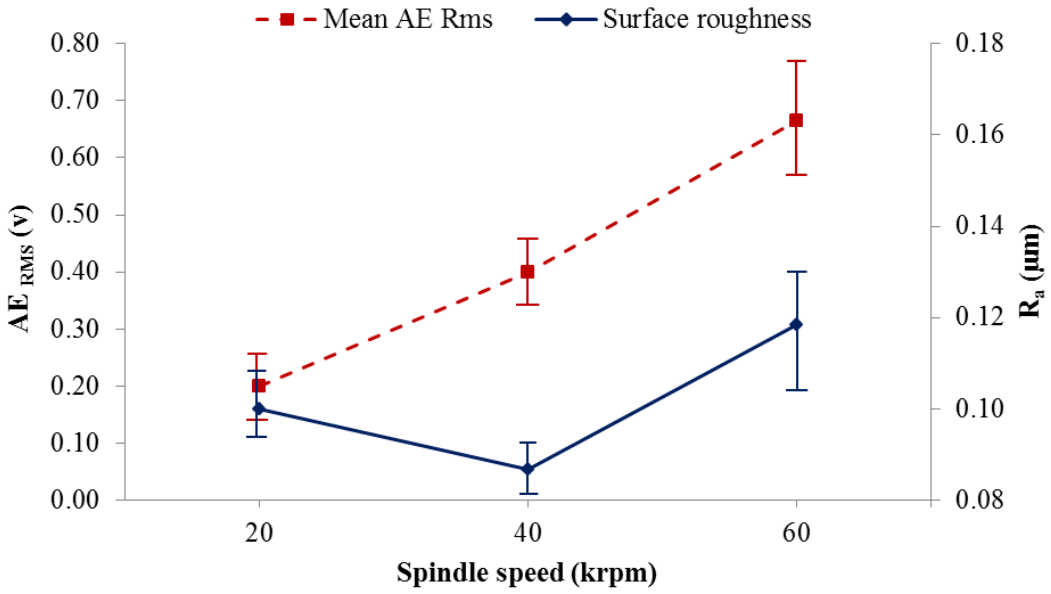

Figure 2.9: Effect of spindle speed on mean AE_{RMS} and R_a

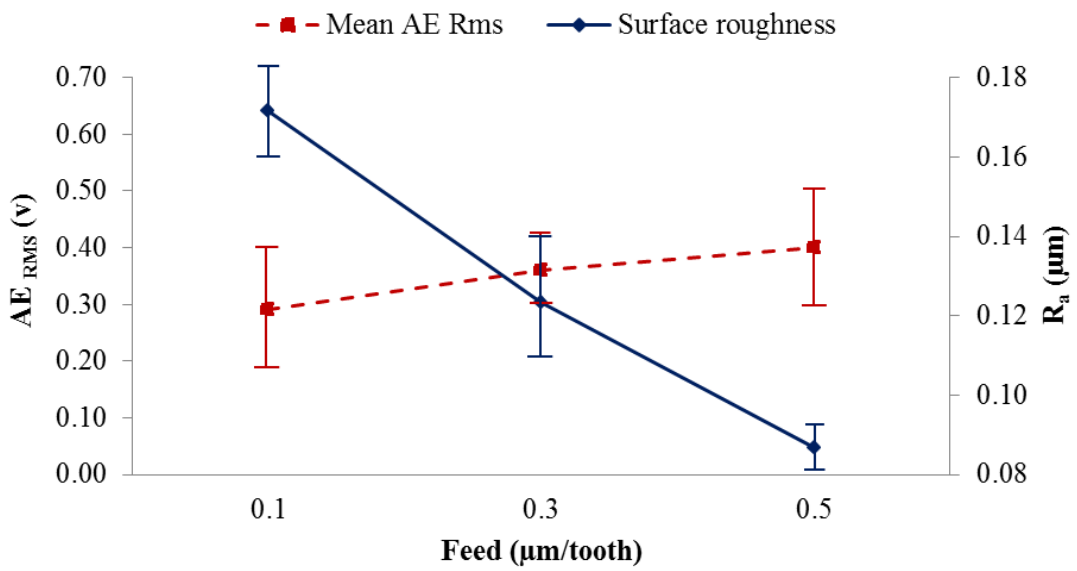

Figure 2.10: Effect of feed per tooth on mean AE_{RMS} and R_a

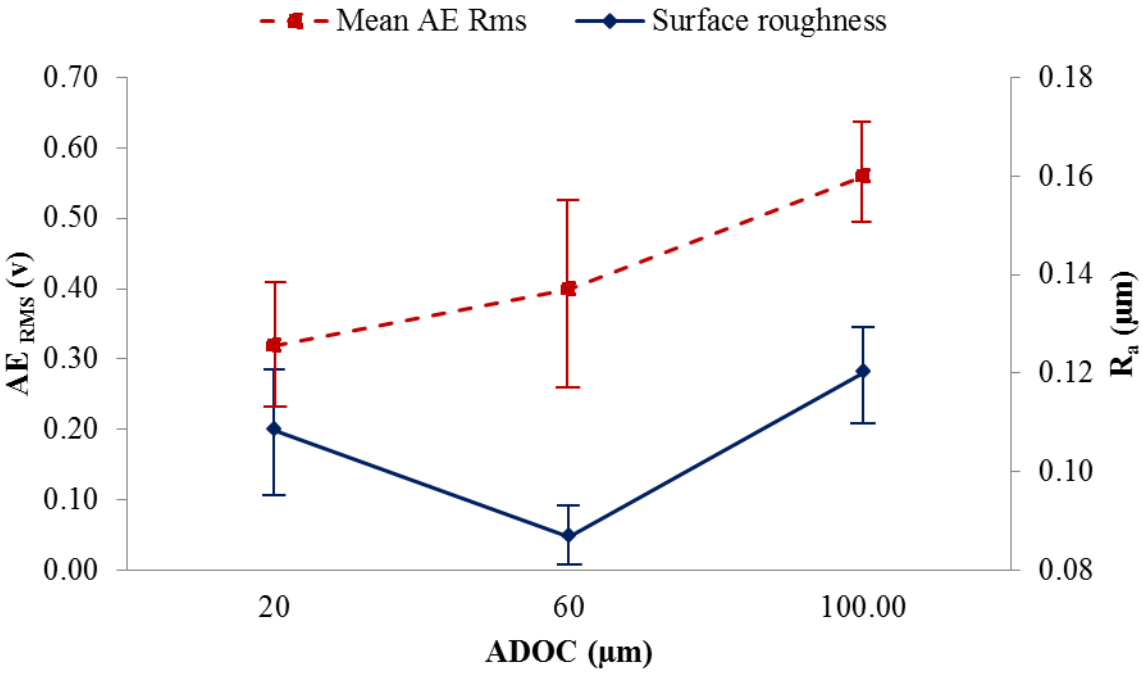

Figure 2.11: Effect of axial depth of cut on mean AE_{RMS} and R_a

In Figure 2.12, it can be observed that the deviation of AE_{RMS} amplitude significantly increases as spindle speed is increased. Also, it seems that an increasing rate of AE_{RMS} amplitude deviation over the testing range of spindle speed is constant. In terms of surface roughness, it does not change according to an increase of the deviation of AE_{RMS} amplitude. However, notice that highly deviatory AE_{RMS} amplitude at high spindle speed results in high surface roughness which clearly leaves strong feed marks appearing on the machined surface.

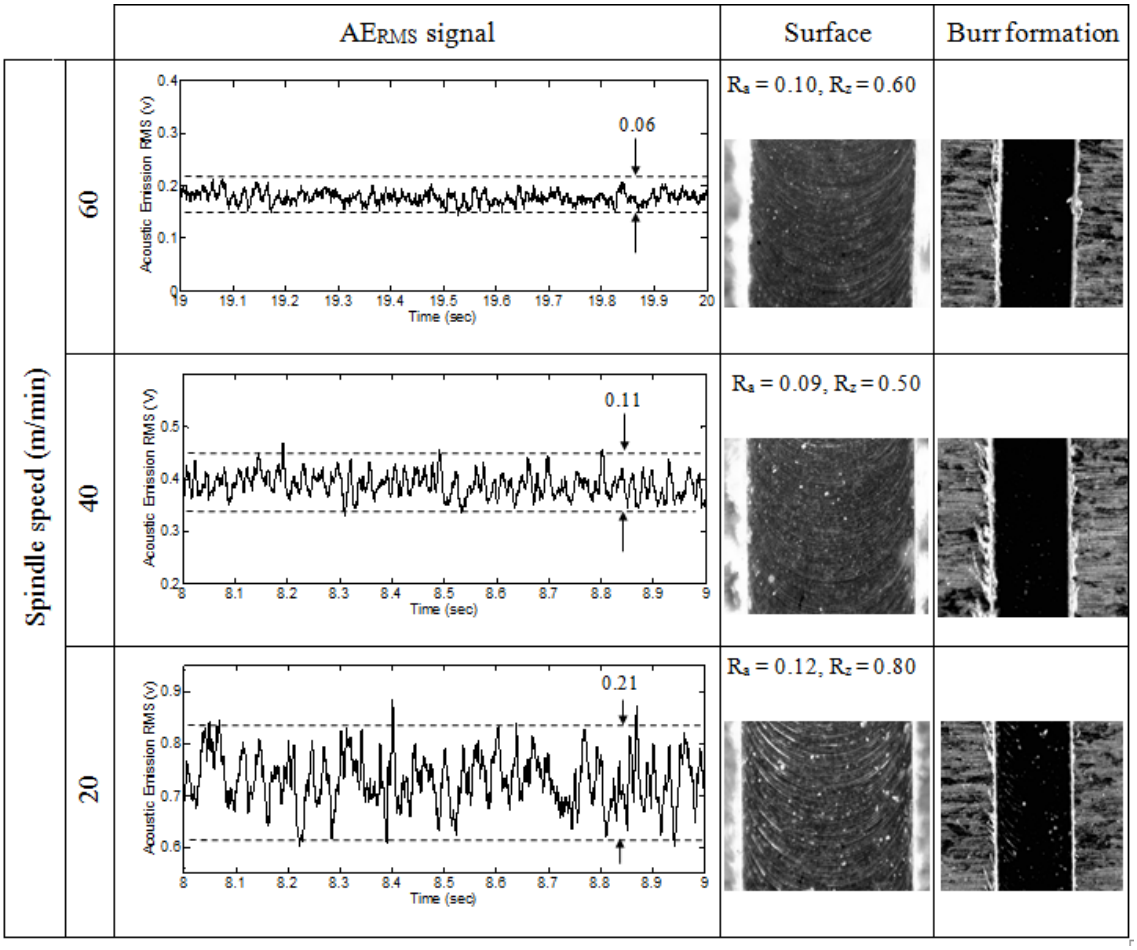

Figure 2.12: Effect of cutting speed on AE_{RMS} signal, surface quality and burr formation

On the other hand, Figure 2.13 indicates that an effect of feed rate on the variation of AE_{RMS} is insignificant. However, in spite of an unchanged AE_{RMS} signal deviation over feed rate, the result shows that surface roughness improves significantly as feed rate is increased. Therefore, the deviation of AE_{RMS} signal may have no correlation with the surface generation. However, notice that the waveform of AE_{RMS} signal is different in each level of feed rate and increased feed rate seems to result in a more uniform and denser waveform. Similarly, surface roughness is improved as the AE_{RMS} signal waveform becomes more uniform and denser.

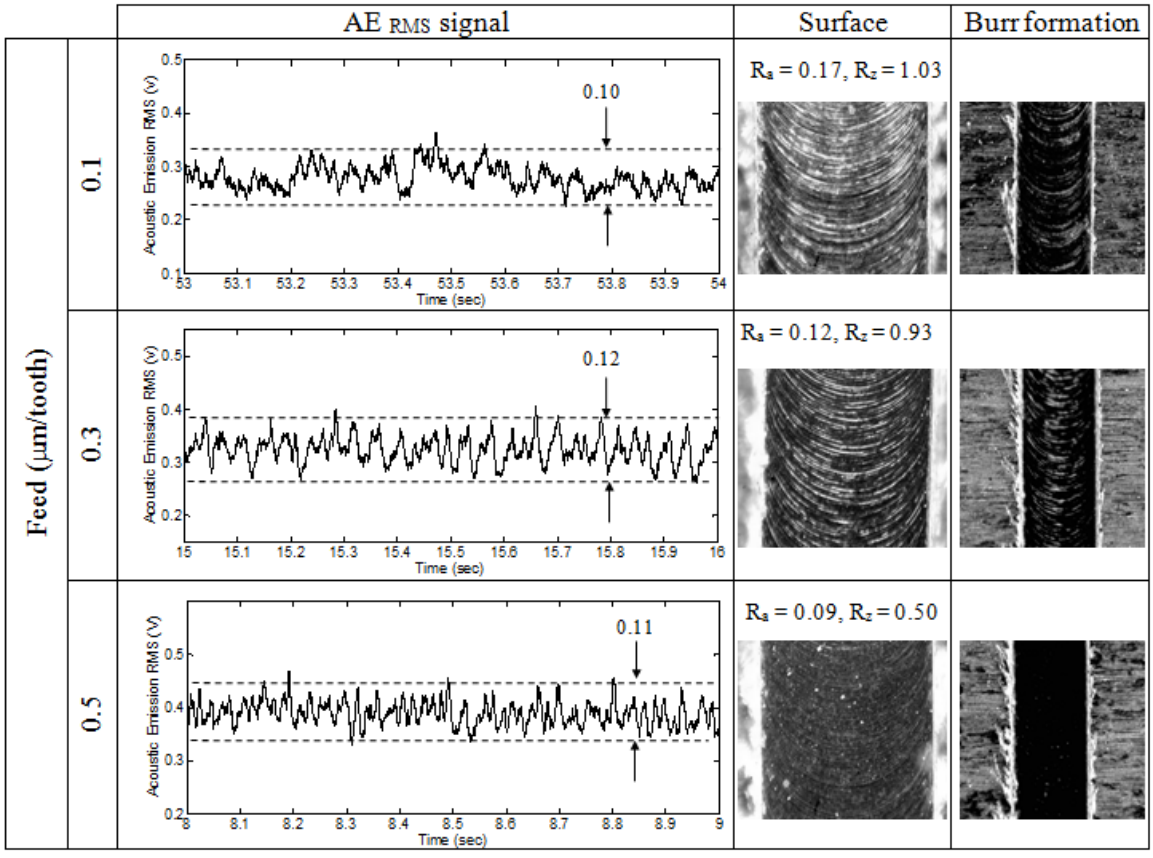

Figure 2.13: Effect of feed per tooth on AE_{RMS} signal, surface quality and burr formation

It is possible that the generation of AE_{RMS} signal is influenced by the ploughing dominated and shearing dominated phenomena occurring in micro-end milling. The ploughing dominated cutting may result in a non-uniform AE_{RMS} signal representing an unsmooth cutting process which generates a surface with higher roughness. In contrast, the shearing dominated condition may generate a uniform AE_{RMS} signal representing a smooth cutting process in which low surface roughness can be achieved.

In Figure 2.14, the effect of axial depth of cut is investigated. The results show an increasing trend of the deviation of AE_{RMS} amplitude which highly increases at higher axial depth of cut. High deviation of AE_{RMS} amplitude at high axial depth of cut seems to result in high surface roughness compared to the others.

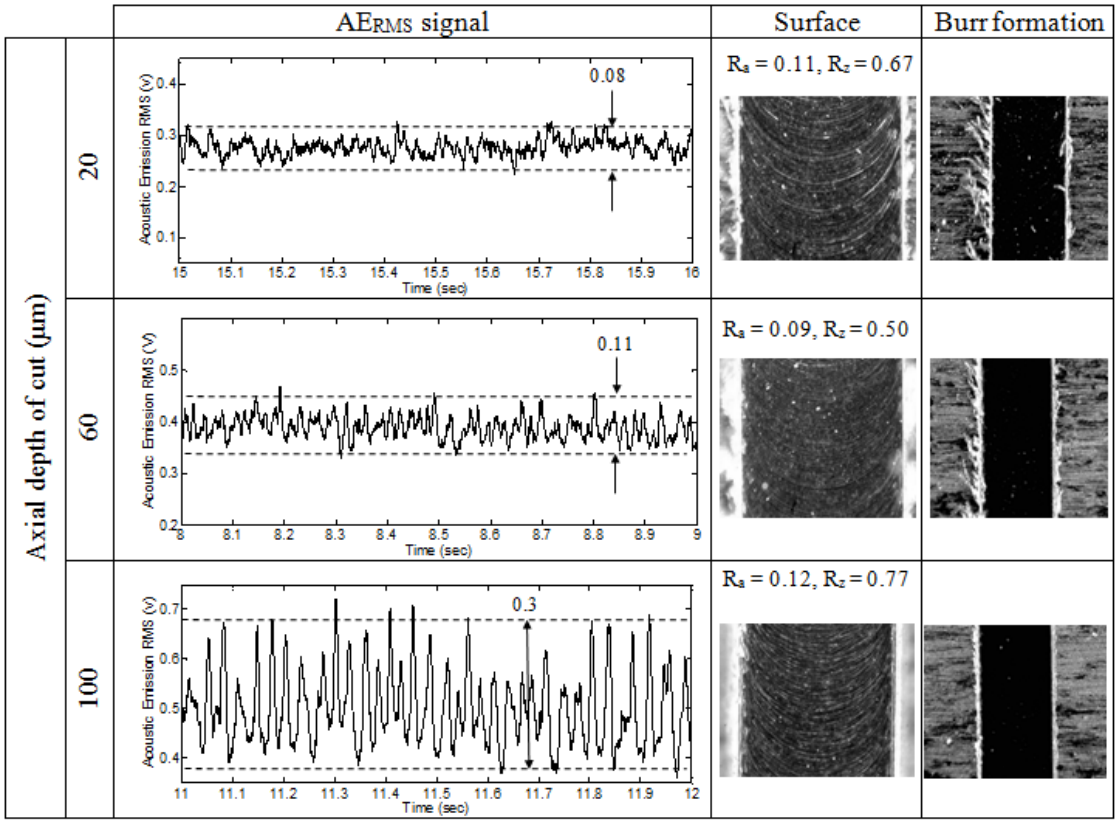

Figure 2.14: Effect of axial depth cut on AE_{RMS} signal, surface quality and burr formation

Based on what was previously discussed, we may be able to conclude that the waveform of AE_{RMS} signal can represent changing of cutting parameters and the surface generation. Increasing spindle speed and axial depth of cut increase the deviation of the signal but increasing feed rate increases the density of the AE_{RMS} signal. A good surface is often obtained when AE_{RMS} signal shows uniformity and low deviation.

5.2 Modeling results

Based on the experimental result in Table 2.4, the second-order RSM models for both responses, total top-burrs width (B_T) and average surface roughness (R_a), were formulated. The estimated regression coefficients were obtained using the method of least square. Eq. (2.8) represents the RSM model for average surface roughness (R_a) and Eq. (2.9) represents the RSM model for total top-burrs width (B_T). Please note that, the analysis was done using coded units and the models only include the significant terms.

$$R_a = 0.13883+0.00729\,A - 0.02762\,B - 0.01442\,C + 0.02225\,C^2 + 0.02226\,AC + 0.04190\,BC \quad \text{Eq. (2.8)}$$

$$B_T = 0.28017-0.0593\,A + 0.013\,B - 0.05092\,C - 0.06967\,B^2 - 0.0316\,BC \quad \text{Eq. (2.9)}$$

Since the analysis was done using coded units, the variables A, B and C were given as coded variables and can be calculated by using Eqs. (2.10), (2.11) and (2.12), respectively, where Ω is spindle speed (krpm), f_z is feed per tooth (μm/tooth) and a_p is axial depth of cut (μm)

$$A = \frac{\Omega - 40}{20} \quad \text{Eq. (2.10)}$$

$$B = \frac{f_z - 0.3}{0.2} \quad \text{Eq. (2.11)}$$

$$C = \frac{a_p - 60}{40} \qquad \text{Eq. (2.12)}$$

To measure models' adequacy, R-square, predicted R-square and adjusted R-square were calculated. For the surface roughness model, R-square, predicted R-square and adjusted R-square were found as 93.55%, 82.78% and 90.03%, respectively, and for the top-burrs width model these value were found as 82.91%, 62.95% and 75.79%, respectively. Since, both models obtain satisfactory high value of all R-squares; the models are well fitted to the real data points.

Table 2.8 presents the comparison of fitted values computed by the predictive models and the actual data points obtained from the experimental results. Figure 2.15 and Figure 2.16 present the error plots of the average surface roughness prediction and the total top-burr width prediction.

Table 2.8: Prediction values vs. experimental results.

Run	Factors				Results					
	Tool	Ω (krpm)	fz (µm/tooth)	ap (µm)	B_T (mm)			R_a (µm)		
					Model	Exp.	Error	Model	Exp.	Error
1	WC/Co Ø 635 µm	20	0.1	20	0.276	0.276	0.000	0.260	0.260	0.000
2		20	0.3	60	0.339	0.339	0.001	0.131	0.127	0.005
3		20	0.5	100	0.200	0.210	-0.010	0.131	0.128	0.003
4		40	0.1	60	0.197	0.209	-0.012	0.166	0.172	-0.005
5		40	0.3	100	0.229	0.197	0.032	0.146	0.155	-0.008
6		40	0.5	20	0.306	0.307	-0.001	0.106	0.108	-0.002
7		60	0.1	100	0.118	0.113	0.006	0.161	0.157	0.005
8		60	0.3	20	0.271	0.257	0.015	0.160	0.158	0.003
9		60	0.5	60	0.164	0.149	0.015	0.118	0.118	0.001

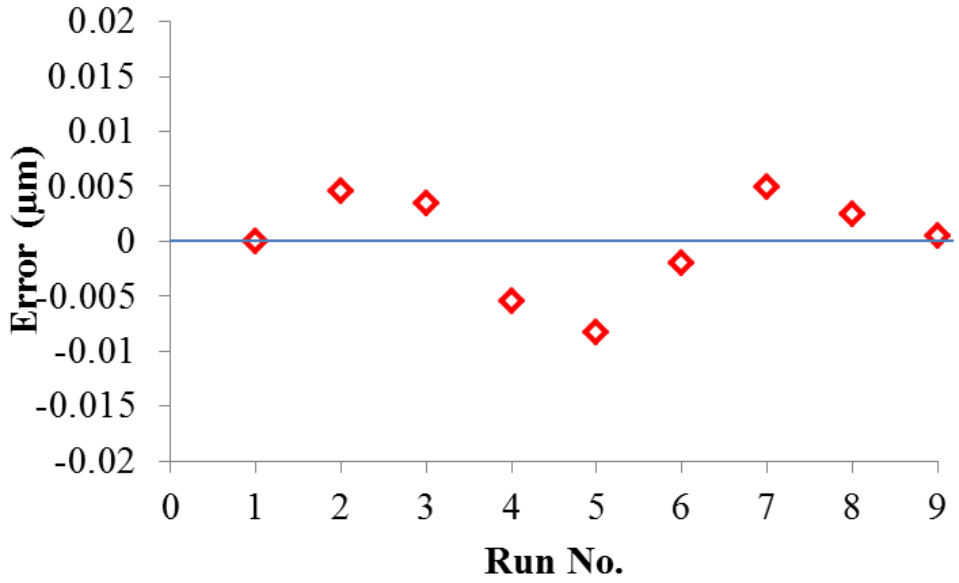

Figure 2.15: Surface roughness prediction error.

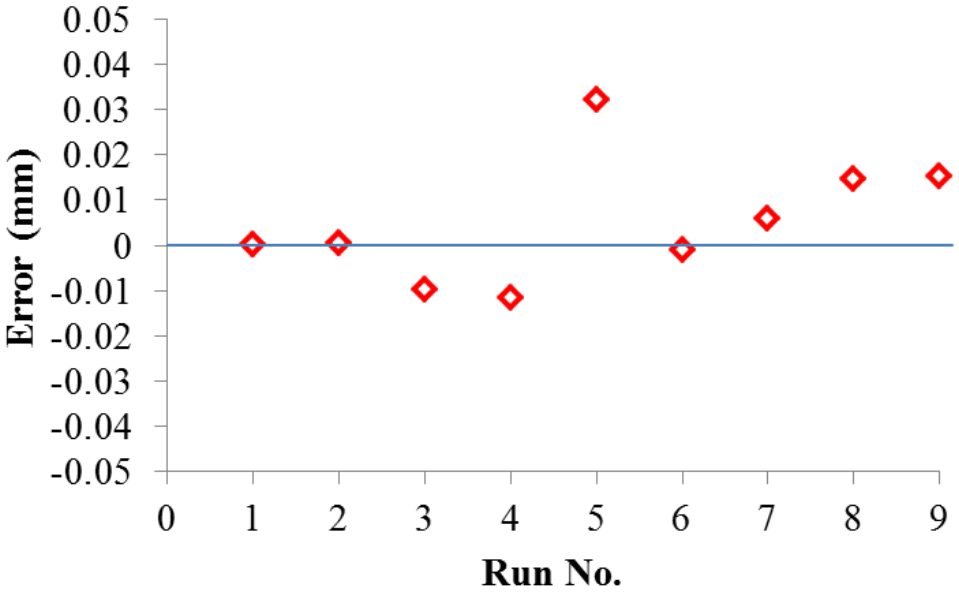

Figure 2.16: Total top-burr width prediction error.

Also, the analysis of variance (ANOVA) was conducted in order to guarantee the model adequacy and to see the effect of linear, square and interaction terms. Table 2.9 shows the ANOVA table for surface roughness model and Table 2.10 shows the ANOVA table for top-burrs width model. At the significant level of 0.05, it can be seen that both models are statistically significant since their p-value of regression are lower than 0.05. For the surface roughness model, all linear, square and interaction effects are significant. For the top-burrs model, only linear and square effects are significant, however, adding the interaction term BC into the model significantly increases the R-squares value. Therefore, we decided to have it remain in the model. Furthermore, for the lack-of-fit test, both models had shown that there were no strong evidences of lack-of-fit in the models. In brief, the models developed by RSM are adequately present the real relationship of process parameters (independent variables) and process performance (responses).

Table 2.9: ANOVA for average surface roughness model.

Source	**DF**	**Adj SS**	**Adj MS**	**F**	**P-value**
Regression	6	0.032261	0.005377	26.58	< 0.001
Linear	3	0.008851	0.002950	14.59	< 0.001
Square	1	0.001980	0.001980	9.79	0.010
Interaction	2	0.007526	0.003763	18.60	< 0.001
Residual Error	11	0.002225	0.000202		
Lack-of-Fit	2	0.000342	0.000171	0.82	0.472
Pure Error	9	0.001883	0.000209		

Using the developed RSM models, the surface plots and contour plots of each model were created. An extra parameter in the surface plots was held at the middle level. The surface and contour plots of the average surface roughness against process parameters are shown in Figures 2.17, 2.18 and 2.19 while the surface and contour plots of total top-burrs width against process parameters are shown in Figures 2.20, 2.21 and 2.22.

Table 2.10: ANOVA for total top-burrs width model.

Source	DF	Adj SS	Adj MS	F	P-value
Regression	5	0.080252	0.016050	11.65	<0.001
Linear	3	0.059512	0.019837	14.39	<0.001
Square	1	0.019414	0.019414	14.09	0.003
Interaction	1	0.004993	0.004993	3.62	0.081
Residual Error	12	0.016538	0.001378		
Lack-of-Fit	3	0.003569	0.001190	0.83	0.512
Pure Error	9	0.012968	0.001441		

It should be noted that there are some conflicts in terms of recommended parameters level obtained from the main effects plots (Figure 2.6 and Figure 2.7) and what was obtained from the surface plots. This can be explained by the fact that the main effect analysis is a quick and simple experimental analysis which only considers the influence of each factor individually and does not concern with any interaction or squared effects. It aims to quickly capture the effects of the process factors to the process responses. On the other hand, the RSM models included all interaction and squared effects, and in this study it has been shown that these effects are significant (see Table 2.9 and Table 2.10).

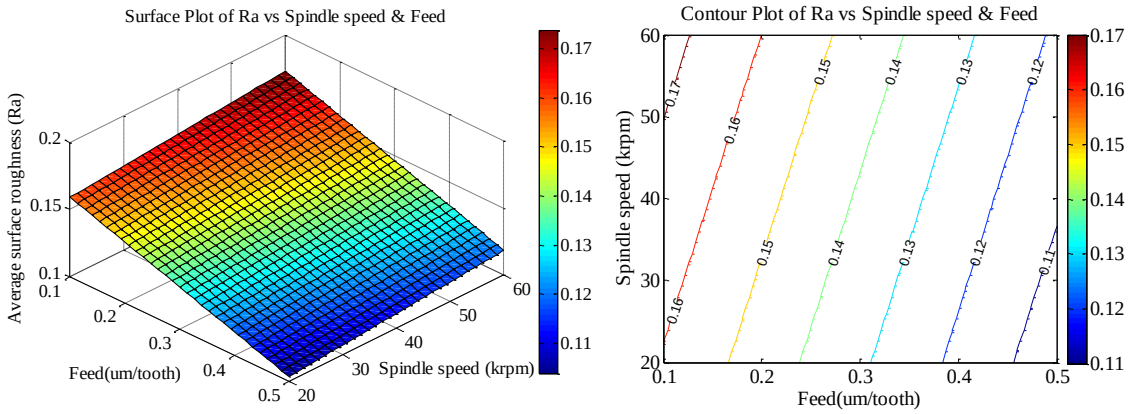

Figure 2.17: Surface and contour plots of average surface roughness (Ω in krpm vs. f_z in µm/tooth).

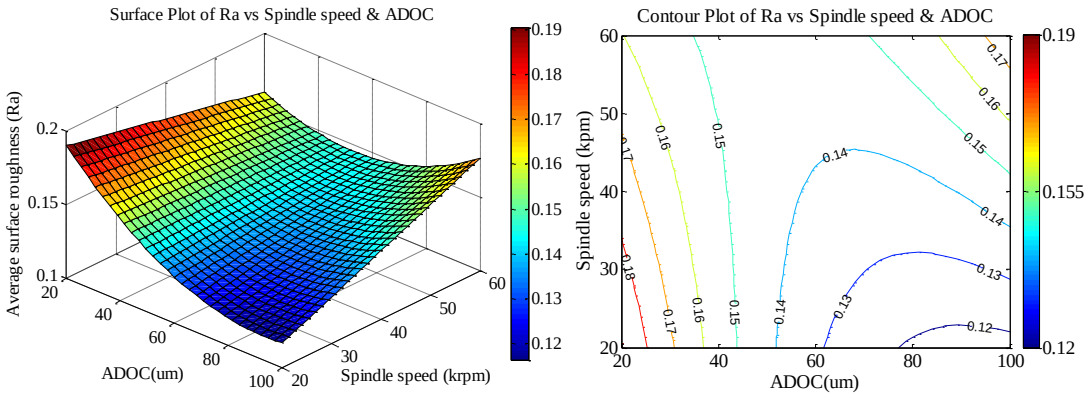

Figure 2.18: Surface and contour plots of average surface roughness (Ω in krpm vs. a_p in µm).

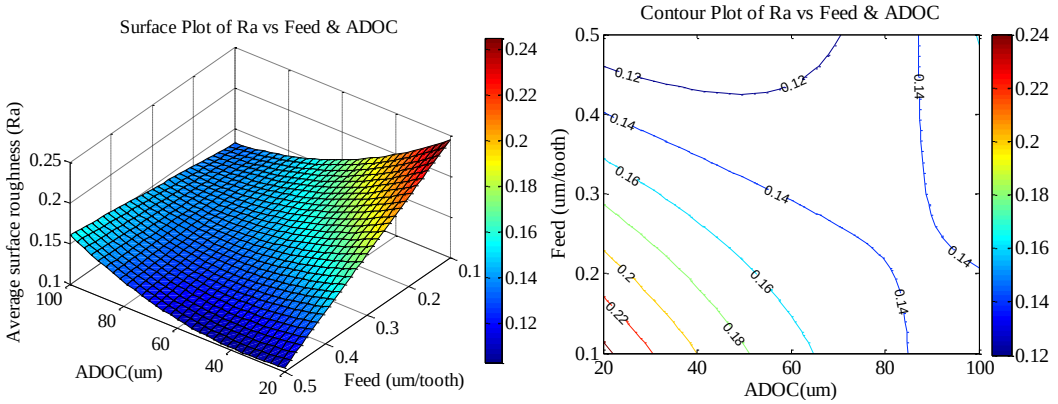

Figure 2.19: Surface and contour plots of average surface roughness (f_z in µm/tooth vs. a_p in µm).

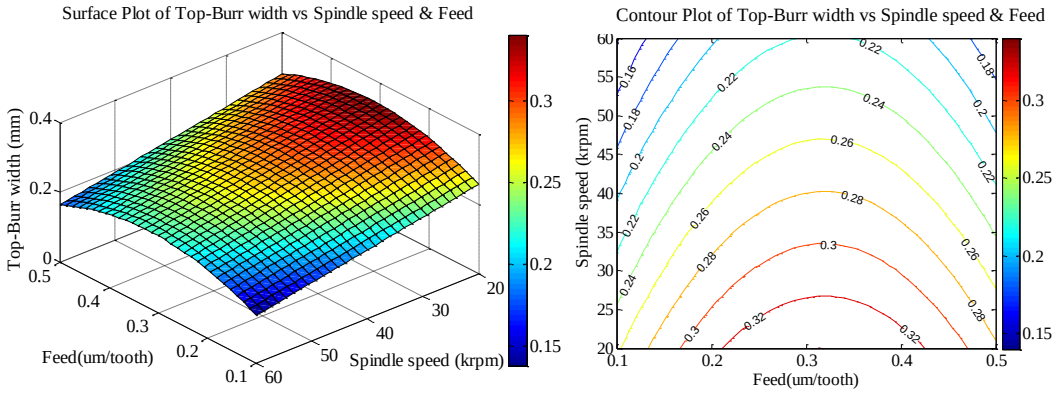

Figure 2.20: Surface and contour plots of top-burr width (Ω in krpm vs. f_z in µm/tooth).

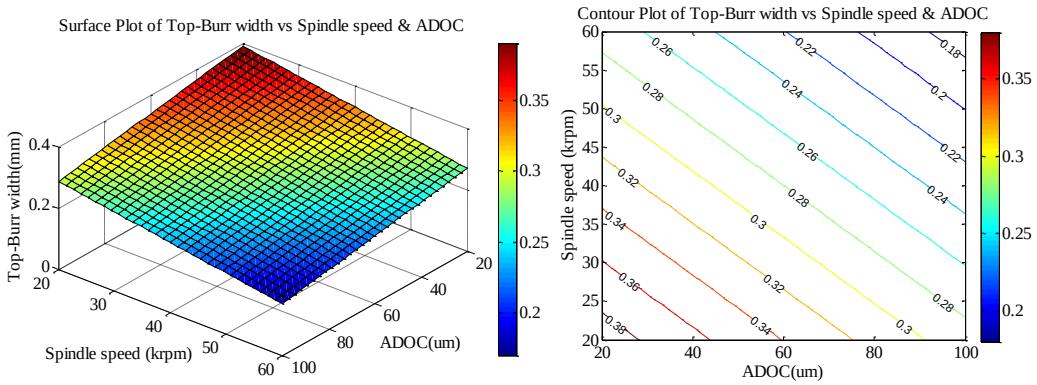

Figure 2.21: Surface and contour plots of top-burr width (Ω in krpm vs. a_p in µm).

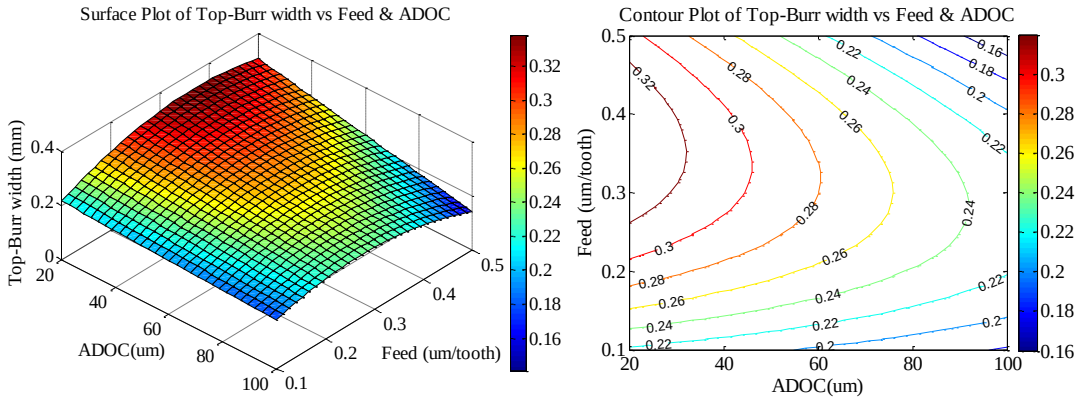

Figure 2.22: Surface and contour plots of top-burr width (f_z in µm/tooth vs. a_p in µm).

5.3 Optimization results

In this study, since there is a trade-off between surface roughness and burr formation, a multi-objective optimization becomes necessary. Finding the optimal process parameters to achieve the desired level of response (minimum average surface roughness and minimum burr formation) can be performed. Multi-objective optimization problem with two objective functions can be generally formulated as following:

$$\textit{Minimize} \quad \{f(\boldsymbol{x}), g(\boldsymbol{x})\} \qquad \text{Eq. (2.13)}$$

$$\textit{s.t.} \quad \boldsymbol{x} \in \boldsymbol{X}$$

where $\boldsymbol{x}$ represent micro-milling process parameters; $\boldsymbol{x} = x_1, x_2, \ldots, x_n$ $(x_1 = \Omega, x_2 = f_z,\ x_3 = a_p)$. $\boldsymbol{X}$ represents the solution space with all feasible values for the micro-milling process parameters. The function $f(\boldsymbol{x})$ represents the objective function for surface roughness and the function $g(\boldsymbol{x})$ represents the objective function for total top-burr width.

The simulations are run by using a particle swarm population of 250 and a maximum number of 500 iterations. After obtaining the best particle value in each iteration of the simulation, the particles are plotted in a two-dimensional objective space for viewing. This procedure is repeated until a clear Pareto frontier forms. The simulations usually take less than 30 minutes in a PC with Intel Dual Core 2.40 GHz processor. Therefore, the Pareto frontiers of the solution sets are obtained by using this multi-objective PSO method.

The Pareto frontier of the non-dominated solutions for two objective functions minimizing surface roughness, *min* (R_a), and minimizing total top-burr width, *min* (B_T), is presented in Figure 2.23a. Micro-end milling process parameters that minimize both top-burr width and surface roughness are identified along the axial depth of cut axis at the highest spindle speed tested (60 krpm) and at the highest feed per tooth (0.5 μm) in the solution (decision variable) space (see Figure 2.23b).

Three distinct regions have been identified along the Pareto frontier of the solution set in Figure 2.23a. These are marked as “Minimize burr”, “Balance burr and R_a”, and “Minimize R_a”. Corresponding regions in the solution (decision variable) space

are also indicated in the Figure 2.23b. A set of micro-end milling process parameters falling in these regions should provide decision maker (operator) a feasible solution set to achieve desired average surface roughness and total top-burr width.

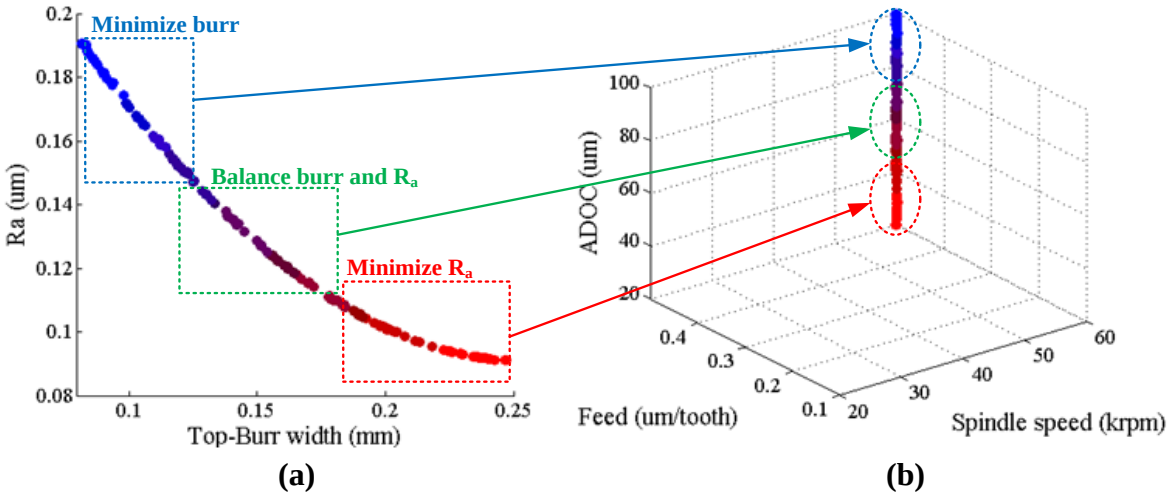

Figure 2.23: MOPSO results (a) Pareto front of optimal objective value (b) optimal solution in variable domain.

In addition, optimum process parameters that satisfy both objective functions in minimizing surface roughness and top burr width are utilized in a set of experiments. At first a set of process parameters is employed (Ω = 60 krpm, f_z = 0.5 µm/tooth, and a_p = 100 µm) which is found optimum for obtaining minimum top-burr width as shown in Figure 2.24a. Another set is employed in micro-end milling a channel (Ω = 60 krpm, f_z = 0.5 µm/tooth, and a_p = 60 µm) which is determined to be an optimum set for minimizing both surface roughness and top-burr width equally as shown in Figure 2.24b. Finally another set of optimum process parameters for minimizing surface roughness only (Ω = 60 krpm, f_z = 0.5 µm/tooth, and a_p = 20 µm) is utilized in Figure 2.24c. As it is evident

from the validation experiments, the smaller the axial depth of cut, the larger the top burr width.

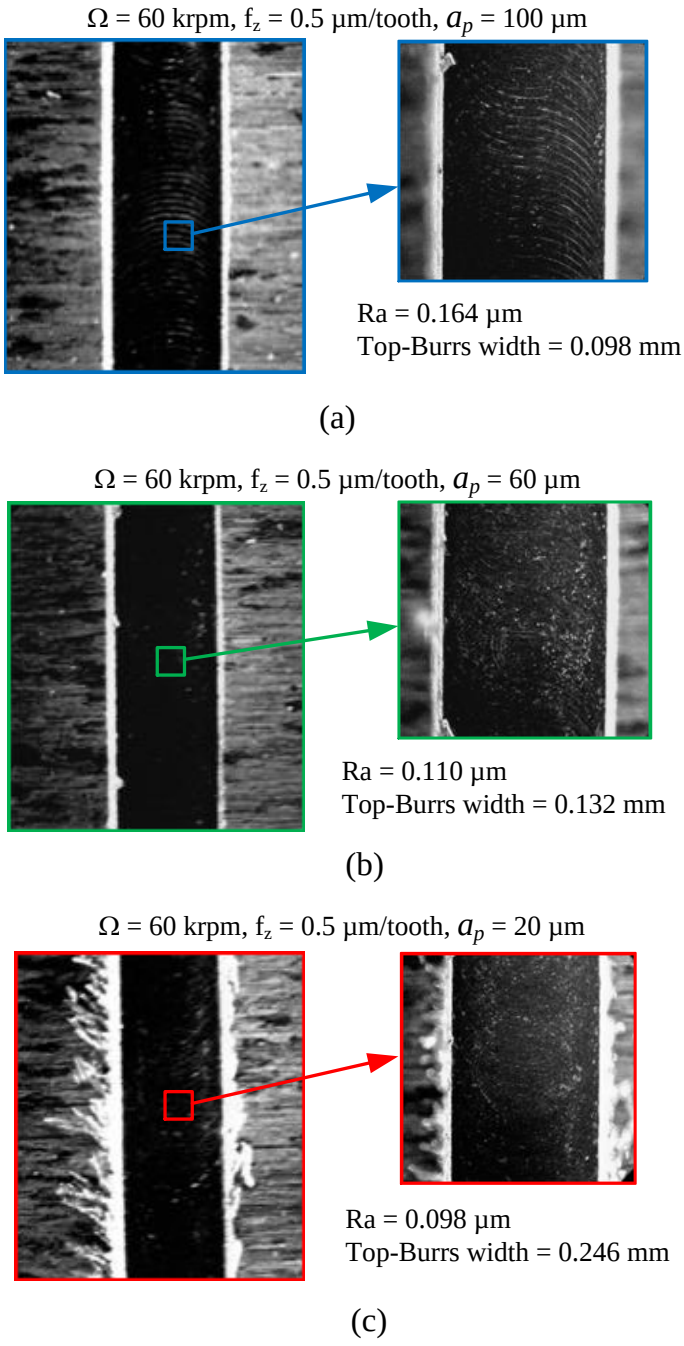

Figure 2.24: Examples of channel quality based on the result from MOPSO (a) channel with minimum top-burrs width (b) channel with balanced top-burrs and surface roughness (c) channel with minimum surface roughness

6. Conclusions

The experiments have revealed that the AE_{RMS} signal and its waveform respond precisely to most change in process parameters. The signal also represents the condition of surface generated by the micro-end milling process fairly accurately. This capability of AE_{RMS} signal can be used in assisting process control by allowing a selection of process parameters in micro-end milling to carry out the desired surface quality effectively.

Based on this study, it is proven that surface quality and burr formation in micro-end milling of Ti-6Al-4V are highly affected by the selection of process parameters. Employing inappropriate process parameters can cause severe burr formation or very poor surface quality which totally ruins the machined part or feature. Therefore, the optimization of process parameters is very essential. The multi-objective optimization using a combination of response surface methodology (RSM) and multi-objective particle swarm optimization (MOPSO) can be very helpful in supporting the decision making process. It allows the selection of process parameters based on the desired results. Based on the results of this study, the axial depth of cut was found to be the major process parameter affecting top-burr formation while feed per tooth was found to be the most influential process parameter determining the surface roughness.

CHAPTER 3

MICRO-END MILLING WITH UNCOATED AND CBN COATED TOOLS

1. Introduction

For the tool-based machining process such as micro-end milling, cutting tool is the most important element. Therefore, cutting tool design is one of the major areas in machining research and development. Two important selections about the cutting tools are geometrical shape and material. The shape of a cutting tool defines a shape of the machined feature while the tool material limits its capability in withstanding the shearing force, temperature and wear.

In micro-end milling, the tool is called micro-end mill. It is generally made of tungsten carbide in a cobalt matrix (WC/Co). To increase the performance of the micro-end mill, coating can be applied. A thin layer of hard material coated on the surface of the WC/Co micro-end mill can significantly improve tool life and quality of machined surfaces. In the conventional macro-machining, coated tools have only one drawback that it is more expensive than the uncoated tools. However, in the micro-machining, there are more issues to be concerned about applying coating on micro-tools since the coating layer may significantly increase the geometry of the tool resulting in an undesirable performance. Furthermore, the performance of the coated tools in micro-machining is not yet fully understood.

In this chapter, performance studies of cubic boron nitride (cBN) coated WC/Co micro-end mills will be discussed and compared with the performance of the uncoated WC/Co tools. The performance will be evaluated in terms of surface roughness, burr

formation and tool wear. Moreover, modeling and optimization will be conducted to provide decision support for micro-end milling of titanium alloy, Ti-6Al-4V.

2. Review of Micro-End Milling with Coated Tools

There are several hard materials which are commonly used as tool coating materials; for example, diamond, cBN, TiN, TiCN, TiAlN CrN, CrTiAlN, etc. These coating materials are different in terms of their physical and chemical properties; therefore, they are implemented in different applications. Several researchers have shown the potential of applying these coatings in micro-end milling of some particular materials which will be discussed next.

Heaney et al. (2008) has shown the possibility of coating fine-grained diamond, average grain size 30-300 nm, onto WC/Co micro-end mills (see Figure 3.1). They found that the performance of diamond coated tools was improved dramatically when dry machining 6061-T6 aluminum. The fine grained diamond coating reduced the thrust and the main cutting forces by approximately 90% and 75%, respectively compared with uncoated tools. Also, the chip adhesion did not develop as long as the coating remained intact. Furthermore, the surface generated for coated tools was uniform and no burr has occurred.

Aramcharoen et al. (Aramcharoen et al. 2008) have studied the effect of coating materials in micro-end milling process; they have reported that CrTiAlN coated WC/Co micro-end mills provide distinct advantages over uncoated WC/Co end-mills in terms of tool wear reduction and machined surface quality improvement. They also compared the effect of coating materials on micro-end mills for machining hardened H13 tool steel (45 HRC). TiN, TiCN, TiAlN CrN, and CrTiAlN layers were PVD coated onto two-flute

WC/Co micro-end mills with a layer thickness of 1.50±0.15 μm, then evaluated a cutting performance at the same cutting condition. The results indicated that TiN coatings offer the best performance in terms of tool wear and chipping reduction, surface roughness improvement, and decreasing burr size. Moreover, they found that at the beginning of cutting (burn-in-period) the coated tools did not outperform the uncoated tools in terms of surface finish quality. Hence, it implied that an ultra-fine coating surface or self-lubricating, low friction top coat would be required for a better performance of coated WC/Co micro-end mills.

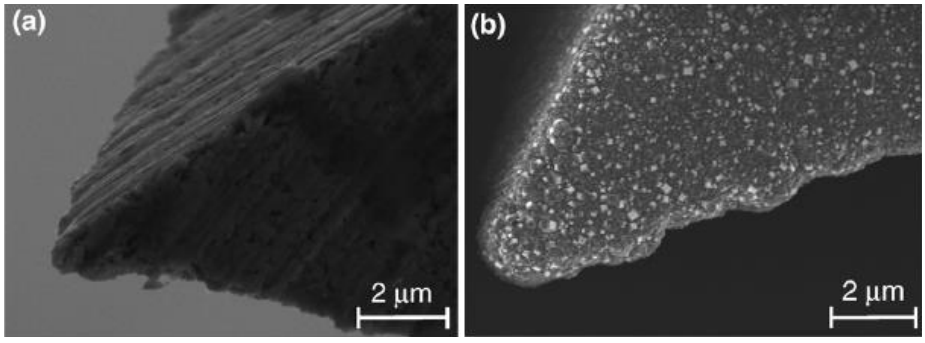

Figure 3.1: Comparison of fabricated tool edges: (a) uncoated WC/Co tool, (b) fine-grained diamond coated tool (Heaney et al. 2008).

Biermann et al. (Biermann et al. 2013) have investigated the performance of different coatings for micro-end milling of austenitic stainless steel. The hard coatings namely CrN, TiN, AlCrN, AlTiN and TiAlN were applied on the solid WC/Co micro-end mills using a PVD technique. The cutting edge radius of the tools was about 6 μm. Forces, tool wear and surface quality were analyzed. Their results indicated that AlCrN

and TiAlN coatings produced the best results in terms of tool wear. Relating to the best surface quality, the AlTiN coating provided the best results.

Ucun et al. (Ucun et al. 2013) studied the effect of coating materials on tool wear in micro-end milling of Inconel 718 super alloy. Coated and uncoated WC/Co micro-end mills were tested under dry and minimum quantity of lubricant (MQL) conditions. This study was focusing on wear behavior of single layer (diamond, AlTiN and AlCrN) and multi-layer (TiAlN+AlCrN and TiAlN+WC/C) coated micro-end mills. Wear mechanisms and the effect of reduction of tool diameter to increasing edge radius ratio on machined geometry were also discussed. The results showed that the coated tools outperform the uncoated tools in terms of tool wear.

One of the coating materials which has been used extensively in conventional macro-machining is cubic boron nitride (cBN). The application of cBN coated tools in the metal cutting industry can be broadly broken down into a number of workpiece material categories, namely high speed machining of abrasive ferrous materials such as pearlitic grey cast iron, and also a process referred to as hard machining. Superalloys and sintered irons and steels are also machined with cBN coated tools. Due to its high hardness, tool life of cBN coated tools increase significantly. Moreover, the advantage of cBN over diamond is that it can be used in machining of ferrous based materials such as alloy steels. In spite of its potentials, applications of cBN coatings on micro-end mills have never been investigated before. Therefore, in this chapter, the performance of cBN coated micro-end mills will be explored. The study also includes the optimization of process parameters to be used with the cBN coated micro-end mills.

3. Experimental Methodology

The methodology of this study is similar to what was described in Chapter 2. However, in addition to surface roughness and burr formation, tool wear was included into the performance evaluation. In terms of modeling and optimization, the reader is referred to Sections 2.3 and 2.4 in Chapter 2.

3.1 Experimental setup

In this chapter, the process of micro-end milling of Ti-6Al-4V was selected as the case study (the same as in Chapter 2). The experimental setup is the same as the setup explained in Chapter 2 which is shown in Figures 2.2 and 2.3.

The WC/Co flat micro-end mills with the diameter of 381µm (0.015") and 508 µm (0.020") were chosen in this work. One set of the micro-end mills was coated with cubic boron nitride (cBN). The coatings were done by magnetron sputtering system at the Metal Forming Center of Excellence, ATILIM University in Turkey at a deposition pressure of $3x10^{-3}$ Torr, heater temperature of 100 ºC, fixed magnetron power of 900 W, argon to nitrogen gas ratio of 5/1, and at the lowest bias voltage to obtain uniform cBN coatings on tungsten carbide substrate (Özel et al. 2011). It should be noted that cBN coatings increase the tool edge radius as well as the nominal diameter of the micro-tools. Based on the increase of mean edge radius and the nominal diameter, the cBN coating layer was assumed to have a thickness of about 2 µm. Thus the edge radius of coated tools was increased to approximately by 5 µm and the nominal diameters were increased to 385µm and 512 µm.

Figures 3.2 and 3.3 show the images of WC/Co and cBN coated micro-end mills and their close-up surfaces, respectively. It is clearly shown that the cBN coated WC/Co

micro-end mills have a smoother surface compared to the uncoated WC/Co micro-end mills. The cBN coating layer covered all the marks left by the grinding process on the tungsten carbide surface.

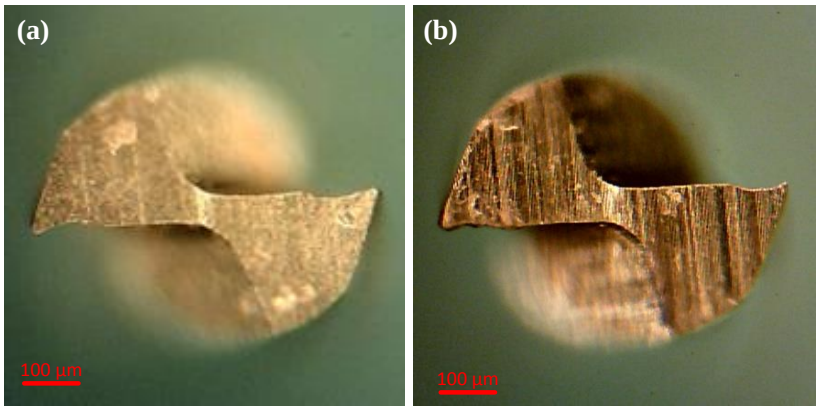

Figure 3.2: Images of the micro-end mills obtained with digital optical microscopy (a) cBN coated micro-end mill, and (b) uncoated micro-end mill.

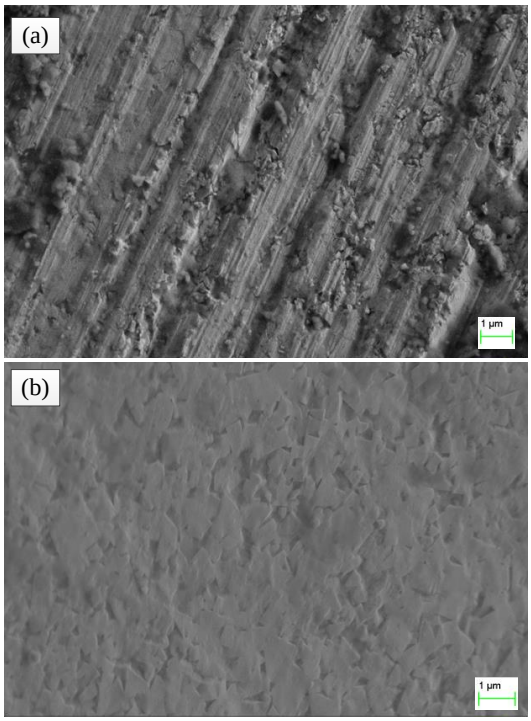

Figure 3.3: Images of the micro-end mills surface obtained with SEM (a) uncoated micro-end mill, and (b) cBN coated micro-end mill.

3.2 Tool wear measurements

Tool heavily engages with workpiece at the cutting edges. As a result, the cutting edges are worn out before other parts of the tool would. As wear progresses, the cutting edge radius will get larger and consequently tool wear will reduce the effective tool diameter. Therefore, in this study, tool wear was evaluated in terms of a reduction of effective diameter and an increase of edge radius. After a certain period of cutting, worn tools were taken off the spindle and examined with optical microscopy. The image was captured; the tool edge radius and tool effective diameter were measured. The edge radius was measured form both edges, then the average was taken. Figure 3.4 shows the measurement of tool edge radius and the resultant effective tool diameters.

3.3 Experimental designs

The experiments are divided into two sets of experiments namely Experiment 1 and Experiment 2. For Experiment 1, the uncoated WC/Co micro-end mills with the diameter of 508 μm (0.020”) were used. The tool diameter was increased to 512 μm after the cBN coating. The experiment was designed based on L18 Taguchi orthogonal array as shown in Table 3.1. In Experiment 2, the uncoated WC/Co micro-end mills with the diameter of 381 μm (0.015”) were used. The tools were then coated with cBN which increased their diameter size to 385 μm. The experiments were designed based on the central composite design (CCD) as shown in Table 3.2.

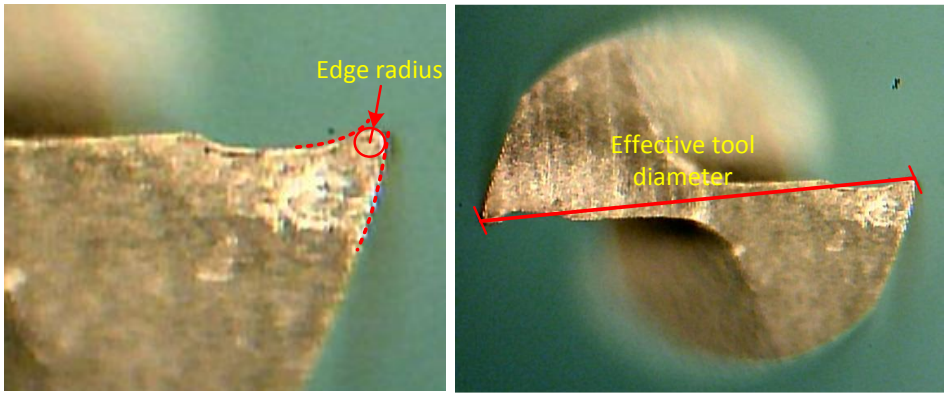

Figure 3.4: Measurement of tool wear: tool edge radius (left) and effective tool diameter (right)

Table 3.1 Experimental conditions for Experiment 1(Ø508 µm).

Run	Tool	Ω (krpm)	f_z (µm/tooth)	a_p (µm)
1	Uncoated WC/Co Ø 508 µm	16	0.5	40
2			2.5	70
3			4.5	100
4		32	0.5	40
5			2.5	70
6			4.5	100
7		48	0.5	70
8			2.5	100
9			4.5	40
10	cBN coated WC/Co Ø 512 µm	16	0.5	100
11			2.5	40
12			4.5	70
13		32	0.5	70
14			2.5	100
15			4.5	40
16		48	0.5	100
17			2.5	40
18			4.5	70

Table 3.2: Experimental conditions for Experiment 2 (Ø381 µm).

Run	Tool	Ω (krpm)	f_z (µm/tooth)	a_p (µm)
1	1) Uncoated WC/Co, Ø 381 µm 2) cBN coated WC/Co, Ø 385 µm	42	0.75	40
2		42	0.75	70
3		42	2.5	40
4		42	2.5	70
5		62	0.75	40
6		62	0.75	70
7		62	2.5	40
8		62	2.5	70
9		52	1.625	55
10		52	1.625	29.773
11		52	1.625	80.227
12		52	0.153	55
13		52	3.097	55
14		35.2	1.625	55
15		68.8	1.625	55
16		52	1.625	55

4. Results and Discussions

The results and discussions are divided into four sections: results of Experiment 1, results of Experiment 2, the influence of cutting speed, feed per tooth and axial depth of cut, and tool wear analysis. First, the results of Experiment 1 will be discussed following by the results of Experiment 2. Then the integration of both experiments was done to study the influence of process parameters such as cutting speed, feed per tooth and axial depth of cut. Finally, the analysis of tool wear will be explained.

4.1 Results of Experiment 1

The result of Experiment 1 is shown in Table 3.3. The main effects plots of average surface roughness and the total top-burr width are illustrated in Figures 3.5 and 3.6. The ANOVA tables for average surface roughness and total top-burr width are shown in Tables 3.4 and 3.5, respectively. Based on these results, it can be seen that the

use of cBN coating significantly improves surface roughness but also increases burr formation. Therefore, it is suggested that cBN coated tools should be selected when a low surface roughness is the first priority. Among all tested process parameters feed per tooth is the most significant factor affecting the surface roughness and top-burr formation. Increasing feed per tooth significantly reduced the top-burr formation. However, excessive increase of feed per tooth has a negative effect on the surface roughness, since the optimal value of feed per tooth to achieve the best surface roughness was at the value between 0.5 μm and 4.5 μm. In terms of spindle speed and axial depth of cut, using the high value of these process parameters would result in lower surface roughness and a small top-burr width.

In order to accurately predict the process performance, second order regression models were developed based on the experimental results (see Chapter 2, section 3). The coefficients of the models are shown in Tables 3.6 and 3.7. The basic terms consist of tool type (T), spindle speed (Ω), feed per tooth (f_z) and axial depth of cut (a_p). The models only include terms which are statistically significant.

Table 3.3: Experimental results of Experiment 1 (Ø508 µm).

Run	Tool	Ω (krpm)	f_z (µm/tooth)	a_p (µm)	R_a (µm)				B_T (mm)			
					Rep. 1	Rep. 2	Avg.	Std.	Rep. 1	Rep. 2	Avg.	Std.
1	Uncoated WC/Co Ø508 µm	16	0.5	40	0.143	0.167	0.155	0.021	0.247	0.291	0.269	0.031
2			2.5	70	0.133	0.123	0.128	0.010	0.074	0.187	0.130	0.080
3			4.5	100	0.140	0.133	0.136	0.010	0.065	0.076	0.070	0.008
4		32	0.5	40	0.140	0.157	0.148	0.013	0.273	0.253	0.263	0.014
5			2.5	70	0.150	0.133	0.141	0.016	0.061	0.160	0.110	0.070
6			4.5	100	0.157	0.130	0.143	0.023	0.035	0.060	0.047	0.018
7		48	0.5	70	0.127	0.143	0.135	0.020	0.113	0.184	0.148	0.050
8			2.5	100	0.120	0.123	0.121	0.015	0.042	0.042	0.042	0.003
9			4.5	40	0.130	0.153	0.141	0.016	0.067	0.105	0.086	0.027
10	cBN coated WC/Co Ø512 µm	16	0.5	100	0.147	0.147	0.147	0.010	0.204	0.229	0.216	0.018
11			2.5	40	0.100	0.117	0.108	0.017	0.133	0.240	0.186	0.076
12			4.5	70	0.133	0.133	0.133	0.016	0.055	0.083	0.069	0.020
13		32	0.5	70	0.160	0.157	0.158	0.013	0.232	0.236	0.234	0.003
14			2.5	100	0.110	0.113	0.111	0.008	0.114	0.075	0.094	0.028
15			4.5	40	0.110	0.130	0.120	0.017	0.084	0.131	0.107	0.033
16		48	0.5	100	0.143	0.123	0.133	0.019	0.236	0.259	0.247	0.016
17			2.5	40	0.103	0.137	0.120	0.024	0.191	0.258	0.224	0.047
18			4.5	70	0.127	0.143	0.135	0.025	0.027	0.093	0.060	0.047

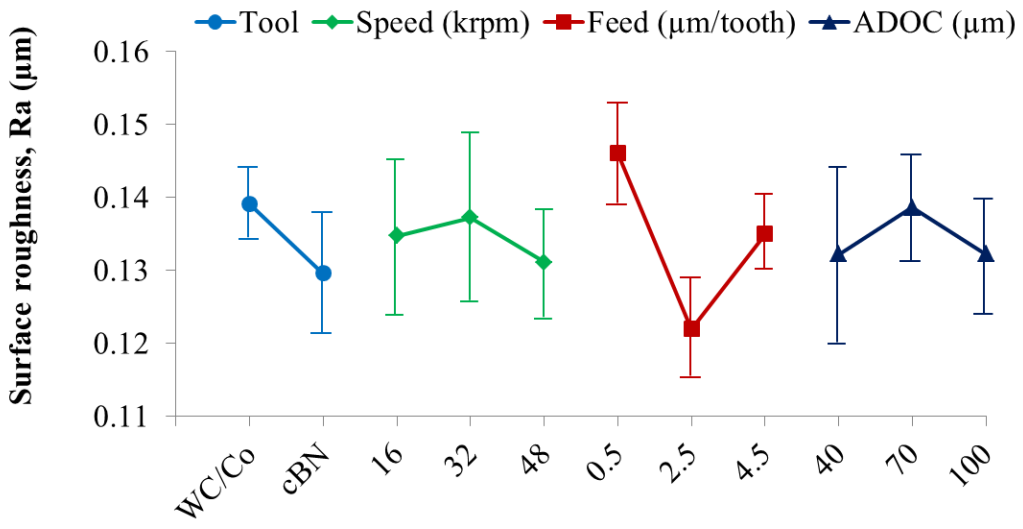

Figure 3.5: Main effects plot for average surface roughness (Ø508 µm).

Table 3.4: ANOVA table for average surface roughness (Ø508 µm).

Source	DF	Adj SS	Adj MS	F-value	P-value
Tool	1	0.0008028	0.0008028	5.04	0.033
$\boldsymbol{\Omega}$	2	0.0002265	0.0001133	0.71	0.500
f_z	2	0.0035117	0.0017559	11.02	0.000
a_p	2	0.0003265	0.0001633	1.02	0.372
Error	28	0.0044617	0.0001593		
Total	35	0.0093293			

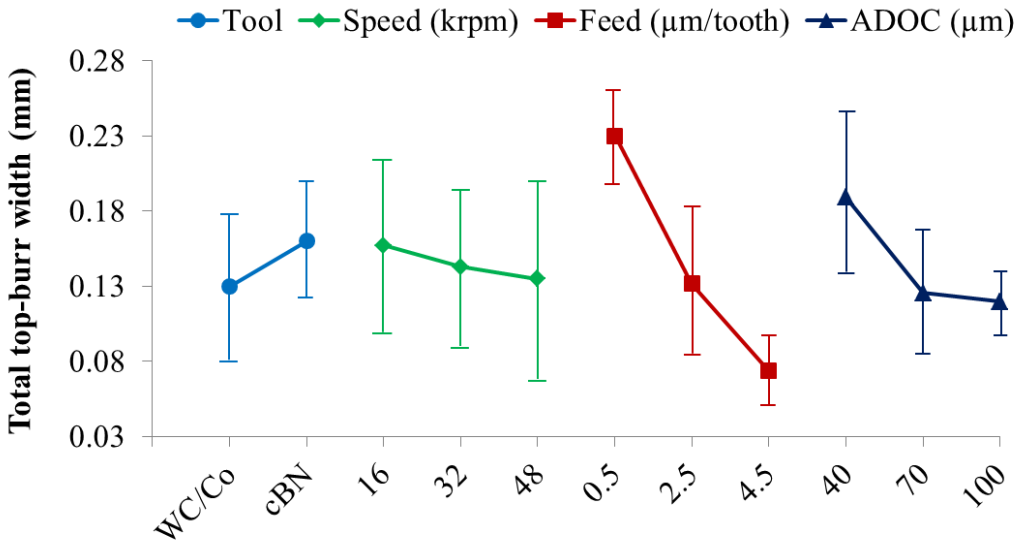

Figure 3.6: Main effects plot for total top-burr width (Ø508 µm).

Table 3.5: ANOVA table for total top-burr width (Ø508 µm).

Source	DF	Adj SS	Adj MS	F-value	P-value
Tool	1	0.008251	0.008251	4.74	0.038
$\boldsymbol{\Omega}$	2	0.003044	0.001522	0.87	0.428
f_z	2	0.149894	0.074947	43.06	0.000
a_p	2	0.035926	0.017963	10.32	0.000
Error	28	0.048739	0.001741		
Total	35	0.245854			

Table 3.6: Estimated regression coefficients for average surface roughness (R_a)

Term	Coefficient	Standard error	T-value	P-value
Constant	0.131449	0.016959	7.751	0.000
T	0.010778	0.006820	1.580	0.153
Ω	-0.000651	0.000205	-3.178	0.013
f_z	-0.042292	0.005537	-7.639	0.000
a_p	0.001792	0.000488	3.674	0.006
f_z^2	0.005069	0.000732	6.926	0.000
a_p^2	-0.000015	0.000004	-4.295	0.003
$T*f_z$	-0.005619	0.002185	-2.571	0.033
$\Omega*f_z$	0.000285	0.000070	4.054	0.004
a_p*f_z	0.000122	0.000045	2.701	0.027
R^2	92.74%			
R^2 (adj)	84.00%			

Table 3.7: Estimated regression coefficients for the total top burr width (B_T)

Term	Coefficient	Standard error	T-value	P-value
Constant	0.480508	0.042775	11.233	0.000
T	-0.009343	0.022921	-0.408	0.694
Ω	-0.001395	0.000586	-2.379	0.045
f_z	-0.047370	0.011646	-4.068	0.004
a_p	-0.004976	0.001236	-4.026	0.004
f_z^2	0.005042	0.001869	2.698	0.027
a_p^2	0.000025	0.000009	2.772	0.024
$T*\Omega$	0.002641	0.000539	4.895	0.001
$T*f_z$	-0.017952	0.005333	-3.366	0.010
$\Omega*f_z$	-0.000248	0.000178	-1.394	0.201
R^2	98.35%			
R^2 (adj)	96.50%			

To evaluate the models adequacy, the predicted values calculated from the models are compared with the experimental results. The prediction errors are calculated and shown in Table 3.8. The error plots of surface roughness prediction and total-top burr width prediction are shown in Figures 3.7 and 3.8, respectively. Approximately, the surface roughness model can predict with the accuracy of ±0.01 μm; the total top-burr width model can predict with the accuracy of ±0.2 mm.

Table 3.8: Predictive values vs. experimental results (Ø508 µm).

Run	Tool	Ω (krpm)	f_z (µm/tooth)	a_p (µm)	R_a (µm)			B_T (mm)		
					Model	Exp.	Error	Model	Exp.	Error
1	Uncoated WC/Co Ø508 µm	16	0.5	40	0.153	0.155	-0.002	0.274	0.269	0.005
2			2.5	70	0.131	0.128	0.003	0.133	0.130	0.003
3			4.5	100	0.137	0.136	0.001	0.078	0.070	0.008
4		32	0.5	40	0.145	0.148	-0.003	0.249	0.263	-0.014
5			2.5	70	0.132	0.141	-0.009	0.101	0.110	-0.009
6			4.5	100	0.147	0.143	0.004	0.037	0.047	-0.010
7		48	0.5	70	0.143	0.135	0.008	0.157	0.148	0.009
8			2.5	100	0.119	0.121	-0.002	0.045	0.042	0.003
9			4.5	40	0.143	0.141	0.002	0.089	0.086	0.003
10	cBN coated WC/Co Ø512 µm	16	0.5	100	0.146	0.147	-0.001	0.206	0.216	-0.010
11			2.5	40	0.114	0.108	0.006	0.189	0.186	0.003
12			4.5	70	0.129	0.133	-0.004	0.053	0.069	-0.016
13		32	0.5	70	0.159	0.158	0.001	0.248	0.234	0.014
14			2.5	100	0.115	0.111	0.004	0.108	0.094	0.014
15			4.5	40	0.119	0.120	-0.001	0.123	0.107	0.016
16		48	0.5	100	0.129	0.133	-0.004	0.242	0.247	-0.005
17			2.5	40	0.116	0.120	-0.004	0.209	0.224	-0.015
18			4.5	70	0.149	0.135	0.014	0.057	0.060	-0.003

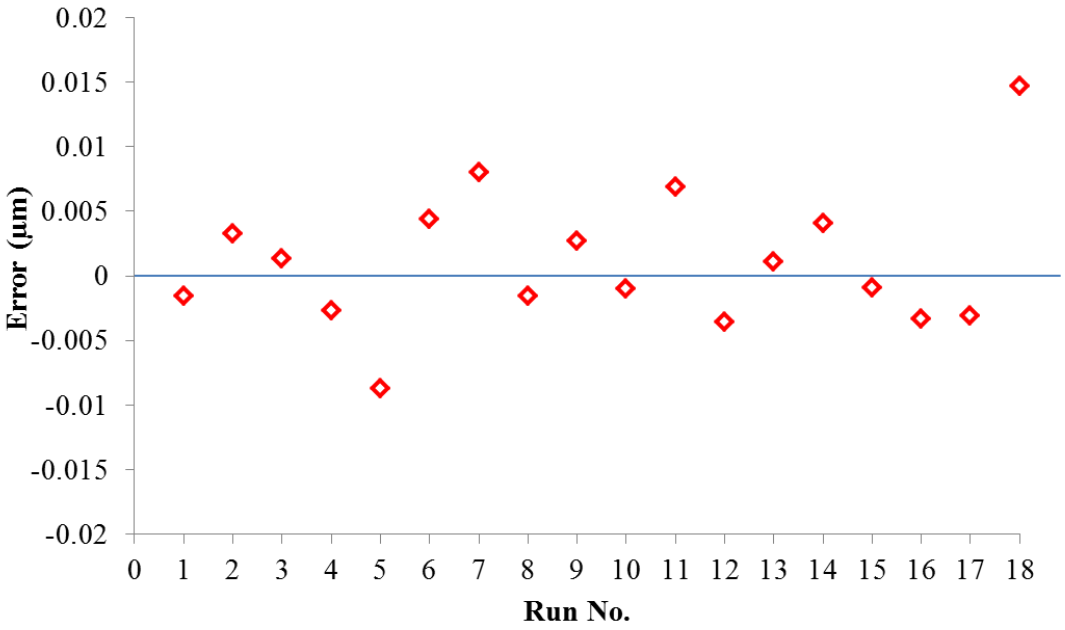

Figure 3.7: Average surface roughness prediction error (Ø508 µm).

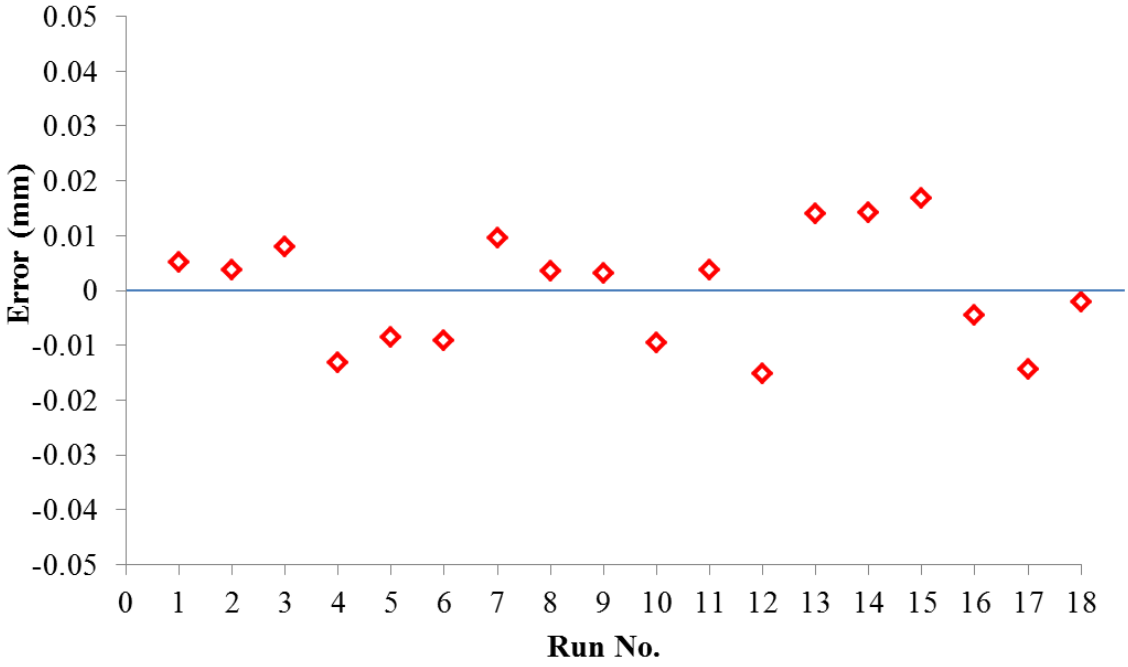

Figure 3.8: Total top-burr width prediction error (Ø508 µm).

The multi-objective particle swarm optimization (MOPSO) was conducted; the result is shown in Figure 3.9. The Pareto fronts indicate the advantage of the cBN coated WC/Co tool over the uncoated WC/Co tool in terms of surface roughness reduction. However, the uncoated WC/Co tool is better in terms of top-burr minimization. Thus, it infers that the cBN coated WC/Co tool should be selected in an application where surface roughness is more important and the uncoated WC/Co tool should be selected when top-burr is required to be minimized. Also both Pareto fronts indicated the trade-off between the surface roughness and top-burr formation. It is necessary for the user to decide the process parameters that reflect their desired process performance levels.

In terms of optimal process parameters, it can be seen that both tools reach the optimum value at the axial depth of cut of 100 μm and vary over the feed per tooth level. However, it is clearly shown that both optimal sets are different in terms of spindle speed; the cBN coated WC/Co tool has the optimum value at the spindle speed of 16 krpm while the uncoated WC/Co tool has the optimum value at the spindle speed of 48 krpm. Therefore, if the material removal rate (MMR) is concerned the uncoated WC/Co tool may be a better choice.

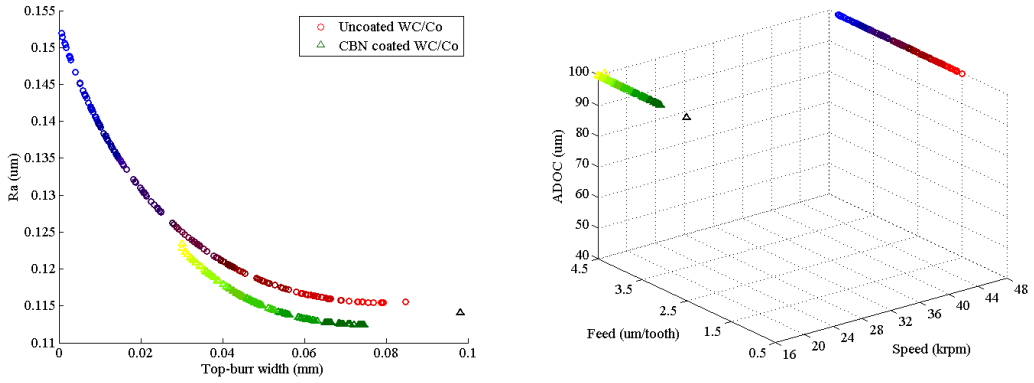

Figure 3.9: Optimal micro-end milling parameters for the tool diameter of Ø508 µm; (left) objective function space, and (right) decision variable space.

4.2 Results of Experiment 2

The result of Experiment 2 is shown in Table 3.9. The results can be illustrated as main effects plots as shown in Figures 3.10 and 3.11. The influences of each process parameter are analyzed using ANOVA tables as shown in Tables 3.10 and 3.11. From the main effect plot in Figures 3.10 and 3.11, it can be observed that the use of cBN coating increases the surface roughness and burr formation. This may be contributed to the fact that cBN coating layer increases the cutting edge radius which consequently reduces the sharpness of the tool. However, the effect of cBN coating was not statistically significant.

Surface roughness and burr formation were significantly affected by the feed per tooth. The width of top-burr was significantly dropped as the feed per tooth increases. However, too high feed per tooth resulted in an increase of surface roughness. In addition, increase of spindle speed and axial depth of cut seems to increase the surface roughness and burr formation.

Table 3.9: Experimental results of Experiment 2 (Ø381 µm).

Run	Ω (krpm)	f_z (µm/tooth)	a_p (µm)	WC/Co				cBN coated			
				R_a (µm)		B_T (mm)		R_a (µm)		B_T (mm)	
				Avg.	Std.	Avg.	Std.	Avg.	Std.	Avg.	Std.
1	42	0.75	40	0.103	0.006	0.137	0.006	0.110	0.010	0.137	0.006
2	42	0.75	70	0.110	0.000	0.157	0.092	0.123	0.015	0.282	0.004
3	42	2.5	40	0.103	0.006	0.143	0.020	0.103	0.012	0.112	0.002
4	42	2.5	70	0.120	0.010	0.115	0.019	0.107	0.012	0.074	0.010
5	62	0.75	40	0.113	0.015	0.209	0.040	0.130	0.000	0.317	0.037
6	62	0.75	70	0.117	0.006	0.159	0.062	0.133	0.012	0.270	0.016
7	62	2.5	40	0.143	0.015	0.127	0.027	0.143	0.006	0.082	0.005
8	62	2.5	70	0.130	0.020	0.261	0.094	0.140	0.010	0.086	0.030
9	52	1.625	55	0.113	0.006	0.132	0.031	0.103	0.006	0.212	0.025
10	52	1.625	29.8	0.103	0.006	0.128	0.043	0.097	0.006	0.222	0.023
11	52	1.625	80.2	0.110	0.000	0.159	0.004	0.130	0.010	0.165	0.001
12	52	0.153	55	0.180	0.000	0.293	0.003	0.163	0.015	0.268	0.015
13	52	3.097	55	0.117	0.012	0.119	0.016	0.123	0.006	0.106	0.007
14	35.2	1.625	55	0.107	0.012	0.194	0.008	0.110	0.010	0.173	0.007
15	68.8	1.625	55	0.103	0.015	0.156	0.000	0.113	0.006	0.178	0.016
16	52	1.625	55	0.107	0.006	0.195	0.011	0.107	0.006	0.199	0.014

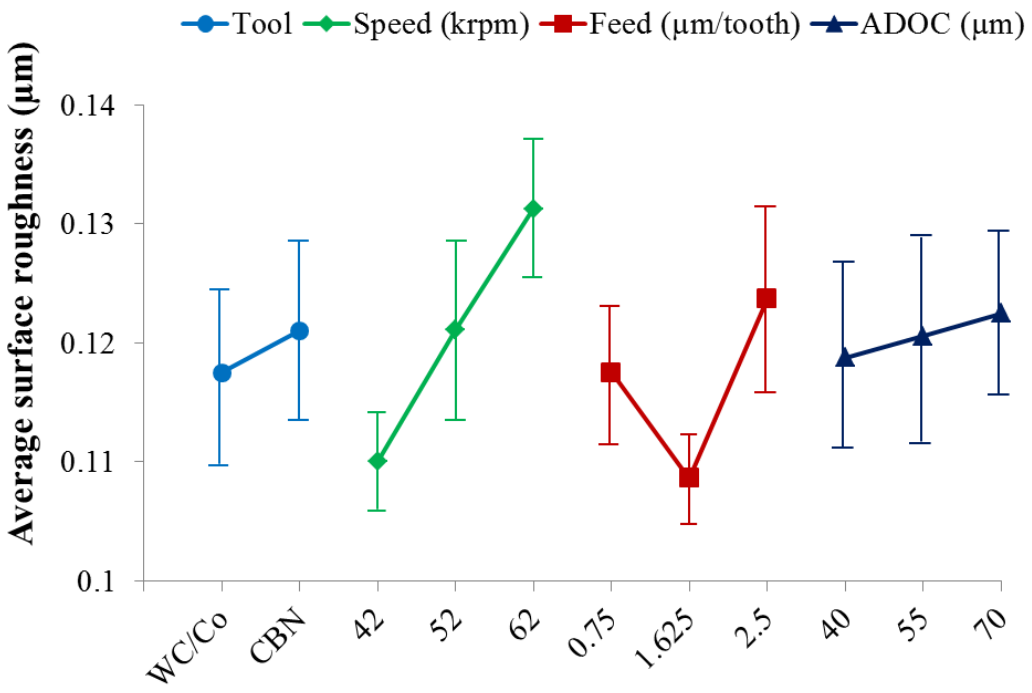

Figure 3.10: Main effects plot for average surface roughness (Ø381 µm)

Table 3.10: ANOVA table for average surface roughness (Ø381 µm).

Source	DF	Adj SS	Adj MS	F-value	P-value
Tool	1	0.0001003	0.0001003	0.53	0.475
$\boldsymbol{\Omega}$	2	0.0027219	0.0013609	7.14	0.004
f_z	2	0.0047728	0.0023864	12.52	0.000
a_p	2	0.0002969	0.0001484	0.78	0.470
Error	24	0.0045746	0.0001906		
Total	31	0.0124670			

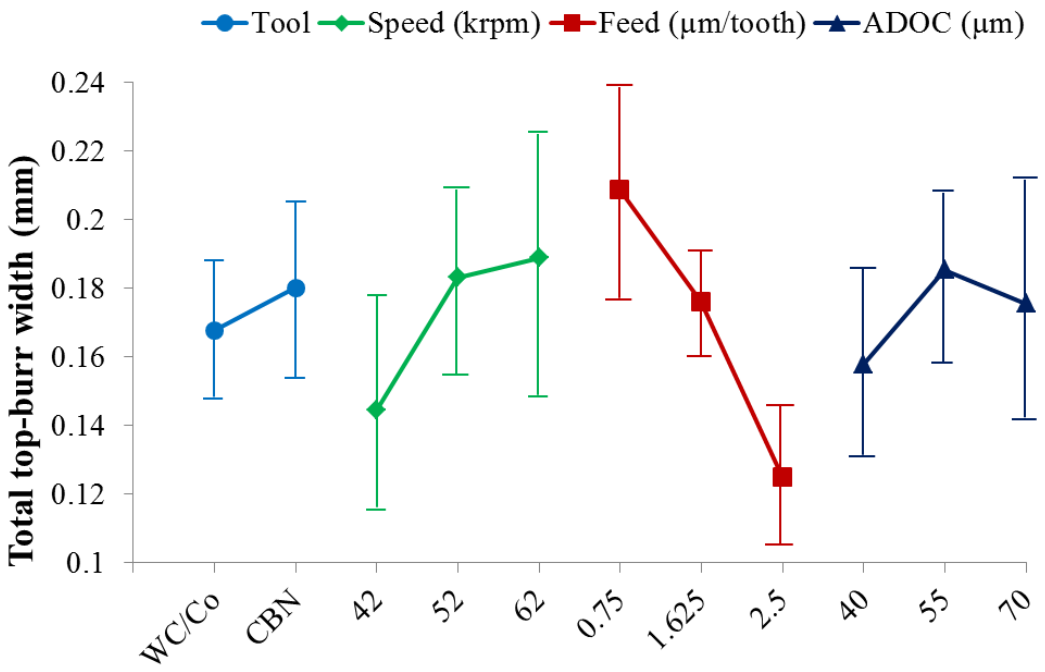

Figure 3.11: Main effects plot for total top-burr width (Ø381 µm)

Table 3.11: ANOVA table for total top-burr width (Ø381 µm).

Source	DF	Adj SS	Adj MS	F-value	P-value
Tool	1	0.001238	0.001238	0.44	0.512
Ω	2	0.008411	0.004205	1.51	0.242
f_z	2	0.052262	0.026131	9.36	0.001
a_p	2	0.000895	0.000448	0.16	0.853
Error	24	0.066994	0.002791		
Total	31	0.129800			

Similar to Experiment 1, the response surface models was developed based on the experimental results as shown in Table 3.12. To compare the fitted values and the actual experimental data, the Table 3.13 is constructed. Also, the plots in Figures 3.12 and 3.13 show the prediction error of surface roughness model and total-top burr width model, respectively. The results reveal that the surface roughness model has an approximate

accuracy of ±0.03 µm; the total top-burr width model has an approximate accuracy of ±0.08 mm.

The MOPSO was performed and the result is shown in Figure 3.14. In case of the smaller micro-end mill (Ø381 µm) the results are different from the results of large micro-end mill (Ø508 µm). The Pareto frontier indicates that the cBN coated WC/Co tool outperformed the uncoated WC/Co tool in terms of minimizing top-burr formation. In case of surface roughness, both tools give approximately the same results, however, the uncoated WC/Co tool yielded smaller top-burr formation. Hence, for the balance of surface roughness and burr formation, the uncoated WC/Co tool should be more preferable.

Table 3.12: The regression coefficients for the predictive models.

Term	**Regression coefficient**			
	Uncoated tool		**cBN coated tool**	
	R_a	**B_T**	**R_a**	**B_T**
β_0	-0.057952	0.327114	0.104325	-0.063972
Ω	0.005681	-0.001576	0.000627	0.005965
f_z	-0.082361	-0.089490	-0.057504	0.123466
a_p	0.002486	-0.003104	0.000469	0.000952
Ω^2	-0.000052	0	0	0
f_z^2	0.027847	0.008990	0.015275	0
a_p^2	-0.000020	0	0	0
$\Omega * f_z$	0	0	0	-0.002871
$\Omega * a_p$	0	0.000047	0	0
$f_z * a_p$	0	0.000724	0	-0.000829
R^2	86.61%	84.83%	81.06%	84.10%
R^2(adj)	77.69%	74.72%	74.18%	76.15%

Table 3.13: Predicted values vs. experimental results (Ø381 µm).

Run	Tool	Ω (krpm)	f_z (µm/tooth)	a_p (µm)	R_a (µm)			B_T (mm)		
					Model	Exp.	Error	Model	Exp.	Error
1	Uncoated WC/Co, Ø381 µm	42	0.75	40	0.109	0.103	0.006	0.174	0.137	0.037
2		42	0.75	70	0.116	0.110	0.006	0.156	0.157	-0.001
3		42	2.5	40	0.123	0.103	0.020	0.120	0.143	-0.023
4		42	2.5	70	0.130	0.120	0.010	0.139	0.115	0.024
5		62	0.75	40	0.115	0.113	0.002	0.180	0.209	-0.029
6		62	0.75	70	0.122	0.117	0.005	0.190	0.159	0.031
7		62	2.5	40	0.129	0.143	-0.014	0.125	0.127	-0.002
8		62	2.5	70	0.136	0.130	0.006	0.173	0.261	-0.088
9		52	1.625	55	0.111	0.113	-0.002	0.150	0.132	0.018
10		52	1.625	29.8	0.092	0.103	-0.011	0.138	0.128	0.010
11		52	1.625	80.2	0.104	0.110	-0.006	0.163	0.159	0.004
12		52	0.153	55	0.159	0.180	-0.021	0.200	0.293	-0.093
13		52	3.097	55	0.183	0.117	0.066	0.140	0.119	0.021
14		35.2	1.625	55	0.092	0.107	-0.015	0.134	0.194	-0.060
15		68.8	1.625	55	0.101	0.103	-0.002	0.167	0.156	0.011
16		52	1.625	55	0.111	0.107	0.004	0.150	0.195	-0.045
17	cBN coated WC/Co, Ø385 µm	42	0.75	40	0.114	0.110	0.004	0.201	0.137	0.064
18		42	0.75	70	0.128	0.123	0.005	0.211	0.282	-0.071
19		42	2.5	40	0.101	0.103	-0.002	0.148	0.112	0.036
20		42	2.5	70	0.115	0.107	0.008	0.115	0.074	0.041
21		62	0.75	40	0.127	0.130	-0.003	0.278	0.317	-0.039
22		62	0.75	70	0.141	0.133	0.008	0.288	0.270	0.018
23		62	2.5	40	0.113	0.143	-0.030	0.124	0.082	0.042
24		62	2.5	70	0.127	0.140	-0.013	0.091	0.086	0.005
25		52	1.625	55	0.109	0.103	0.006	0.182	0.212	-0.030
26		52	1.625	29.8	0.097	0.097	0.000	0.192	0.222	-0.030
27		52	1.625	80.2	0.121	0.130	-0.009	0.172	0.165	0.007
28		52	0.153	55	0.154	0.163	-0.009	0.287	0.268	0.019
29		52	3.097	55	0.131	0.123	0.008	0.077	0.106	-0.029
30		35.2	1.625	55	0.099	0.110	-0.011	0.160	0.173	-0.013
31		68.8	1.625	55	0.120	0.113	0.007	0.204	0.178	0.026
32		52	1.625	55	0.109	0.107	0.002	0.182	0.199	-0.017

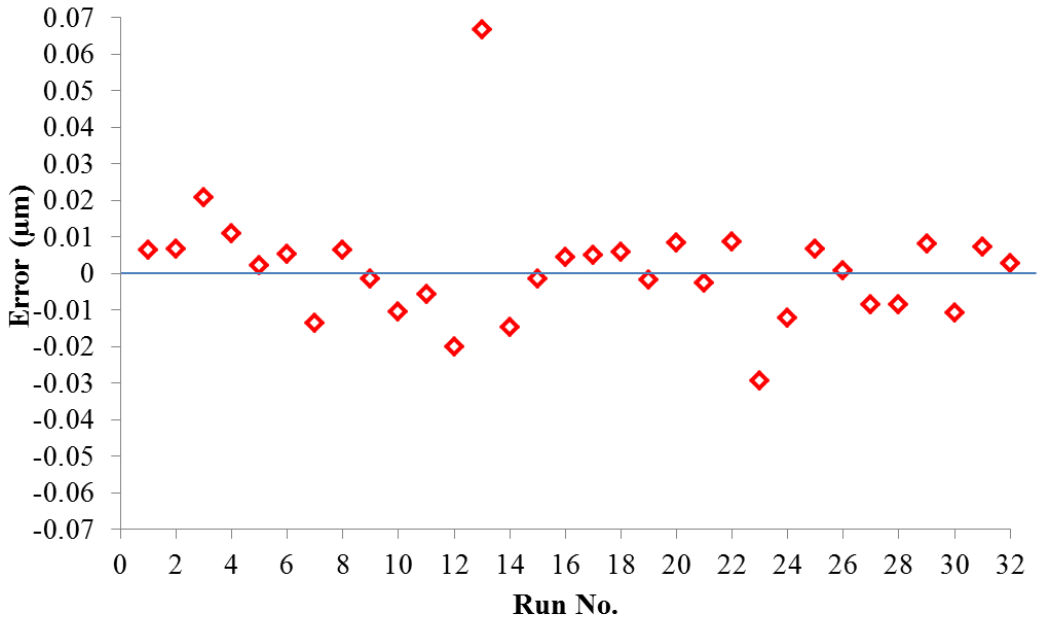

Figure 3.12: Average surface roughness prediction error (Ø381 µm).

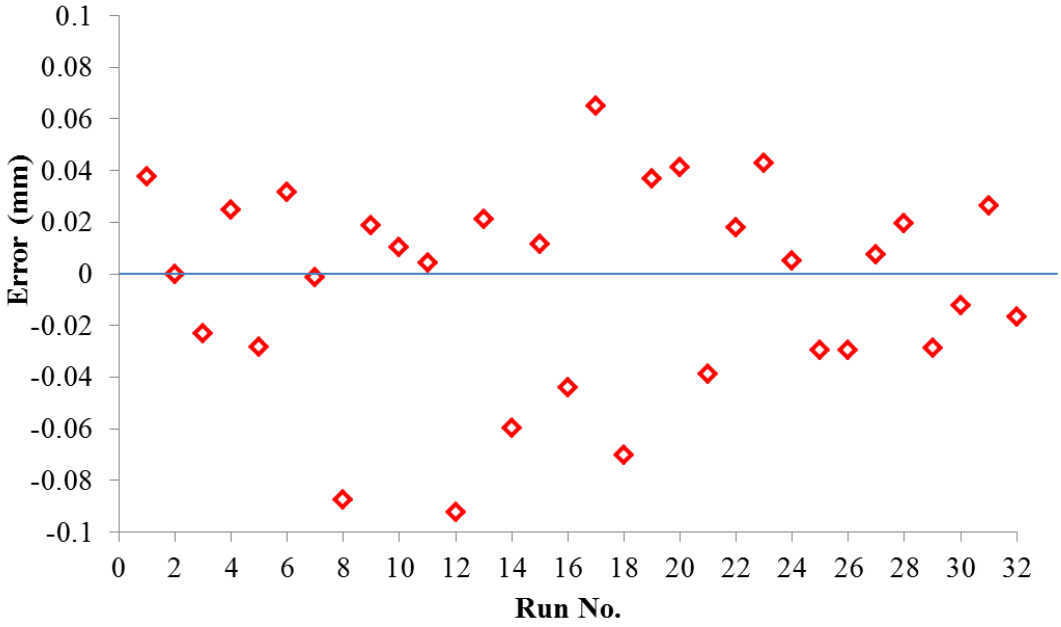

Figure 3.13: Total top-burr width prediction error (Ø381 µm).

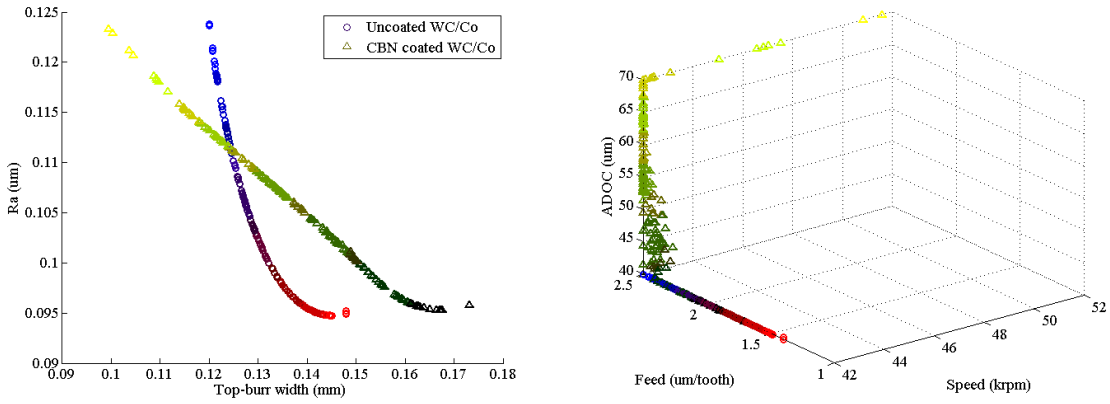

Figure 3.14: Optimal micro-end milling parameters for the tool diameter of Ø381 µm; (left) Objective function space, and (right) decision variable space.

4.3 Influence of cutting speed, feed and axial depth of cut

In order to study the influence of process parameters, the results from both experimental sets were plotted together as shown in Figures 3.15 and 3.16. The data points represent the main effect value at that particular level of cutting parameters. It can be seen that increasing the cutting speed has a negative effect on both surface roughness and top-burr formation (see Figures 3.15a and Figure 3.16a). The influence is more significant in the small tool (Ø381 µm). The relationship between feed per tooth and average surface roughness (see Figure 3.15b) suggested that feed per tooth significantly affects the surface roughness. In conventional macro-machining, it is well established that increasing feed per tooth increases the surface roughness. Hence, the feed per tooth is commonly kept small whenever a fine surface is required. However, in micro-machining, too small feed per tooth will result in ploughing (minimum chip thickness effect) which deteriorates the surface roughness. Therefore, in order to achieve the best attainable surface roughness the optimal level of feed per tooth has to be found. However, Figure

3.16b suggests that increasing feed per tooth reduces top-bur formation. In Figure 3.15c and 3.16c, only the Ø508 μm uncoated WC/Co tool shows the significantly positive effect of axial depth of cut on average surface roughness and top-burr formation while the others show no significant influence.

4.4 Tool wear analysis

Another mean to analyze the tool performance is by looking at the tool wear. In this study, tool wear was analyzed in terms of reduction of nominal diameter and edge radius. The results in Figure 3.17 shows that the cBN coated WC/Co tool can maintain its original diameter and edge radius longer than WC/Co tool which implies that tool life of the cBN coated WC/Co tool is longer than tool life of uncoated WC/Co tool. The SEM images of the worn tools taken after 540 mm of cut are shown in Figure 3.18. The material adhesion and cutting edge chipping can be observed on the cBN coated WC/Co tool.

As the tool edge radius increases due to tool wear, the minimum chip thickness required also increases. Since the feed per tooth was constant throughout the experiment, the ploughing of the tool and workpiece increasingly took place and dominated the cutting process. As a result, tool wear rate may be significantly increased after tool wear reaches to a certain point.

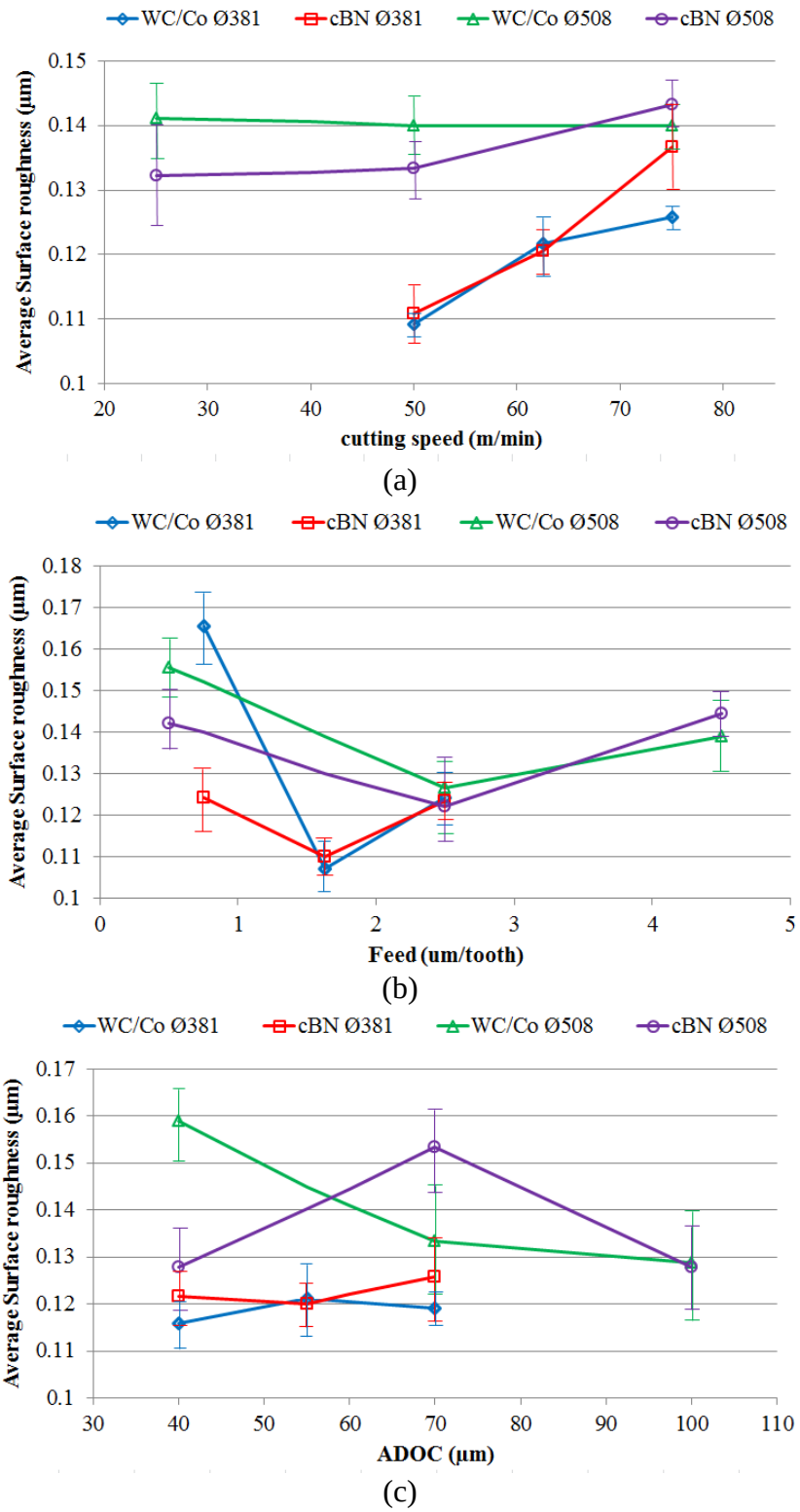

Figure 3.15: Effect of process parameters on average surface roughness; (a) effect of cutting speed, (b) effect of feed per tooth, and (c) effect of axial depth of cut.

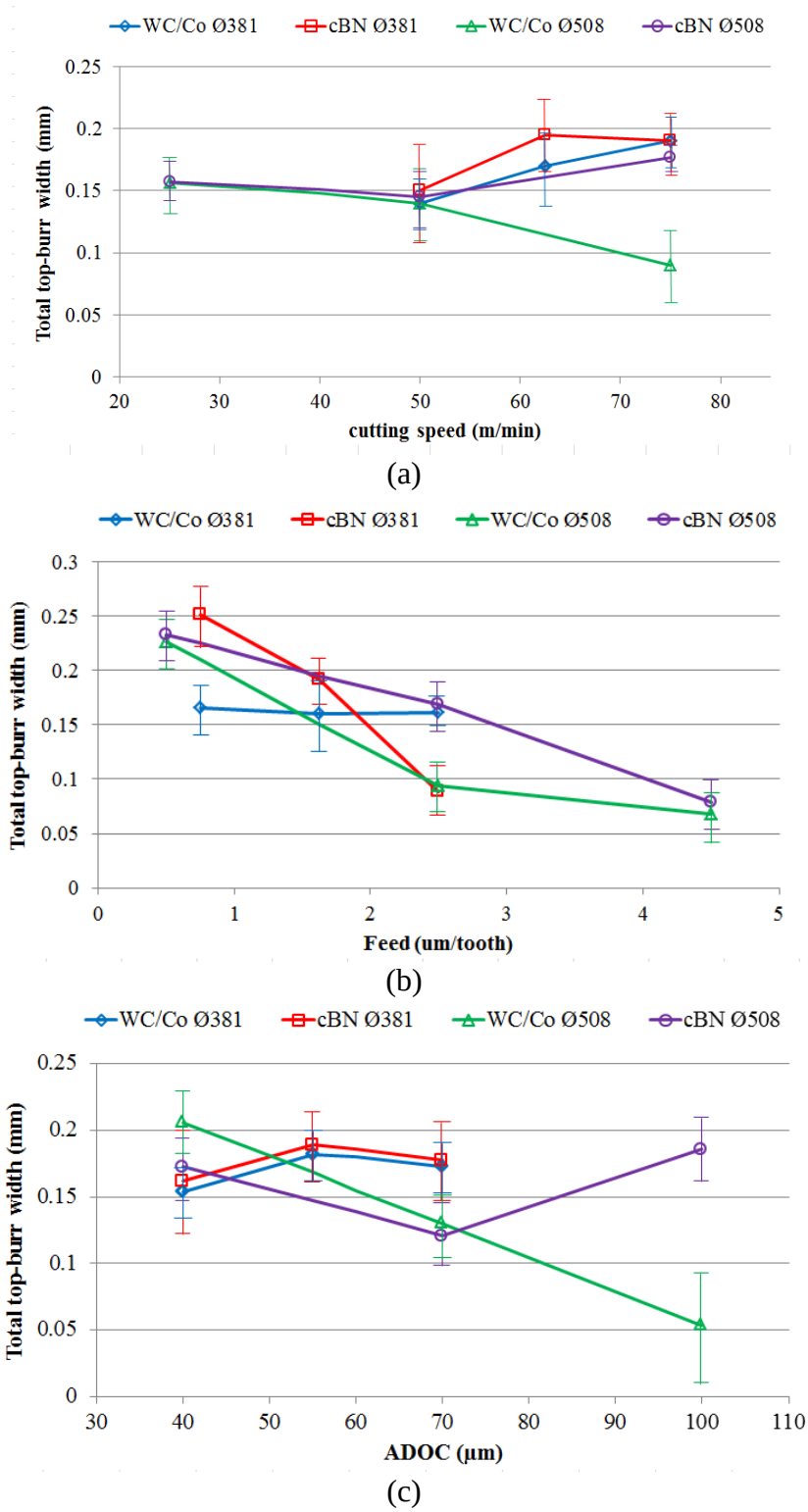

Figure 3.16: Effect of process parameters on top-burr width; (a) effect of cutting speed, (b) effect of feed per tooth, and (c) effect of axial depth of cut.

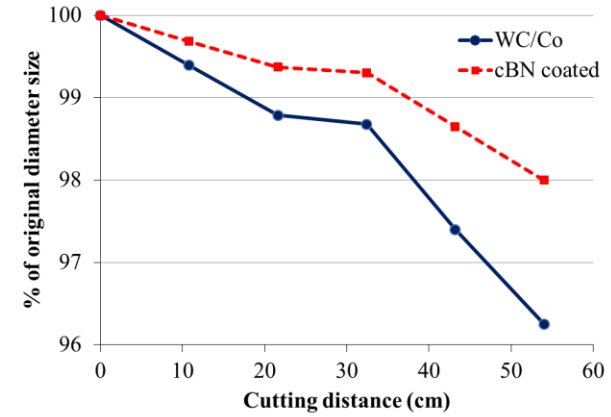

(a)

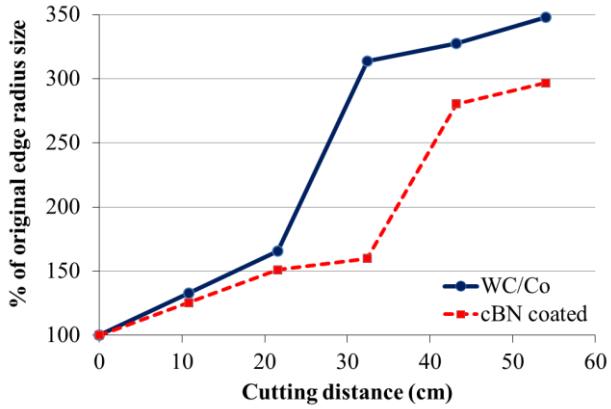

(b)

Figure 3.17: Tool wear; (a) change in the tool diameter and (b) change in the tool edge radius

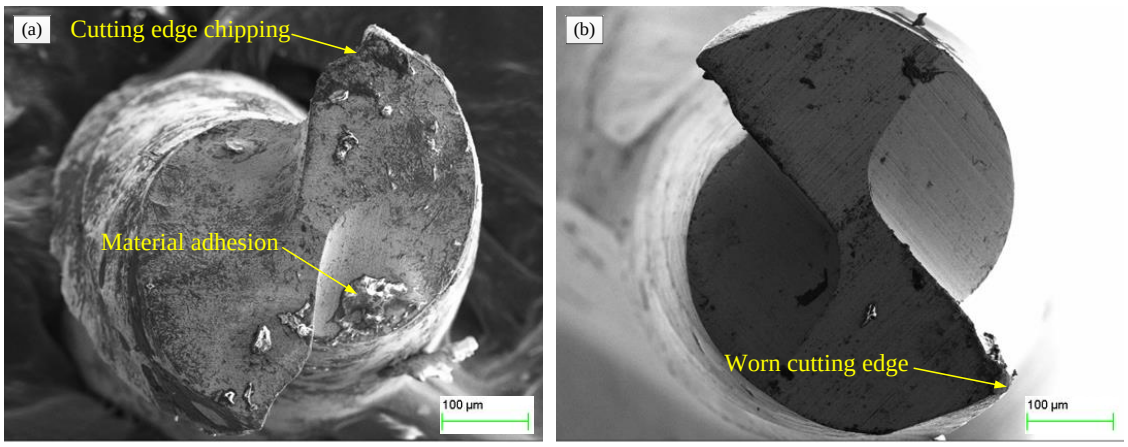

Figure 3.18: Images of the worn micro-end mills obtained with SEM; (a) cBN coated micro-end mill and (b) Uncoated micro-end mill.

Approximately, it is expected that the cBN coating would be worn out until the WC/Co begin to expose once the edge radius reach to 6.5 μm (130% of the original edge radius) and is fully exposed when the edge radius reached to 7.5 μm (150% of the original edge radius). Based on Figure 3.17, the measured result obtained from the experiment of cBN coated tool shows rapid tool wear after 30 cm of cutting in which the edge radius has increased by 150%. It is possible to conclude that the rapid wear rate occurring in cBN coated tool was a result of depletion of the cBN coating plus the ploughing caused by increased edge radius.

5. Conclusions

Based on these results, it seems that the major benefit of applying cBN coatings on the WC/Co micro end mill tools is the improvement of tool life. The ability to maintain its original geometry is very important for a micro-tool since the dimensional accuracy of the machined part depends on it and the tolerance of a micro-product is very tight. The high hardness of cBN coating helps protecting the tool from abrasive wear which may be the major type of wear occurring in the micro-milling process.

This study reveals that the major drawback of cBN coated micro-end mills is the increase of top-burr formation. The main reason may be an increase in the edge radius due to the thickness of coating layer added on the original tools. Large edge radius promotes ploughing which may be the cause of top-burr formation. In terms of surface roughness, there is not enough evidences to conclude that surface roughness values obtained from the cBN coated WC/Co tool and the uncoated WC/Co tool are significantly different.

Top-burr formation is one of the major problems in micro-milling of Ti-6Al-4V. Without the proper selection of process parameters, the size of top-burr is quite significant and a subsequent burr-removal process is required. However, if the optimal condition is selected, this problem of top-burr formation can be minimized or eliminated. Based on this study, to minimize top-burr formation, it is recommended that feed per tooth and axial depth of cut should be set at the highest process level. Also the tool should be as sharp as possible (small cutting edge radius), thus coated tools may not be a good choice for this objective.

Surface roughness obtained from micro-end milling of Ti-6Al-4V depends significantly on the selection of feed per tooth. Selecting too low feed per tooth would result in ploughing of the tool on the workpiece which deteriorates the surface roughness while selecting too high feed per tooth would result in larger feed marks which increases the surface roughness. Therefore, the optimal level of feed per tooth has to be found in order to achieve the best surface roughness. Based on this study, it appears that the optimal level of feed per tooth is around 50-60% of the edge radius. Also, it is possible to conclude that this number represents the minimum chip thickness requirement for micro-machining Ti-6Al-4V.

It can be seen that experimentation can give the solutions for many problems of micro-machining. However, there are still questions beyond what can be observed experimentally. For example, the role of cutting temperature, how the material behaves during the chip formation and the heat transfer between tool and workpiece. The ability to answer these questions is limited by the technology that can be applied in the experimentation. Therefore, other means of finding solution must be introduced. In the

next chapter, finite element (FE) modeling and simulation will be introduced for the process of micro-end milling of Ti-6Al-4V. The FE simulation will be used to support the finding of these experiments and also to seek some answers beyond the capability of experimentation.

CHAPTER 4

2-D FINITE ELEMENT MODELING AND SIMULATIONS

1. Introduction

In the previous chapters, experiments have been conducted to investigate the performance of the micro-end milling process. The results have led to some important conclusions. However, not all answers can be obtained from the experiments alone. For instance, the cutting temperature in micro-end milling is extremely difficult to measure, thus it was not included into the experimental studies. It was not only in this study where some of the important process performance measures have to be excluded from the experimental studies due to the difficulty in obtaining some credible data; many other researchers also faced similar problems (Aramcharoen et al. 2008, Biermann et al. 2013, Ucun et al. 2013). Therefore, it can be claimed that experimentation alone cannot fulfill the desire for understanding the micro-end milling process; other methods of obtaining the data are required.

Numerical modeling and simulation can be used to expand the investigation and provide a support to the experimentation. One of the powerful methods of numerical modeling is the finite element (FE) modeling and simulation. FE modeling and simulation is widely used in analysis of cutting and formation processes (Arrazola et al. 2013). FE modeling can provide a rich set of results including stress, strain, temperature, and displacement fields (Arrazola et al. 2013, Özel et al., 2010). Its benefits have been proven in many studies both in macro-scale and micro-scale cutting (Afazov et al. 2010, Ding et al. 2011, Mackerle 1998, Mackerle 2003, Mamalis et al. 2001, Özel et al. 2010,

Özel et al. 2011, Özel & Zeren 2007, Sima & Özel 2010, Umbrello 2008, Yen et al. 2004).

Due to the advancements in computer technology, FE simulations are now more powerful than before. Also, a lot of commercial FE modeling and simulation software are available with many options and tools which can satisfy the user's need. These software create the opportunity for researchers to utilize the FE modeling and simulation method as a supporting tool or even an alternative to the expensive and time consuming physical experiments. The vision of replacing all the physical experiments with modeling and simulation may be achieved in near future.

This chapter is a continuation of the previous experimental study given in Chapter 3. FE modeling and simulation was utilized to support the experimental results. The micro-end milling of Ti-6Al-4V using coated and uncoated tools were modeled and simulated. The results were obtained in terms of cutting force, cutting temperature, and tool wear rate. In addition, the influence of material assumptions in FE modeling and simulation was also studied.

2. 2-D Finite Element Simulations

In this section details about 2-D FE modeling and simulation of micro-end milling will be discussed including FE simulation procedures, material constitutive modeling, tool and workpiece geometry and their properties, boundary conditions, friction, and heat transfer, tool wear modeling, and simulation controls.

2.1 Finite element simulation of machining process

Machining processes are difficult to model for various reasons. Unlike metal forming processes, where almost the whole workpiece get plastically deformed, in

machining process, the plastic deformation is localized near the cutting edge. Therefore, the analysis of only a small region of the workpiece around the cutting edge is needed. As a result, the selection of the domain dimensions and the appropriate boundary condition becomes a difficult task. Furthermore, even at a moderate cutting velocity, the strain rates are quite high and the temperature rise is also quite large. As a result, the viscoplasticity and temperature-softening effects become more important compared to strain-hardening. Therefore, the material properties associated with these two effects should be known. Additionally, to incorporate the temperature rise in the analysis, one needs to solve the heat transfer equation governing the temperature field in conjunction with the usual equations governing the deformation field. For plastic deformations, these equations are coupled, and hence difficult to solve. However, the problem can be decoupled by first estimating the average temperature in the cutting zone, then solving the governing equations of the deformation field by evaluating the material properties at the estimated temperature.

In this study, the 2-D FE simulations were conducted by utilizing the commercial software DEFORM-2D. DEFORM-2D finite element code is based on an implicit updated Lagrangian computational routine; the finite element mesh is linked to the workpiece and follows its deformation. To simulate the chip formation a remeshing procedure is performed very frequently, so that the workpiece mesh is frequently updated and modified to follow the tool progress. This technique makes it possible to simulate chip separation from the workpiece without any arbitrary predefinition.

The general procedures of FE modeling and simulation of machining process can be divided into 8 steps:

1) Create and position the tool and the workpiece geometry.
2) Divide the tool and the workpiece into pieces: elements with nodes (meshing).
3) Assign material properties to the tool and the workpiece.
4) Define the contact between the tool and the workpiece and assign friction properties.
5) Define mechanical boundary conditions and thermal boundary conditions.
6) Define the tool and the workpiece movements.
7) Solve the system of equations involving unknown quantities at the nodes (e.g., displacements and temperature).
8) Calculate desired quantities (e.g., strains, stresses) at the element of the mesh.

2.2 Material constitutive modeling

The Johnson–Cook (J-C) material model is widely used for analysis of material flow stress, especially for those materials which their flow stress is highly influenced by temperature and strain rate; the influence of strain, strain rate and temperature on the flow stress is defined by three multiplicative yet distinctive terms: strain hardening, strain rate sensitivity and thermal softening behavior (Johnson & Cook 1983). However, the J-C model still has some deficiency in representing high strain rate or flow softening type of material behavior and coupling effects of strain, strain rate and temperature. Thus, some modifications to the J-C model have been proposed (Calamaz et al. 2008).

In machining of titanium alloys, material plastic instability related localized flow softening phenomenon has been observed which can be described as offering less resistance to local plastic deformations due to rearrangement of dislocations caused by subsequent cycling or dynamic recrystallization in the material (Guo et al. 2006). This

phenomenon is usually observed during an increase in strain beyond a critical strain value together with a rapid rise in material temperature. Flow softening is believed to cause adiabatic shearing within the primary shear zone. Thus, chip segmentation with shear bands are formed as the deformed material leaves this zone. For this reason, a modified material constitutive model with flow softening at elevated strains and temperatures was proposed. Sima and Özel (Sima & Özel 2010) have proposed and validated the modified J-C model including flow softening effects on orthogonal macro-machining of Ti-6Al-4V proving a capability in simulating the serrated chip formation.

The modified J-C material model with temperature-dependent parameters and strain softening proposed by Sima and Özel (Sima & Özel 2010) was utilized in this study as shown in Eq. (4.1). In this model, the flow softening is defined with a decreasing behavior in flow stress with increasing strain beyond a critical strain value. Nonetheless, below that critical strain, the material still exhibits strain hardening. In addition to the original J-C model which is defined by three multiplicative terms namely strain hardening, strain rate sensitivity, and thermal softening behavior, this model includes one more term namely temperature-dependent flow softening. Also the strain hardening term is modified to include flow softening at higher strain values.

$$\sigma = \left[A + B\varepsilon^{n}\left(\frac{1}{exp(\varepsilon^{a})}\right)\right]\left[1 + Cln\frac{\dot{\varepsilon}}{\dot{\varepsilon_0}}\right]\left[1 - \left(\frac{T-T_0}{T_m-T_0}\right)^{m}\right]\left[D + (1-D)\left[tanh\left(\frac{1}{(\varepsilon+p)^{r}}\right)\right]^{s}\right]$$

Eq. (4.1)

where $D = 1 - \left(\frac{T}{T_m}\right)^{d}$, $p = \left(\frac{T}{T_m}\right)^{b}$, σ is flow stress, ε is true strain, $\dot{\varepsilon}$ is true strain rate, $\dot{\varepsilon_0}$ is reference true strain rate, T is work temperature, T_m is material melting temperature, T_0 is ambient temperature, and A, B, n, a, C, m, d, b, r, s are the model constants. The values of A=782.7 MPa, B= 498.4 MPa, n=0.28, a=2, C=0.028, $\dot{\varepsilon_0}$=10^{-5}, m=1.0, d=0.5,

r=2, b=5, s=0.05, T_0=20°C and a melting temperature of T_m=1450°C have been utilized in this model (Özel et al. 2010). Figure 4.1 shows the flow stress of modified J-C material model at the temperature (T) of 1200 °C.

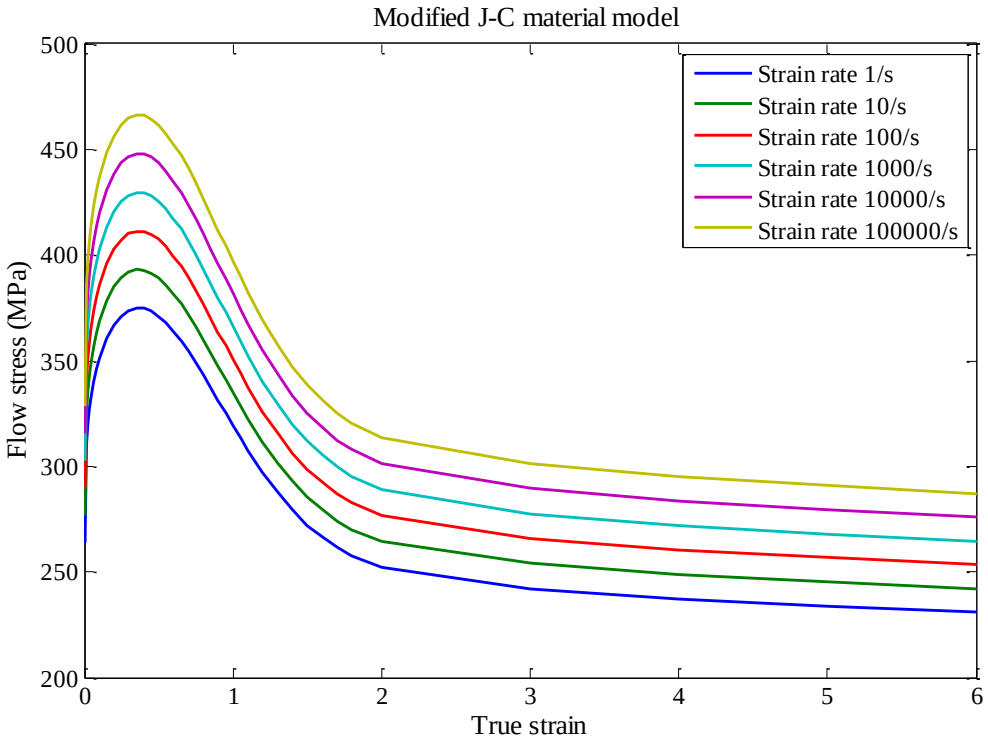

Figure 4.1: Flow stress of modified J-C material model (T = 1200 °C)

2.3 Modeling of micro-end milling process using finite element simulations

2-D FE simulation models for the full immersion (slotting) micro-milling process were developed. The positioning of the tool and workpiece as well as the tool movement is illustrated in Figure 4.2. The FE simulations began at the tool rotation angle of $\phi = 0°$, where the first cutting edge is initially in contact with the workpiece. By assuming that there is no chip formation from the previous pass (no chip load at the second cutting edge), the cutting forces at $\phi = 0°$ is assumed to be zero. The simulation continues until a

rotation angle of ϕ = 185° to capture the behavior of the chip close to the separation point.

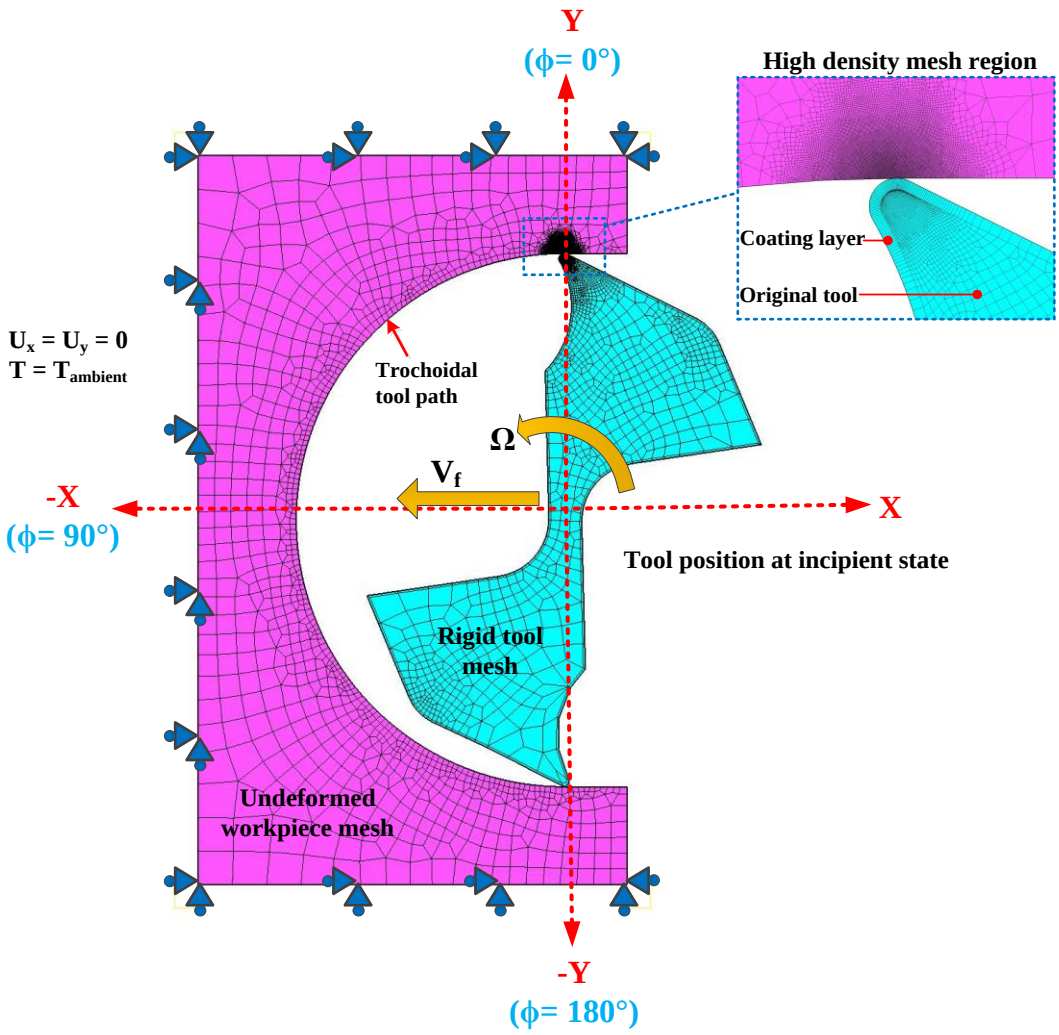

Figure 4.2. The setup of FE model for micro-end milling.

2-D two-flute end mill geometry was created based on the data provided from the tool manufacturer. For an uncoated WC/Co micro-end mill, the tool diameter is ∅508 µm and the tool edge radius (r_β) is 3±0.5 µm. The tool material is fine grain tungsten carbide (WC) in a cobalt (Co) matrix, hence it will be represented with WC/Co. For a cBN coated

WC/Co micro-end mill, a cBN coating layer of 2 µm was added to the original tool geometry resulting in an increase of tool diameter and edge radius. Thus, the final tool geometry after coating has a diameter of ∅512 µm and an edge radius (r_β) of 5±0.5 µm (see Figure 4.3).

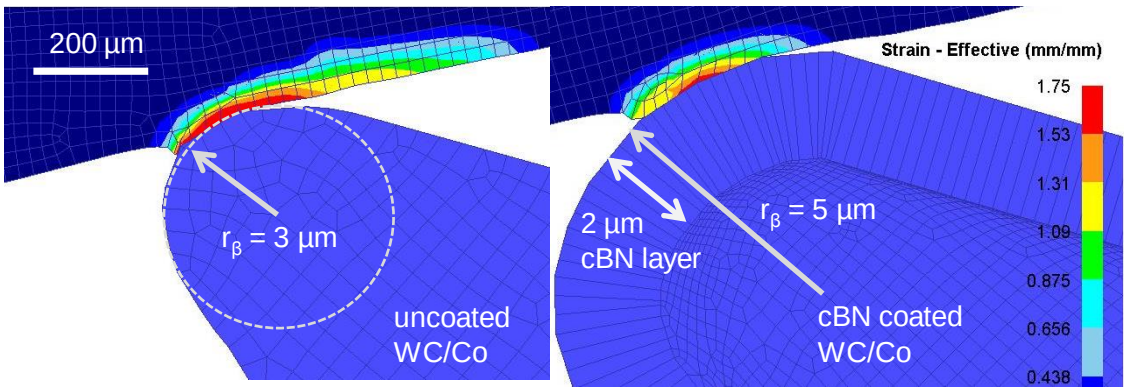

Figure 4.3: FE simulation model for uncoated WC/Co and cBN coated micro-end mills with their edge radii (Özel et al. 2011).

The coated and uncoated tools were modeled as rigid objects. The thermal properties of tool materials are listed in Table 4.1. Tool was meshed into 2,500 elements (4-node quadrilateral) with the high mesh density around the active cutting edge. The minimum element size is approximately 0.1 µm. Tool moved along the -X direction while rotating around the tool center. The heat was allowed to transfer throughout the whole profile of the tool.

A section of a workpiece around the slot was taken to create the undeformed workpiece geometry. The curve represents the pre-machined surface that was created based on the trochoidal tool path which imitates the real geometry of milled profile. The

workpiece geometry is shown in Figure 4.2.Workpiece geometry was then meshed into 25,000-30,000 4-node quadrilateral elements with minimum element size of 0.1 μm. A high mesh density window was placed around the tool-workpiece contact zone, and it follows this zone as the simulation goes on. The workpiece material was Ti-6Al-4V which was assumed to be homogeneous and isotropic. The mechanical and thermal properties of Ti-6Al-4V are shown in Table 4.1. The material flow stress followed the modified J-C model with temperature-dependent parameters and strain softening which discussed earlier. Figures 4.4 through 4.7 show the mechanical and thermal properties of Ti-6Al-4V plotted against temperature.

Table 4.1: Mechanical and thermal properties of work and tool materials used in FE simulations.

Properties	**Ti-6Al-4V**	**WC/Co**	**cBN**
Thermal conductivity, κ (N sec^{-1} °C^{-1})	$7.039e^{0.0011*T}$	55	100
Heat capacity, C_p (N mm^{-2} °C^{-1})	$2.24e^{0.0007*T}$	0.005*T+2.07	3.26352
Thermal expansion coefficient, α (°C^{-1})	3.10^{-9}*T+7.10^{-6}	$4.7*10^{-6}$	$5.2*10^{-6}$
Young's modulus, *E*	0.7412*T+113375	Not used	Not used
Poisson's ratio, ν	0.31	Not used	Not used

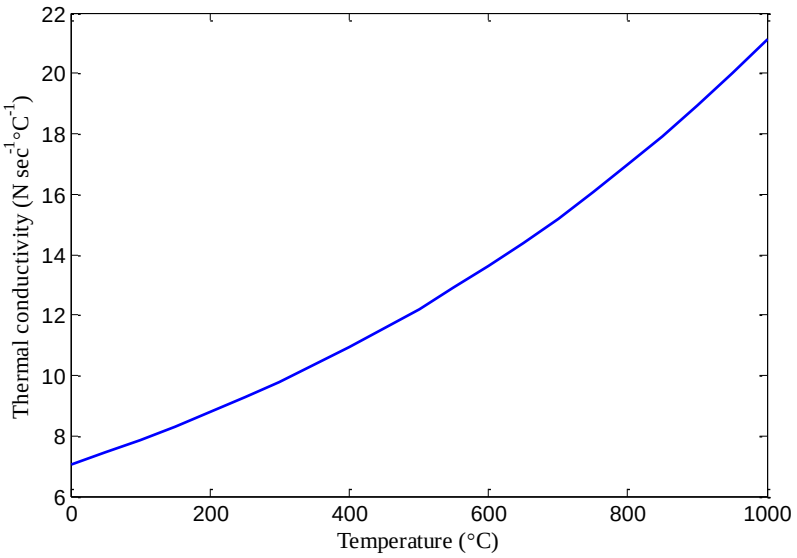

Figure 4.4: Thermal conductivity of Ti-6Al-4V.

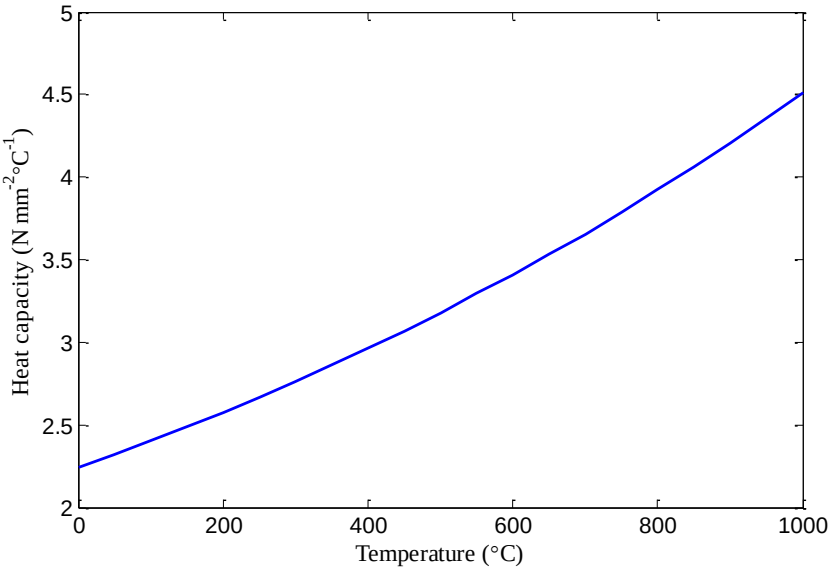

Figure 4.5: Heat capacity of Ti-6Al-4V.

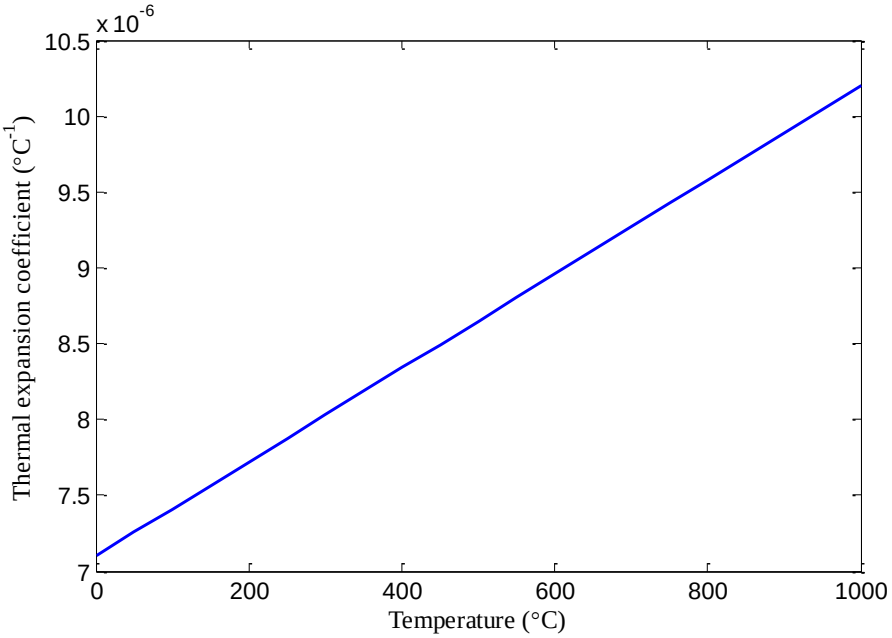

Figure 4.6: Thermal expansion coefficient of Ti-6Al-4V.

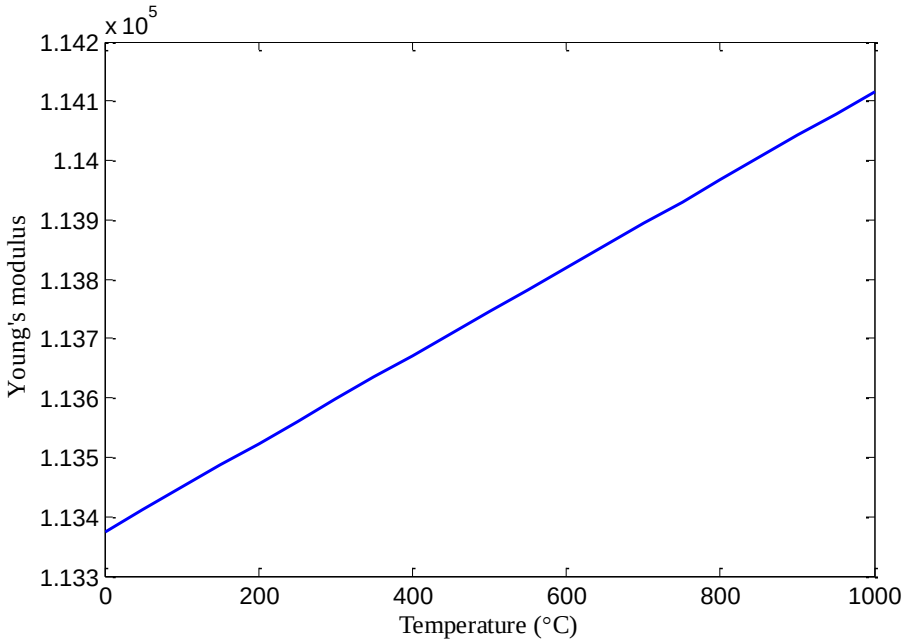

Figure 4.7: Young's modulus of Ti-6Al-4V.

2.4 Boundary conditions

The workpiece was set stationary by constraining some boundaries on both X and Y direction as shown in Figure 4.2. Some thermal boundary conditions were assigned. On the workpiece, the heat was only allowed to transfer along the tool path line while the nodal temperatures were fixed at the ambient temperature along with the other boundaries. On the tool, the heat was allowed to exchange on the whole surface of the tool. The ambient temperature was set at 20 °C.

2.5 Friction and heat transfer

The contact between tool and workpiece was the contact between cBN and Ti-6Al-4V materials for the case of the coated tool and the contact between WC/Co and Ti-6Al-4V for the uncoated tool. Two types of contact were assigned along the contact length: (i) sticking contact, and (ii) sliding contact. The sticking contact was defined by $\tau_f = mk$ where k is the work material shear yield stress, m is the shear friction factor and τ_f is the frictional stress. The sliding contact was defined by $\tau_f = \mu p_i$ where μ is the Coulomb friction factor and p_i is the interface pressure. If $\mu p_i < mk$, that contact was considered a sliding contact; but if $\mu p_i \geq mk$, sticking contact was applied. Between cBN and Ti-6Al-4V contact, the constant μ and m value were given as 0.4 and 0.9, respectively. In case of WC/Co and Ti-6Al-4V contact, the constant μ and m value were given as 0.7 and 0.9, respectively. The contact between chip and workpiece was assigned as a sliding contact with the constant friction coefficient (μ) of 0.2.

Heat transfer was allowed between tool and workpiece contact with the thermal contact conductance of 10^7 N sec^{-1} mm^{-1} $°C^{-1}$. The ambient temperature was set at 20 °C.

Heat transferred from workpiece and tool to the environment by convection with the convection coefficient of 0.02 N sec^{-1} mm^{-1} $°C^{-1}$.

2.6 Tool wear rate model

A wear rate model based on the sliding wear proposed by Usui et al. (1978) has been utilized in this study. Since the temperature rise in micro-end milling is never reaching the level of oxidation, chemical wear can easily be assumed negligible. This tool wear rate model calculates the rate of volume loss on the tool per unit area per unit time and uses interface temperature (T), normal stress (σ_n) and sliding velocity (v_s) at the tool surfaces as inputs and yields a wear rate (dW/dt) distribution in the tool as shown in Eq. (4.2).

$$\frac{dW}{dt} = c_1 \sigma_n v_s e^{-c_2/T} \qquad \text{Eq. (4.2)}$$

The model constants of c_1 and c_2 are material-dependent and were set as 7.8×10^{-9} and 2.5×10^{3}, respectively for Ti-6Al-4V titanium alloy (Özel et al. 2010).

2.7 Simulation controls

A convergence of a solution is highly sensitive to the step size, especially in the elasto-viscoplastic model. A preliminary test was conducted to optimize this value so that the convergence can be achieved within a small number of iterations. Finally, the simulations were performed with the step time increment of 10^{-8} sec. The workpiece was remeshed at every 50 steps or when the interference depth between tool and workpiece reaches 0.5 μm. Chip was manually removed at a certain length to keep a high mesh density without increasing mesh number. The simulation stops after a pass of single cutting edge was completed (ϕ =180°). After the simulations are complete, desired

process responses were collected. Tool wear and tool temperatures were extracted and averaged from seven points along the round cutting edge.

2.8 Comparison of coated and uncoated tools

In order to compare the performance of cBN coated WC/Co tool and uncoated WC/Co tool, a set of simulations was conducted for the coated and uncoated tools based on the process parameters given in Table 4.2. All simulation conditions conducted in this study are given in Table 4.3. In these simulations workpiece material were assumed to be viscoplastic material; tool was assumed to be rigid. The evaluation was done in terms of tool wear, cutting forces, and temperature. It should be noted that these process performances could not be evaluated in the previous experimental study.

Table 4.2: Parameters and levels assigned for the simulation and experiment.

Process parameters	**Levels**		
	1	**2**	**3**
Spindle speed, Ω (rpm) *(Cutting speed, v_c (m/min))*	16,000 *(25)*	32,000 *(50)*	48,000 *(75)*
Feed per tooth, f_z (μm/tooth)	0.5	2.5	4.5

Table 4.3: FE simulation conditions for comparison of coated and uncoated tools.

Run	Tool	Edge radius (µm)	Spindle speed (krpm)	Feed per tooth (µm/tooth)
1	cBN coated WC/Co	5	16	0.5
2				2.5
3				4.5
4			32	0.5
5				2.5
6				4.5
7			48	0.5
8				2.5
9				4.5
10	Uncoated WC/Co	3	16	0.5
11				2.5
12				4.5
13			32	0.5
14				2.5
15				4.5
16			48	0.5
17				2.5
18				4.5
19		5	16	4.5
20			32	
21			48	

2.9 Comparison of viscoplastic and elastic-viscoplastic simulations

In this study, the aim was to compare the influence of workpiece material assumption. Therefore, the simulations were conducted at the same micro-milling condition using two different material assumptions: elasto-viscoplastic material and viscoplastic material. The elasto-viscoplastic material assumption is supposed to be more accurate, since the micro-milling process may undergo a significant amount of elastic deformations compared to plastic deformations. However, the drawback of using elasto-viscoplastic material assumption is the time consumed and the difficulty of simulation controls. Therefore, this study focused on exploring advantages and disadvantages of

using the elasto-viscoplastic material assumption. Table 4.4 shows the parameter settings used in this simulation.

Table 4.4: Parameter settings for comparison of viscoplastic and elastic-viscoplastic simulations.

Tool	cBN coated WC/Co micro-end mill
Edge radius (r_β)	5 µm
Workpiece	Ti-6Al-4V
Spindle speed (Ω) *(Cutting velocity)*	48,000 rpm *(≅75 m/min)*
Feed per tooth (f_z)	4.5 µm/tooth

3. Results and Discussions

The results are discussed mainly in terms of cutting force generation, temperature distribution in cutting tool and workpiece, tool wear, chip formation and simulation time. The discussions also refer to the experimental results obtained in Chapter 3 for a comparison and model validation.

3.1 Effects on cutting force generation

Cutting forces obtained from FE simulations are presented in terms of forces in X and Y axis directions; F_x, F_y and resultant force (only magnitude) are shown in Figures 4.8a, 4.8b and 4.8c respectively. Each cutting force is represented by a sixth-degree polynomial equation. Based on these force plots, it can be seen that the cBN coated tool generates higher cutting forces compared to those generated by the WC/Co tool. It should be noted that cBN coated tool has a larger edge radius of $r_\beta = 5\pm0.5$ µm due to the coating layer while WC/Co tool has edge radius of $r_\beta = 3\pm0.5$ µm. Therefore, higher cutting forces can be expected. Among all cutting parameters, the parameter that influences

cutting forces the most is the feed per tooth. Increasing feed per tooth significantly increases cutting forces. The cutting speed seems to have very little influence on the cutting force generation when compared to the influence from the feed per tooth. The results also show an opposite trend that cutting forces increase when cutting speed is reduced. It should be noted that the reason in which the cutting forces do not drop to zero as the tool rotation exceeded 180° is based on the two facts that: (i) to complete the chip formation of one cutting edge, it requires geometrically more than 180° and (ii) another cutting edge begins to engage the workpiece at 180° resulting in the contact of both edge simultaneously. The zero cutting force was only assumed at the beginning of the simulation.

When comparing the cutting force trends among all conditions, it seems that the cutting forces obtained from the FE simulation at a feed per tooth of f_z = 0.5 µm/tooth developed a different trend compared to those obtained from FE simulations with higher feed per tooth values. A significantly lower cutting force at the beginning of tool rotation implies that ploughing might have taken place (due to an uncut chip thickness lower than the minimum chip thickness) at the early stage of tool entrance into material before full shearing took place.

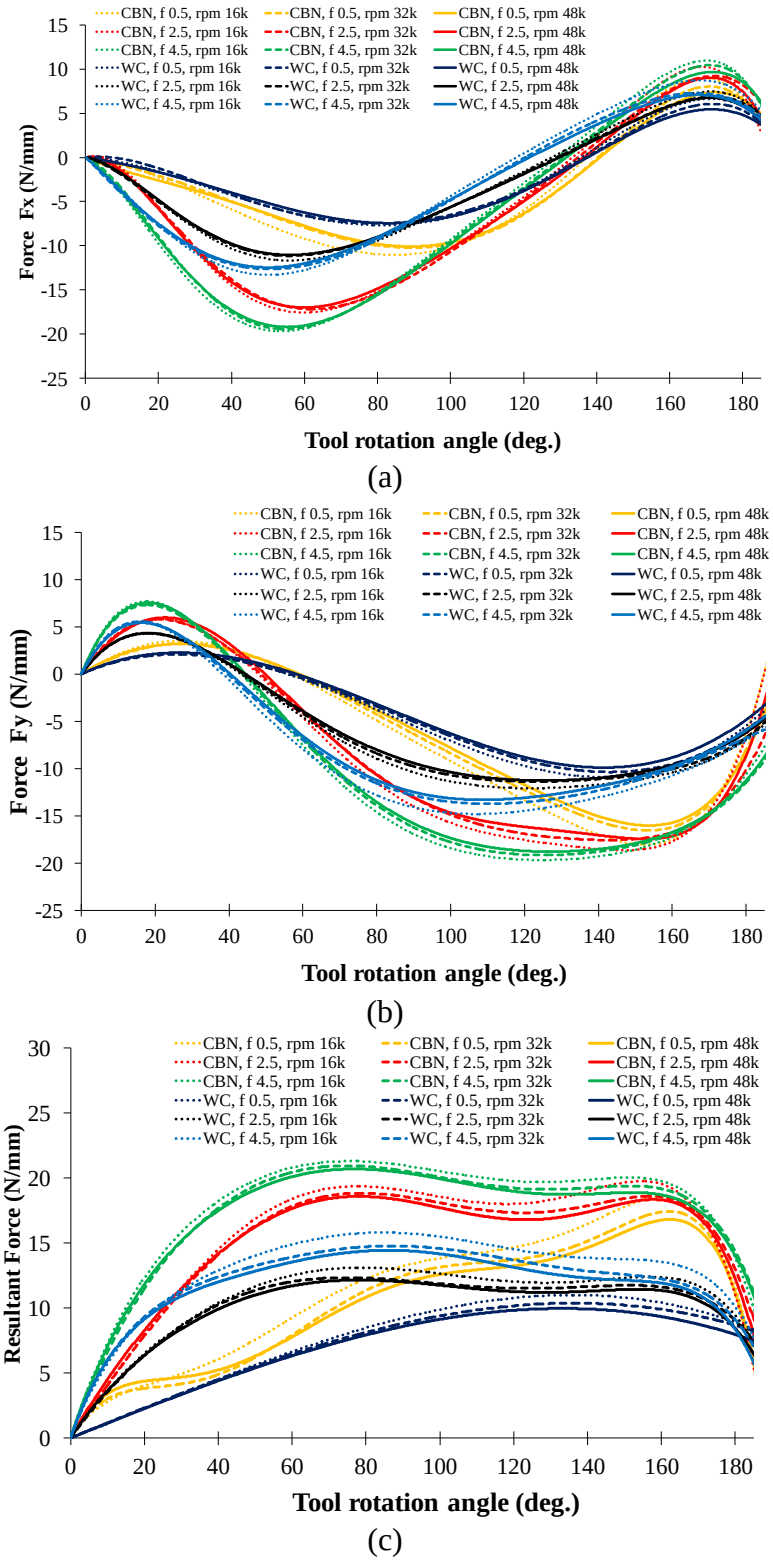

Figure 4.8: Cutting forces obtained from FE simulations; (a) F_x, (b) F_y, and (c) resultant force.

3.2 Effects on temperature generation

An average temperature of seven point measurements extracted along the tool cutting edge are plotted against the tool rotational angle as shown in Figure 4.9. The result shows that average tool temperatures of cBN coated tools are lower than those of WC/Co tools in every condition. Also, average tool temperature increases as cutting speed and feed per tooth increase (material removal rate increases). It should be noted that in spite of generating almost no different cutting forces at different cutting speeds, average tool temperatures significantly increase as cutting speed increases. Again, no identical trend for temperature was obtained from the simulation at feed per tooth of f_z = 0.5 µm/tooth.

In Figure 4.10, the temperature distribution at the cutting zone is shown using the same temperature scale. Both simulations were done at the same condition but the difference was in the tool coating. It can be seen that on average, the temperature in the cutting zone is lower when using cBN coated tool than the one when using uncoated WC/Co tool. The maximum temperatures were also different almost by 100 °C. In addition, it also shows that most of the heat generated during the deformation went into the chip.

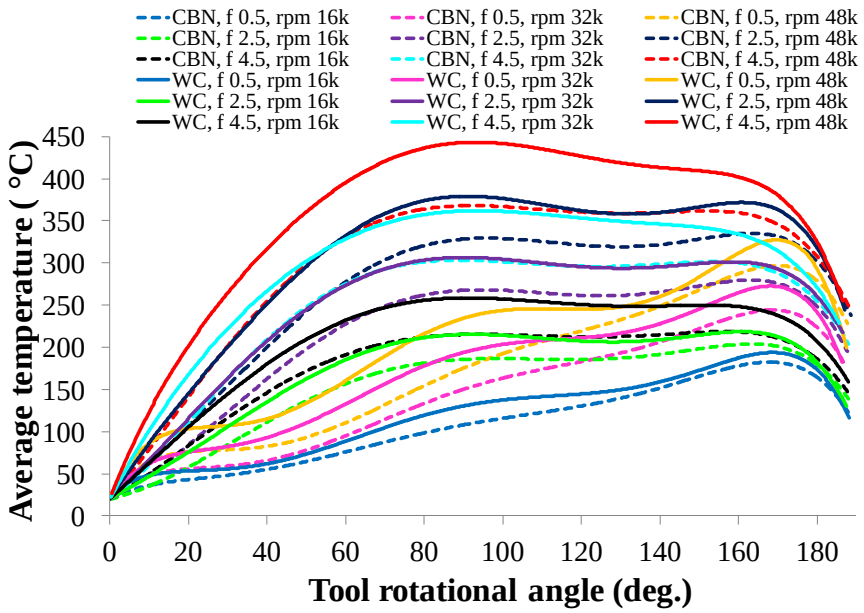

Figure 4.9: Average tool tip temperatures for uncoated and cBN coated WC/Co tools.

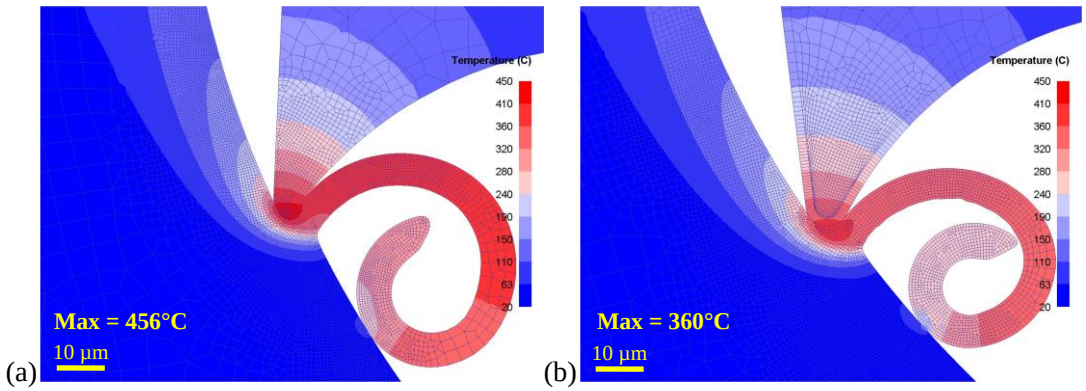

Figure 4.10: Comparison of tool and workpiece temperature distribution (Ω = 48,000 rpm, f_z = 4.5 µm/tooth, ϕ = 120°); (a) WC/Co and (b) cBN coated WC/Co micro-end mills.

The close up figures of temperature distribution between tool and workpiece are shown in Figure 4.11. It is interesting that the maximum temperature has occurred at a

different zone. In case of cBN coated tool, the maximum heating zone is located beneath the contact region along the shear plane due to cBN layer's higher thermal conductivity**;** but in case of uncoated WC/Co tool, it is right at the contact region.

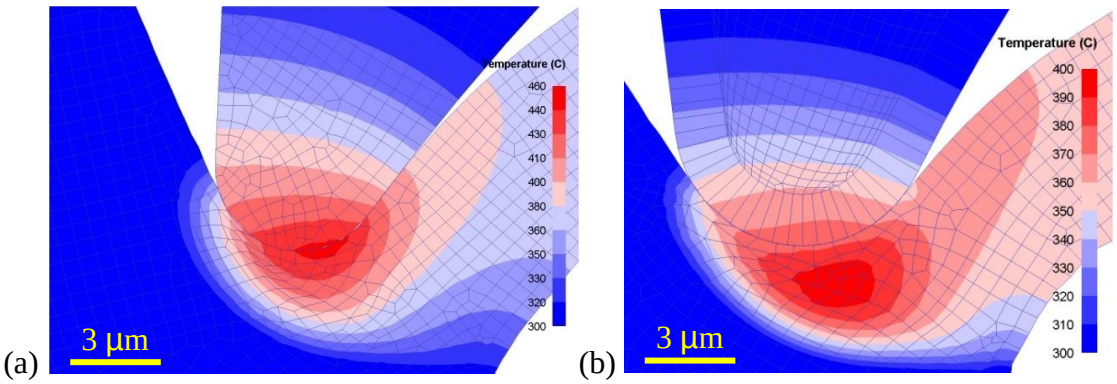

Figure 4.11: Temperature distribution at the cutting zone (Ω = 48,000 rpm, f_z = 4.5 µm/tooth, ϕ = 120°); (a) WC/Co (b) cBN coated WC/Co.

3.3 Effects on tool wear

Tool wear generation was investigated using FE simulations and compared to the experimental results obtained in Chapter 3. Tool wear results obtained from both approaches were compared in terms of cumulative tool wear. Figure 4.12 shows the comparison of edge radius due to wear and Figure 4.13 shows the reduction of the tool diameter as a result of tool wear. It can be seen that the estimated tool wear based on simulated wear rate is in agreement with measured ones. These results also validate the Usui's wear model and the model parameters used for machining Ti-6Al-4V titanium alloy. It should be noted that the cumulative tool wear calculated from the FE simulation

results do not include the effect of increasing edge radius due to tool wear; wear rate was treated as constant based on the wear rate of the unworn tool.

Figures 4.12 and 4.13; show that cBN coated tool can maintain its original diameter and edge radius longer than WC/Co tool does which implies that tool life of cBN coated tool is longer than tool life of uncoated WC/Co tool. It should be noted that the increase of edge radius due to tool wear is also accounted for the decrease of tool diameter. And the decrease of tool diameter of only 1% (approximately 5 μm) would be enough to significantly affect the geometrical accuracy of any micro-features in which tolerances are normally within a few micron ranges. Therefore, an increase in effective tool life of micro-end mills would be very beneficial.

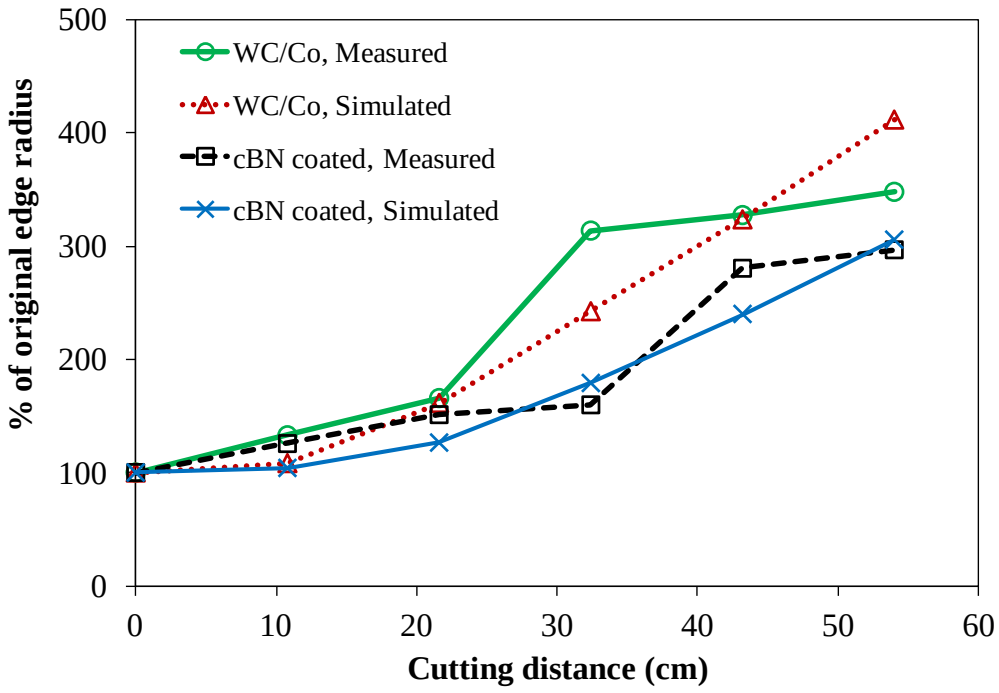

Figure 4.12: Comparison of measured and simulated tool wear based on an increase in edge radius.

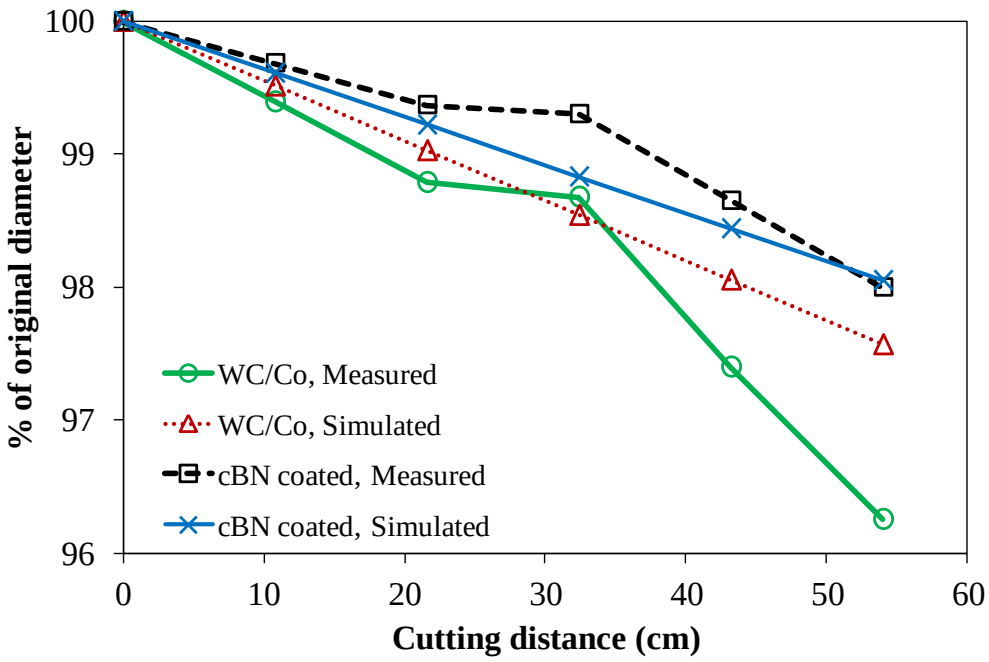

Figure 4.13: Comparison of measured and simulated tool wear based on a reduction in tool diameter.

These investigations reveal that instead of generating higher cutting forces (see Figure 4.8), tool wear rate reduces noticeably when using the cBN coated tool, especially at a condition where high cutting speed and high feed per tooth were applied as shown in Figure 4.14. Tool wear rate increases as feed per tooth and/or cutting speed increases. In general, micro-end milling tools wear at the highest rate when tool rotational angle is approximately 80° which also yields to the maximum resultant forces and maximum average tool temperatures (see Figure 4.8c and Figure 4.9, respectively). However, there is a condition where this does not apply; it is when the feed per tooth is at 0.5 μm/tooth, which probably too low to promote shearing.

Figure 4.15 shows the plot of wear depth accumulated during cutting. It can be seen that in every cutting condition, the wear depth of WC/Co tool is higher than the wear depth of cBN coated tool. The maps of tool wear along the contact length at a tool rotation angle of 180° shown in Figure 4.16 reveal that the area of deep wear (red color zone) on WC/Co tool is distributed along the edge of the tool, unlike on cBN coated tool where the deep wear is concentrated only on a small area. Therefore, the edge of WC/Co tool would be worn faster than the cBN coated tool. In other words, edge roundness of WC/Co tool increases faster due to higher wear rate than the cBN coated tool.

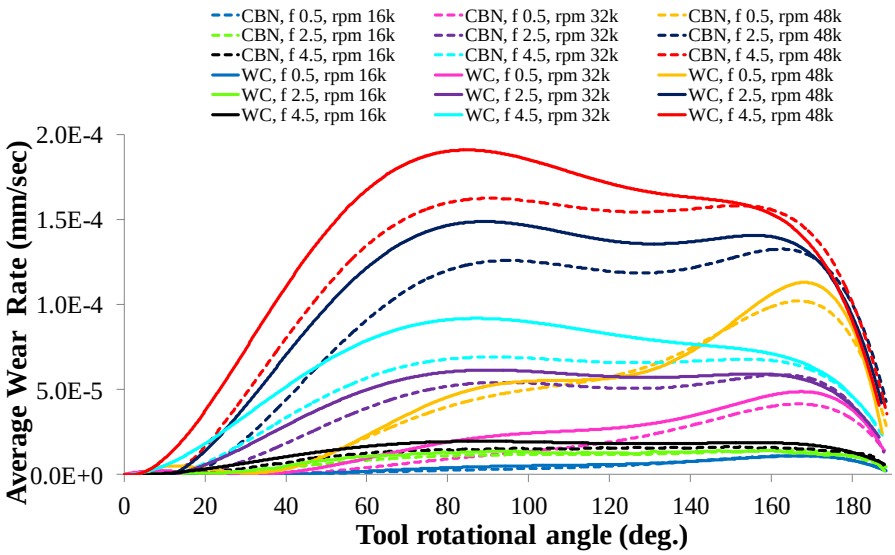

Figure 4.14: Average tool wear rate for uncoated and cBN coated WC/Co micro-tools.

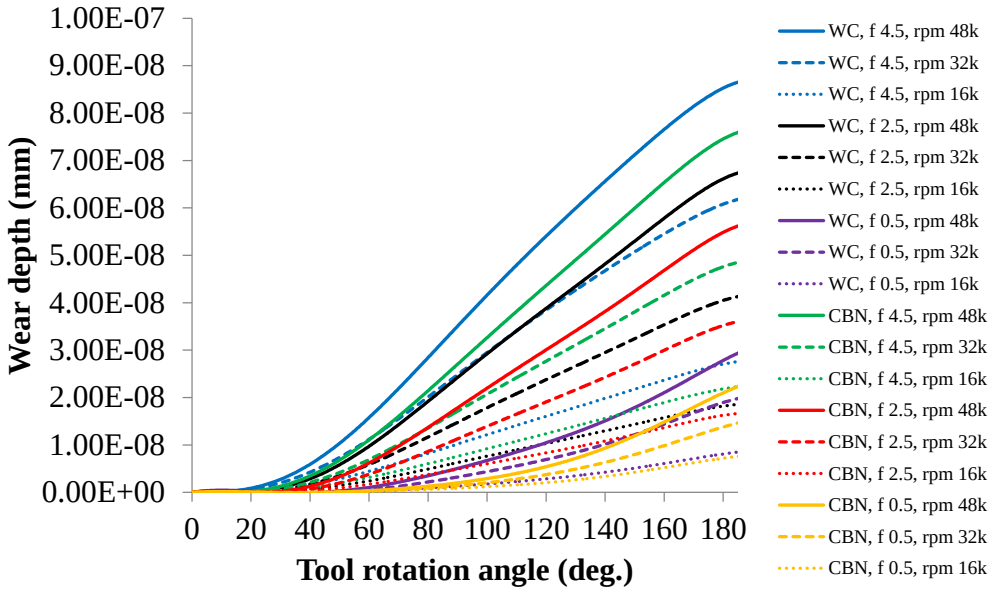

Figure 4.15: Tool wear depth progress during single tooth passes for uncoated and cBN coated WC/Co micro-tools.

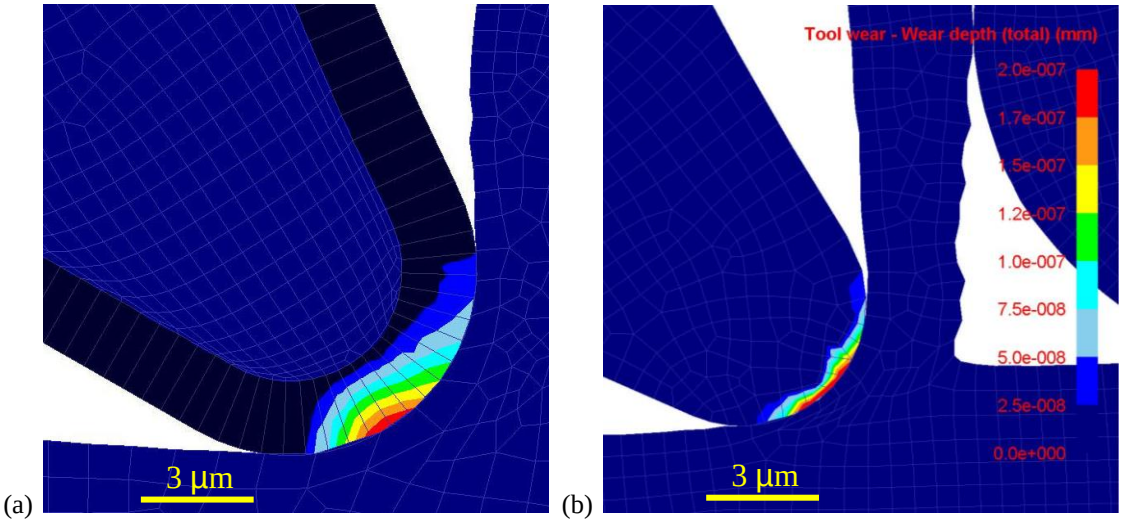

Figure 4.16: Comparison of tool wear depth (Ω = 48,000 rpm, f_z = 4.5 µm/tooth, ϕ = 180°); (a) cBN coated WC/Co and (b) WC/Co micro-tools.

In order to unravel the source of the difference in tool wear rate and depth, the components of Usui's tool wear rate equation (Eq. 4.2) have been individually extracted from the FE simulations and plotted in Figures4.17, 4.18 and 4.19. It was observed from Figure 4.17 that the contact temperatures obtained from cBN coated tool were lower than the one obtained from WC/Co tool in every cutting condition. The difference became more pronounced at the high feed per tooth. However, the sliding velocities obtained from the cBN coated tool are higher than the sliding velocities obtained from the WC/Co tool (see Figure 4.18). In all cutting conditions, the contact pressures obtained for cBN coated and WC/Co tool are not significantly different (see Figure 4.19). Therefore, based on Eq. (4.2) the contact temperature is the dominating factor in reducing tool wear rate of cBN coated tool.

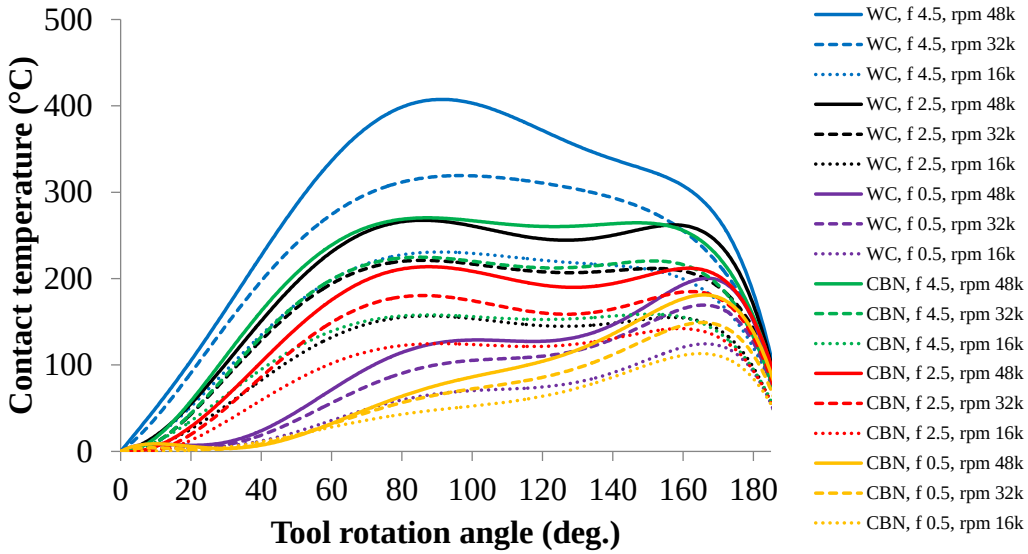

Figure 4.17: Average contact temperature for uncoated and cBN coated WC/Co micro-tools.

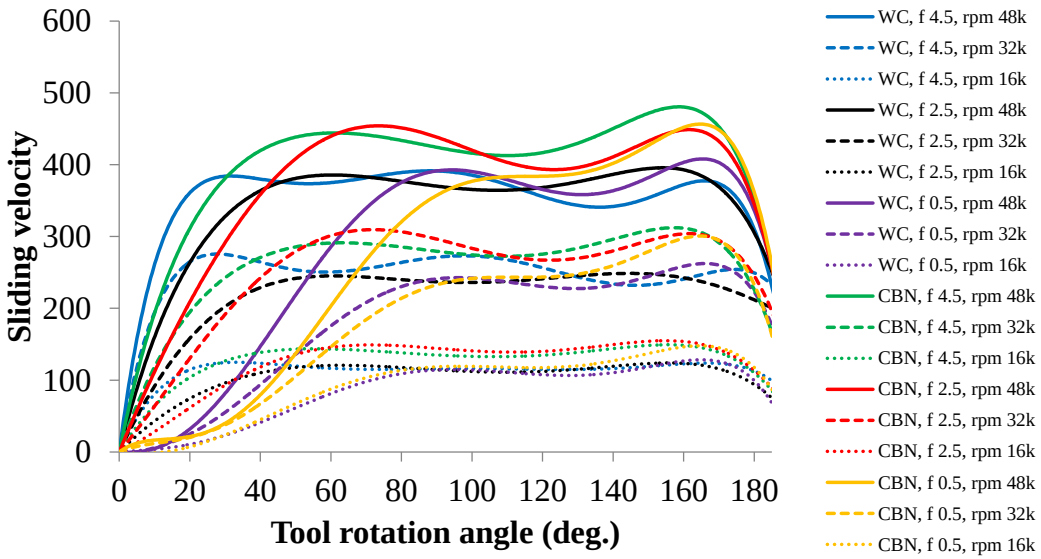

Figure 4.18: Average sliding velocity for uncoated and cBN coated WC/Co micro-tools.

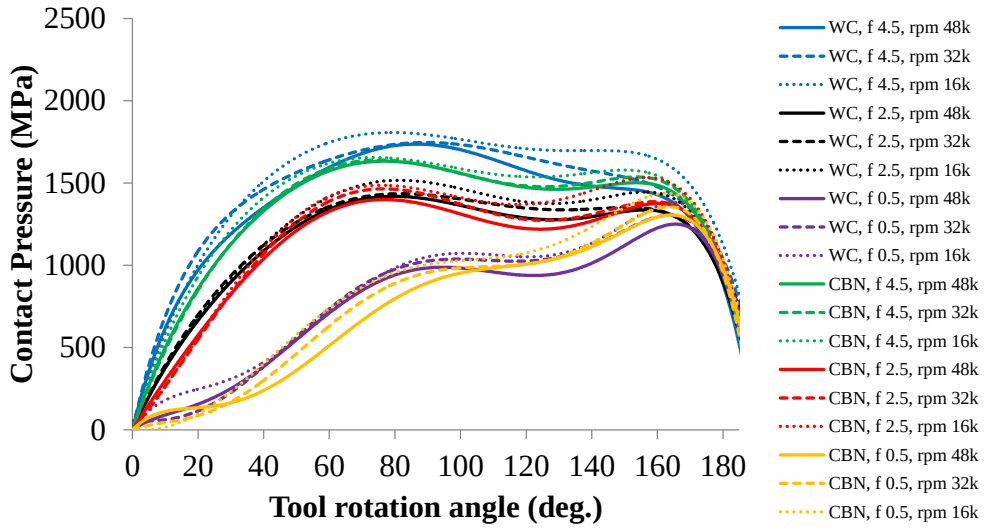

Figure 4.19: Average contact pressure for uncoated and cBN coated WC/Co micro-tools.

3.4 Effect of tool edge radius

Since cBN coated and WC/Co tools have different edge radii, there must be an effect contributing to the tool performance from this difference. Therefore, FE simulations were conducted using the uncoated WC/Co tools having the increased edge radius of r_β = 5±0.5 µm (equal to the edge radius of cBN coated tool) in order to investigate the influence of edge radius. A comparison between three different tools; WC/Co tool with edge radius of r_β = 3±0.5 µm (WC R3), WC/Co with edge radius of r_β = 5±0.5 µm (WC R5) and cBN coated tool with edge radius of r_β = 5±0.5 µm (CBN R5) in terms of predicted resultant force, average tool temperature and average tool wear rate is given in Figures 4.20, 4.21 and 4.22 respectively.

The cutting forces obtained from the cBN coated tool are equivalent to the cutting forces obtained from uncoated WC/Co tool with the same edge radius (r_β = 5±0.5 µm) as shown in Figure 4.20. But the cutting forces obtained from the uncoated WC/Co tool with the edge radius of r_β = 3±0.5 µm are much lower. Therefore, an increase of cutting force when using cBN coated tool (see Figure 4.8) is majorly contributed from an increase of tool edge radius. Therefore it is concluded that the cBN coating thermal properties would not significantly affect the resultant cutting forces but the increased edge radius would.

The effect of edge radius to average tool temperature is also given in Figure 4.21. In case of uncoated WC/Co tool, tool temperature is getting lower as edge radius decreases from r_β = 5±0.5 µm to r_β = 3±0.5 µm. However, in case of the cBN coated tool (edge radius of r_β = 5±0.5 µm); significantly lower temperatures were obtained when compared to both uncoated WC/Co tools with edge radius of r_β = 5±0.5 µm and r_β =

3±0.5 µm, despite the fact that they generate higher cutting forces. This may be due to the higher thermal conductivity of the cBN coated layer.

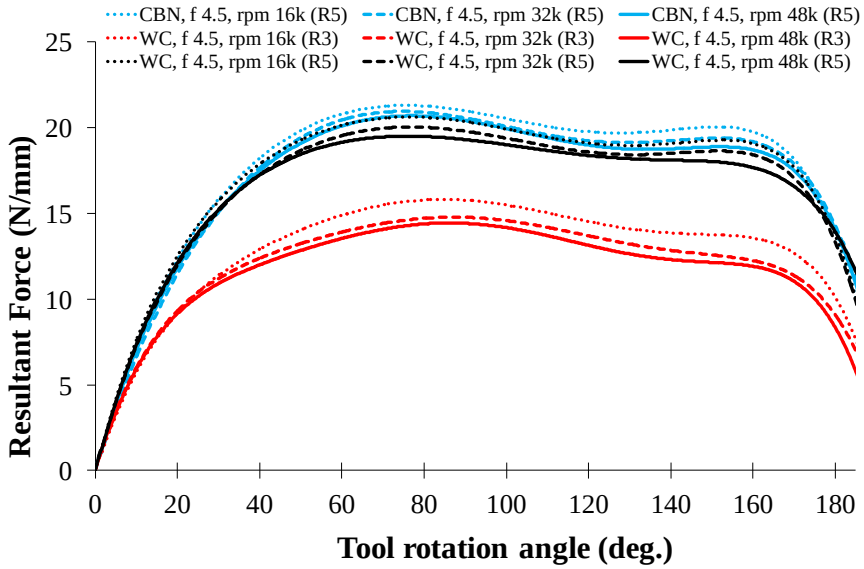

Figure 4.20: Contribution of cBN coating to an increase in resultant cutting force.

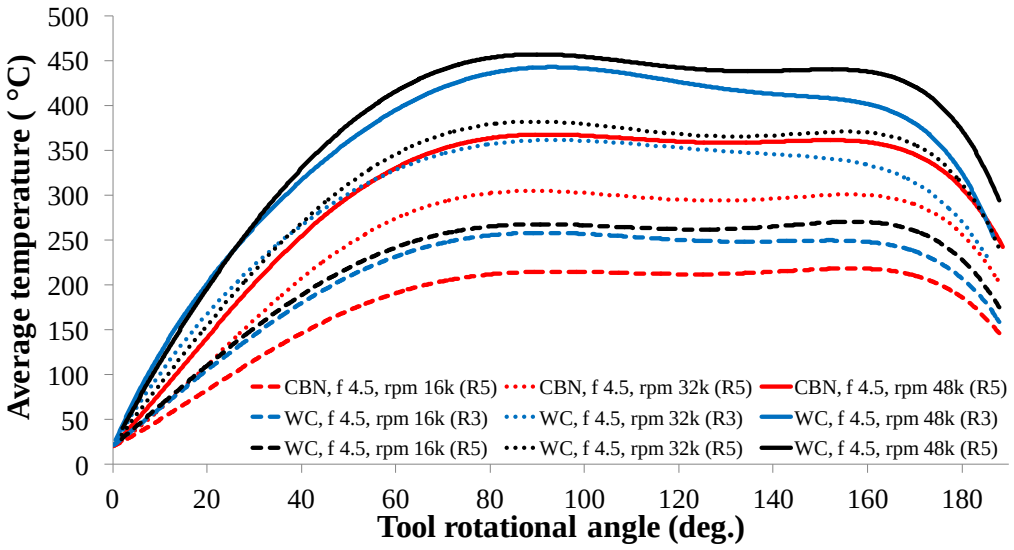

Figure 4.21: Contribution of cBN coating to average tool temperature.

A conclusion can be drawn from the tool wear rate comparison given in Figure 4.22 is that the tool wear rate of cBN coated tool is lower when compared to WC/Co tools with edge radius of r_β = 5±0.5 µm and r_β = 3±0.5 µm. Hence, the increase of edge radius due to added cBN coating layer does not reduce advantages of using the cBN coating to extend the tool life of micro-end mills. However, in case of uncoated WC/Co tool; having an increased edge radius contributes to a higher tool wear rate.

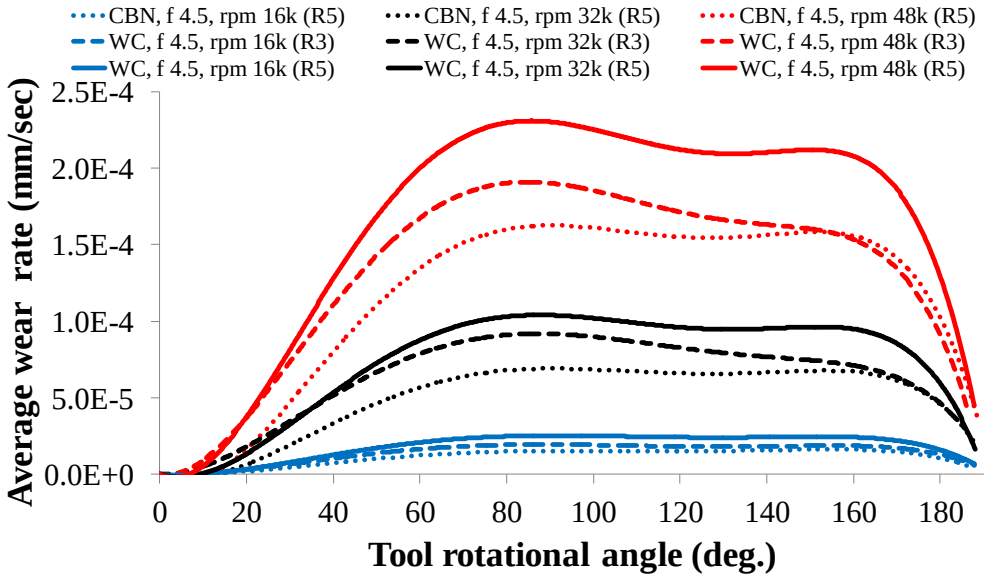

Figure 4.22: Contribution of cBN coating to average wear rate.

3.5 Effect of workpiece material deformation assumptions

In this section, the results of the simulations comparing the influence of viscoplastic and elasto-viscoplastic material deformation assumptions will be discussed. The comparison was conducted in terms of chip formation, cutting force, temperature, tool wear and computational time.

3.5.1 Chip formation

The obvious influence of the material assumption can be observed from the chip formation (see Figure 4.23). By changing the material assumption from viscoplastic to elasto-viscoplastic, serrated chip formation was obtained instead of continuous chip formation. The serrated chip formation has been reported in conventional macro-machining of titanium alloy (Gente et al. 2001, Komanduri & Von Turkovich 1981, Molinari et al. 2002). Also the use of modified J-C material model with temperature-dependent parameters and strain softening has proven that the serrated chip is generated when FE simulation using sharp-like (Calamaz et al. 2008) and round tool edges (Sima & Özel 2010). This study has shown that the serrated chip can be generated even when cutting with a round edge tool as well. Compared to the serrated chip obtained from the macro-cutting with sharp-like edge tool, the physical characteristics of serrated chip obtained from the micro-cutting with round edge tool are similar. Also the mechanism of serrated chip formation is not quite different.

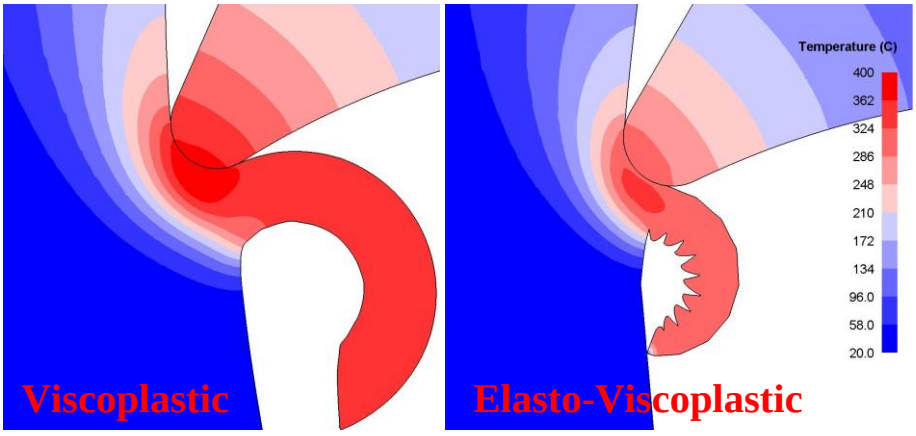

Figure 4.23: A comparison of chip formation

In order to observe the mechanism of serrated chip formation, the images of effective strain rate, effective elastic strain, effective plastic strain, effective stress and temperature were taken from the results of FEM simulations (see Figure 4.24). Each response was taken from the same simulation step; four steps were picked to represent the serrated chip formation cycle.

The images of strain rate clearly show the development of a narrow shear zone. The plastic deformation progresses from the end of the tool-workpiece contact length (close to the flank face) towards the stress concentration point in front of the chip. Based on these results, each cycle of serrated chip formation may be divided into three steps: (i) the energy starts to accumulate after the completion of the previous chip segment, as can be seen by an increase of stress and elastic strain- the plastic deformation slowly begins from the end of the contact length; (ii) the shearing takes place at the stress concentration point starting a new chip segment, more heat is being generated and strain rate rapidly increases, thus, the flow stress drops and the material becomes easier to deform; (iii) the shear zone is hardened and the temperature drop resulting in an increase of flow stress and consequently resisting further deformations. Thus the deformation then seeks a new path and a new shear zone is formed.

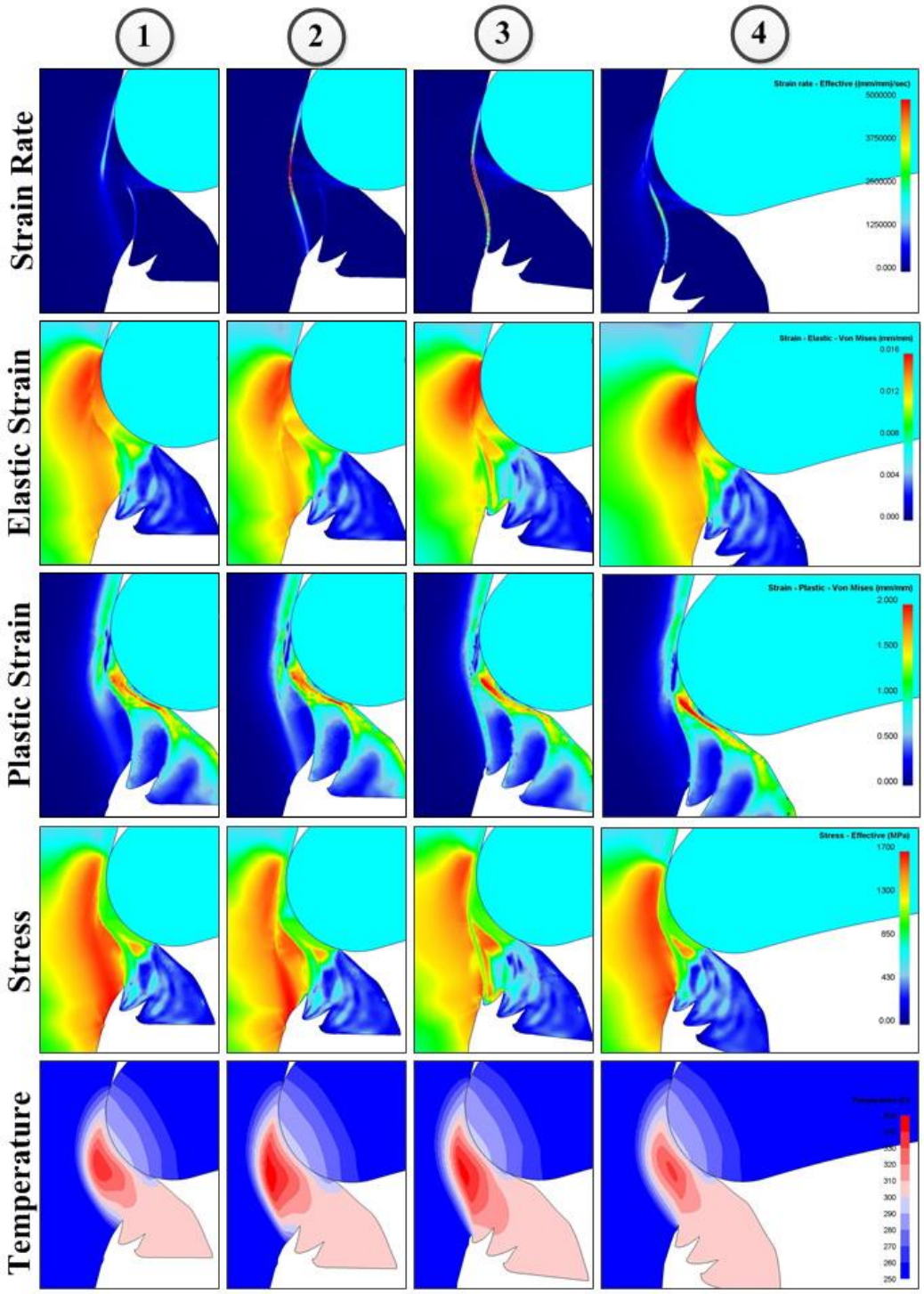

Figure 4.24: Sequence of serrated chip formation obtained from the elasto-viscoplastic FE model.

In case of viscoplastic FE model, a common continuous chip formation was obtained. Figure 4.25 shows strain, strain rate, stress, and temperature developing during the simulation of the viscoplastic FE model. Even though, the degree of plastic strain is approximately as high as 12,500 % of the elastic strain, neglecting this small amount of elastic deformation could result in a totally different mechanism of chip formation.

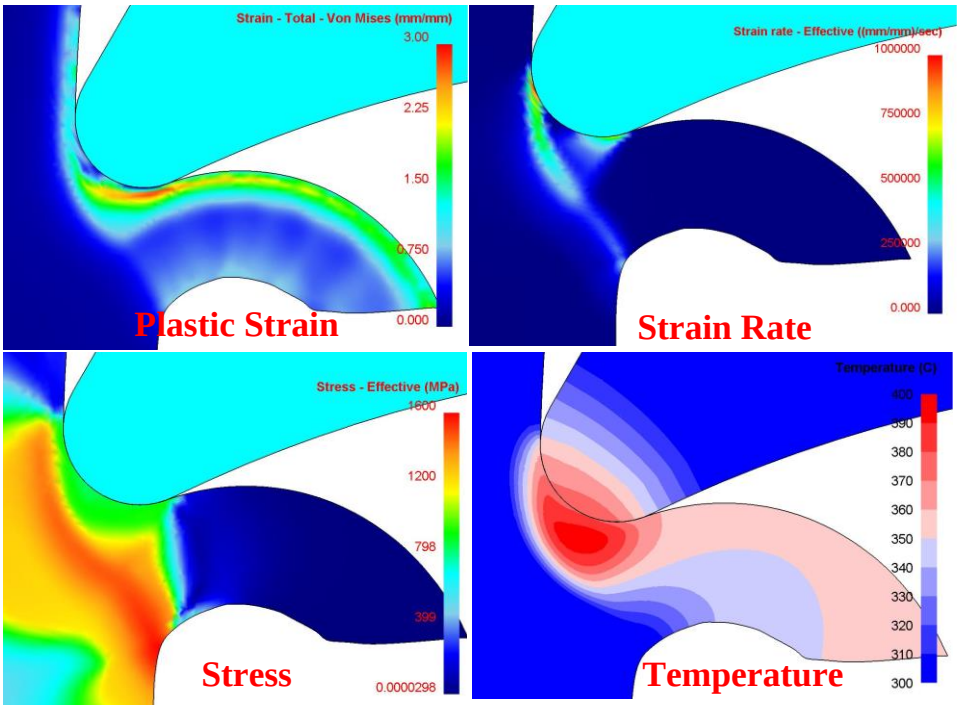

Figure 4.25: The responses obtained from viscoplastic model.

3.5.2 Cutting forces

Figure 4.26 presents the comparison of cutting forces predicted from the models with viscoplastic and elasto-plastic material assumptions. Overall, the predicted forces from both cases were distributed in a similar trend. The force curves of viscoplastic seem to shift to the left; this might be due to the fact that chip started to form sooner as a result

of ignoring the elasticity. Considering the maximum forces, it can be seen that, the viscoplastic FE model may be enough to predict the maximum force at the deviation of approximately 1% from the elasto-plastic FE model.

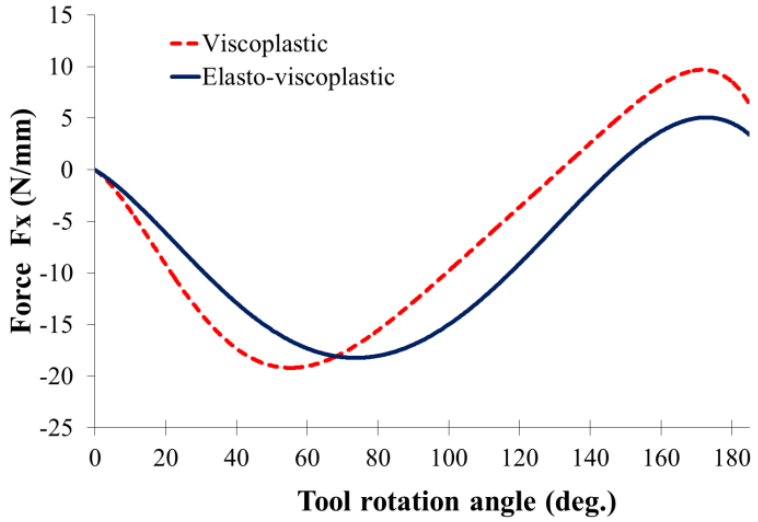

(a)

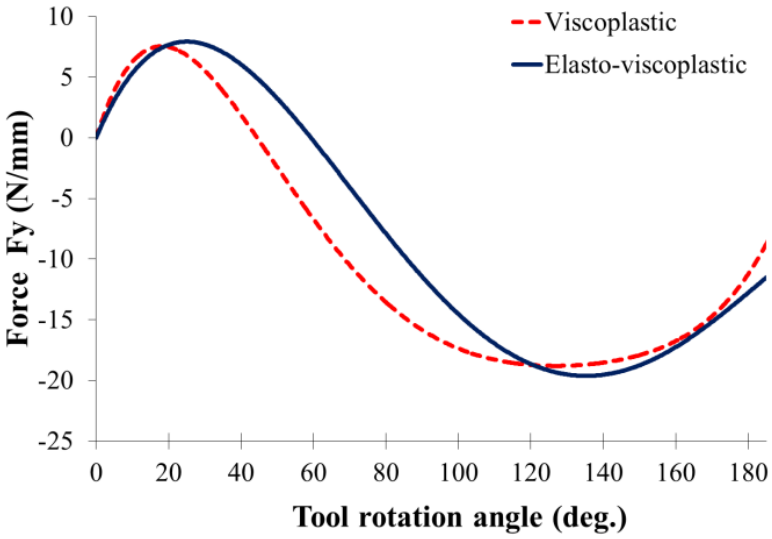

(b)

Figure 4.26: A comparison of cutting forces (a) F_x and (b) F_y.

3.5.3 Temperature

The temperatures predicted from both models are shown in Figure 4.27. It can be clearly seen that the viscoplastic FE model predicts a higher temperature compared to the elasto-viscoplastic model. Since some of energy was stored as strain energy instead of converting to heat when the material is deformed elastically, the viscoplastic FE model tends to overpredict the temperature. In this case, this was about 15-20% over the elasto-viscoplastic FE model.

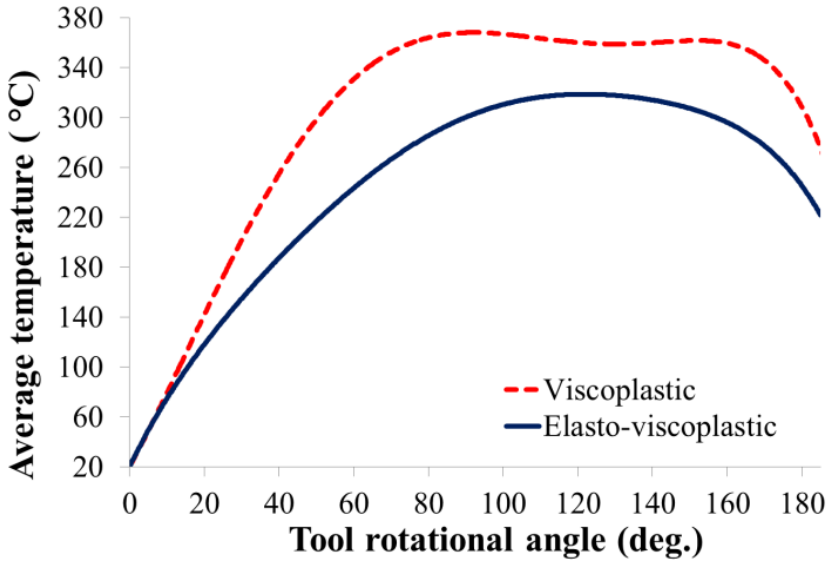

Figure 4.27: A comparison of average temperature.

3.5.4 Tool wear

In terms of tool wear prediction (Figure 4.28), the viscoplastic FE model predicted a slightly higher tool wear compared to the elaso-viscoplastic FE model. The error was about 5-10% over the elaso-viscoplastic model. Over predicting tool wear when using viscoplastic model was mainly due to two reasons. First, the higher temperature

was predicted as shown earlier. Second, the sliding velocity at the tool surface was higher due to the nature of serrated chip formation.

Figure 4.29 shows a similarity of a distribution of wear depth between the two models. Since the chip curl radius is higher in case of viscoplastic FE model, the chip-tool contact length was longer towards the tool rake face. Therefore, wear develops into that area.

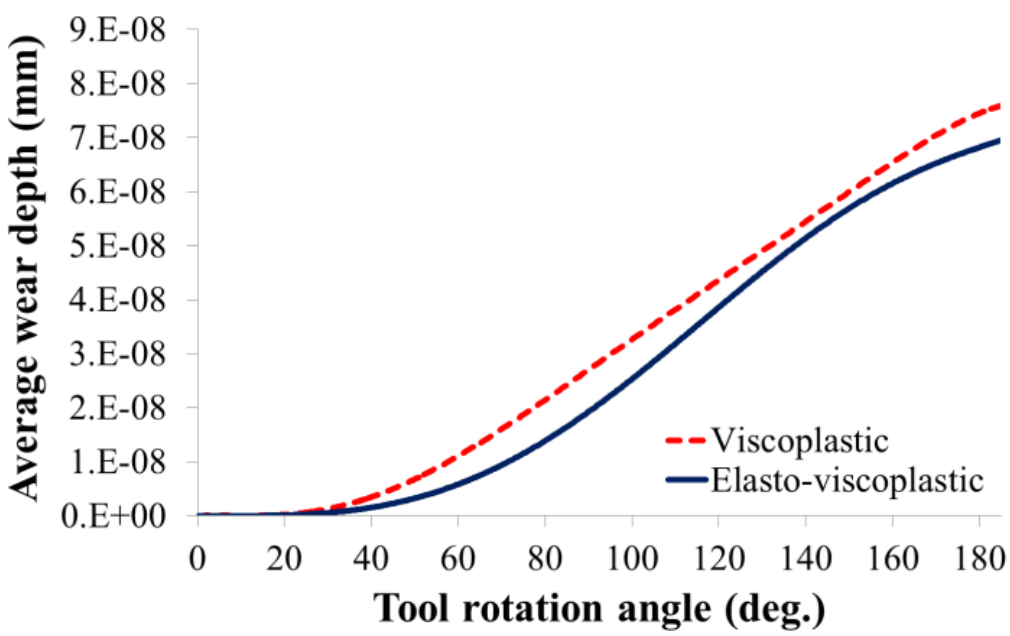

Figure 4.28: A comparison of average wear depth.

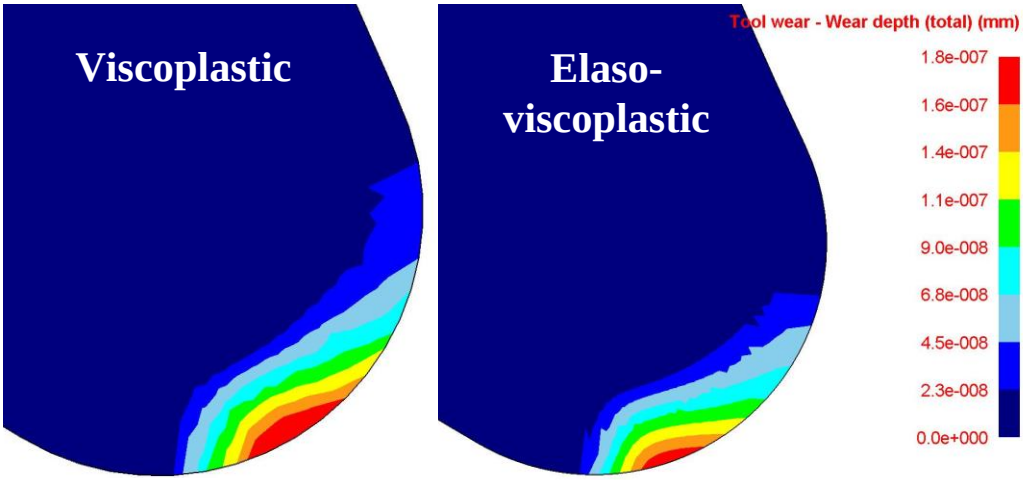

Figure 4.29: A comparison of wear depth distribution

3.5.5 Computational time

In terms of computational time, on the same machine (The Intel Core 2 Quad processor, 2.83 GHz, 3.25 GB RAM) the viscoplastic FE model required approximately 60 hours to complete a single simulation while the elasto-viscoplastic model required approximately 500 hours (8.3 times). It took significantly more time for the solution of the elasto-viscoplastic FE model to converge compared to the viscoplastic FE model, given that the same condition was applied. The significantly different computational time suggests that user should evaluate the cost and effect before employing the elasto-viscoplastic FE model.

4. Conclusions

The use of cBN coating was expected to improve the performance of the micro end-mills, especially in terms of tool life. However, applying coating on the tool surface increases tool edge radius which is a critical factor determining the cutting performance in micro-machining. Large edge radius in tool geometry is generally not preferred.

Therefore, this issue may create doubts about potential benefits provided by the cBN coating. This study has revealed supporting evidences demonstrating the advantages of applying cBN coating on the tungsten carbide micro-end mills. The results obtained from FE simulations together with experimental results lead to some conclusions here.

Titanium alloy Ti-6Al-4V has a very low thermal conductivity which makes it difficult to be processed since temperature rise in the cutting zone accelerates the rate of tool wear. The simulation results show that most of the heat is removed with the chips in micro-end milling of titanium alloy.

The reduction of localized cutting temperature when using the cBN coated tool may be contributed from the fact that thermal conductivity of cBN is higher (twice) than the uncoated WC/Co tool material, hence more heat can be dissipated through the cBN coating at the tool surface. Consequently, the temperature in the cutting zone is reduced. This is evident as shown in Figure 4.6 that the maximum temperature zone when cutting with the cBN coated tool is below the tool-workpiece interface and is not at the interface as in the case of cutting with uncoated WC/Co tool.

The simulation results agreed well with the experimental results that tool wear decreases when tools are coated with cBN material. Tool wear reduction may be contributed from the superior properties of cBN which can resist wear much better than WC/Co and from the reduction of temperature in the tool-workpiece interface.

In micro-end milling of Ti-6Al-4V titanium alloy, the influence of feed per tooth on the cutting forces dominates over the influence of the cutting speed. However, it does not dominate on tool temperatures and tool wear rate but plays an equal role with the cutting speed. Increased feed and cutting speed generally increases tool temperatures and

tool wear rate significantly. Similarly, in terms of surface roughness and top-burr formation; feed per tooth is also the most dominating parameter while the effect from cutting speed is not so significant.

Feed per tooth determines the uncut chip thickness in milling process, the uncut chip thickness is not uniform; it starts from a thickness of zero, increases to the specified feed per tooth and then decreases to zero again. Therefore, there exists a problem in terms of minimum chip thickness. The results from FE simulations show that at the feed per tooth of f_z = 0.5 µm, the behavior of cutting is different than at a higher feed per tooth. Also, the surface roughness at this feed per tooth was the highest one observed. These provide the evidence that the main material removal mechanism is under the influence of ploughing rather than shearing. Therefore, the minimum chip thickness of Ti-6Al-4V can be estimated to be about 10% - 20% of edge radius.

The edge radius has a significant influence on the cutting force and wear rate but not on the cutting temperature. The smaller edge radius reduces the wear rate and the cutting forces. However, the temperature seems to be less dependent upon the tool edge radius as investigated in this study.

In short, the FE simulations and experiments have evidently shown that coating of a thin layer of cBN on a surface of conventional WC/Co micro-end mills resulted in increased tool life. In addition, it was observed that increased edge radius due to the coating applied does not hinder the benefits obtained from the cBN coating. Therefore, cBN coating is another option for improving tool performance in micro-machining of Ti-6Al-4V titanium alloy. Sliding wear based Usui’s wear rate model with the model

parameters reported in this work are experimentally validated in estimating tool life in micro-milling Ti-6Al-4V titanium alloy.

This study has also shown the effects of material assumption upon the results of FE simulation of micro-end milling. The viscoplastic FE model has an advantage in terms of lowering the computational time which makes it more practical. In contrast to the the time consumed, the elasto-viscoplastic model is better in terms of capturing the reality of the process physics. The implementation of both models still depends on the objectives and constraints of the FE simulation. Based on the results of this study, the viscoplastic model can replace the elasto-viscoplastic model for an application of predicting the cutting force. The magnitude of predicted cutting force is not significantly affected by the material assumption. For the purpose of predicting tool wear, the viscoplastic FE model may be adequate; since the only factor contributed to the estimation of tool wear which is strongly affected by the material assumption is the temperature. Also, the viscoplastic FE model tends to predict higher temperature compared to the elasto-viscoplastic FE model. Therefore, the predicted tool life tends to be shorter than what it really is. A suitable compensation may be needed. To study the chip formation in micro-cutting processes, it is necessary to employ the elasto-viscoplastic FE model, despite resulting in a long computational time. A small degree of elastic deformation is significant for cutting analysis when a round cutting tool edge is considered.

Chapter 5

3-D Finite Element Modelling and Simulations

1. Introduction

In Chapter 4, the 2-D FE modeling and process simulations were introduced. Utilizing the 2-D FE simulation in analysis of micro-end milling process has been proven to be very useful. Obviously the micro-end milling process is a form of oblique cutting process (3-D cutting). Using only 2-D FE model cannot capture the entire physical behavior of the chip formation process. However, the 2-D FE model offers several benefits to the analysis of micro-end milling. Firstly, it reduces the complexity of the 3-D problem down to the size that can be easily handled in 2-D plane strain analysis. Secondly, the results are easy to be interpreted and analyzed. Thirdly, it significantly reduces the amount of required computational time and resource compared to the 3-D FE model. Nevertheless, the 3-D FE model is still essential for a certain analysis of micro-end milling such as the effects of tool geometry and process parameters on the chip flow, tool wear distribution along the cutting edge, and 3-D temperature distribution. Therefore, in this work, an attempt to use 3-D FE model to simulate chip formation and predict process responses of micro-end milling was carried out. The objectives of this study were to use the developed 3-D FE process simulations to analyze the micro-end milling of titanium alloy Ti-6Al-4V and to assess the necessity of using the 3-D FE model over the 2-D FE model specifically investigate the cutting conditions on chip flow.

2. 3-D Finite Element Modelling and Simulations

The 3-D Finite Element software, DEFORM 3-D, was utilized in this study. As same as the 2-D FE model, the modified Johnson-Cook (J-C) material model was used to model the Ti-6Al-4V workpiece. For comparison purposes, the values of material properties and the setting of friction, heat transfer and tool wear were kept the same as in 2-D FE model. For more detail, please refer to Section 2 in Chapter 4.

Similar to 2-D FE model, the workpiece was considered as viscoplastic material and tool was considered as a rigid body in the 3-D FE model. The tool was modeled by using 3-D CAD software having the same geometrical feature as the physical end milling tool. Figure 5.1 shows the 3-D CAD model of the tool compared to the image of the physical end milling tool. The tool diameter is Ø508 μm with the helix angle (β) of 30°. The fresh tool has the edge radius (r_β) of 3 μm. The tool mesh consists of $3x10^4$ elements with minimum element size of 0.5 μm. The active cutting edge of the tool has a very fine mesh in order to accurately represent the tool characteristics.

The workpiece was modeled for three different types of micro-end milling, full-immersion slot micro-end milling, half-immersion up micro-end milling, and half-immersion micro-end down milling. The workpiece for full-immersion 3-D FEM model as meshed with $2x10^5$ elements and the workpieces for half-immersion 3-D FEM model were discretized with $1.5x10^5$ elements, giving a minimum element size of about 0.5 μm as shown in Figures 5.2, 5.3, and 5.4 respectively. The high density mesh was placed at the cutting zone.

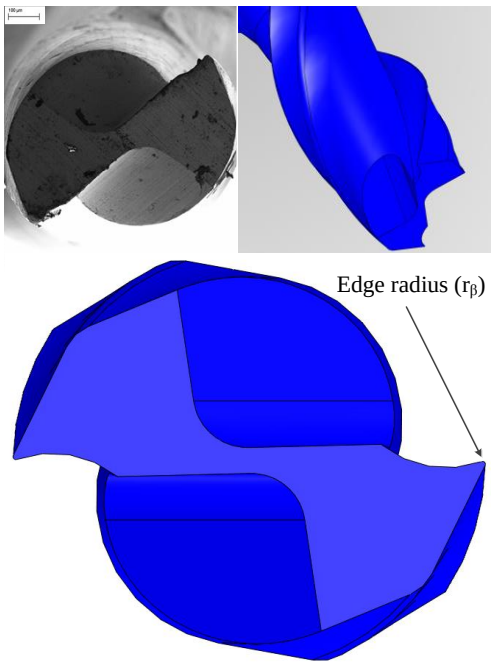

Figure 5.1: SEM image of the micro-end milling tool and its 3-D CAD model.

Heat transfer was allowed at the tool and workpiece contact with a thermal conductance of 10^7 N sec^{-1} mm^{-1} $°C^{-1}$. The ambient temperature was set at 20 °C. Heat was transferred from workpiece and tool to the environment by convection with the convection coefficient of 0.02 N sec^{-1} mm^{-1} $°C^{-1}$. Similar to the 2-D FE model, two types of contact were assigned along the contact length: (i) sticking contact, and (ii) sliding contact by using hybrid friction model available in DEFORM 3-D. The shear friction factor and friction coefficient were kept the same as in 2-D FE model (see Chapter 4, Section 2.5). A wear rate model based on the sliding wear proposed by Usui et al. (1978) has been employed again. All material-dependent parameters were kept the same as in 2-D FE model (see Chapter 4, Section 2.6). The FEM simulations were performed with the step time increment of 10^{-7} sec. The workpiece was remeshed at every 50 steps or when the interference depth between tool and workpiece reaches 0.5 µm.

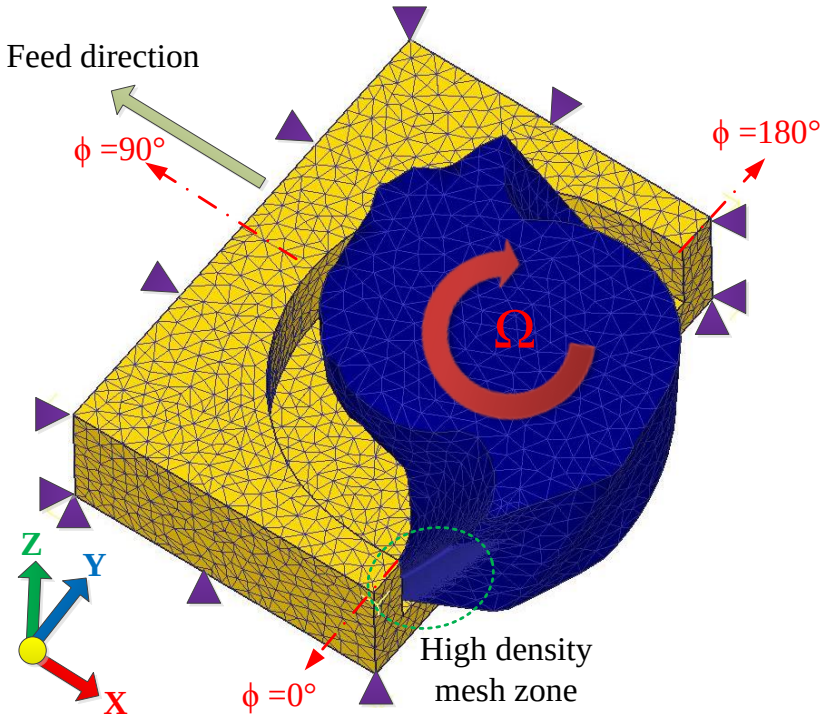

Figure 5.2: 3-D FE model for full-immersion slot micro-end milling.

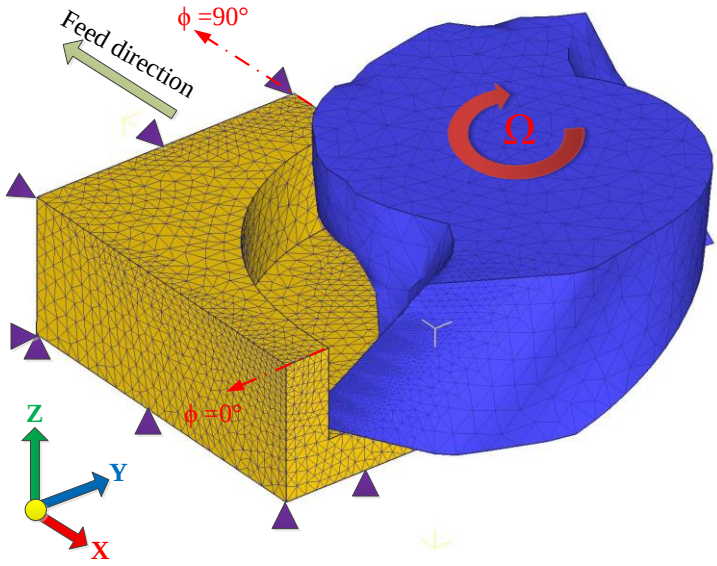

Figure 5.3: 3-D FE model for half-immersion up micro-end milling.

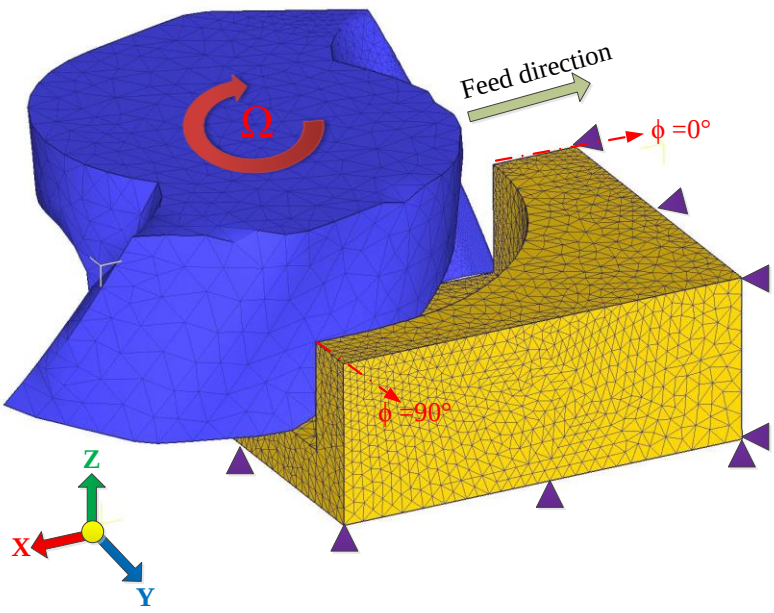

Figure 5.4: 3-D FE model for half-immersion down micro-end milling.

3. Comparison of 2-D and 3-D Finite Element Simulations

One objective of this study is to assess the necessity of using 3-D FE simulation in micro-end milling. Therefore, the comparison of process responses from 2-D and 3-D FE simulations was conducted. Cutting forces, temperature and tool wear were compared.

3.1 Comparison of cutting forces

2-D FE simulation can quickly provide the predicted F_x and F_y force components in terms of force per unit length. Figure 5.5 shows the predicted forces obtained from 2-D FE model with the cutting condition of f_z = 4.5 µm and Ω = 16,000 rpm. The graph shows the distribution of force as the tool rotates for a full 180 degrees rotation. Please note that the uncut-chip thickness varies as the tool rotates by beginning from zero and reaching to f_z in the middle and reducing to zero as the cutting edge of the micro-end milling tool exits.

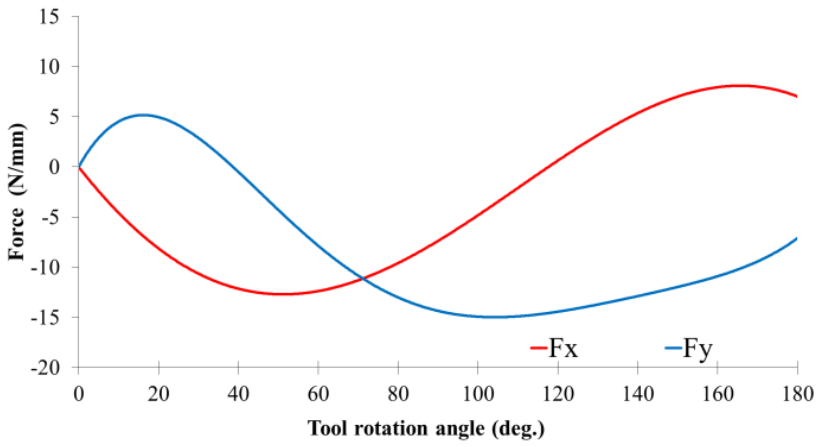

Figure 5.5: Force components predicted from 2-D FE model.

The force prediction from 2-D simulation can be utilized to predict the 3-D forces based on a given axial depth of cut (a_p) and tool helix angle (β). In this work, the 2-D force components in Figure 5.5 were modeled as a function of tool rotational angle in degrees by using five degree polynomial equation with curve fitting (Eq. 5.1 and 5.2).

$$dF_x(\phi) = 2.58244E\text{-}10\phi^5 - 1.60635E\text{-}07\phi^4 + 9.88338E\text{-}06\phi^3 + 4.95855E\text{-}03\phi^2 - 5.08009E\text{-}01\phi \quad \text{Eq. (5.1)}$$

$$dF_y(\phi) = 3.33497E\text{-}09\phi^5 - 1.80993E\text{-}06\phi^4 + 3.61168E\text{-}04\phi^3 - 3.00268E\text{-}02\phi^2 + 7.18163E\text{-}01\phi \quad \text{Eq. (5.2)}$$

By setting $\phi = 0°$ at the tool tip, the integration of force components can be formulated as;

$$Fx(\phi) = \int_{\theta}^{\phi} dF_x(\tau)d\tau \quad \text{Eq. (5.3)}$$

$$Fy(\phi) = \int_{\theta}^{\phi} dF_y(\tau)d\tau \qquad \text{Eq. (5.4)}$$

Where $\theta = \phi - \frac{360a_p}{\pi \emptyset \tan(90-\beta)}$, a_p is the axial depth of cut, β is the helix angle of micro-end mill and $\emptyset$ is the diameter of the micro-end mill.

Figure 5.6 shows the comparison of predicted force components of F_x, F_y and F_z obtained from the 3-D FE simulation and the predicted force components of F_x, F_y derived from 2-D simulation results. It can be seen that the forces derived from the 2-D simulation result is comparable to the forces obtained from the 3-D simulation. Therefore, deriving 3-D forces from the 2-D FE simulation can be an alternative to fully conducting a 3-D FE simulation.

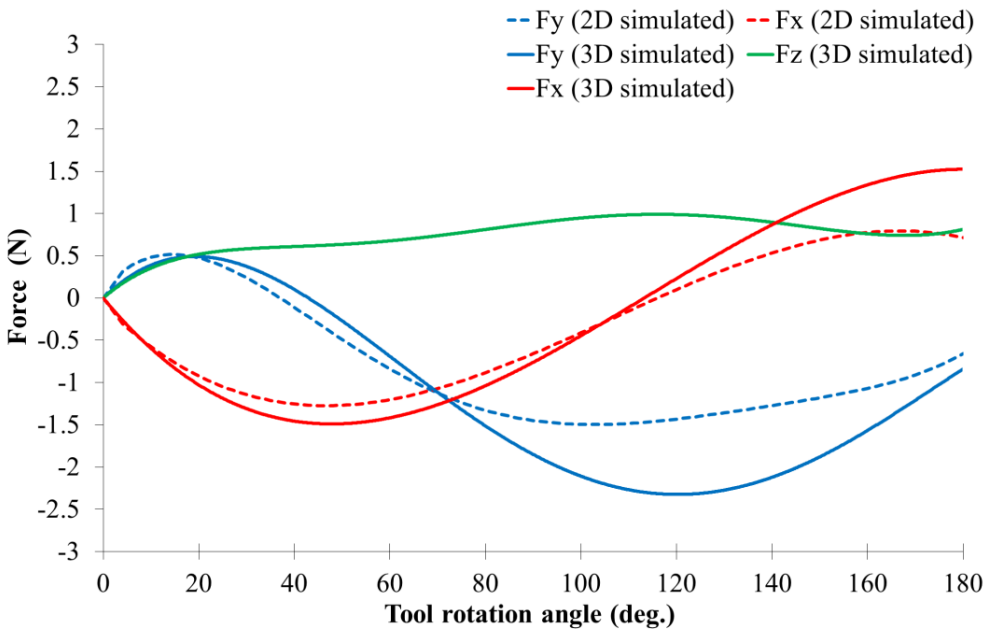

Figure 5.6: Force components directly predicted from 3-D FE model and calculated from 2-D FE model.

3.2 Temperature comparison

The comparison of tool temperature from 2-D and 3-D FE simulations is shown in Figure 5.7. The average temperature was obtained from an area around the cutting edge. The graph clearly shows that the predicted tool temperature from the 3-D simulation is significantly lower than the one obtained from the 2-D simulation. This may contribute to the fact that there is more volume for heat diffusion and dissipation in the 3-D simulation. Therefore, in order to predict the temperature in micro-end milling, a 3-D FE simulation may provide a better result.

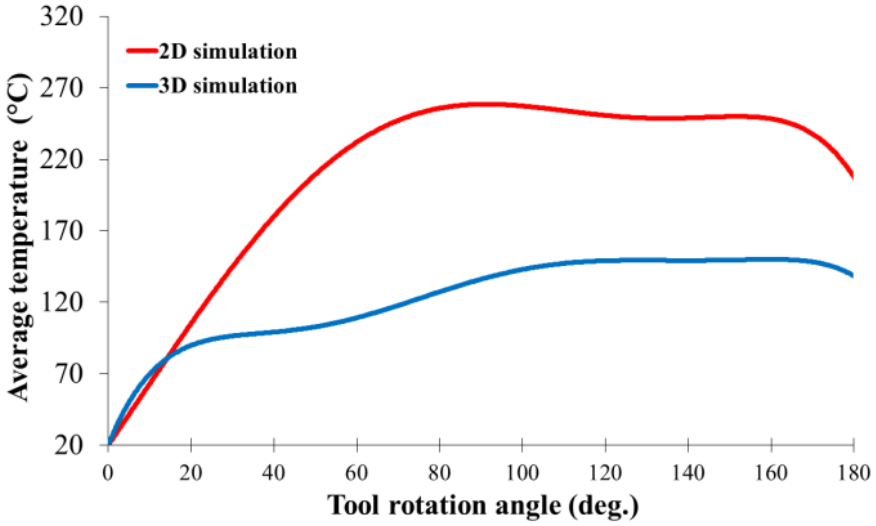

Figure 5.7: Comparison of tool temperature at the tool tip.

Figure 5.8 shows the temperature distribution along the cutting edge. It is interesting that the tool tip is cooler than other sections of cutting edge. This may be a result of heat diffusing and dissipating into the mass of workpiece around the tool tip.

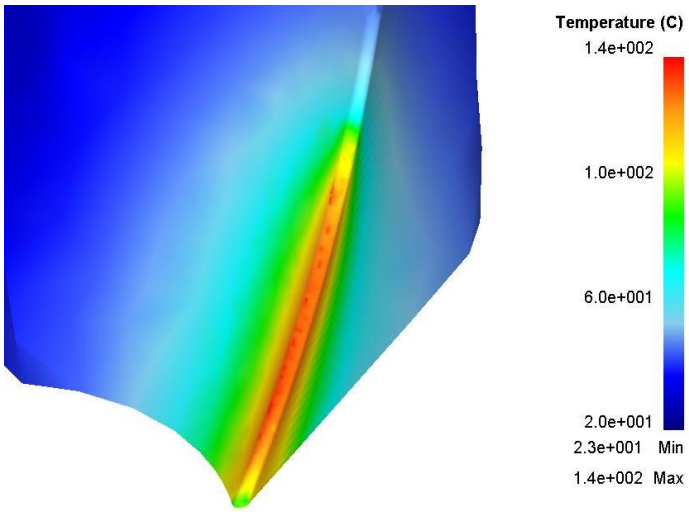

Figure 5.8: Temperature distribution along the cutting edge.

Based on the simulation result, most of the heat generated during the micro-cutting process diffuses and dissipates with the chip (Figure 5.9). Heat also diffuses from workpiece to the tool through the tool-chip contact area. Figure 5.9a shows that only a small area around the cutting edge is in contact with the chip. Therefore, heat flow from chip to tool is quite limited leading to the fact that tool has a lower temperature compared to the chip.

3.3 Tool wear comparison

Wear depth values taken from the tool tip area are compared in Figure 5.10. Both 2-D and 3-D simulations gave a similar trend of wear depth. Based on the previous findings in Chapter 4, we have shown that 2-D FE simulation can be used to predict tool wear and tool life. Also the wear prediction obtained from the 3-D FE simulation further confirms the previous finding on the predicted tool wear.

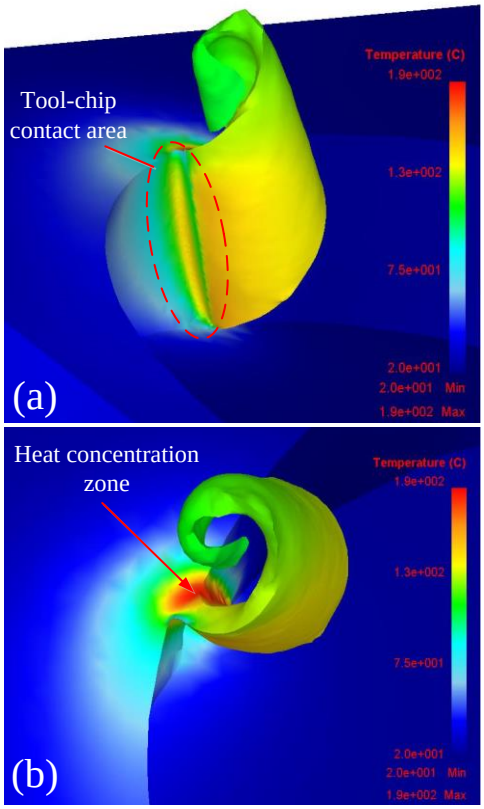

Figure 5.9: Temperature distribution in the chip.

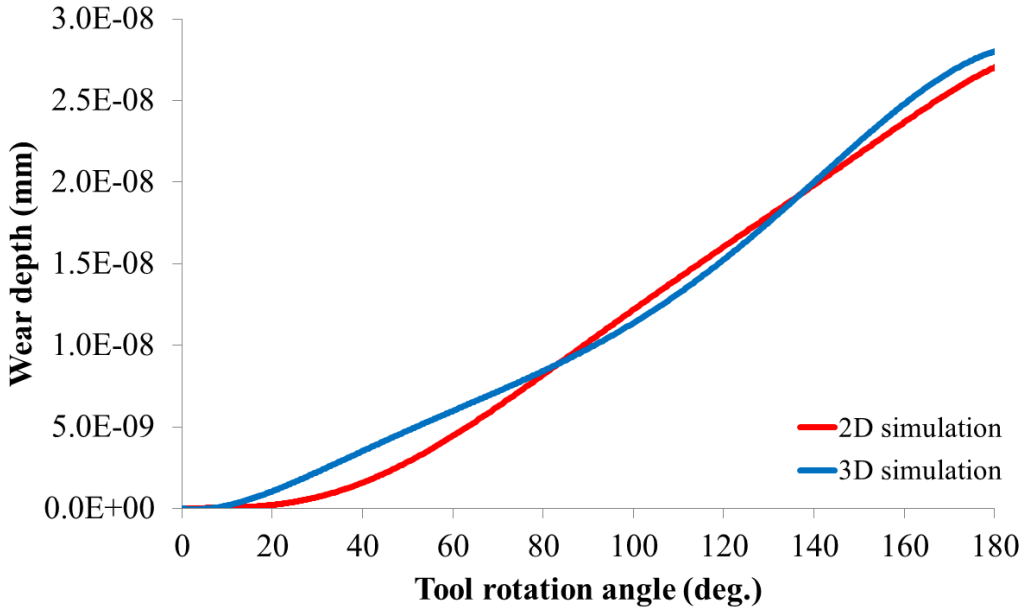

Figure 5.10: Comparison of tool wear depth.

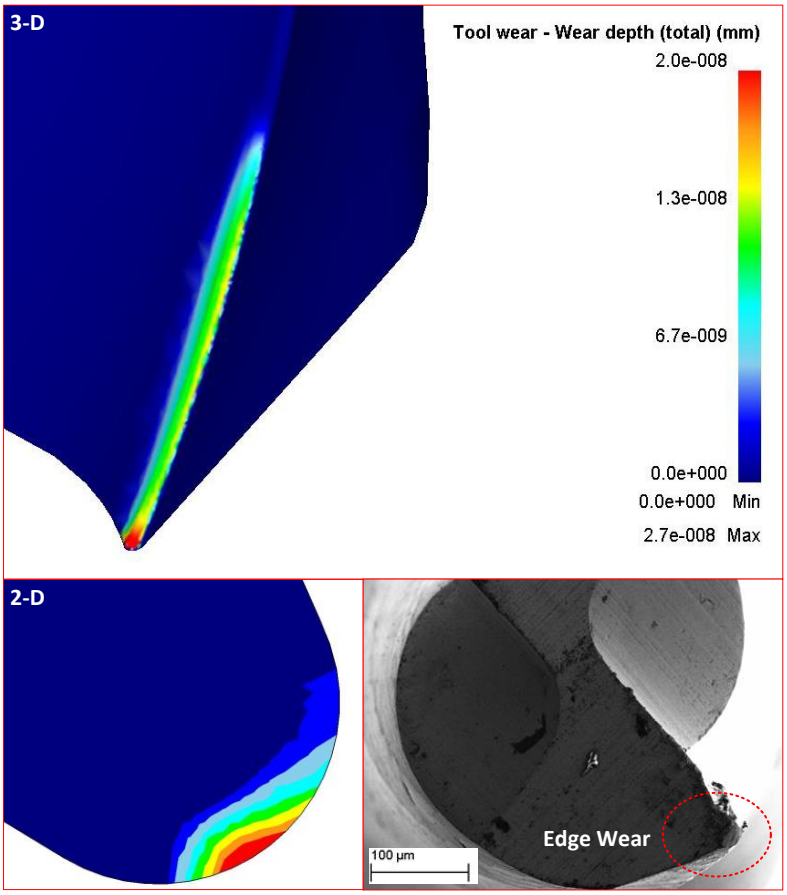

Figure 5.11: Tool wear distribution along the cutting edge.

Even though the active cutting edge was subjected to the same cutting distance, the critical point of the milling tool is still at the tool tip. As shown in Figure 5.11 that the tool heavily wears at the tip, thus it will be the first point that falls below the wear criteria. In spite of having a lower temperature, the tool tip still exhibits a maximum wear. This is due to the fact that the tip is subject to a higher contact pressure compared to other part of cutting edge. For a process such as micro-end milling, it could be claimed that the wear at tool tip determines the tool life. Since the critical point of tool wear is at

the tool tip, the 2-D FE simulation may be recommended over the 3-D FE simulation which takes more computational effort.

4. Tool Wear Effects in Micro-End Milling

Tool wear is a major factor influencing the performance of micro-end milling. However, it is very difficult to investigate its effect experimentally. Therefore, in this study, the influence of tool wear in micro-end milling was investigated using 3-D FE process simulations. Three types of micro-end milling were studied including full-immersion slot micro-end milling, half-immersion down micro-end milling and half-immersion up micro-end milling.

Based on the previous studies (Thepsonthi & Özel 2012b), it was found that tool wear gradually increases the edge radius (r_β) of the tool. Therefore, to investigate the influence of tool wear in micro-end milling process, three levels of edge radius were employed. The tool edge radius of r_β = 3 µm represents the unworn tool while the tool edge radius of r_β = 6 µm and r_β = 12 µm represent different stages of the worn tools. All simulations were conducted at the spindle speed (Ω) of 16,000 rpm, feed per tooth (f_z) of 4.5 µm and axial depth of cut (a_p) of 100 µm. All process parameters used in the study are shown in Table 5.1.

4.1 Full-immersion slot micro-end milling results

One advantage of 3-D over 2-D simulations is the prediction of chip formation, specifically 3-D chip flow. In the 2-D model chip flow is limited to take place only on X-Y plane resulting in an excessive chip accumulation in front of the tool. With the 3-D simulation, a more realistic chip flow and curling can be predicted. Figure 5.12 shows how the chips were formed during full-immersion slot micro-end milling process using the tools with different edge radii. It can be noticed that chip formation was significantly

influenced by the size of edge radius. At the tool edge radii of r_β = 3 μm and r_β = 6 μm, 3-D chip form is a spring type chip with a smaller curl radius. But at the tool edge radius of r_β = 12 μm, the chip form becomes C-type chip with a larger curl radius. Analysis of 3-D chip formation can be useful to predict burr formation and to improve the design of tool geometry.

Table 5.1: Process parameters in 3-D FE simulation experiments.

Milling process	Full-immersion slot micro-end milling Half-immersion down micro-end milling Half-immersion up micro-end milling
Workpiece	Ti-6Al-4V
Cutting tool	Two-flute flat end-mill, uncoated WC/Co
Tool diameter ($\varnothing$)	508 μm
Tool helix angle (β)	30°
Tool edge radius (r_β)	3 μm, 6 μm, and 12 μm
Spindle speed (Ω)	16,000 rpm
Feed per tooth (f_z)	4.5 μm
Axial depth of cut (a_p)	100 μm
Radial depth of cut (a_e)	508 μm, and 254 μm

Figure 5.13 shows the temperature distribution during micro-end milling at each edge radius size. It can be observed that most of the heat is kept in the chip. This may be due to the intensive plastic deformation which took place in the chip. Also, heat transfer between tool and chip is quite limited due to a small tool-chip contact area. Figure 5.13 also shows that a large tool edge radius generates a higher cutting temperature compared to a small tool edge radius. This may indicate that a larger shear zone resulting from enlarged edge radius which then decreases the shear angle.

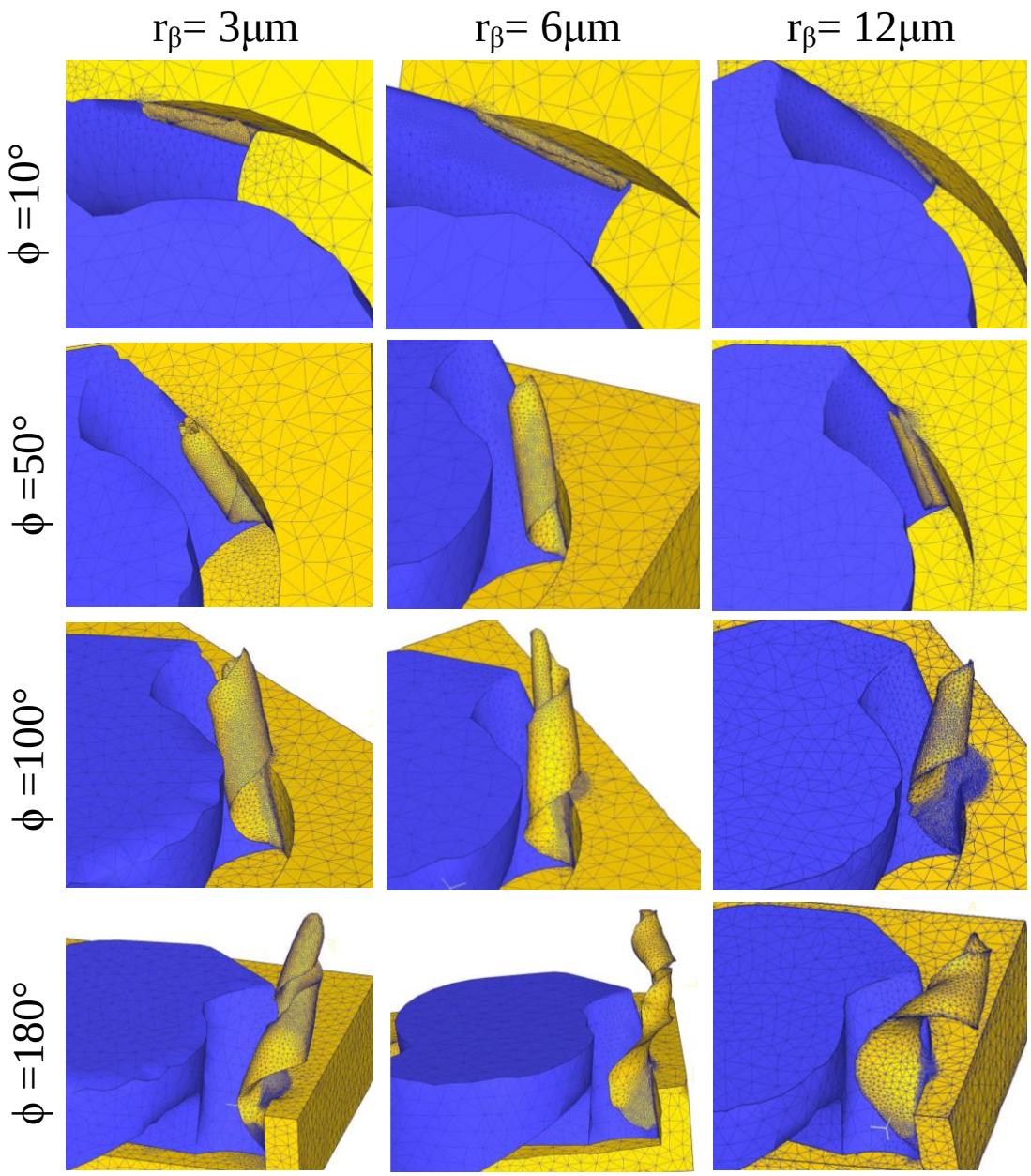

Figure 5.12: Predicted 3-D chip formation and chip flow.

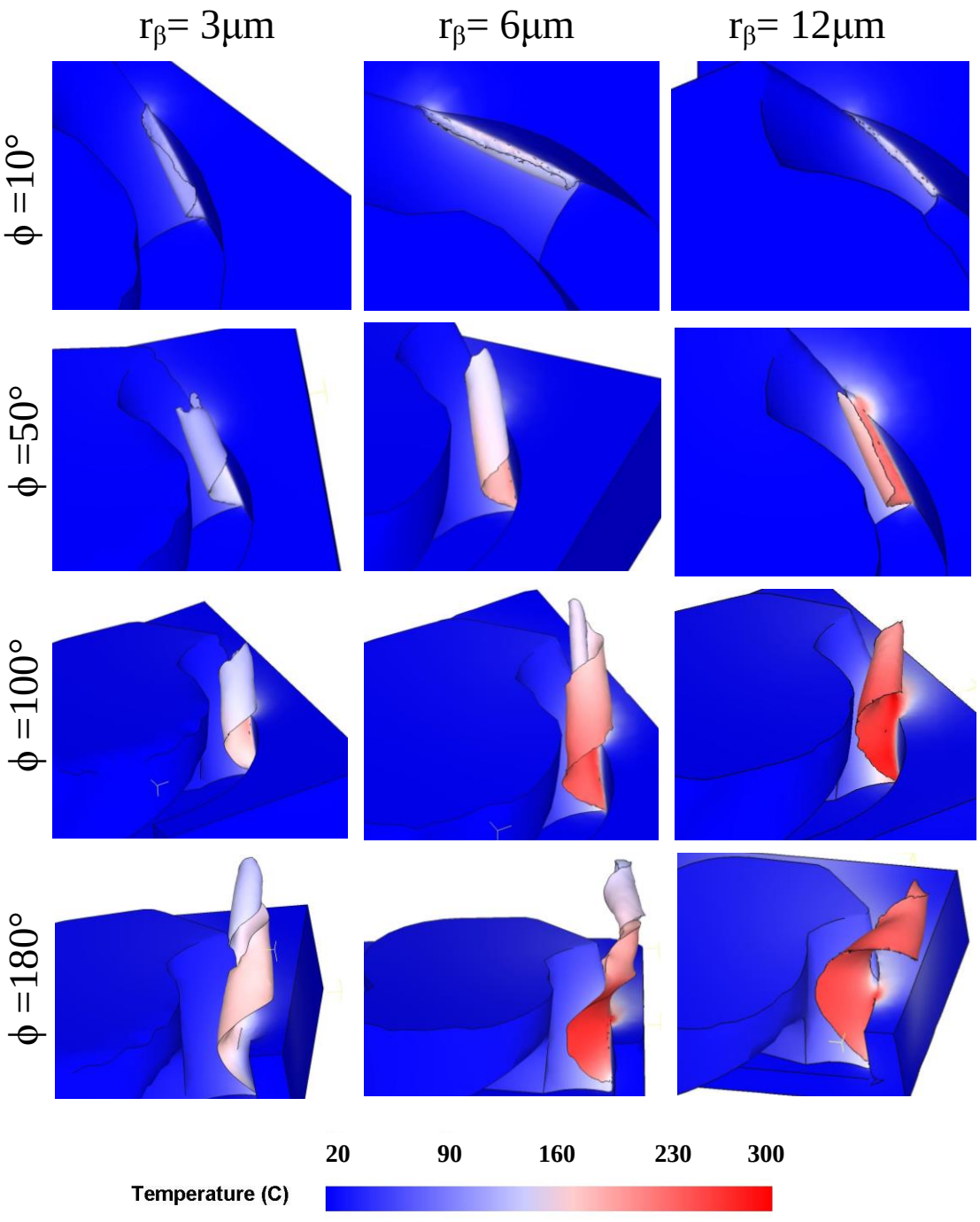

Figure 5.13: Predicted temperature distributions.

To investigate the temperature rise in the tool, the temperatures were collected from four different points along the cutting edge then their average values were used. Figure 5.14 shows the rising of average temperature along the cutting edge as the tool cuts through the workpiece. The graph shows that average temperature at the cutting edge increases as the edge radius increases. This implies that tool wear increases the temperature at the cutting zone.

In Figure 5.15, the temperature distributions along the cutting edge are shown. Based on the result, heat is concentrated on the cutting edge where tool and workpiece are in contact. The temperature of the tool is lower than the temperature of the chip. This indicates a limited heat transfer between tool and chip.

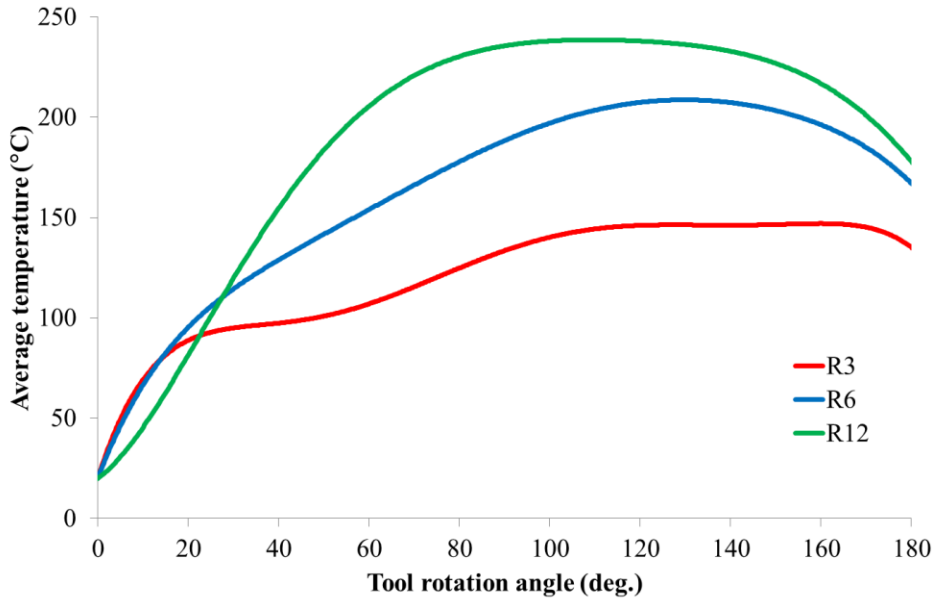

Figure 5.14: Average temperature along the cutting edge of the micro-end milling tool for three different edge radii.

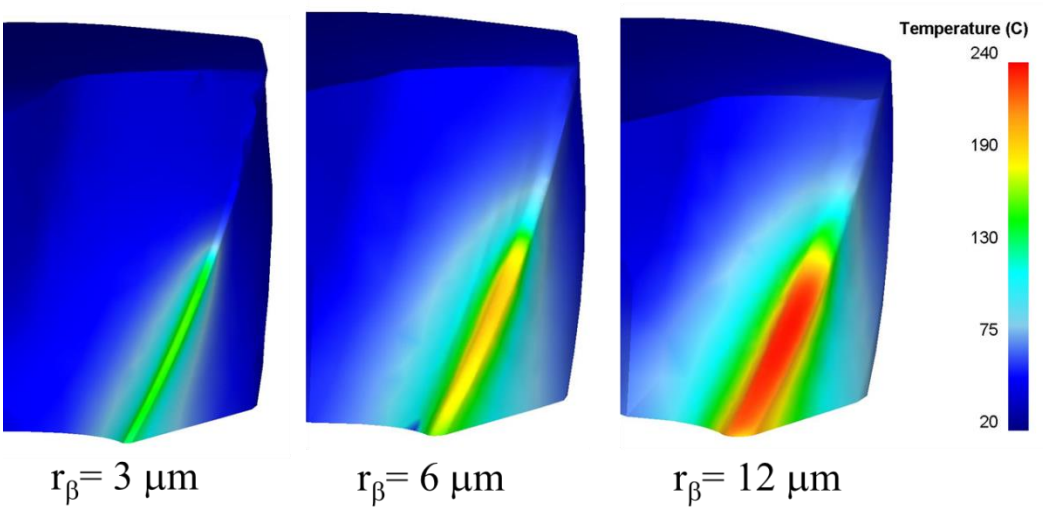

Figure 5.15: Temperature distribution along the cutting edge for three different edge radii.

The cutting force components, F_x, F_y and F_z obtained from the simulations are shown in Figure 5.16. It can be observed that all force components increase with the increasing cutting edge radius. The increase of cutting force may be caused by the increasing rake angle provided by the increasing edge radius. The more negative rake angle results in a larger shear zone which then causes the cutting force to increase.

It can be seen that the cutting force components of F_x and F_y increase approximately around 3 to 5 times as the edge radius increases from r_β = 3 μm to r_β = 12 μm. This infers that the worn tool was subject to the cutting forces 3 to 5 times higher than when it started to cut as the unworn tool. This increase in the cutting force can easily lead to a tool breakage or damaging the machined feature or the machined surface. Therefore, in selecting process parameters, one should consider the cutting force as an important factor. The process parameters which may result in higher cutting forces should be avoided.

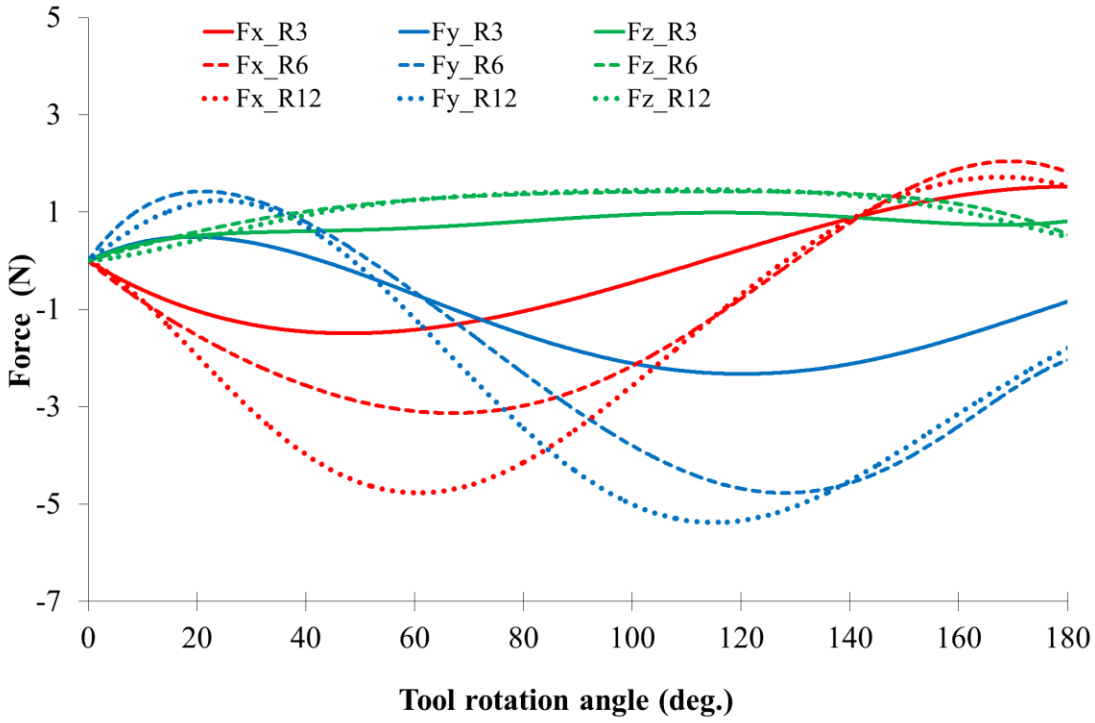

Figure 5.16: Predicted cutting forces in micro-end milling with three different edge radii.

The average tool wear depth values along the cutting edge were collected. The graph of tool wear depth progression is shown in Figure 5.17. This result shows that the tool wear depth increases as the cutting edge radius increases. Since cutting force and cutting temperature also increase with increasing cutting edge radius, the tool wear depth which is influenced by cutting force and cutting temperature should also increase. In addition, the result indicates that the wear rate is not constant but it accelerates as the tool continuously wears and the tool edge radius increases.

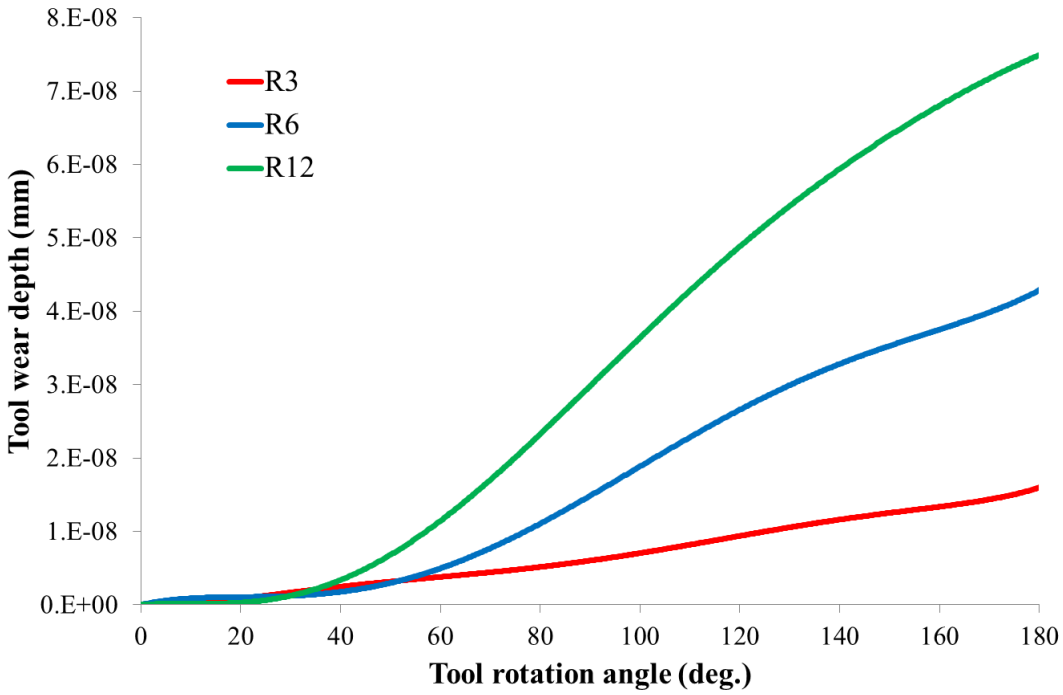

Figure 5.17 Average tool wear depth along the cutting edge for three different edge radii.

Figure 5.18 shows the tool wear depth distribution along the cutting edge. The uniform wear distribution on the cutting edge was obtained from the tools with edge radii of r_β = 3 µm and r_β = 6 µm. This indicates a pure sliding contact between the tool and the workpiece. However, in the case of r_β = 12 µm edge radius, there exists an evidence of sticking contact at the middle of cutting edge. The figure of tool wear distribution at r_β=12 µm clearly shows that very low wear depth at the middle of the cutting edge exists. This may be caused by the built-up edge (BUE) which creates a zone where the workpiece material sticks to the tool. In addition, this figure also shows that the tool wear is more concentrated on the flank face indicating that there is a high level of contact pressure on the flank face.

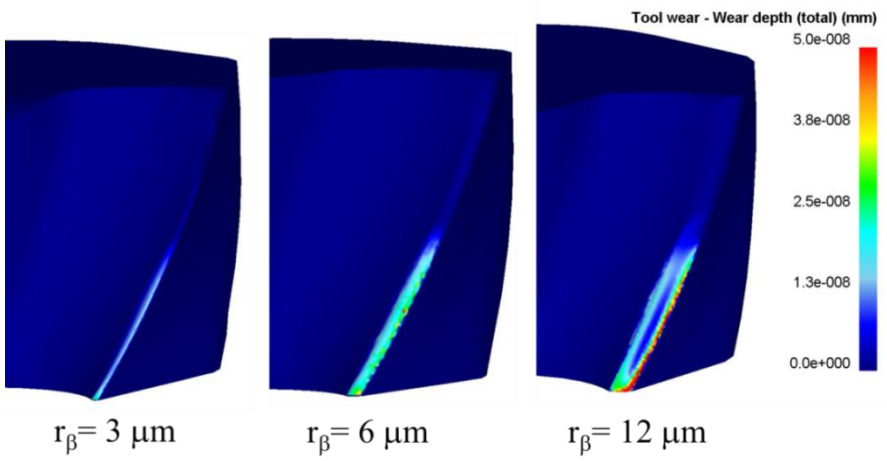

Figure 5.18: Tool wear depth distribution along the cutting edge.

4.2 Half-immersion micro-end milling results

In this study, besides the 3-D FE simulation of a full-immersion micro-end milling process (a_e = 508 μm), the half-immersion milling processes (a_e = 254 μm) were also investigated using 3-D FE simulations. The goal was to investigate the process performance under two different milling strategies; up milling and down milling. After that, the advantages and the disadvantages of each strategy can be discussed.

In up milling, the feed direction of the cutting tool is opposite to its rotation. The chip thickness starts at zero and increases towards the end of the cut. In down milling, the cutting tool is fed with the direction of rotation. The chip thickness starts at the maximum value and decreases towards zero at the end of the cut. In micro-end milling, there is still no general guideline for choosing a strategy among up milling and down milling strategies.

Figure 5.19 shows the chip formation in half-immersion micro-end milling. In spite of having a different tool engagement, no significant difference in terms of chip formation between up milling and down milling can be observed. The spring type chip

formation can be observed in the cases of r_β = 3 µm and r_β = 6 µm, while the C-type chip formation can be observed in the case of r_β = 12 µm. This is no different than the full-immersion milling.

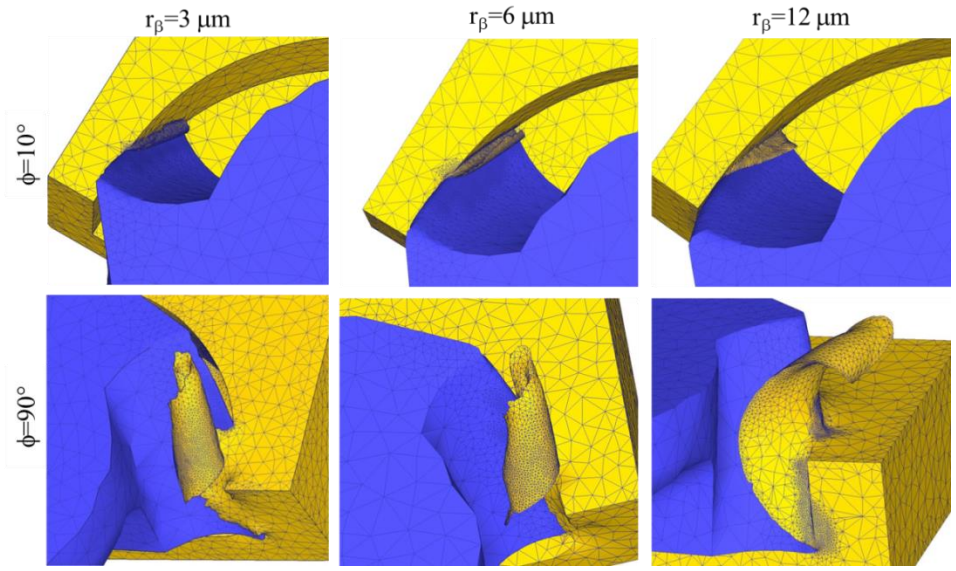

(a)

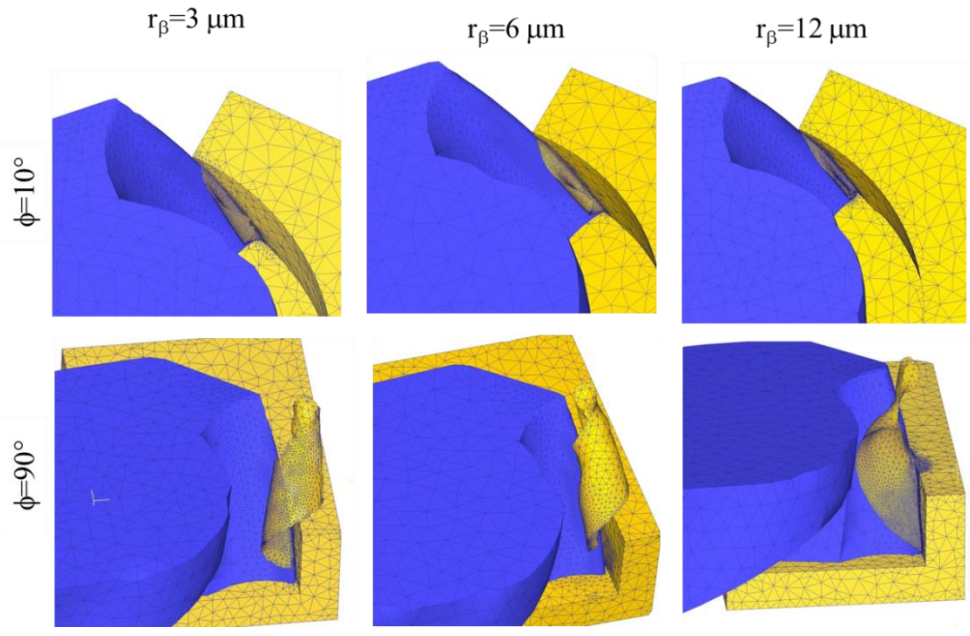

(b)

Figure 5.19: Chip formation in half-immersion micro-end milling (a) up milling, (b) down milling.

The average temperature was taken from the cutting edge to characterize the heat generation during the cutting process. The average tool temperatures along the cutting edge are plotted against the tool rotation angle as shown in Figure 5.20. Based on the graph, the tool with large edge radius tends to have a higher temperature compared to the tool with the smaller edge radius.

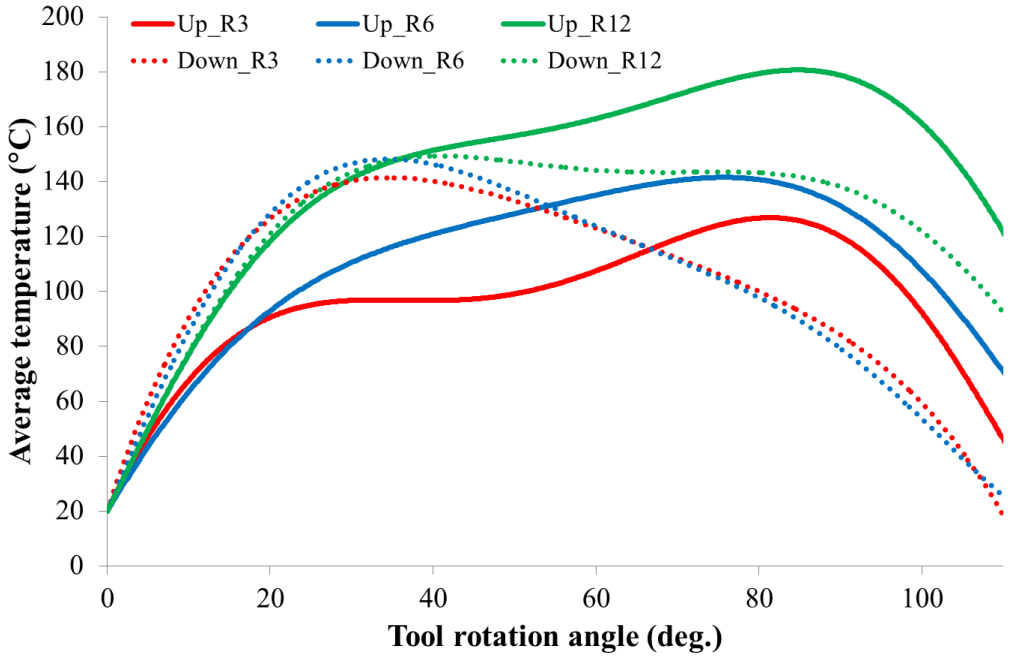

Figure 5.20: Average tool temperatures along the cutting edge in half-immersion micro-end milling.

Figure 5.21 shows the temperature distribution in the tool. It can be seen that the peak temperature is not located at the tool tip but stays above it. This is the same as what was found in full-immersion micro-end milling. Comparison of temperature in half-immersion up and down micro-end milling shows no difference in terms of distribution but shows a difference in terms of maximum temperature.

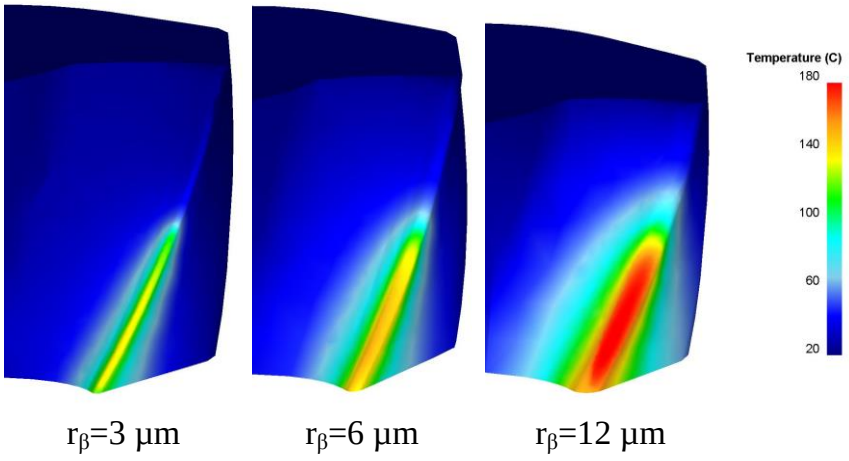

(a)

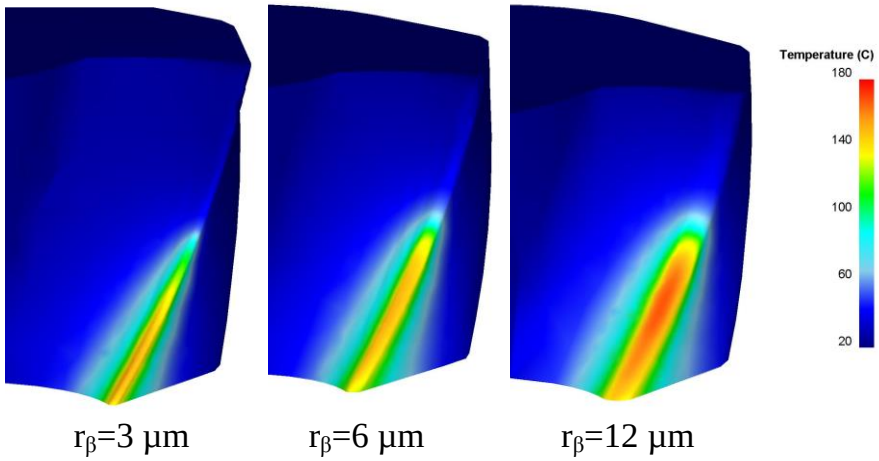

(b)

Figure 5.21: Tool temperatures in half-immersion micro-end milling (a) up milling, (b) down milling cases.

Figure 5.22 shows the cutting force components, F_x, F_y, and F_z obtained from the simulations. The graphs reveal that increasing edge radius increases cutting forces. This implies that cutting with a worn tool generates a higher cutting force compared to cutting with an unworn tool. In terms of maximum cutting forces, no significant difference between up milling and down milling can be observed.

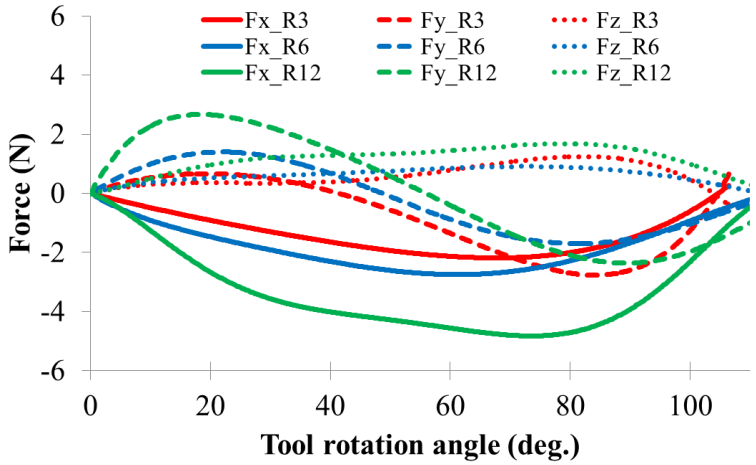

(a)

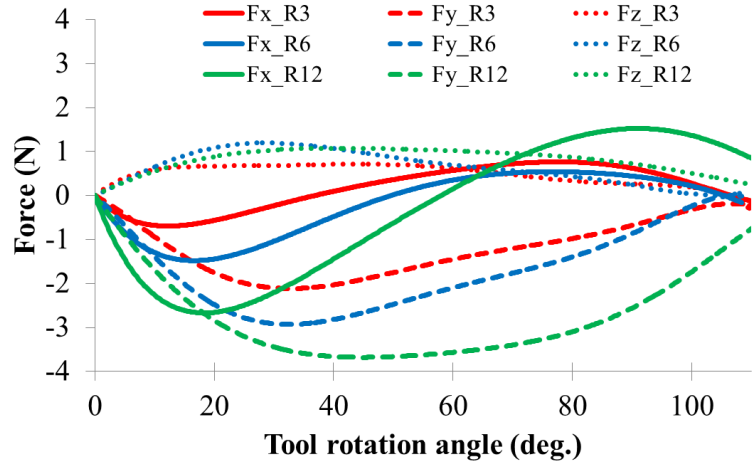

(b)

Figure 5.22: Cutting forces in half-immersion micro-end milling (a) up milling, (b) down milling.

In Figure 5.23, predicted tool wear depths are plotted against tool rotation angle showing the trends of tool wear progression as the tool cuts through the workpiece. In case of half-immersion up micro-end milling, the graph shows a significant increase in tool wear as the edge radius increases. However, for half-immersion down micro-end milling, the increase is not so significant. This may lead to the conclusion that the wear

rate in down milling is constant regardless of the size of the edge radius. In the case of up micro-end milling, the wear rate increases as the edge radius increases.

Based on the information provided by Figure 5.23, two conclusions may be drawn. First, down milling provides more sustainability to the tool since the increase of edge radius does not accelerate the wear rate. This probably makes down milling strategy a first choice when machining a big feature which requires a long lasting tool. Second, the up milling strategy may be more preferred for machining with a short period of time due to the fact that it exhibits a lower wear rate when the tool is unworn.

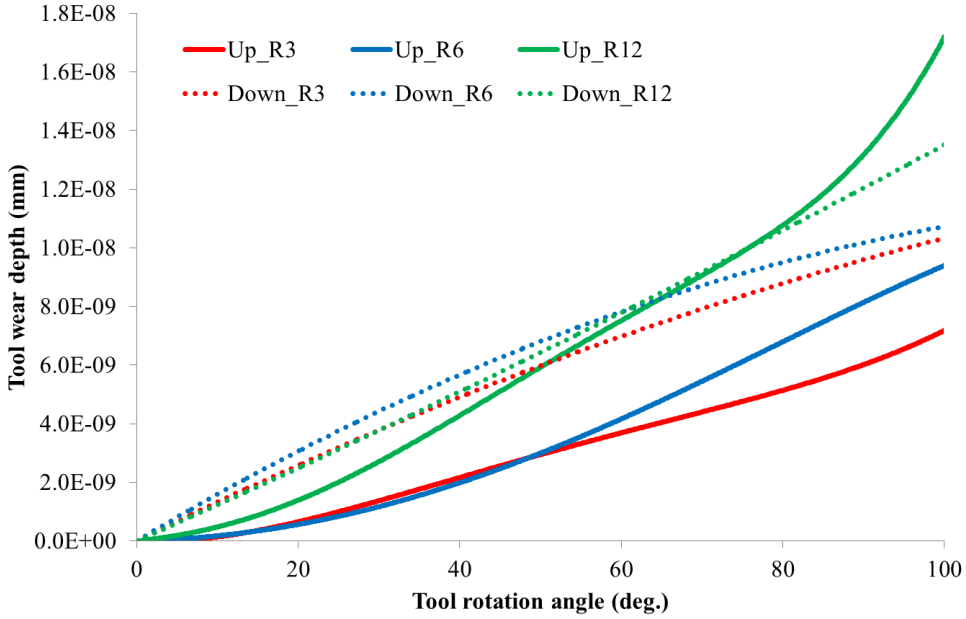

Figure 5.23: Average tool wear depths along the cutting edge in half-immersion micro-end milling with up and down milling strategies.

The area of tool wear in each case is shown in Figure 5.24. It is obvious that tools are worn out only at the edge of the tool. No tool-chip contact has occurred on the rake face thus no crater wear can be detected. Deeper wear can be detected near the flank face

of the tool rather than the rake face of the tool. More built-up edge (BUE) may be occurred in down micro-end milling.

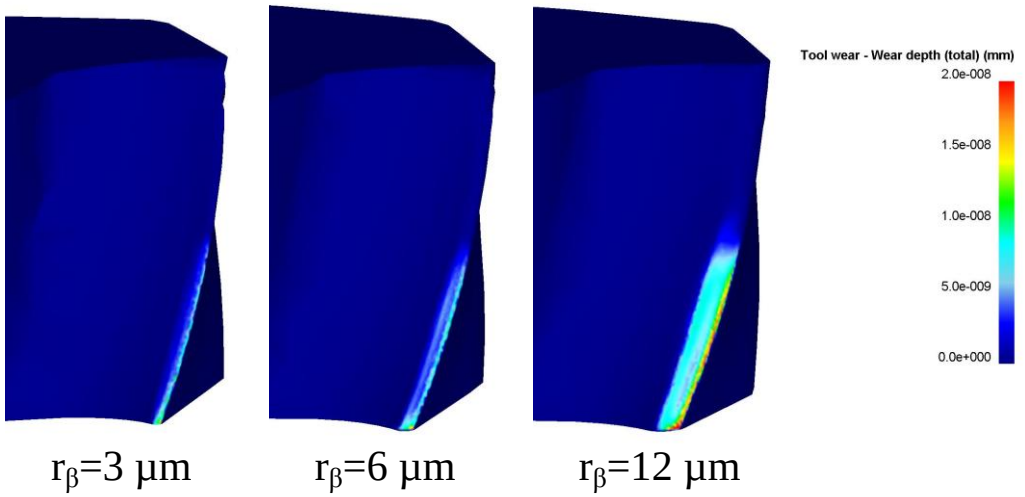

(a)

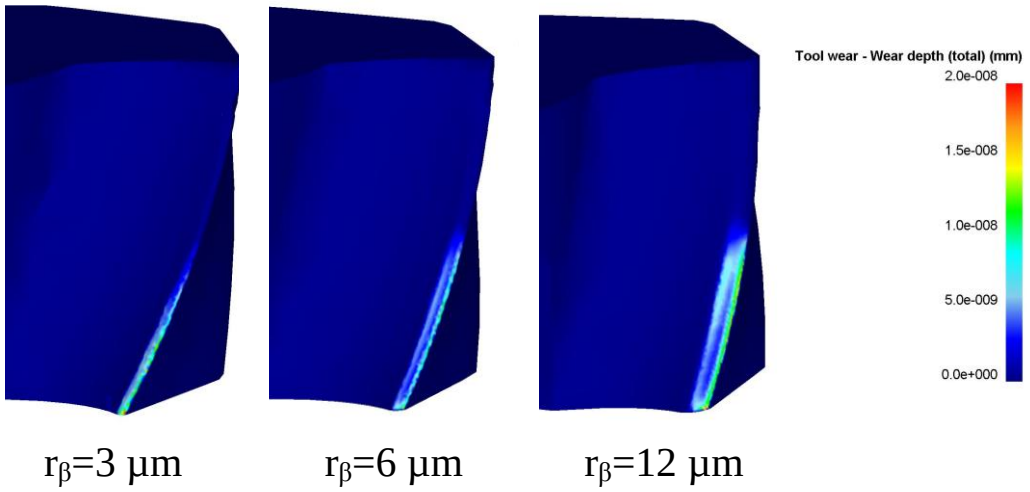

(b)

Figure 5.24: Tool wear depth in half-immersion micro-end milling (a) up milling, (b) down milling strategies.

4.3 Discussions

This study presents 3-D FE based process simulations on micro-end milling of Ti-6Al-4V alloy with uncoated WC/Co micro-end mills. Three types of milling strategies were investigated namely full-immersion slot micro-end milling, half-immersion down micro-end milling and half-immersion up micro-end milling. The results of this study were analyzed in terms of chip formation, tool wear, cutting force, and cutting temperature.

A study on the influence of tool wear to the performance of micro-end milling has pointed out that increasing edge radius (r_β) as a result of tool wear significantly decreases the process performance in terms of increasing tool wear, higher cutting forces, and higher cutting temperatures. In micro-machining, the rake angle is normally negative due to relatively large edge radius compared to the uncut-chip thickness. Increase of the edge radius due to tool wear would result in even higher negative rake angles leading to a smaller shear angle and a larger shear zone. Since the shear zone is enlarged, the resistance to the deformation increases significantly. As a result, more force has to be inserted to generate a plastic deformation. This is evident from Figure 5.16 where the cutting force components increase as the edge radius increases. Also, the energy spent in the plastic deformation transforms into heat and rises up the temperature at the cutting zone. Higher temperature observed when machining with a worn tool (See Figures 5.13, 5.14 and 5.15) indicating a higher degree of plastic deformation resulting from a larger shear zone. In short, tool wear increases cutting forces and cutting temperatures through increasing of negative rake angle which enlarges and widens the shear zone.

Beside sliding velocity, contact pressure, and cutting temperature, tool wear rate is also a function of cutting edge radius (r_β). The results in Figures 5.17 and 5.18 have

shown that the larger the cutting edge radius, the higher the tool wear rate. Since the tool wear rate increases as the edge radius increases and the edge radius increases due to the tool wear, one may be able to conclude that tool is not constantly wearing but the tool wear is accelerated exponentially. In addition, as the tool wears out and reaches to a certain level, a built up edge (BUE) may begin to occur in order to reduce the influence of higher negative rake angle.

A 3-D chip formation can be predicted using the 3-D FE simulation. Based on the results, the chip form in micro-end milling of Ti-6Al-4V can be separated into two types; spring type and C-type chips. When the edge radius is small (r_β=3-6 μm), a spring type chip is formed in which a smaller curl radius occurs. Once the edge radius getting larger (r_β=12 μm) due to wear, a C-type chip begins to form. This may be related to the decreasing shear angle which increases the chip thickness. Thick chips tend to have a larger curl radius compared to a thinner chip.

The comparison of up milling and down milling shows a significant difference only in terms of tool wear. Based on Figure 5.23, it can be observed that the tool wear rate in up milling significantly increases as the edge radius increases but the tool wear rate in down milling does not significantly increase as the edge radius increases. This may be due to the fact that, in down milling, tool enters the workpiece at the maximum chip thickness which then easily shears the workpiece and forms a chip. Thus, down milling encounters less ploughing compared to up milling. The ploughing in up milling may increase as the edge radius increases due to a higher negative rake angle and the minimal chip thickness requirement. This may result in the increase of the tool wear rate in up milling.

5. Conclusions

In this study, 3-D FE simulations of micro-end milling have been developed. 3-D FE simulations offer additional analysis capabilities to the 2-D FE simulations. Prediction of 3-D chip formation, 3-D cutting forces, cutting temperature and tool wear distributions along the flutes of the micro-end mill can be investigated. However, to conduct a 3-D FE simulation, more effort has to be made when compared to conducting a 2-D FE simulation. This study has pointed out that the 2-D FE simulation may be adequate for the analysis of cutting force and tool wear. However, the analysis of chip formation and cutting temperature should be done using a 3-D FE simulation. In addition, the study also shows that tool wear decreases the shear angle resulting in increasing cutting forces, cutting temperatures, and tool wear rate.

CHAPTER 6

PROCESS OPTIMIZATION AND DECISION SUPPORT FOR HIGH PERFORMANCE MICRO-MILLING OF Ti-6Al-4V ALLOYS

1. Introduction

A common problem which manufacturers have to face is determining the suitable process parameters for machining process. Even though this is a common problem, a solution can be very difficult. There are several ways in determining the process parameters. The most common way may be to consult with the tool manufacturer's handbooks. However, the handbooks just simply recommend a range of process parameters for machining specific type of materials. They never provide any possible outcomes of using those process parameters. Thus in order to obtain the desirable machining outcome, most of the time, the users have to rely on their experience or trial-and-error. In addition, many users tend to use a conservative approach by selecting low levels of process parameters in order to avoid any failure; doing so results in a decrease of productivity.

Similar to any other machining process, determining process parameters in micro-end milling is also very difficult. The tool and feature fragility make the selection of process parameters become much more difficult. An improper selection of the process parameter can result in tool breakage and/or ruin of the part feature. To select the process parameters for micro-end milling, the users have to consider two important limitations which are cutting forces and tool life. Excessive cutting forces in micro-end milling will result in the excessive tool deflection or even tool breakage; small or thin machining

feature can be easily bended or ruined by the excessive cutting forces. Tool life limits the cutting distance that the tool can perform before it is excessively worn; a worn tool directly results in a geometrical error of machined feature. Therefore, it is important to finish the machining before the end of the tool life.

Performing micro-end milling involves selection of process parameters such as cutting speed, feed per tooth and axial depth of cut. Under different circumstances, these process parameters can be varied in order to obtain the optimal process performance. Deciding on the level of these process parameters obviously depends on objectives and constraints of the process. In general, the objectives of the machining process are based on the required product qualities such as surface roughness and burr formation. The constraints in machining process may include machine capability, tool life, maximum cutting force, and maximum cutting temperature.

Since, determining the suitable process parameters in micro-end milling is complex and requires a lot of consideration, a systematic methodology and a decision support system are essentially required. Therefore, in this chapter, an attempt will be made on developing a decision support system which can assists the user in selecting proper process parameters that satisfy the specified process objectives and constraints.

2. Methodology

The data collected from both experiments (Chapter 3) and 2-D finite element based process simulations (Chapter 4) were used as inputs for this study. The data in terms of average surface roughness (R_a), total top-burr width (B_T), cutting forces (F_x, F_y) and tool wear depth (W) were mathematically modeled as functions of process parameters (spindle speed, feed per tooth, and axial depth of cut). The average surface roughness (R_a) and

total top-burr width (B_T) models were used as objectives of the process optimization while cutting forces (F_x, F_y) and tool wear depth (W) models were used as constraints. Since the optimization involves multiple objectives, the multi-objective particle swarm optimization (MOPSO) was utilized for searching and providing optimal solution sets. The solution sets obtained from the multi-objective optimization can be used to assist the user in selecting the optimum process parameters which can satisfy product requirements and maximize the process performance. Figure 6.1 shows the overview of this approach.

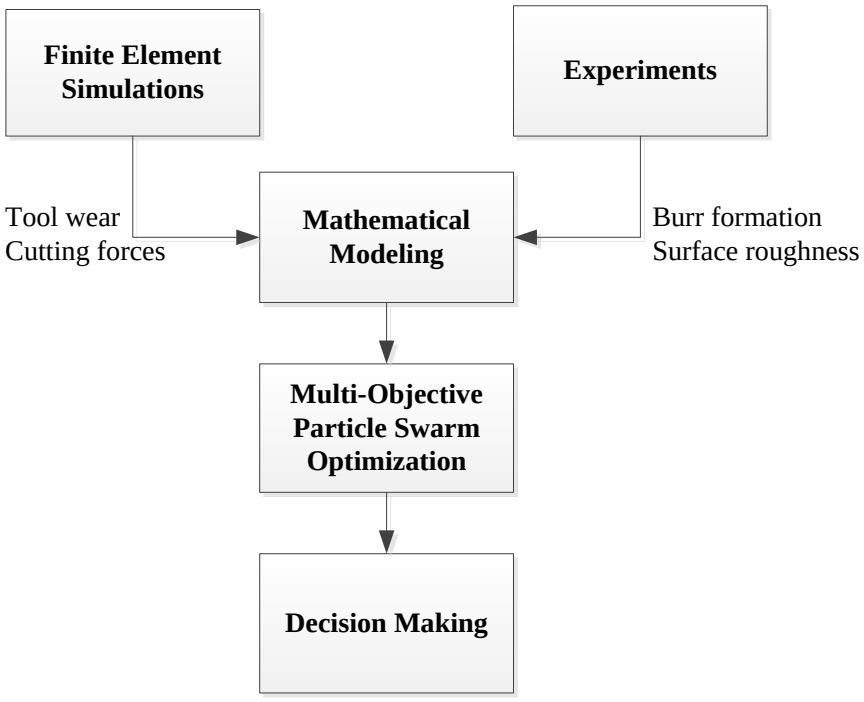

Figure 6.1: An overview of the approach used in this study.

Multi-Objective Particle Swarm Optimization (MOPSO) played a key role in the developed decision support system. Three optimization schemes were developed and tested including constrained multi-objective optimization, unconstrained multi-objective optimization, and weighted sum method based multi-objective optimization. The aim was

to develop a decision support system which is effective and easy to use. Also, the system should allow the transformation of process objectives and constraints (surface roughness, burr formation, tool life, and cutting forces) into working parameters (spindle speed, feed per tooth, and axial depth of cut). Figure 6.2 shows the flow of data in the proposed decision support system.

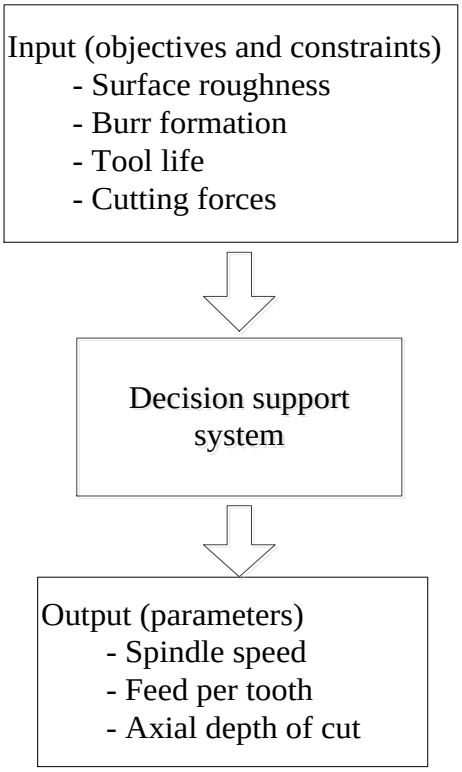

Figure 6.2: Input and output of the proposed decision support system.

3. Predictive Models for Surface Roughness and Top-Burr Width

Experiments were conducted in order to collect data for constructing predictive models for average surface roughness (R_a) and total top-burr width (B_T). These models served as objectives of the process optimization. The experimental setup and methodology were explained in Chapter 2 and Chapter 3. The data obtained from the

experiments were used to construct mathematical models in order to predict the process performances at any combination of process parameters. A well-known method, Response Surface Methodology (RSM), was utilized for this purpose. The second order RSM models for average surface roughness (R_a) and total top-burr width (B_T) were developed based on the experimental results as shown in Eq. (6.1) and Eq. (6.2). The models are functions of three basic terms consist of spindle speed (Ω), feed per tooth (f_z) and axial depth of cut (a_p). To measure the accuracy of the models, R^2(adj) were calculated. The R_a and B_T models have the R^2(adj) of 84% and 96.5% respectively which indicate a good fit to the experimental results.

$$R_a = 0.13145 - 0.00065\Omega - 0.04229f_z + 0.00179a_p + 0.00507f_z^2 - 0.00002a_p^2 + 0.00029\Omega f_z + 0.00012f_z a_p \quad \text{Eq. (6.1)}$$

$$B_T = 0.48051 - 0.00139\Omega - 0.04737f_z - 0.00498a_p + 0.00504f_z^2 + 0.00002a_p^2 + 0.00025\Omega f_z \quad \text{Eq. (6.2)}$$

These models served as the objective functions in the multi-objective optimization. Unfortunately, the current state of FE simulation is not capable of simulating the surface roughness and burr formation; therefore, more expensive experiments had to be conducted in order to obtain the necessary data for constructing these models.

4. Predictive Modeling of Tool Life

Tool life determines how long the tool can be used without causing excessive geometrical error to the machined feature. Determining tool life is very critical in micro-machining since the geometrical tolerance is much smaller compared to the conventional macro-machining. It is very hard to detect tool wear directly while micro-machining is carried out. Two ways to deal with this problem are using an online monitoring system or using a predictive model. In this work, the use of a predictive model for determining tool life based on machining condition is proposed.

To predict tool life, the data obtained from 2-D finite element simulations was utilized. The FE modelling and simulations were explained in Chapter 4. A wear rate model based on the sliding wear proposed by Usui et al. (Usui et al. 1978) has been utilized to predict the wear rate and calculate the wear depth (W). In this study, the tool wear data simulated from the FE simulations were used as an alternative to the data obtained from the experiments. The major reasons are the difficulty of accessing the tool wear in micro-scale and the lengthy and costly experimentation to obtain the tool wear data. The results of tool wear depth obtained from the FE simulations are shown in Figure 6.3 The tool wear depths (W) at the end of single pass are shown in Table 6.1.

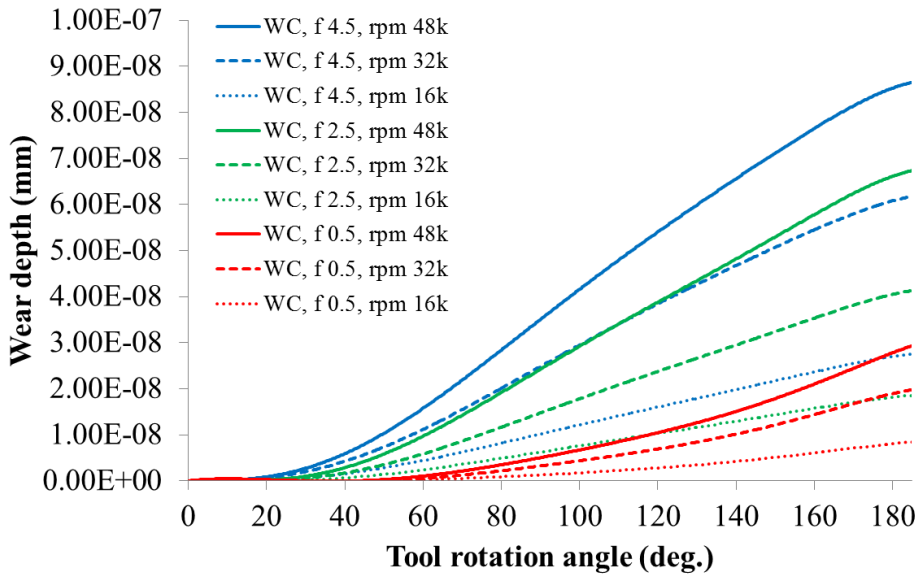

Figure 6.3: Tool wear depth for a single pass (*W*).

Table 6.1: Tool wear depth at the end of single pass (*W*).

v_c (mm/min)	f_z (mm/tooth)	W (mm/pass)	ln V_c	ln f_z	ln W
25000	0.0005	8.62656E-09	10.12663	-7.6009	-18.5684
25000	0.0025	1.86541E-08	10.12663	-5.99146	-17.7972
25000	0.0045	2.78071E-08	10.12663	-5.40368	-17.398
50000	0.0005	1.97544E-08	10.81978	-7.6009	-17.7399
50000	0.0025	4.14902E-08	10.81978	-5.99146	-16.9978
50000	0.0045	6.18887E-08	10.81978	-5.40368	-16.5979
75000	0.0005	2.94823E-08	11.22524	-7.6009	-17.3395
75000	0.0025	6.76734E-08	11.22524	-5.99146	-16.5086
75000	0.0045	8.6692E-08	11.22524	-5.40368	-16.2609

The tool wear depth per pass (*W*) can be formulated using a multiplicative model as shown in Eq. (6.3), where *W* is the tool wear depth per pass (mm/pass) obtained from the FE simulations, v_c, and f_z, are the cutting velocity (mm/min) and feed per tooth (mm/tooth) respectively, *B*, b_0, and b_1, are constants and ϵ is the random error.

$$W = B(v_c^{b_0} f_z^{b_1})\epsilon \qquad \text{Eq. (6.3)}$$

The cutting velocity can be written as a function of spindle speed (Ω) and tool diameter ($\emptyset$) as shown in Eq. (6.4), where $\emptyset$ is in mm and Ω is in rpm.

$$v_c = \pi \emptyset \Omega \qquad \text{Eq. (6.4)}$$

By taking logarithm into Eq. (6.3), we can transform Eq. (6.3) into a linear regression form as shown in Eq. (6.5).

$$\ln W = \ln B + b_0 \ln v_c + b_1 \ln f_z + \epsilon \qquad \text{Eq. (6.5)}$$

Using least squares method, the constant values *B*, b_0, and b_1 can be calculated as shown in Eq. (6.6)

$$\ln W = -25.98593 + 1.11519 \ln v_c + 0.50831 \ln f_z \qquad \text{Eq. (6.6)}$$

Finally, the predictive model of average wear depth per pass can be written as shown in Eq. (6.7). The response surface of tool wear depth per pass can be constructed as shown in Figure 6.4.

$$W = 5.18146 \times 10^{-12} (v_c^{1.11519} f_z^{0.50831}) \qquad \text{Eq. (6.7)}$$

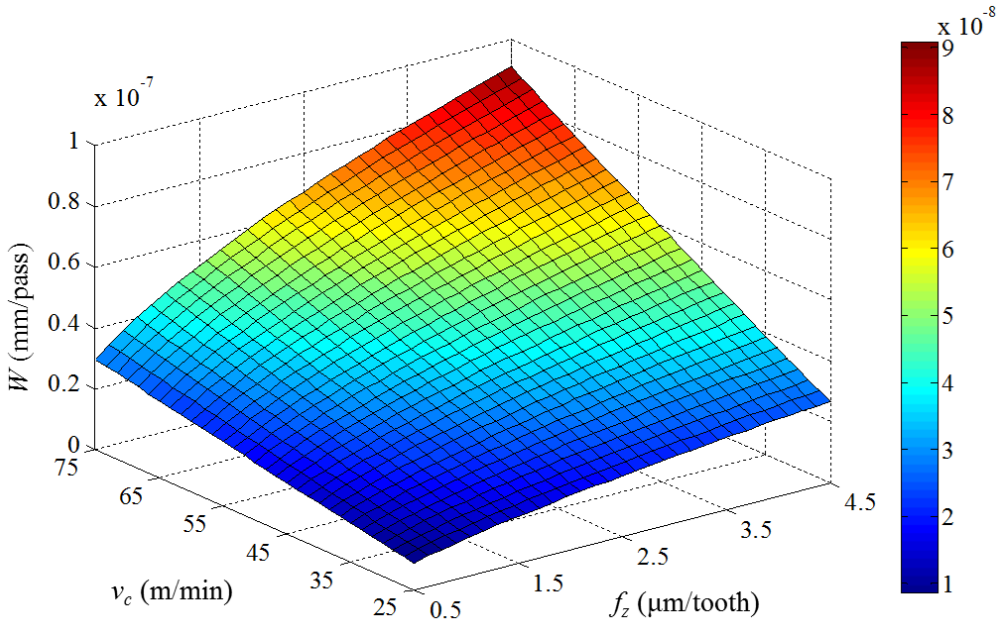

Figure 6.4: Response surface of tool wear depth per pass.

In micro-machining, it is quite necessary to be able to realize that the micro-tool will last without excessive wear or breakage until the end of the operation. Especially in the case of difficult-to-cut material such as Ti-6Al-4V titanium alloy where the micro-tool is worn rapidly, knowing an estimated tool life would be very beneficial. Therefore, it is useful to be able to predict the maximum linear cutting distance and maximum tool life for a single micro-end mill.

In general, the tool life ends when it reaches the maximum allowable wear depth or when it is broken. Considering the maximum allowable wear depth, the maximum linear cutting distance (L in mm) and maximum tool life (T_{life} in min) can be predicted by Eqs. (6.8) and (6.9) respectively, where f_z is feed per tooth (mm/tooth), W is wear depth per pass (mm/pass), W_{max} is maximum allowable wear depth per tooth (mm), v_c is cutting

speed (mm/min), $\emptyset$ is the diameter of the micro-end mill (mm) and n is number of micro-end mill tooth.

$$L = \mathrm{f}_z \frac{W_{max}}{W} \qquad \text{Eq. (6.8)}$$

$$T_{life} = \frac{\pi \emptyset}{n v_c} \frac{W_{max}}{W} \qquad \text{Eq. (6.9)}$$

Figures 6.5 and 6.6 show the predictive maximum linear distance (L) and tool life (T_{life}) based on Eqs. (6.8) and Eq. (6.9) at the maximum allowable wear depth per tooth (W_{max}) of 5 µm. Figures 6.7 and 6.8 show the predictive maximum linear distance (L) and tool life (T_{life}) based on the setting of the maximum allowable wear depth per tooth (W_{max}).

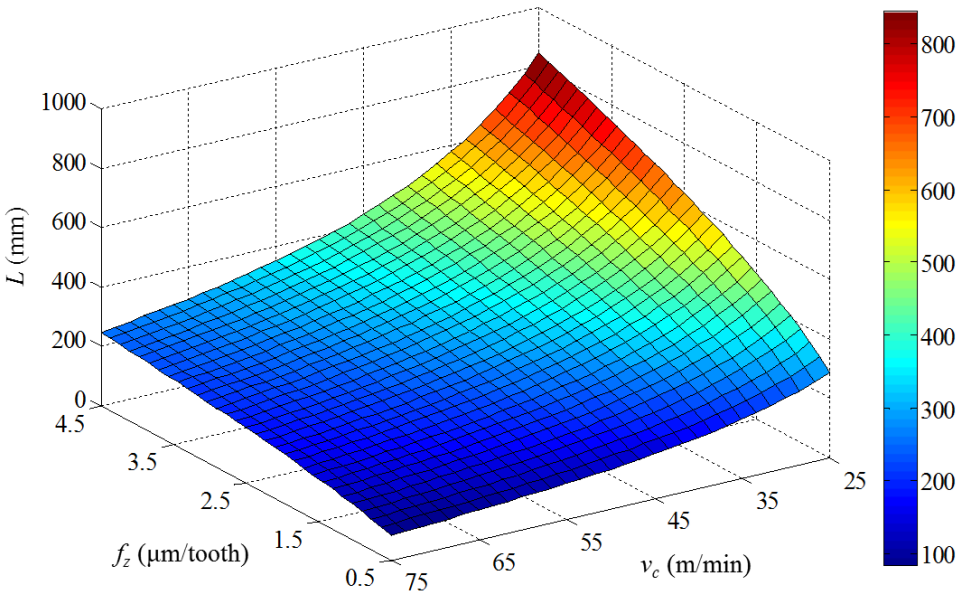

Figure 6.5: Maximum linear cutting distance (W_{max} = 5 µm).

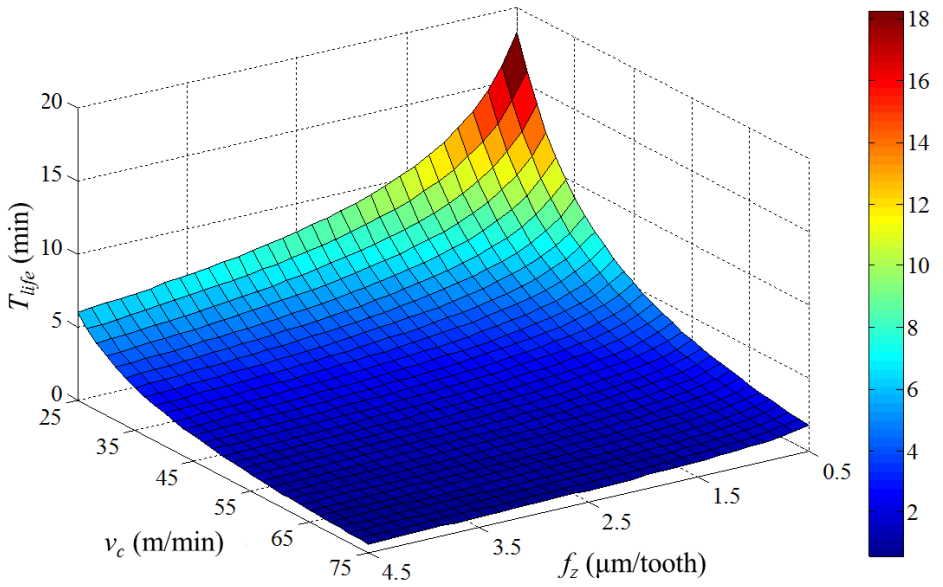

Figure 6.6: Maximum tool life (W_{max} = 5 µm).

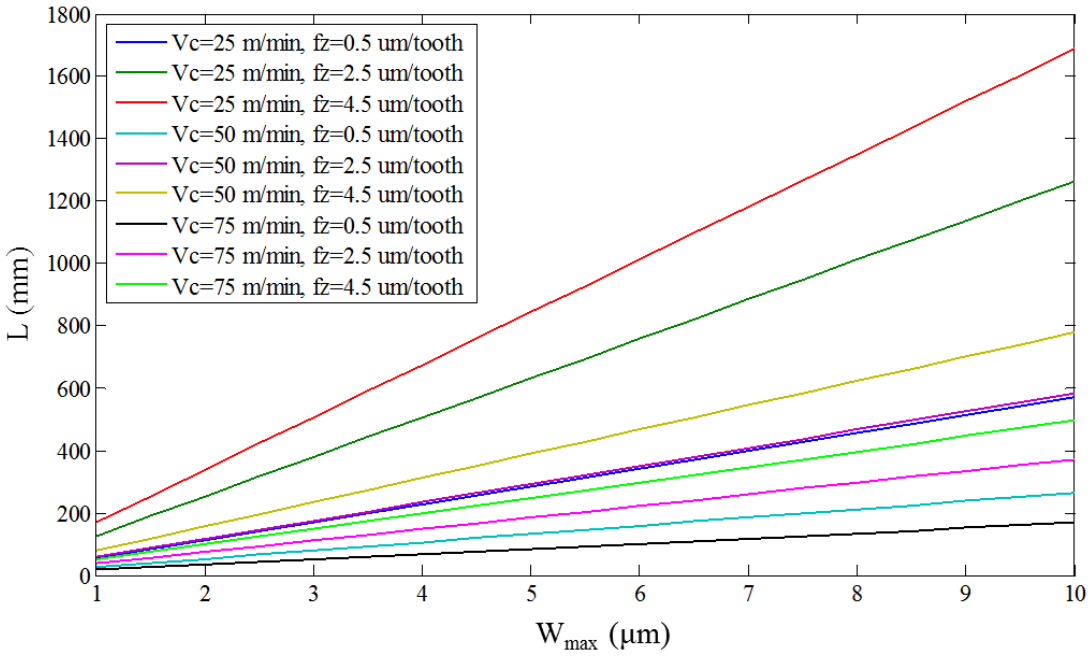

Figure 6.7: Maximum linear cutting length (L) vs. maximum allowable wear depth per tooth (W_{max}).

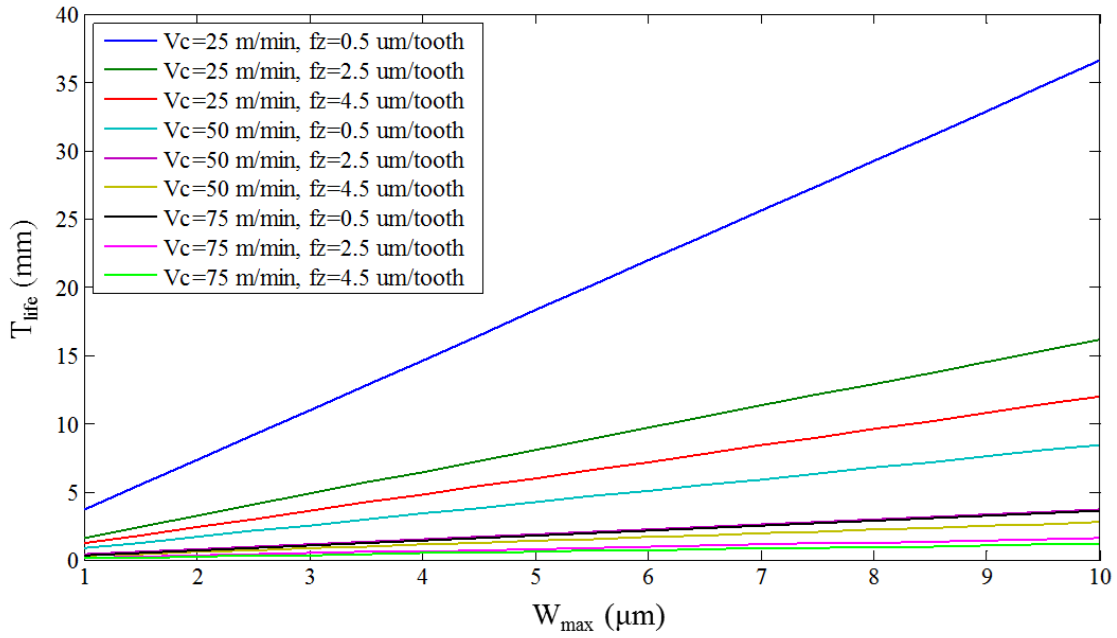

Figure 6.8: Maximum tool life (T_{life}) vs. maximum allowable wear depth per tooth (W_{max}).

5. Predictive Modeling of Cutting Forces

In micro-end milling, controlling cutting forces is very essential since both tool and workpiece have very low rigidity. Excessive cutting forces can easily break the tool or the machined feature. Therefore, cutting forces should be considered when selecting process parameters. Establishing predictive models for cutting forces would facilitate the parameter selection process.

In this study, predictive modeling of cutting forces was formulated based on the cutting force data obtained from 2-D FE simulations as shown in Figure. 6.9. In order to approximate the cutting forces from the 2-D cutting force simulation data, the differential force components dF_x and dF_y were formulated as a function of tool rotational angle (ϕ in

degrees) using six degree polynomial curve fitting. The model can be presented in the form of Eq. (6.10) and the coefficients a_i can be found in Tables 6.2 and 6.3.

$$dF_i(\phi) = a_1\phi + a_2\phi^2 + a_3\phi^3 + a_4\phi^4 + a_5\phi^5 + a_6\phi^6 + \epsilon \qquad \text{Eq. (6.10)}$$

By setting $\phi = 0°$ at the tool tip, the integration of force components can be formulated as shown in Eqs. (6.11) and (6.12), where $\theta = \phi - \frac{360a_p}{\pi\emptyset\tan(90-\beta)}$, a_p is axial depth of cut (µm), β is helix angle of micro-end mill (degrees), $\emptyset$ is diameter of micro-end mill (µm)

$$F_x(\phi) = \int_\theta^\phi dF_x(\tau)d\tau \qquad \text{Eq. (6.11)}$$

$$F_y(\phi) = \int_\theta^\phi dF_y(\tau)d\tau \qquad \text{Eq. (6.12)}$$

Based on Eq. (6.11) and (6.12), the cutting forces at different axial depth of cut (a_p) can be predicted as shown in Figures 6.10 through 6.18. Also, the maximum cutting forces for each micro-machining condition can be obtained as shown in Table 6.4.

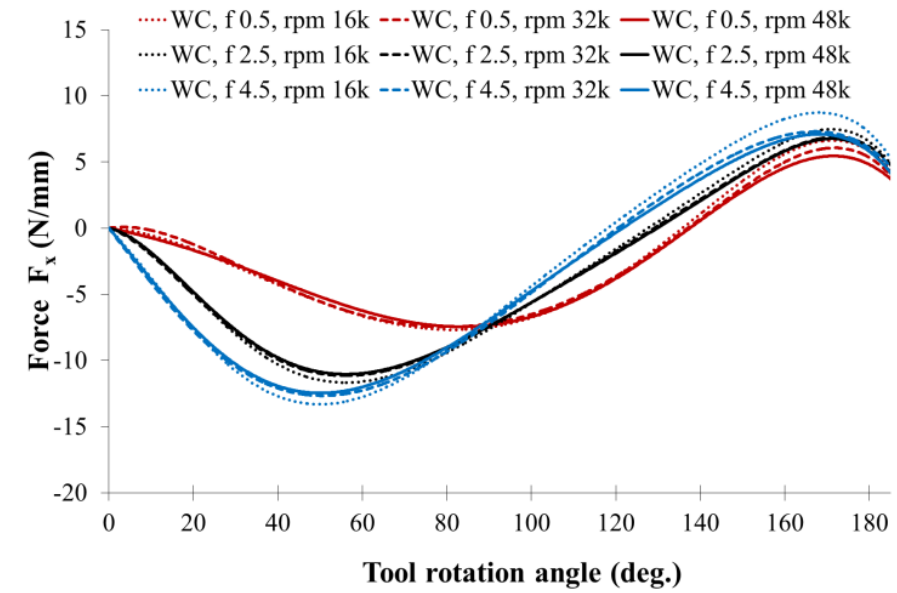

(a)

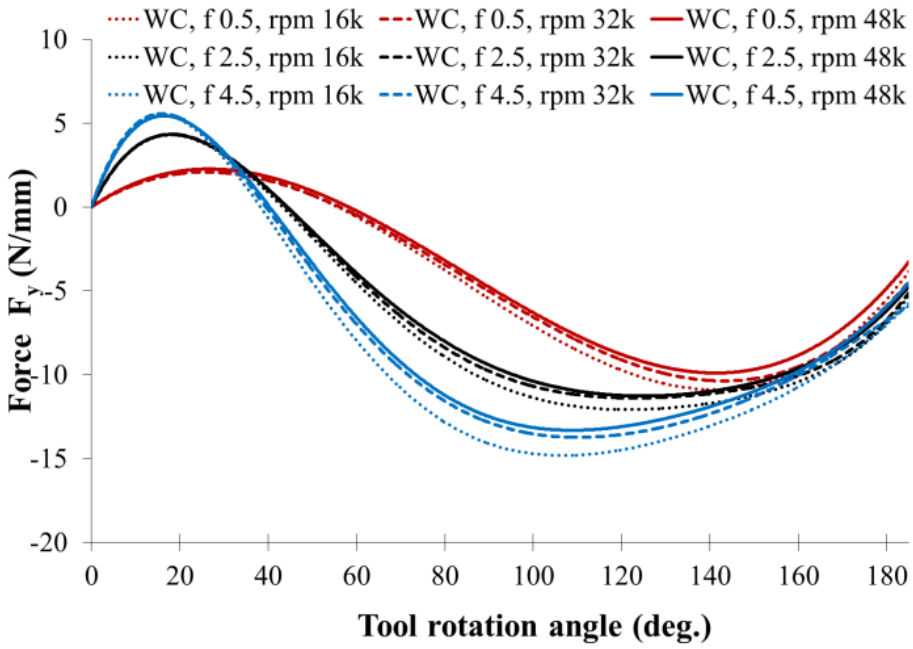

(b)

Figure 6.9: Cutting forces during single pass: (a) F_x, (b) F_y.

Table 6.2: The coefficients of differential force components dF_x.

Ω (krpm)	f_z (µm/tooth)	$dF_x(\phi)$ (N/mm)					
		a_1	a_2	a_3	a_4	a_5	a_6
16	0.5	-1.768E-2	-4.173E-3	6.145E-5	-4.004E-7	2.085E-9	-5.523E-12
16	2.5	-5.296E-2	-1.705E-2	4.446E-4	-4.404E-6	2.015E-8	-3.552E-11
16	4.5	-3.215E-1	-8.340E-3	3.280E-4	-3.540E-6	1.673E-8	-3.004E-11
32	0.5	5.037E-2	-7.977E-3	1.403E-4	-1.144E-6	5.305E-9	-1.072E-11
32	2.5	-9.865E-2	-1.371E-2	3.730E-4	-3.721E-6	1.706E-8	-3.012E-11
32	4.5	-4.158E-1	-1.047E-3	1.546E-4	-1.743E-6	8.150E-9	-1.461E-11
48	0.5	-6.388E-2	-8.567E-4	-1.257E-5	3.490E-7	-1.518E-9	1.115E-12
48	2.5	-6.942E-2	-1.521E-2	4.060E-4	-4.076E-6	1.887E-8	-3.362E-11
48	4.5	-3.705E-1	-3.757E-3	2.207E-4	-2.481E-6	1.189E-8	-2.162E-11

Table 6.3: The coefficients of differential force components dF_y.

Ω (krpm)	f_z (µm/tooth)	$dF_y(\phi)$ (N/mm)					
		a_1	a_2	a_3	a_4	a_5	a_6
16	0.5	1.555E-1	-1.174E-3	-7.800E-5	1.207E-6	-6.724E-9	1.359E-11
16	2.5	5.377E-1	-2.033E-2	2.235E-4	-1.000E-6	1.318E-9	1.548E-12
16	4.5	8.039E-1	-3.590E-2	4.998E-4	-3.275E-6	1.045E-8	-1.296E-11
32	0.5	1.155E-1	2.409E-3	-1.761E-4	2.370E-6	-1.288E-8	2.552E-11
32	2.5	5.407E-1	-2.042E-2	2.281E-4	-1.050E-6	1.501E-9	1.352E-12
32	4.5	8.026E-1	-3.584E-2	5.164E-4	-3.595E-6	1.251E-8	-1.738E-11
48	0.5	1.807E-1	-2.733E-3	-4.885E-5	1.036E-6	-6.623E-9	1.470E-11
48	2.5	5.463E-1	-2.119E-2	2.568E-4	-1.436E-6	3.675E-9	-2.996E-12
48	4.5	7.575E-1	-3.249E-2	4.387E-4	-2.772E-6	8.426E-9	-9.695E-12

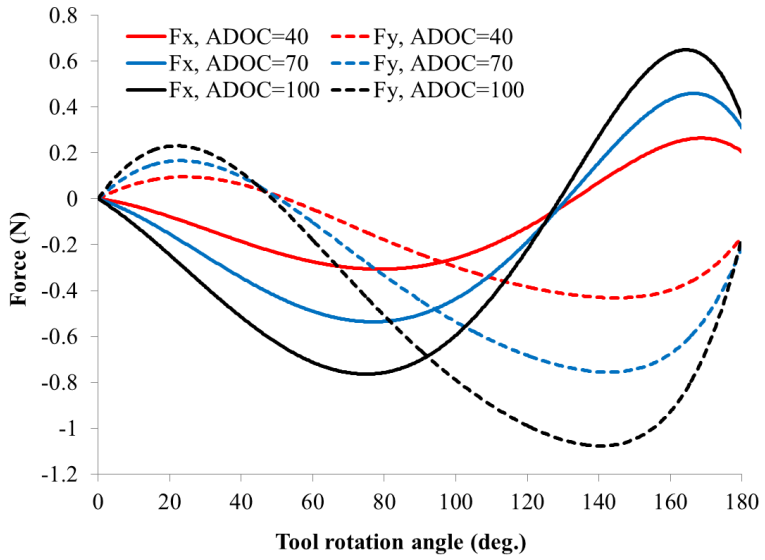

Figure 6.10: Predicted cutting force (Ω = 16 krpm, f_z=0.5 µm/tooth).

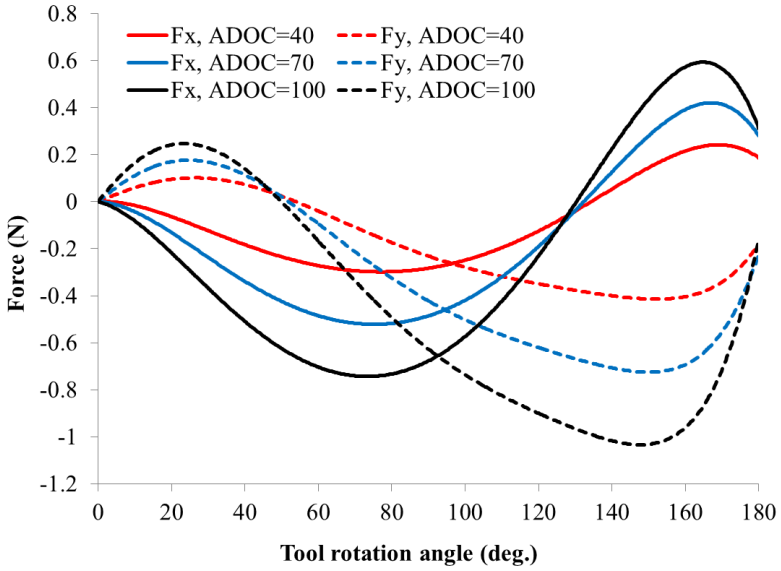

Figure 6.11: Predicted cutting force (Ω = 32 krpm, f_z=0.5 µm/tooth).

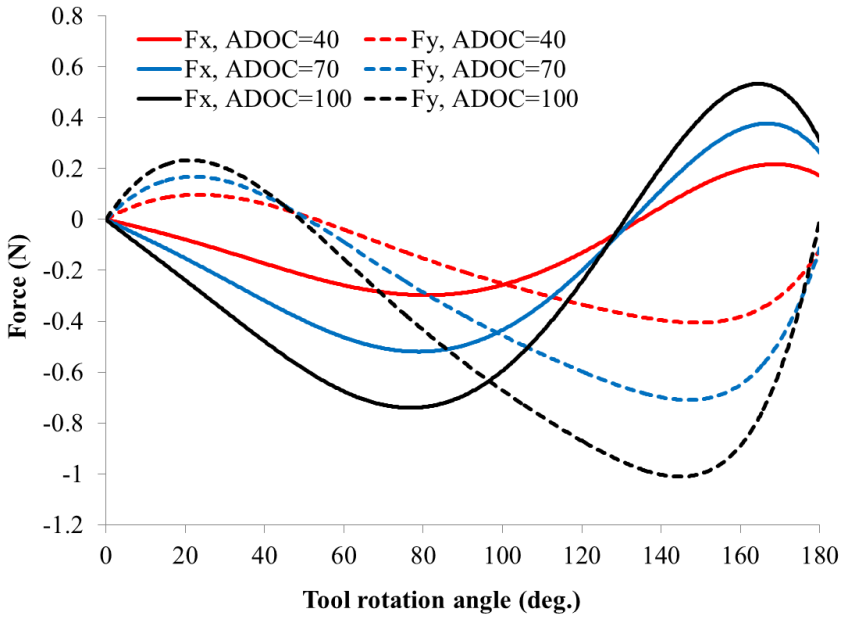

Figure 6.12: Predicted cutting force (Ω = 48 krpm, f_z=0.5 µm/tooth).

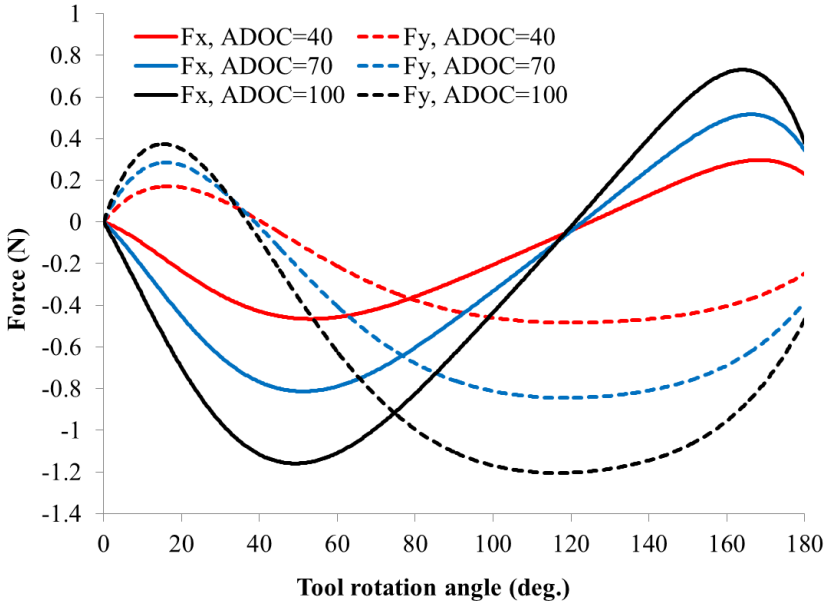

Figure 6.13: Predicted cutting force (Ω = 16 krpm, f_z=2.5 µm/tooth).

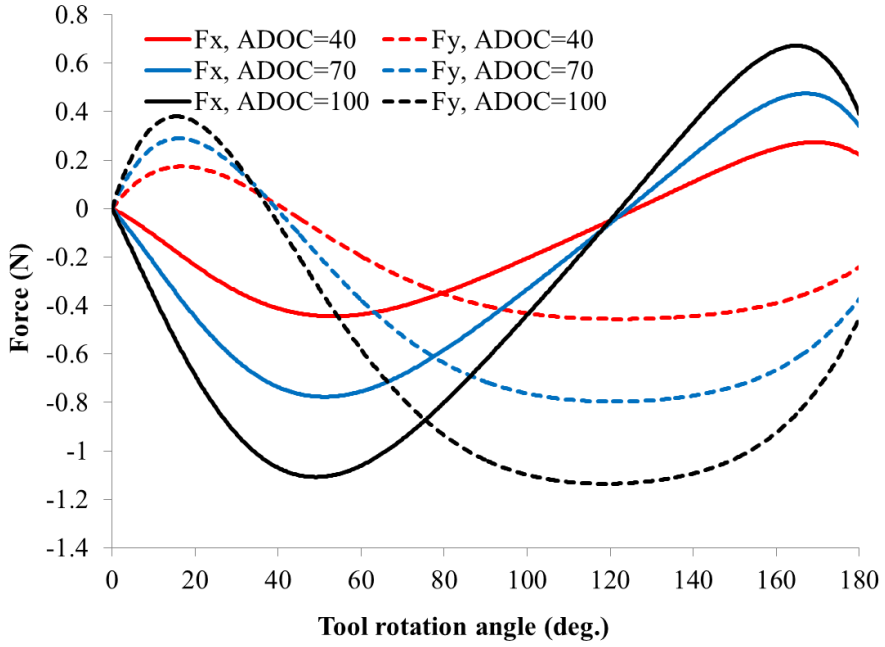

Figure 6.14: Predicted cutting force (Ω = 32 krpm, f_z=2.5 µm/tooth).

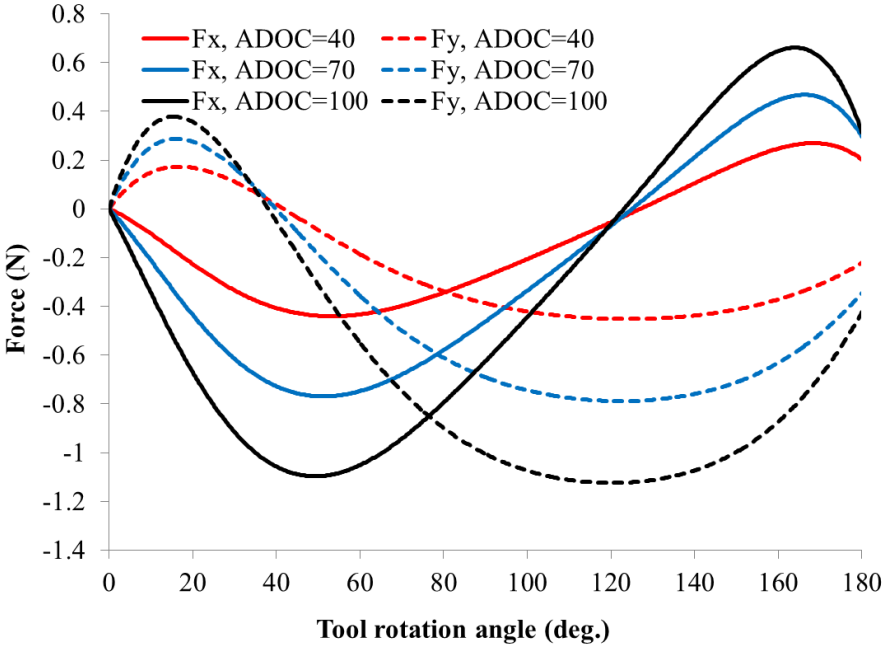

Figure 6.15: Predicted cutting force (Ω = 48 krpm, f_z=2.5 µm/tooth).

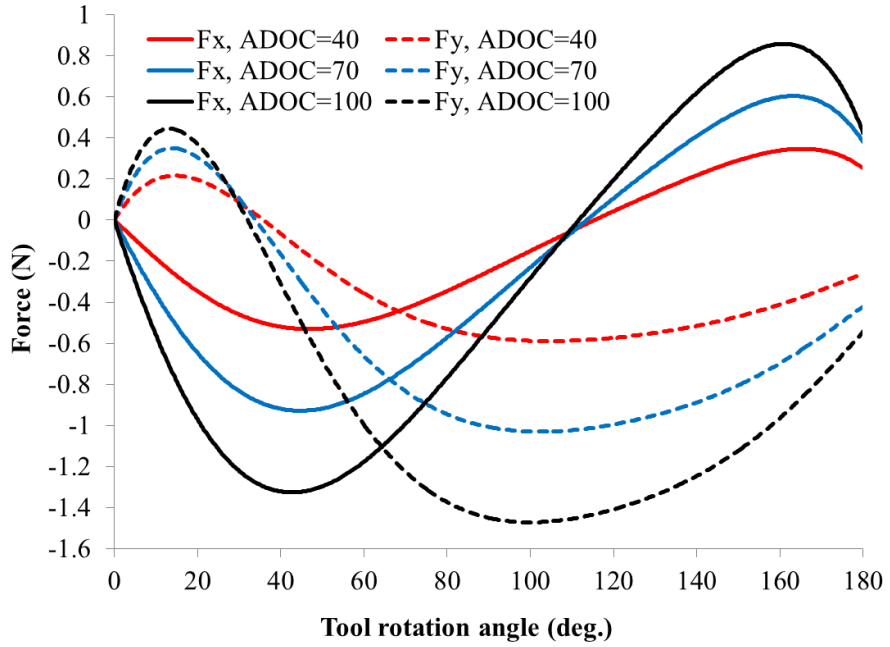

Figure 6.16: Predicted cutting force (Ω = 16 krpm, f_z=4.5 µm/tooth).

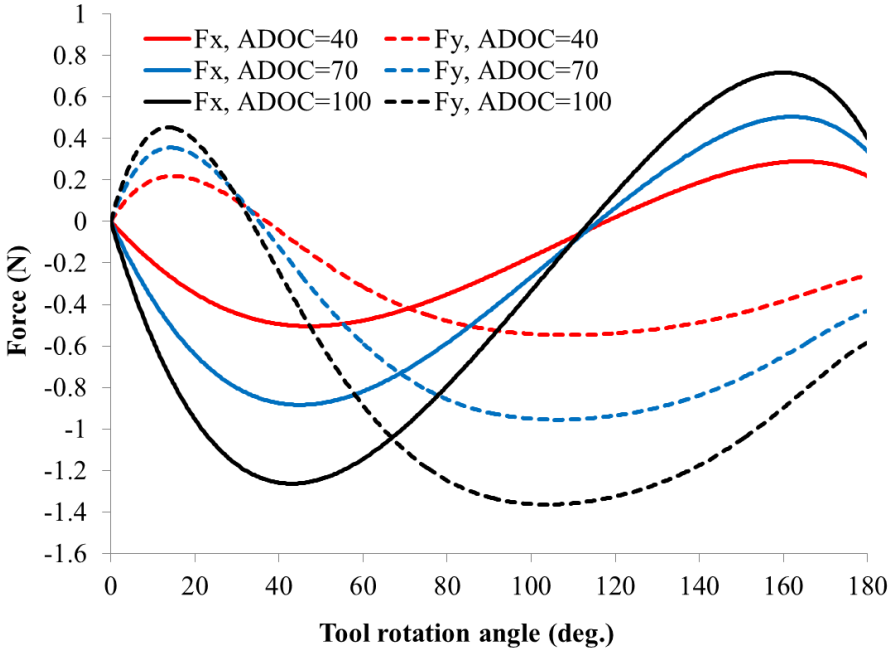

Figure 6.17: Predicted cutting force (Ω = 32 krpm, f_z=4.5 µm/tooth).

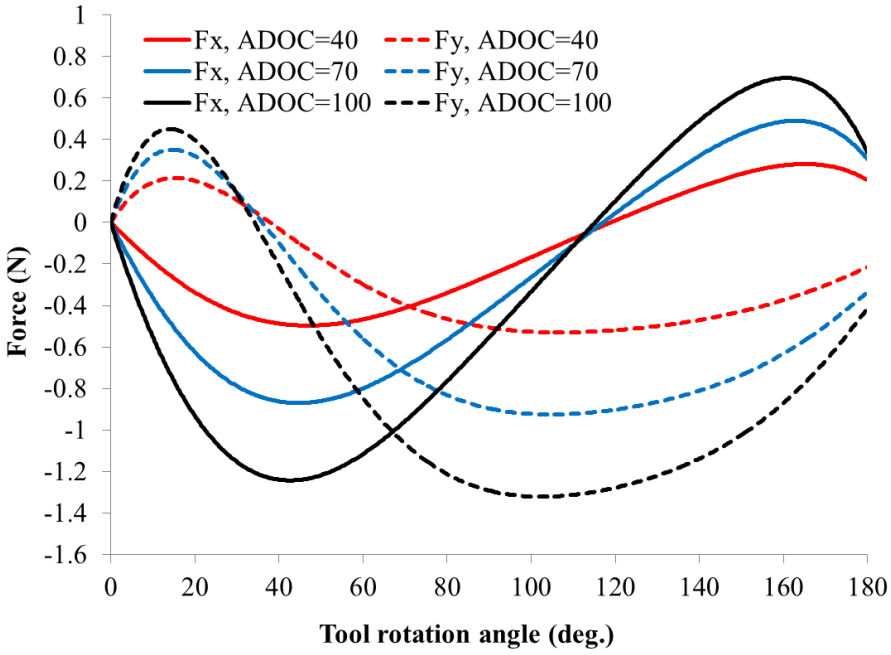

Figure 6.18: Predicted cutting force (Ω = 48 krpm, f_z=4.5 µm/tooth).

Based on the data in Table 6.4, second order RSM models for the maximum cutting forces can be formulated as shown in Eqs. (6.13) and (6.14), where $F_{x_{max}}$ is the maximum cutting force in X direction and $F_{y_{max}}$is the maximum cutting force in Y direction. The significant testing of each term is shown in Tables 6.5 and 6.6.

$$F_{x_{max}} = - 0.027895 - 0.001235\Omega + 0.097579f_z + 0.007191 - 0.019396f_z^{\,2} + 0.001304f_z a_p \qquad \text{Eq. (6.13)}$$

$$F_{y_{max}} = 0.057803 - 0.002956\Omega - 0.037856f_z + 0.010719a_p + 0.000064\Omega^2 + 0.010474f_z^{\,2} - 0.000462\,\Omega f_z - 0.000031\,\Omega a_p + 0.000889f_z a_p \qquad \text{Eq. (6.14)}$$

Table 6.4: Maximum cutting forces predicted for each cutting condition.

Ω (krpm)	f_z (µm/tooth)	a_p (µm)	$F_{x_{max}}$ (N)	$F_{y_{max}}$ (N)
16	0.5	40	0.307	0.431
		70	0.536	0.754
		100	0.764	1.075
	2.5	40	0.466	0.483
		70	0.814	0.846
		100	1.159	1.207
	4.5	40	0.531	0.592
		70	0.928	1.036
		100	1.321	1.479
32	0.5	40	0.298	0.414
		70	0.521	0.724
		100	0.743	1.032
	2.5	40	0.445	0.455
		70	0.778	0.797
		100	1.108	1.138
	4.5	40	0.506	0.549
		70	0.883	0.961
		100	1.259	1.371
48	0.5	40	0.297	0.405
		70	0.519	0.708
		100	0.740	1.009
	2.5	40	0.441	0.450
		70	0.770	0.788
		100	1.097	1.125
	4.5	40	0.497	0.532
		70	0.869	0.931
		100	1.239	1.329

Table 6.5: The RSM model for $F_{x_{max}}$

Term	Coef	SE Coef	T-value	P-value
Constant	-0.02789	0.02344	-1.19	0.247
Ω (krpm)	-0.00123	0.000283	-4.367	0
f_z (µm/tooth)	0.09757	0.011953	8.164	0
a_p (µm)	0.00719	0.000276	26.076	0
f_z*f_z	-0.01939	0.001959	-9.9	0
f_z*a_p	0.00130	0.000092	14.118	0
R^2 (adj)	99.62%			

Table 6.6: The RSM model for $F_{y_{max}}$

Term	Coef	SE Coef	T-value	P-value
Constant	0.05780	0.02773	2.085	0.052
Ω (krpm)	-0.00295	0.001322	-2.235	0.038
f_z (µm/tooth)	-0.03785	0.007987	-4.74	0
a_p (µm)	0.01071	0.000279	38.357	0
Ω * Ω	0.00006	0.000019	3.47	0.003
f_z*f_z	0.01047	0.001188	8.819	0
Ω *f_z	-0.00046	0.000105	-4.407	0
Ω *a_p	-0.00003	0.000007	-4.437	0
f_z*a_p	0.00088	0.000056	15.872	0
R^2 (adj)	99.87%			

6. A Machining Case Study

In order to test the usefulness of the developed decision support system, a case study in micro-end milling of titanium alloy was designed. The feature is a set of circular thin ribs in a block of Ti-6Al-4V as shown in Figure 6.19. The rib thickness is 75 µm with the height of 500 µm. The toolpath strategy is a counterclockwise circular z-level as illustrated in Figure 6.19. The tools were the same as the previous experiments, two flute micro-end mills with a diameter of $Ø$=508 µm and a cutting length of l_c=762 µm from the same manufacturer. To complete a single z-level for this feature, the toolpath requires a cutting distance of $2\pi\sum_{n=0}^{7}(0.246 + 0.583n)$ =114.932 mm. Thus, for multi-pass z-levels, the toolpath would require a cutting distance of $114.932 \times \left\lceil\frac{500}{a_p}\right\rceil$, where a_p is axial depth of cut (µm).

7. Process Parameters Selection and Optimization

In this study, an effective, systematic approach based on mathematical modeling and multi-objective optimization method was proposed for selection of process parameters. So far, all of the models have been readily developed. The next step is to

utilize the multi-objective optimization method to obtain the optimal solution sets. In this study, the Multi-Objective Particle Swarm Optimization (MOPSO) was selected as a preferred method, since it has many advantages over other optimization methods. It works very efficiently to locate the Pareto front of the multi-objective optimization problems. Also it is relatively easy to implement and has a few parameters to adjust. The details of MOPSO have been explained in Chapter 2.

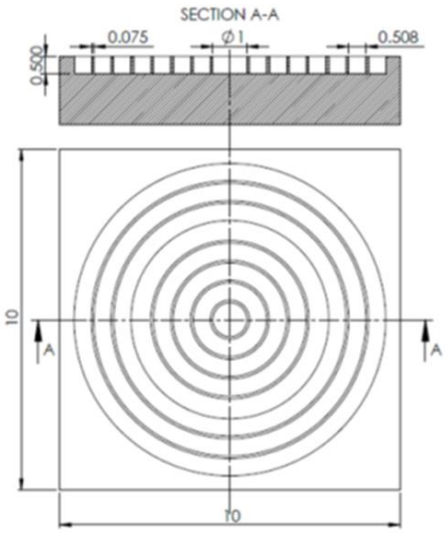

All units are in mm

(a)

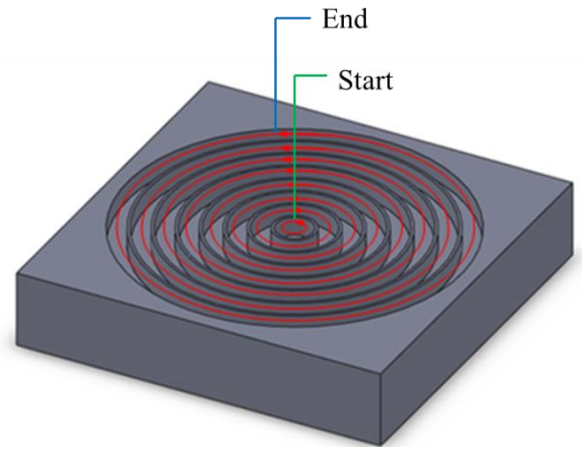

(b)

Figure 6.19: (a) The micro-end milling geometry and (b) the toolpath tested.

7.1 Unconstrained multi-objective optimization

The optimization of the micro-end milling process parameters can be formulated as an unconstrained bi-objective minimization problem as shown in Eq. (6.15), where G_1 and G_2 are objective functions which are the average surface roughness model (Eq. 6.1), and the top-burr width model (Eq. 6.2) respectively. In this problem, the solution space was limited by the range of parameters that construct the models.

$$Min\ [G_1(\Omega, f_z, a_p), G_2(\Omega, f_z, a_p)] \qquad \text{Eq. (6.15)}$$

After implementing the MOPSO algorithm to minimize the top-burr width and average surface roughness as shown in Eq. (6.15). The results are shown in Figure 6.20. Based on the results, the strong trade-off can be identified which imply that both objectives cannot be achieved simultaneously. Since, there exists a trade-off between surface roughness and burr formation, a sacrifice has to be made. In this study, the burr-free micro-machining is considered more important than the quality of the surface, therefore the process parameters which minimize the burr formation were selected. In this case, Ω = 48 krpm, f_z=4.2 µm/tooth, and a_p = 100 µm were chosen as the optimum process parameters.

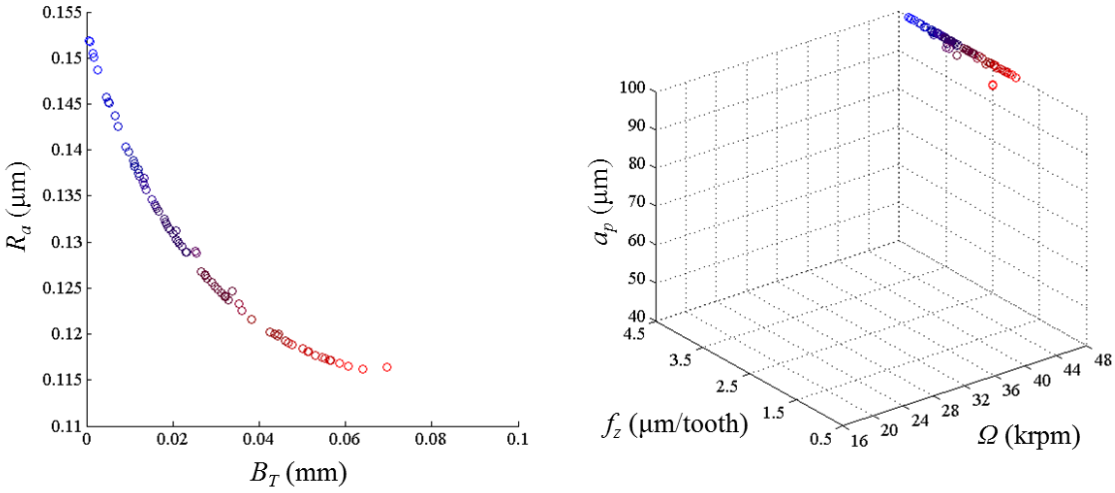

Figure 6.20: MOPSO results: (left) objective function space, (right) decision variable space.

The validation test has been conducted; the result is shown in Figure 6.21. The circular thin ribs were successfully fabricated; however, the feature is full of burrs which made it totally unacceptable. Based on the model and optimization, burr formation was supposed to be at the minimum level but the micro-machining test showed otherwise. The causes may be contributed to the fact that the process constraints such as cutting forces and tool life were not considered during the optimization process.

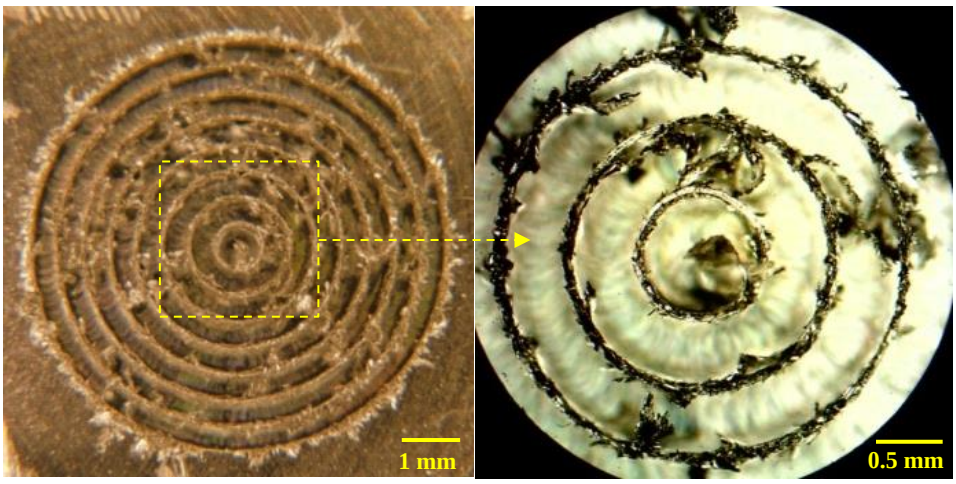

Figure 6.21: The machining result obtained from MOPSO solution.

7.2 Multi-objective optimization using weighted sum method

Since the cutting distance of the tested feature is relatively long, tool wear can have a significant impact on the machining performance. The use of unconstrained multi-objective optimization approach to locate the suitable process parameters may not be satisfactory, since tool wear was not included in the consideration. Therefore, in this approach, tool wear was included as one of the objective functions.

By setting tool wear as one of the objective functions in the unconstrained bi-objective optimization, the optimal solution set can be found as shown in Figures 6.22 and 6.23. In both figures, it can be seen that there was a trade-off between average surface roughness and tool wear depth as well as a trade-off between top-burr formation and tool wear depth. This implies that the set of process parameters which minimize tool wear would result in low performance in terms of surface roughness and top-burr formation. Also, the set of process parameters which minimize tool wear would lead to low productivity.

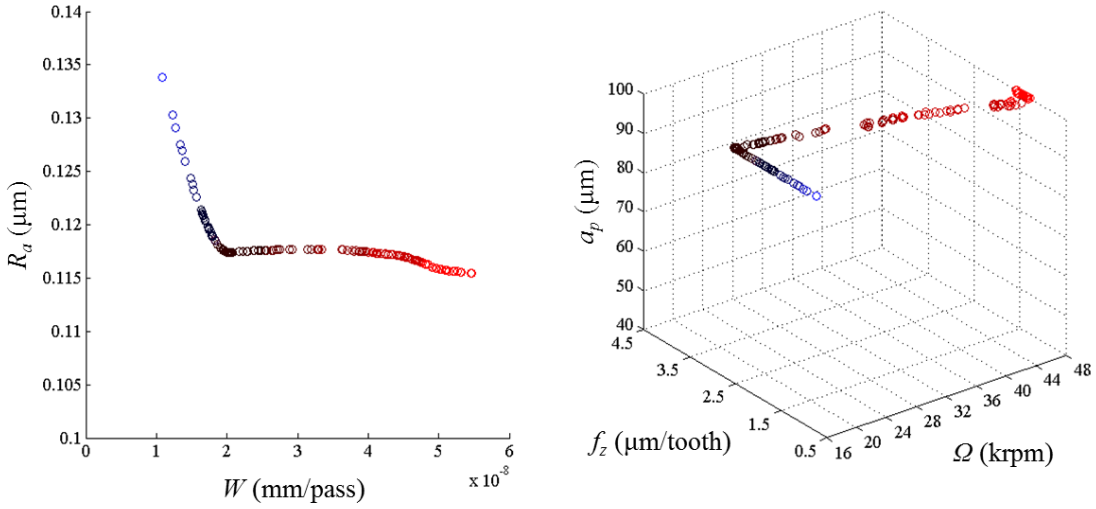

Figure 6.22: Optimal solution for minimization of average surface roughness and tool wear depth: (left) objective function space, (right) decision variable space.

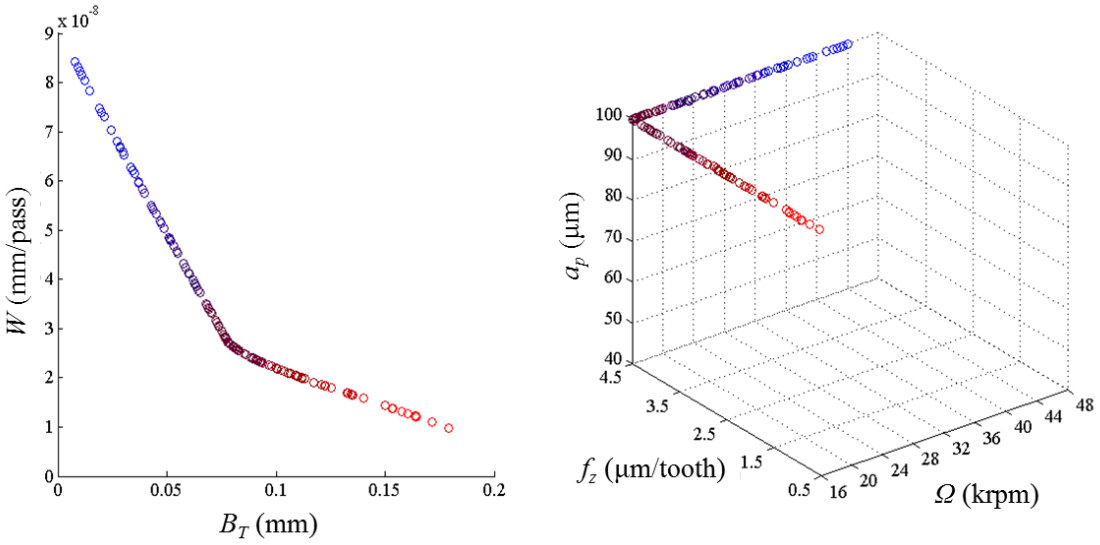

Figure 6.23: Optimal solution for minimization of total top-burr width and tool wear depth: (left) objective function space, (right) decision variable space.

In order to include tool wear into the consideration, the weighted sum method was utilized. The approach was to combine two objective functions into one objective function using weighted sum method. In this case, the average surface roughness model and tool wear depth model were selected due to its low trade-off (see Figure 6.22). The bi-objective minimization problem with weighted sum objective function can be formulated as follow;

$$Min\ [G_1(\Omega, f_z, a_p), G_2(\Omega, f_z, a_p)] \qquad \text{Eq. (6.16)}$$

where G_1 is total top-burr width model (Eq. 6.2), and G_2 is a weighted sum objective function of average surface roughness and tool wear depth

$$G_2 = 0.5\,\theta_1\,W + 0.5\,\theta_2\,R_a \qquad \text{Eq. (6.17)}$$

where $\theta_i = \frac{1}{Z_i^N - Z_i^U}$ is normalization factor, Z_i^U is Utopia point, Z_i^N is Nadir point, R_a is average surface roughness model (Eq. 6.1) and W is tool wear depth model (Eq. 6.7)

The result of MOPSO with weighted sum objective is shown in Figure 6.24. The strong trade-off between top-burr formation and weighted sum function of surface roughness and tool wear depth can be observed.

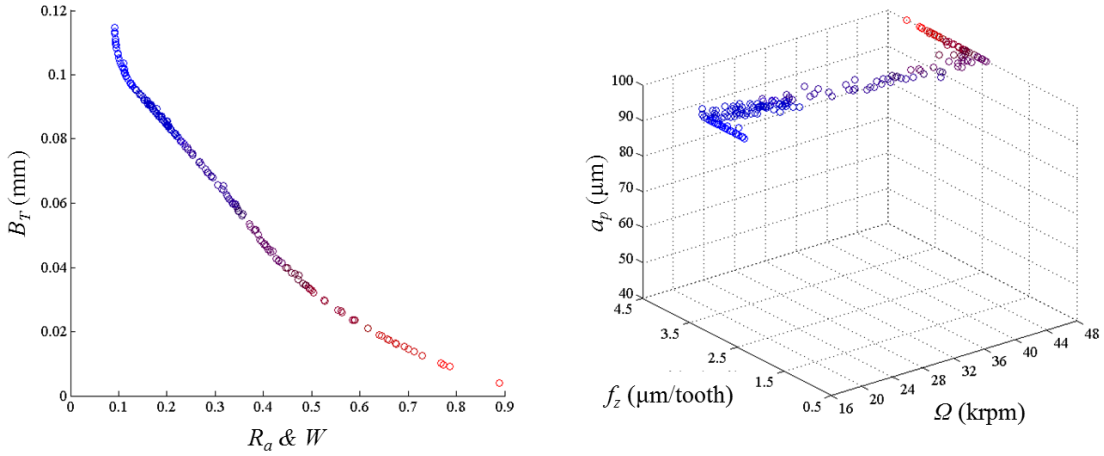

Figure 6.24: MOPSO with weighted sum objective: (left) objective function space, (right) decision variable space.

Based on the MOPSO result, the set of process parameters which balance all the objective functions was selected for the verification test. In this case, Ω = 32 krpm, f_z=3 µm/tooth, and a_p = 100 µm were chosen. The machining test result is shown in Figure 6.25. It can be seen that the quality of the machined feature is not as good as expected; top-burr formation is still severe.

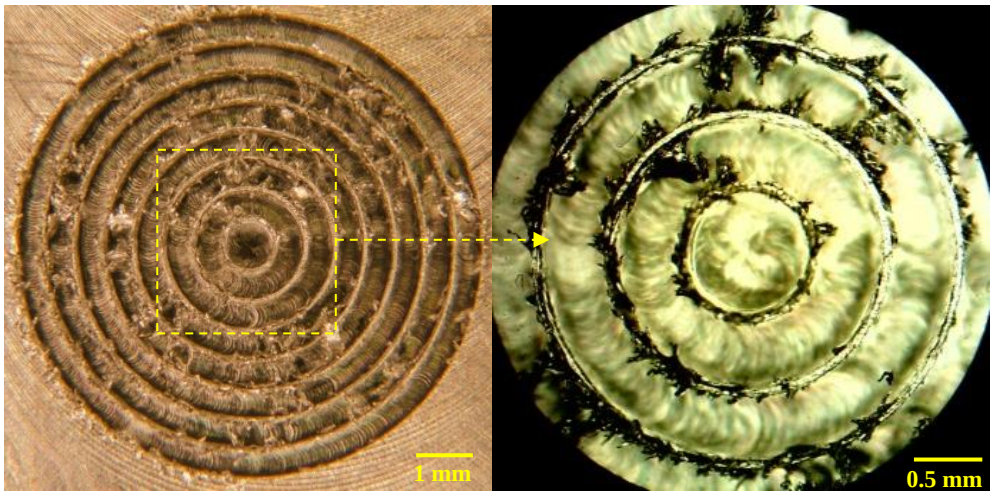

Figure 6.25: The validation test result obtained from MOPSO with weighted sum objective function approach.

7.3 Constrained multi-objective optimization

Based on the previous experiment, it can be hypothesized that tool life and cutting forces may play a very important role in machining performance of Ti-6Al-4V. Therefore, the next approach aimed to include both cutting forces and tool life into consideration, thus the Constrained Multi-Objective Particle Swarm Optimization (CMOPSO) was implemented. The problem was formulated as shown in Eq. (6.18).

$$
\begin{aligned}
Min \quad & [G_1(\Omega, f_z, a_p), G_2(\Omega, f_z, a_p)] \\
\text{s.t.} \quad & L(\Omega, f_z) \geq L_{req} \\
& F_{x_{max}}(\Omega, f_z, a_p) \leq F_{x_{\max\_allow}} \\
& F_{y_{max}}(\Omega, f_z, a_p) \leq F_{y_{\max\_allow}}
\end{aligned}
\qquad \text{Eq. (6.18)}
$$

G_1 and G_2 are the same objective functions as before, L is the maximum linear cutting distance model (Eq. 6.8), $F_{x_{max}}$ and $F_{y_{max}}$ are the maximum cutting forces in X and Y directions (Eq. 6.13 and 6.14). L_{req} is the required cutting distance which is equal

to $114.932 \times \left\lceil \frac{500}{a_p} \right\rceil$, $F_{x_{\max\_allow}}$ and $F_{y_{\max\_allow}}$ are the maximum allowable cutting forces in X and Y directions which were set at 1.3 N.

In this study, the penalty function method was selected to handle the constraints. Thus, the reformulation of the objective functions can be written as shown in Eqs. (6.19) and (6.20), where p_1, p_2 , and p_3 are the penalty values.

$$G_1' = G_1 + p_1(L_{req} - L) + p_2(F_{x_{max}} - F_{x_{\max\_allow}}) + p_3(F_{y_{max}} - F_{y_{\max\_allow}})$$

Eq. (6.19)

$$G_2' = G_2 + p_1(L_{req} - L) + p_2(F_{x_{max}} - F_{x_{\max\_allow}}) + p_3(F_{y_{max}} - F_{y_{\max\_allow}})$$

Eq. (6.20)

After reformulating the objective function, the problem can be solved as an unconstraint multi-optimization problem as shown in Eq. (6.21). The results are shown in Figure 6.26.

$$Min\ [G_1'(\Omega, f_z, a_p), G_2'(\Omega, f_z, a_p)] \qquad \text{Eq. (6.21)}$$

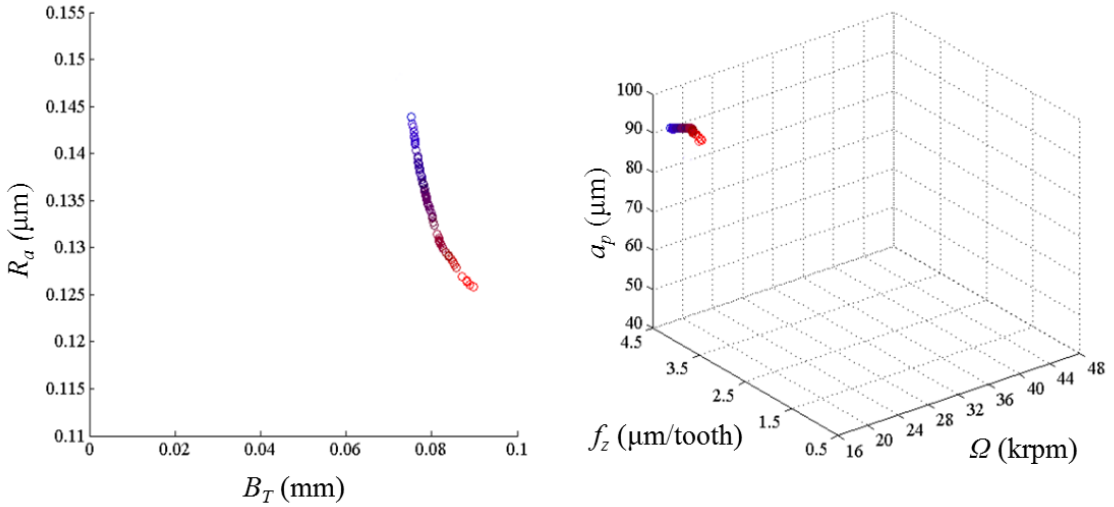

Figure 6.26: CMOPSO results: (left) objective function space, (right) decision variable space.

The results from CMOPSO are clearly different from the previous results of the unconstrained MOPSO. This indicates the effect of the constraints to this optimization problem. By picking the solution where burr formation is minimized (Ω = 16 krpm, f_z=4.2 µm/tooth and a_p = 90 µm), hence as a result, the validation test result shows significant improvement in terms of top-burr formation as shown in Figure 6.27.

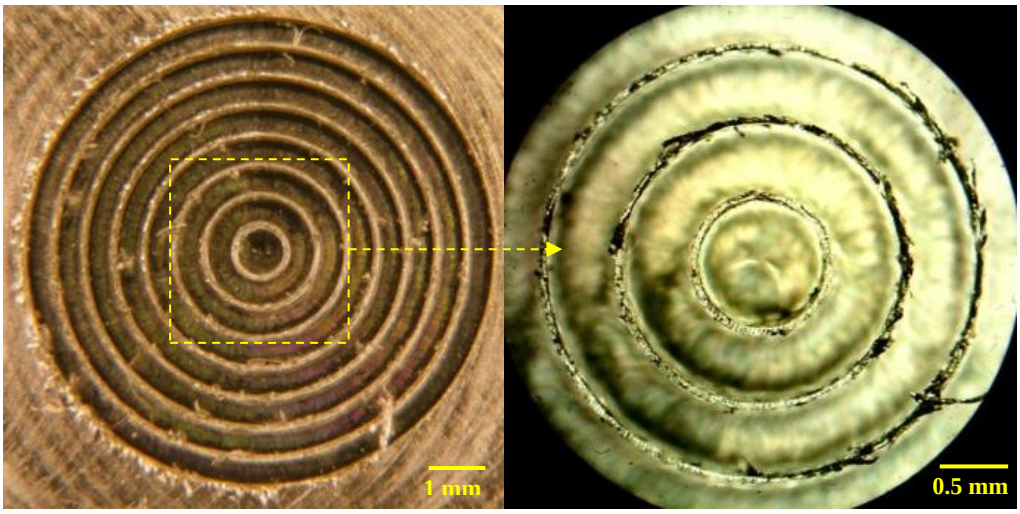

Figure 6.27: The validation test result obtained from CMOPSO solution.

7.4 Adaptive multi-objective optimization approach

In practice, one of the machining strategies is to adjust the process parameters according to the tool engagement. In this tested feature, there are two differences in tool engagement. First one is at the first z-level where the tool is on the surface of the feature. Second one is at the consecutive z-level where the tool goes deeper into the channel. The different in tool engagement may result in the different chip flow which may consequently affects burr formation. Thus, in this approach, different sets of process parameters were assigned to the different tool engagement. The sets of process parameters were taken from the previous optimization results.

At the first z-level, the process parameters were set at Ω = 48 krpm, f_z=4.2 µm/tooth and a_p = 100 µm (see Figure 6.20). The aim was to minimize top-burr formation. At the consecutive z-levels the process parameters were set at Ω = 16 krpm, f_z=4.2 µm/tooth and a_p = 90 µm (see Figure 6.26). For this setting, the aim was to minimize burr formation while maintaining cutting forces and tool life to be within the limits. The validation test result is shown in Figure 6.28. It can be seen that the result of this approach was not better than the result from the CMOPSO approach.

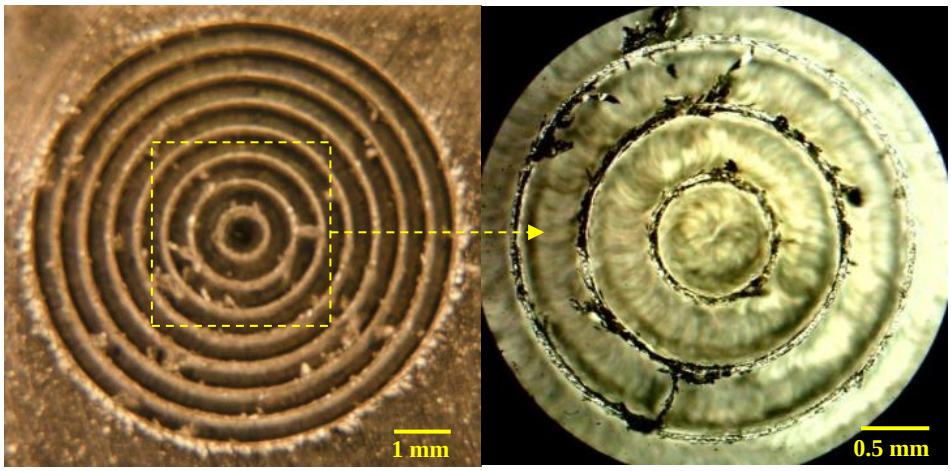

Figure 6.28: The validation test result obtained from adaptive approach.

8. Discussions

Four optimization approaches were performed in order to locate the optimum process parameters. The machining tests were conducted to validate the selected process parameters which aim to minimize top-burr formation. Table 6.7 summarizes the experiments in this study, showing the approach and its selected process parameters. Approximated top-burr widths were taken from the machined features in order to compare the performance of each approach.

Table 6.7: Results of the optimization studies.

Approach	Selected process parameters	Top-burr width
Unconstrained Multi-Objective Optimization	Ω = 48 krpm, f_z=4.2 µm/tooth, a_p = 100 µm	<0.5 mm
Multi-Objective Optimization Using Weighted-Sum Method	Ω = 32 krpm, f_z=3 µm/tooth, a_p = 100 µm	< 0.5 mm
Constrained Multi-Objective Optimization	Ω = 16 krpm, f_z=4.2 µm/tooth, a_p = 90 µm	< 0.2 mm
Adaptive Multi-Objective Optimization	First z-level: Ω = 48 krpm, f_z=4.2 µm/tooth, a_p = 100 µm. Consecutive z-levels: Ω = 16 krpm, f_z=4.2 µm/tooth, a_p = 90 µm	< 0.3 mm

This study points out the necessity of considering the machining constraints such as maximum cutting force and maximum tool life in the process optimization. It shows that neglecting these constraints can lead to a totally wrong decision causing a poor micro-machining process performance. Besides cutting forces and tool life that were included in this study, estimated cutting temperature is another promising constraint that should be included to improve the machining performance.

The Constrained Multi-Objective Particle Swarm Optimization (CMOPSO) implemented in this study has proven that it is capable of locating the Pareto frontier which is a set of optimal solutions. Making a decision based on this set of solutions can theoretically assure the best possible micro-machining outcome. However, it should be noted that the data that is used to construct the models came from the experiments and FE simulations of a simple shallow slot milling while the implemented feature is a more complicated circular thin rib. The justification behind this is that the utilization of data

from experimentation and simulation of a simple feature is more practical and cost effective.

Comparing the micro-machining results from all four cases, a significant level of burr formation can be observed. In Figures 6.21 and 6.25, burrs are severely formed all over the feature indicating a poor micro-machining performance contributed from the set of process parameters. Therefore, by just selecting the proper process parameters, the micro-machining performance can be enhanced and resultant burr formation is significantly reduced (see Figures 6.27 and 6.28). Nevertheless, the ultimate goal of burr-free micro-machining still has not been achieved. A small degree of burrs is still formed throughout the machined feature (see Figure 6.27). It seems like a burr-free micro-end milling of Ti-6Al-4V may require more than just the optimal process parameters. An improvement in micro-end mill geometry, especially selection of a different helix angle may be necessary. Also, the use of coolant or lubricant may be beneficial.

9. Conclusions

This study has proven the usefulness of having a physics-based support system for decision making in such a difficult micro-manufacturing process, micro-end milling of Ti-6Al-4V alloys. The proposed decision support system based on CMOPSO can successfully guide the user to select the optimal combination of process parameters based on the process requirements and constraints.

This study also shows that FE simulations can be used as a supplement or an alternative to the experiments reducing cost and time for data acquisition in the process optimization. In addition, FE-based simulations are continuously benefiting from the

advances in computer and software technology, making them more and more attractive for process design and optimization.

Based on the micro-machining test, optimal process parameters can assure only a certain level of process performance. In order to make further improvements, other factors such as design of new tool geometry and application of lubrication should be considered as well.

CHAPTER 7

MICRO-END MILLING APPLICATIONS AND TOOLPATH STRATEGIES

1. Introduction

The use of products with micrometer sized components has been rapidly increasing during the last several decades. Miniaturization is now becoming a standard requirement for most product designs in response to the demand in higher mobility, power conservation, accessibility, and cost reduction in many advanced technology products. Examples of these products include electronic devices, sensors, and medical devices.

Precision fabrication of micro features using mechanical micro-machining is very challenging. It requires a lot more than just high precision machine tools and equipment. The machining strategies such as toolpath design, parameter setting, and tool selection are also very important for successful fabrication of micro features. Unfortunately, machining strategies developed specifically for mechanical micro-machining are still very limited. The user still relies on the techniques and strategies used in mechanical macro-machining which sometimes does not work well for the mechanical micro-machining due to several factors discussed earlier.

In the previous chapters, several investigations on the micro-end milling process have been presented; the aim was to optimize and understand the influence of process parameters. The machining experiment was only limited to the simple slot feature due to ease of machining and data collection. Similarly, many investigations conducted by other researcher also limited in their studies to simple geometrical features such as straight

slots, channels, grooves or plane and simple surfaces (Aramcharoen & Mativenga 2009, Bissacco et al. 2005, Chern et al. 2007, Ko & Dornfeld 1991, Liu et al. 2006, Rahman et al. 2001, Saptaji et al. 2012, Schueler et al. 2010, Vogler et al. 2005). Moreover, the investigation of micro-milling strategies is hardly found in the literature. Therefore, this chapter will be designated to the discussion of developing machining strategies for fabrication of different micro-features in different workpiece materials.

2. Review of Micro-End Milling Applications and Toolpath Strategies

Similar to macro-machining, one very important application of micro-machining is the machining of dies and molds. The small scale of micro-machining allows the precision machining of micro-dies and molds to be realized. Bissacco et al. (Bissacco et al. 2005) have presented the possibility of using micro-end milling process applied to the manufacturing of micro-injection molding mold cavities in hardened tool steel. Fleischer and Kotschenreuther (Fleischer and Kotschenreuther 2007) fabricated a micro-mold for planetary gear wheel components. They have reported the achievable tolerances to be ±2 µm to ±5 µm depending on the material-tool-machine-process combination. Suzuki et al. (Suzuki et al. 2007) developed a technique for machining micro aspheric molds and dies made of ceramics. They develop a special micro-milling tool made of polycrystalline diamond (PCD). Some micro aspheric molding dies made of binderless tungsten carbide were cut with the developed PCD milling tool in the ductile mode. The form accuracies of the micro aspherical mold and the micro lens array mold obtained were less than 100 nm P-V and the surface roughness of 15 nm R_z. Özel and Liu (Özel and Liu 2009) have developed the process planning for micro-end milling of mold cavities in aluminum. In their study, the process parameters for machining micro-pocket such as axial depth of cut

and feed per tooth were studied extensively. These results provide a decision support system for selecting process parameters for rough and finish machining of square pocket micro-mold cavities.

An application of micro-end milling which has been extensively studied is the machining of high aspect ratio thin walls and columns. Several studies concerning thin wall and column milling can be found in literature. Unfortunately, only a few of them focuses on finding the best machining condition to obtain good quality features; most of them simply show the capability to machine very challenging high aspect ratio walls or columns.

Friedrich & Vasile (Friedrich & Vasile 1996) and Friedrich et al. (Friedrich et al. 1997) have demonstrated the usefulness of the micro-end milling process by micro-machining a pattern of exponential spirals with straight radial trench on PMMA (polymethyl methacrylate). They have achieved such thin walls with the minimum thickness of 8 µm and the depth of 62 µm (aspect ratio of almost 8). However, the authors did not point out the relationship between process parameters and workpiece quality.

Bang et al. (Bang et al. 2005) have tested a self-made PC-based 5-axis micro-milling machine. To validate their design, the authors machined several features such as thin walls, high aspect ratio pins, micro impellers and micro blades as shown in Figure 7.1. They succeeded in milling 25 µm x 650 µm walls (corresponding to an aspect ratio of 26) on brass. However, there was no different process parameter set that was investigated and no quality measurements were performed.

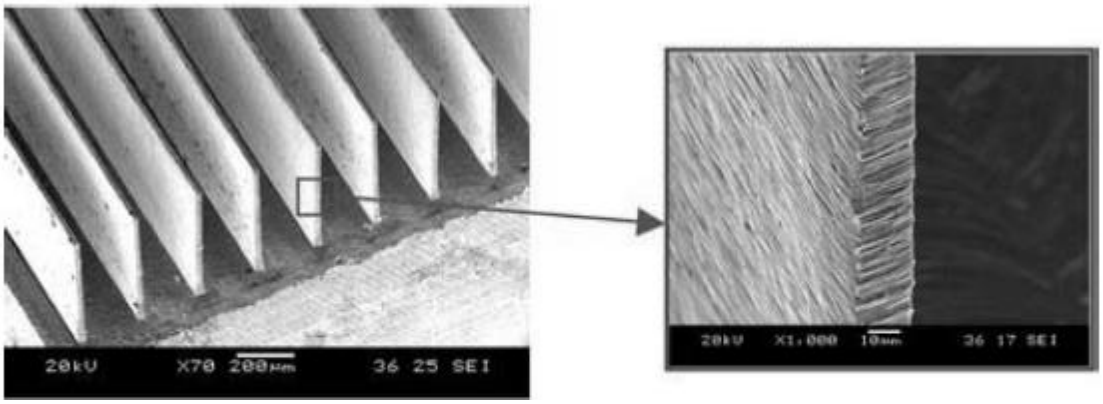

Figure 7.1: Micro walls (workpiece material: brass, carbide flat micro-end mill of 200 µm diameter, a spindle speed of 25000 rpm, a cutting depth of 5 µm, and a feed rate of 1 mm/s) machined by Bang et al. (Bang et al. 2005).

Chern et al. (Chern et al. 2007) machined micro thin-walled structures with a thickness of 80, 31 and 5 µm, and a height of 60 µm. A self-fabricated micro-tool was used. It was found that there exists severe deformations on the 5 µm wall which may be caused by some unexpected vibrations occurred and/or lateral bending occurred by cutting forces during micro-machining. However, the micro-machining result of the other two samples was successful (see Figure 7.2).

Li et al. (Li et al. 2010) reported a successful micro-milling of 15 µm thick and 800 µm high micro thin walls (aspect ratio of 54) on Böhler M261 mold steel (see Figure 7.3). Their work is devoted to study the challenges in micro-milling thin walls with high aspect ratio and takes into account the effect on the wall surface of different cutting parameters, milling strategies and tool paths. Finite Element Analysis was used to predict the tool path effect on the machined thin wall flatness. The authors also investigated the

relationship between machining parameters (namely feed per tooth, depth of cut, and width of cut) and cutting forces by means of an analytical cutting force prediction model.

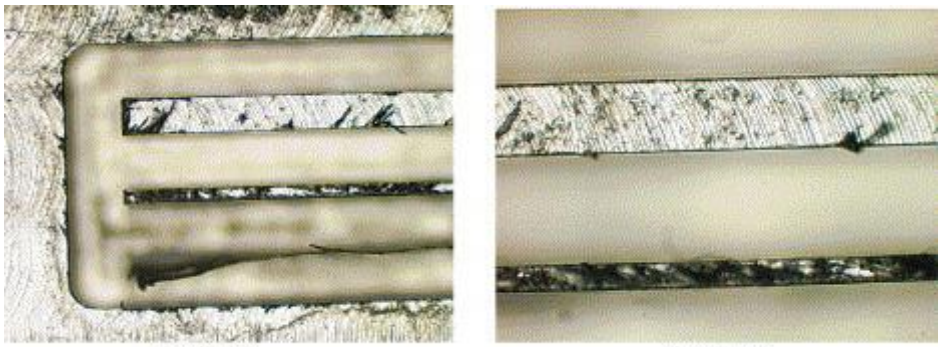

Figure 7.2: Image of micro thin-walled structure machined by Chern et al. (Chern et al. 2007).

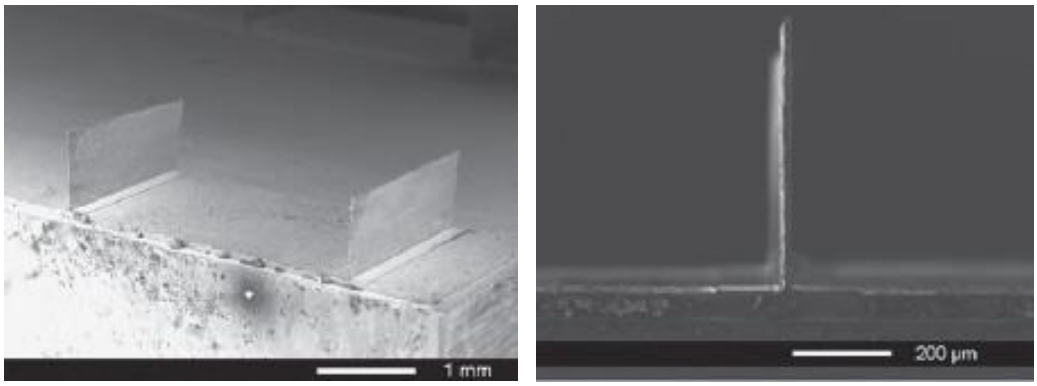

Figure 7.3: Micro thin walls (15 µm thick and 0.8 mm high) as machined by Li et al. (Li et al. 2010).

Annoni et al. (Annoni et al. 2013) evaluated the effect of wall thickness, the milling strategy, and toolpaths on the cutting force in 0.4% carbon steel (C40) in thin wall micro-end milling. The authors focused on a feasibility study of using cutting force

to control the quality of machined micro thin wall. In this study, instead of a conventional waterline toolpath strategy, the step support toolpath strategy was applied. The analysis of covariance (ANCOVA) has been used in order to remove the tool wear effect.

Another application of micro-end milling is in prototyping of micro-products. Friedrich (Friedrich 2002) has demonstrated the capability of micro-end milling in rapid fabrication of design prototypes, electroforming molds, and rotary hot embossing masters. Filiz et al. (Filiz et al. 2008) have studied the feasibility of micro-end milling to fabricate micro-scale mechanical attachment components. The particular attachment components were referred to as microbarbs, which include a sharp piercing edge and a re-entrant feature obtained by undercutting. The custom design tools were made for this study. A design of experiments study is conducted on a biocompatible polymer polymethyl methacrylate (PMMA) to investigate the effects of cutting conditions (feed, speed, and axial depth of cut) on micro-milling forces, surface roughness, and burr formation. Moreover, to demonstrate the material capability, microbarbs were also created from other biocompatible materials, including a bioresorbable material polylactic acid (PLA) and fibrin-based plastics, and a non-bioresorbable 304 stainless steel.

3. Micro-Milling of Thin Walls with High Aspect Ratios

One of the general problems encountered in macro-mechanical machining is tool and workpiece deflections. Since mechanical forces are used as a mean to remove unwanted material, the result of reaction forces can cause the tool and workpiece to be deflected. The deflections affect the geometrical accuracy, especially the low rigidity features such as thin walls. Achieving the right profile in low-rigidity parts increasingly depends on the use of optimal cutting strategies and toolpaths in the CAD/CAM

packages. NC program generation for complex surfaces has been well supported by significant developments in toolpath optimization and verification techniques for conventional milling processes (Alting et al. 2003). However, these features in micro-parts are smaller, thinner, narrower, and have higher aspect ratios compared to conventional macro-parts. The small micro-features with very low-rigidity can be easily deflected by small forces applied from the tool during micro-machining. In addition, the elastic recovery of the work material caused by insufficient chip thickness exerted at the tool edge may contribute a surface generation error during the micro-milling process. As a result, obtaining high accuracy and precision in micro-milling is very challenging.

There are several metallic micro-product geometries which are normally consisted of thin wall features; for example, micro-heat-sinks, micro-packages/shells, micro-propellers, micro-structures, micro-dies for electrical discharge machining (EDM) etc. Hence, developing an effective and efficient micro-milling strategy for fabricating metallic thin-featured micro-products would enhance further developments in many micro-applications. Therefore, in this work, the main objective was to develop a robust process for micro-milling of metallic thin-features. The scope of this study was to optimize the process parameters and tool path strategy for micro-milling of metallic thin walls with application in micro-heat-sink fabrication.

3.1 Experimental methodology

The experiments were conducted in two phases. The first phase was to preliminarily determine cutting parameters suitable for micro-machining of micro thin-wall, and the second phase was to investigate the robustness of micro-machining of micro thin-wall. In addition to the experiments, verification of the results was also conducted.

The workpiece material selected for the experiment was brass. A block of workpiece was clamped on the fixture mounted on the table of the inhouse developed 4-axis micro-end milling machine. The tool was mounted directly to the ceramic bearing electrically driven precision spindle (NSK ASTRO-E 800). The air-blow was used to cool the cutting zone and facilitate chips evacuation. Figure 7.4 shows the experimental set-up.

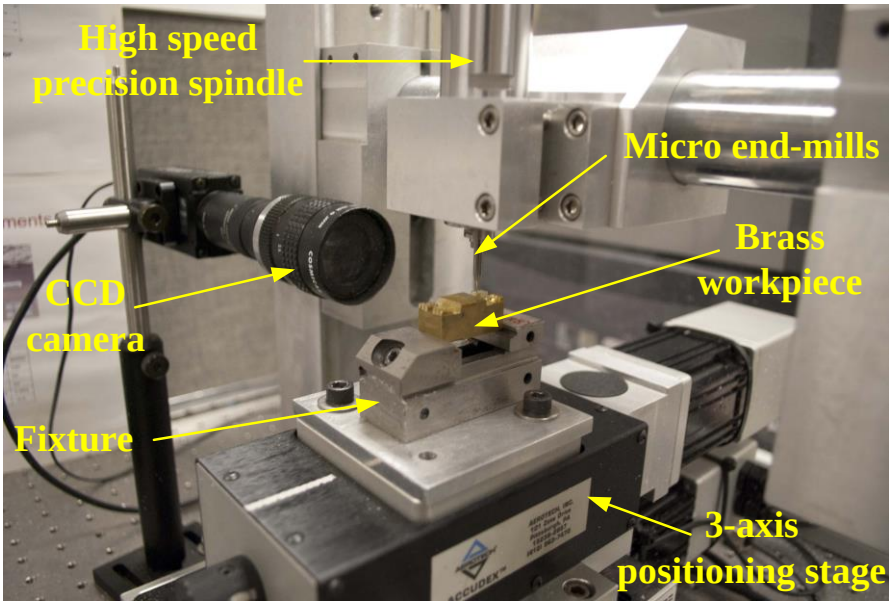

Figure 7.4: The experimental set-up.

In the first phase, three factors were selected, including milling type (i.e. down/up milling), spindle speed (Ω in rpm), feed per tooth (f_z in μm /tooth) and axial depth of cut (a_p in μm). The experimental design for the first phase was based on Taguchi L8 orthogonal array designed for four factors with two levels. Table 7.1 shows the experimental condition used in the first phase. The submicron grade solid carbide center cutting end mills from Kyocera with 2 flutes, square end, 0.02" ($\varnothing$=508μm) diameter,

0.03" (l_c=762 μm) effective cutting length and 30° helix angle (β) was used for all experimental runs. The micro thin walls with a thickness of 50 μm, a height of 762 μm and a length of 10 mm were machined using double steps Z-level tool path strategy where the first step provided an allowance of 25 μm thick on both sides of the wall then the second step finished to the final thickness. Figure 7.5a illustrates the toolpath strategy used in this experiment. The responses of this experiment were measured in terms of surface roughness (R_a) and average wall-thickness error.

Table 7.1: Experimental conditions for the first phase.

Run no.	**Factors**			
	Milling type	**Spindle speed, Ω (krpm)**	**Feed per tooth, f_z (μm/tooth)**	**ADOC, a_p (μm)**
1	Down milling	25	2	191
2			3	381
3		35	2	381
4			3	191
5	Up milling	25	2	381
6			3	191
7		35	2	191
8			3	381

The second phase was designed based on the best machining condition obtained from the first phase. In this case, a new experimental design using Taguchi L9

orthogonal array was applied for experiment of four factors with three levels. Table 7.2 shows the Taguchi L9 orthogonal array and the assigned levels. The submicron grade solid carbide center cutting end mills from Kyocera with 2 flutes, square end, 0.02" ($\varnothing$=508μm) diameter, 0.06" (l_c=1.524 mm) effective cutting length and 30° helix angle (β) was used for this experiment. In this experiment spindle speed was kept constant at 35,000 rpm and the wall heights were fixed at 1.5 mm. In each experimental set, two replications were performed. The responses of this experimental phase were the quality measurements of the machined thin wall.

Table 7.2: Experimental conditions for the second phase.

Run no.	**Factors**			
	Thickness	**Strategy**	**ADOC, *ap* (μm)**	**Feed per tooth, f_z (μm/tooth)**
1	25	double steps Z-level	150	0.7
2		single step Z-level	250	1.4
3		Ramp cut	500	2.1
4	50	double steps Z-level	250	2.1
5		single step Z-level	500	0.7
6		Ramp cut	150	1.4
7	75	double steps Z-level	500	1.4
8		single step Z-level	150	2.1
9		Ramp cut	250	0.7

There were three tool path strategies used in the experiment as shown in Figure 7.5. Two main strategies were z-level and ramp cut. The z-level is a toolpath strategy in which the micro-milling is done in layered manner; tool is fed in axial direction (Z-direction) then the milling is carried out until material is completely removed from that layer. In this experiment, there were two approaches in applying the z-level toolpath strategy. The first one is the single step z-level approach in which a thin-wall was milled to the final size in only one step and by using the z-level toolpath strategy. The second one is a double step z-level approach in which a thin-wall was milled with the machining allowance of 25 μm in the first step, then the second step was done to finish to the desired size. The ramp cut is a toolpath strategy in which the milling is done in horizontal and vertical directions simultaneously. In this study, a thin-wall was pre-machined to the allowance of 25 μm by using z-level strategy then the thin wall was ramp cut along the wall length using a defined axial depth cut.

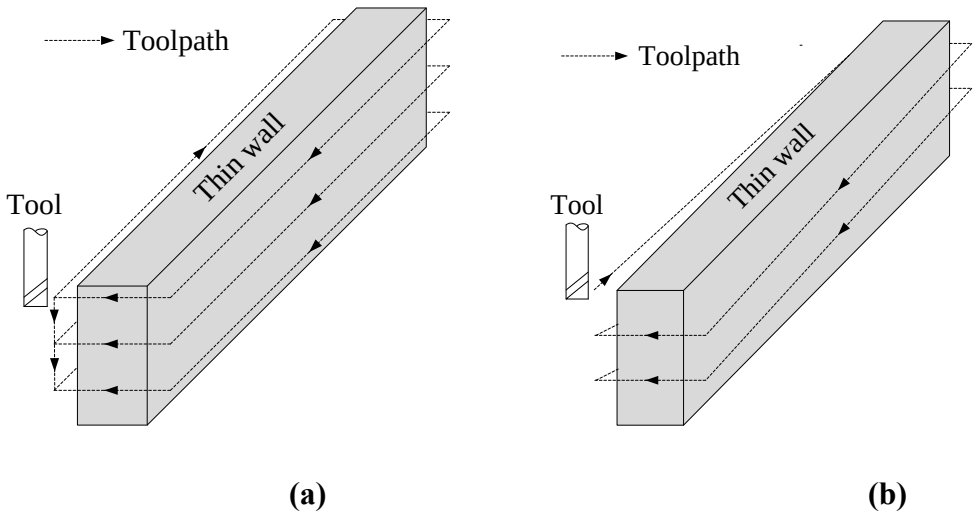

Figure 7.5: Tool path strategies (a) Z-level (b) Ramp cut.

In the second phase the experiment was attempted to create the heat-sink like specimen as shown in Figure 7.6. This specimen mimics the fin type heat-sink consisting of 18 fins. Three fin thicknesses were selected: 25, 50 and 75 µm. each fin has a width of 1.2 mm and a height of 1.5 mm. The platform size is 5 × 5.2 mm^2, small enough to be used in many miniature product.

A dimension of the micro thin wall was measured under the microscope; an average of three measurements was used. Surface roughness was measured using Sensofar Neox non-contact optical 3D profiling with a dual core 3D measuring microscope combined with confocal and interferometry capabilities. An average surface roughness was taken from an average of ten measurements and they were taken from ten different locations.

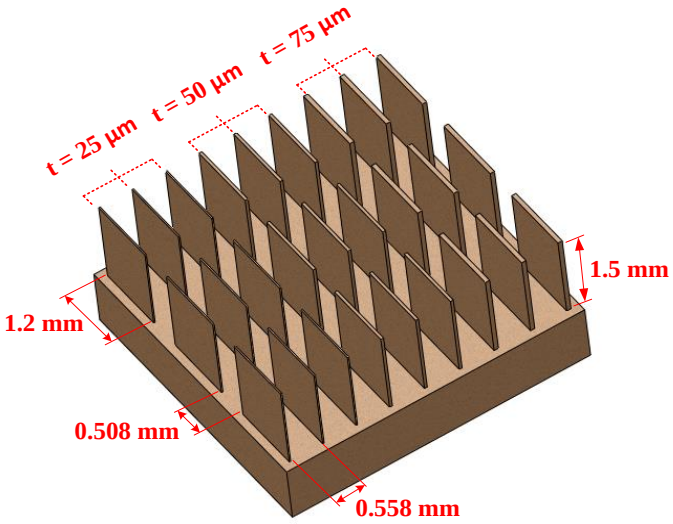

Figure 7.6: Thin-wall array designed for the experiment.

3.2 Results and discussions

The results and discussions are divided into three section based on the order of the experiments.

3.2.1 First phase

The experimental results measured in terms of average surface roughness (R_a) and average wall-thickness error as shown in Table 7.3. The average thicknesses of thin walls were taken from three different locations: top, left and right side of thin walls. The average wall-thickness error was calculated from the difference between the measurement value and the desired wall-thickness (50 μm). The average error was then determined from the average magnitude of those three errors. The surface roughness (R_a) was measured from both sides of the thin-wall. The average R_a value was recorded.

Main effect plots of surface roughness and average wall-thickness error are presented in Figures 7.7 and 7.8, respectively. It can be seen clearly that down milling and spindle speed of 35,000 rpm were preferred, since at these levels, surface roughness and wall-thickness errors were both minimum. The trade-off occurred in choosing feed per tooth, since the minimum surface roughness was obtained at 2 μm/tooth, but the minimum wall-thickness error was obtained at 3 μm/tooth. Since, feed per tooth was the most important factor influencing surface roughness, the feed per tooth of less than 2 μm/tooth will be chosen for the next phase. The effect of axial depth of cut was seemingly insignificant.

Table 7.3: The results of the first phase experiments.

Run no.	Factors				Measurement	
	Milling type	**Ω (krpm)**	**f_z (µm/tooth)**	**a_p (µm)**	**R_a (µm)**	**Thickness error (µm)**
1	Down milling	25	2	191	0.27	4.40
2			3	381	0.23	5.93
3		35	2	381	0.26	1.13
4			3	191	0.29	5.00
5	Up milling	25	2	381	0.37	7.87
6			3	191	0.29	4.87
7		35	2	191	0.22	7.47
8			3	381	0.27	7.60

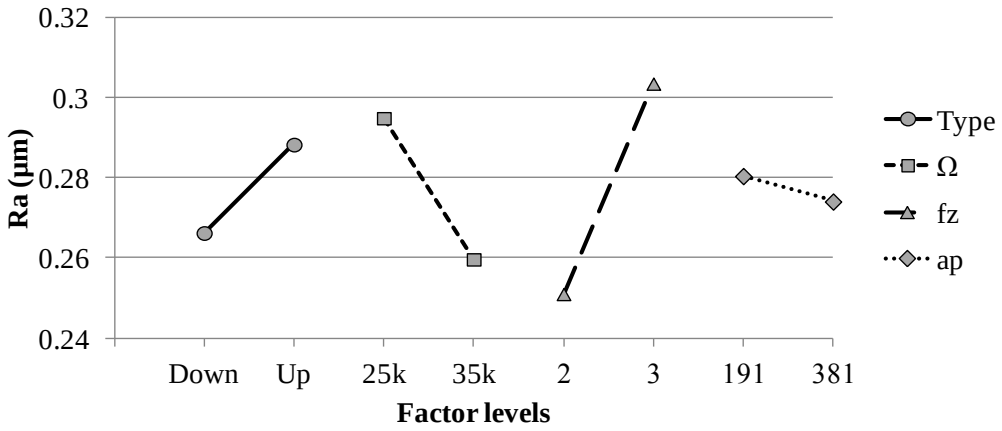

Figure 7.7: Main effects plot of surface roughness.

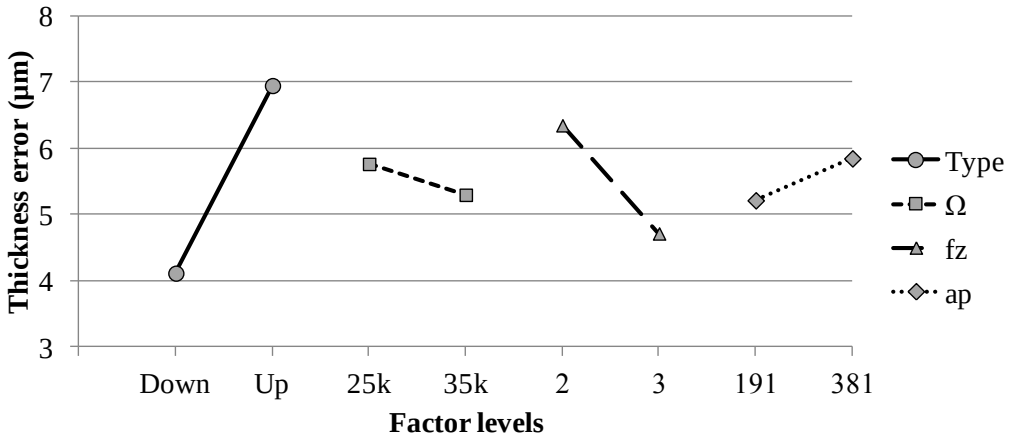

Figure 7.8: Main effects plot of average wall-thickness error.

Based on these results, the best condition for achieving minimum surface roughness was down milling strategy with a spindle speed of 35,000 rpm, a feed per tooth of 2 µm/tooth, and an axial depth of cut of 381µm. In terms of average wall-thickness error, the best condition was down milling strategy with a spindle speed of 35,000 rpm, a feed per tooth of 3 µm/tooth, and an axial depth of cut of 191µm.

The negative value of errors indicated that the feature is smaller than the desired feature while the positive value implies otherwise. It could be observed that the geometry of the thin-wall in all experiments had the shape of a trapezoid instead of rectangle as it is supposed to be. The top parts of the walls are smaller than the desired value (50 µm) while the bottom parts are larger. This may be a result of wall deflection.

3.2.2 Second phase

In this phase, the design of experiment was based on the preliminary results obtained from the first phase. The purpose of this phase was to optimize both machining parameters and strategy. Also, the attempt was made to find the limitation of micro-milling of thin walls in terms of wall thickness.

Figure 7.9 shows the experimental results of this phase. It can be seen that some of the thin walls are ruined by the excessive micro-milling condition, especially at the small wall thickness (25 and 50 µm). After observation, the ruined walls are machined by the experimental run number 2, 3 and 5 which were having the single Z-level tool path strategy and an axial depth of cut of 500 µm in common. Furthermore, at the wall thickness of 75 µm, most of the thin-walls were machined successfully regardless of the machining condition. Hence, it may be concluded that the micro-milling of brass thin-walls is quite robust to typical machining conditions until the thickness reduces to 75 µm. To further achieve even thinner walls, a specific machining condition needed to be selected.

Since, some of the thin-walls were ruined; the quantitative measurements could not be performed. Therefore, some qualitative measurements were used based on the condition of machined thin-wall. Four number scales and criteria were defined as shown in the Table 7.4 and the measurement results are shown in Table 7.5 for analysis purpose, the main effects plot were created as shown in Figure 7.10.

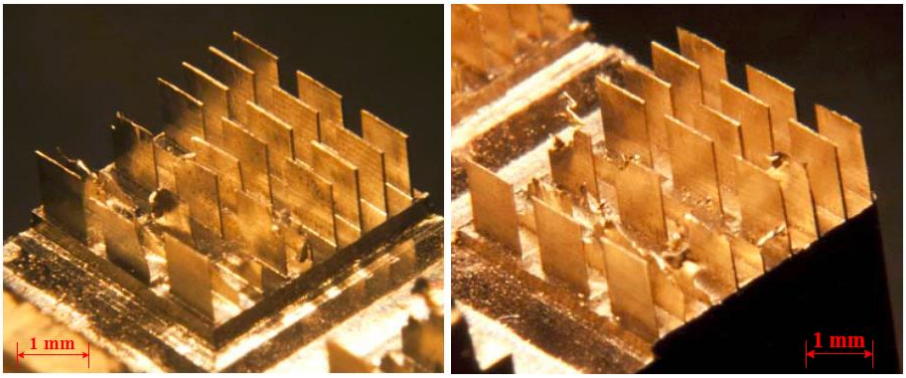

(a) **(b)**

Figure 7.9 Experimental results from the second phase (a) replication 1 (b) replication 2.

Table 7.4: The qualitative measurements of thin-wall condition.

Score	Wall condition
3	Good; *an intact thin wall as desired*
2	Acceptable; *a bended or stepped thin wall*
1	Partially failed; *partially torn thin wall*
0	Totally failed; *totally ruined thin wall*

Table 7.5: Qualitative evaluation of thin-wall conditions.

Run no.	Thickness (μm)	Toolpath strategy	a_p (μm)	f_z (μm/tooth)	Wall condition	
					Rep#1	Rep#2
1	25	Double Z-level	150	0.7	2	2
2		Single Z-level	250	1.4	0	0
3		Ramp cut	500	2.1	0	0
4	50	Double Z-level	250	2.1	1	0
5		Single Z-level	500	0.7	0	0
6		Ramp cut	150	1.4	2	2
7	75	Double Z-level	500	1.4	3	2
8		Single Z-level	150	2.1	3	3
9		Ramp cut	250	0.7	2	2

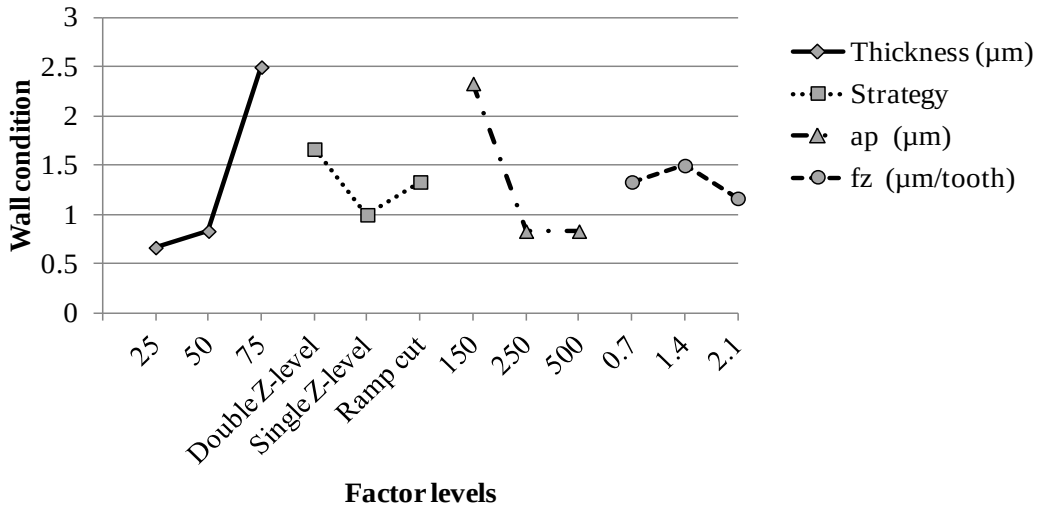

Figure 7.10: Main effects plot of the thin-wall condition.

Based on the main effects plot, some conclusion can be drawn as following. In terms of toolpath strategy, a significant influence on the success of machining was clearly observed. Double Z-level toolpath strategy had been proven to be the best toolpath strategy for micro-milling of a very thin brass wall. The robustness of micro-milling of 75 µm thin-wall was significantly higher than those of 25 and 50 µm thin walls. Small axial depth of cut was more preferable due to the fact that it produces lower forces. The selected range of feed per tooth showed no significant effect to the success of thin wall machining. Therefore; from the results, the best machining condition was found as double Z-level tool path strategy with an axial depth cut of 150 µm, a feed per tooth of 1.4 µm/tooth, a down milling strategy and a spindle speed of 35,000 rpm.

3.2.3 Verification phase

The information obtained from the previous experiments was condensed and used in identifying the final micro-milling parameters and strategy for machining of micro thin

wall. This condition was expected to yield a high success rate and high quality of the thin wall. Then, the verification test was conducted and investigated.

Figure 7.11 shows the machining steps used in this verification test. *Step 1*: mill the workpiece down to the desired size. *Step 2:* mill the groove which perpendicular to the thin wall face. *Step 3:* using Z-level tool path strategy to rough mill the thin wall leaving the clearance of 25 μm on both sides of the walls. *Step 4:* Finishing using Z-level tool path strategy. Figure 7.12 shows the close-up details of the strategy for machining each individual thin wall. The machining parameters were down milling strategy together with double Z-level tool path strategy, an axial depth cut of 150 μm, a feed per tooth of 1.4 μm/tooth, and a spindle speed of 35,000 rpm. The tool was a solid carbide center cutting end mill with 2 flutes, square end, 0.02" (508μm) in diameter with 0.06" (1,524 μm) effective cutting length and 30° helix angle.

The results (see Figure 7.13) showed a satisfactory machined thin-wall array. Two out of six of the 25μm thin walls were failed while the rest were intact. From the observation during the machining process, it was concluded that the failure of those two thin walls were caused from large piece of exit burrs which are randomly generated at the end of the thin wall. Unexpectedly, these burrs were along the way of a toolpath causing a cutting situation in the direction perpendicular to the thin wall face. Since the 25μm thin wall has a very low rigidity, a small cutting force against it can easily cause the bending or shearing. In addition, these burrs were as thick as the thin wall itself. Beside the two failures, all thin walls were perfectly machined. From the SEM images (Figure 7.14), micro burr can be observed along all edges of the thin walls; these micro-burrs were

approximately less than 5 µm thick and less than 30 µm high. These micro-burrs were forming more during micro-milling of the 25 µm thin walls.

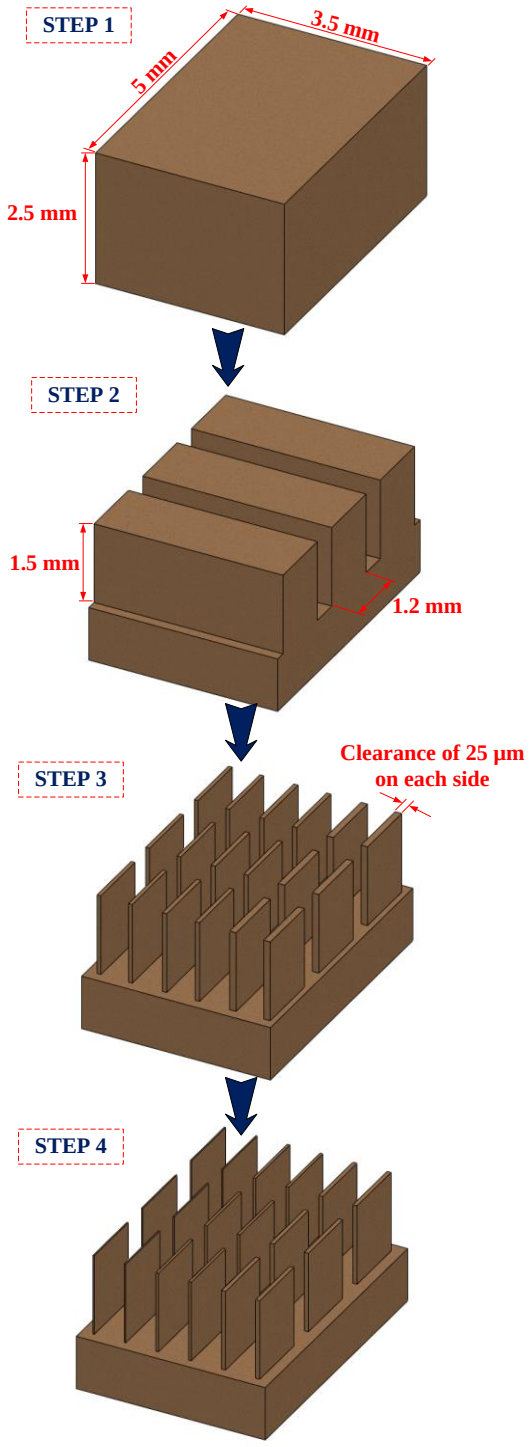

Figure 7.11: Work flow of micro-milling of thin-walls.

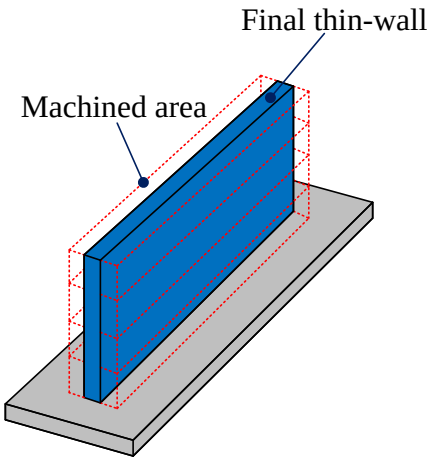

Figure 7.12: The machined area for an individual thin wall.

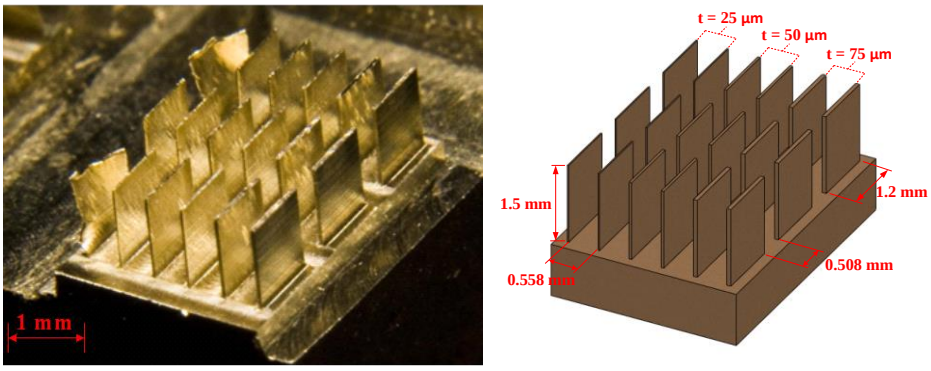

Figure 7.13: The image of the thin-wall array from the verification test.

3.3 Conclusions

This study has shown the feasibility of using micro-milling to fabricate the brass thin walls having the thickness of a micron scale. With an appropriate machining parameter set, toolpath strategy, and work flow, the thin-wall can be machined successfully down to the thickness of 25 µm. These micro thin-wall arrays can be utilized as a heat-sink for miniature products. In this study, the platform of the 18 fin heat-sink

was only 5×5.2 mm^2. In short the basic principles of micro-milling such thin walls can be summarized as follow;

- Down milling strategy should be preferred at all times.
- For the finishing, avoid cutting in the direction perpendicular to the wall surface.
- The Z-level toolpath is recommended.
- A clearance of 10-25 μm for the rough cut is recommended.
- Low axial depth of cut and feed per tooth values should be used.
- The design of the toolpaths should be done in a way that entry and exit cuts are minimized to avoid entry and exit burr formulation.

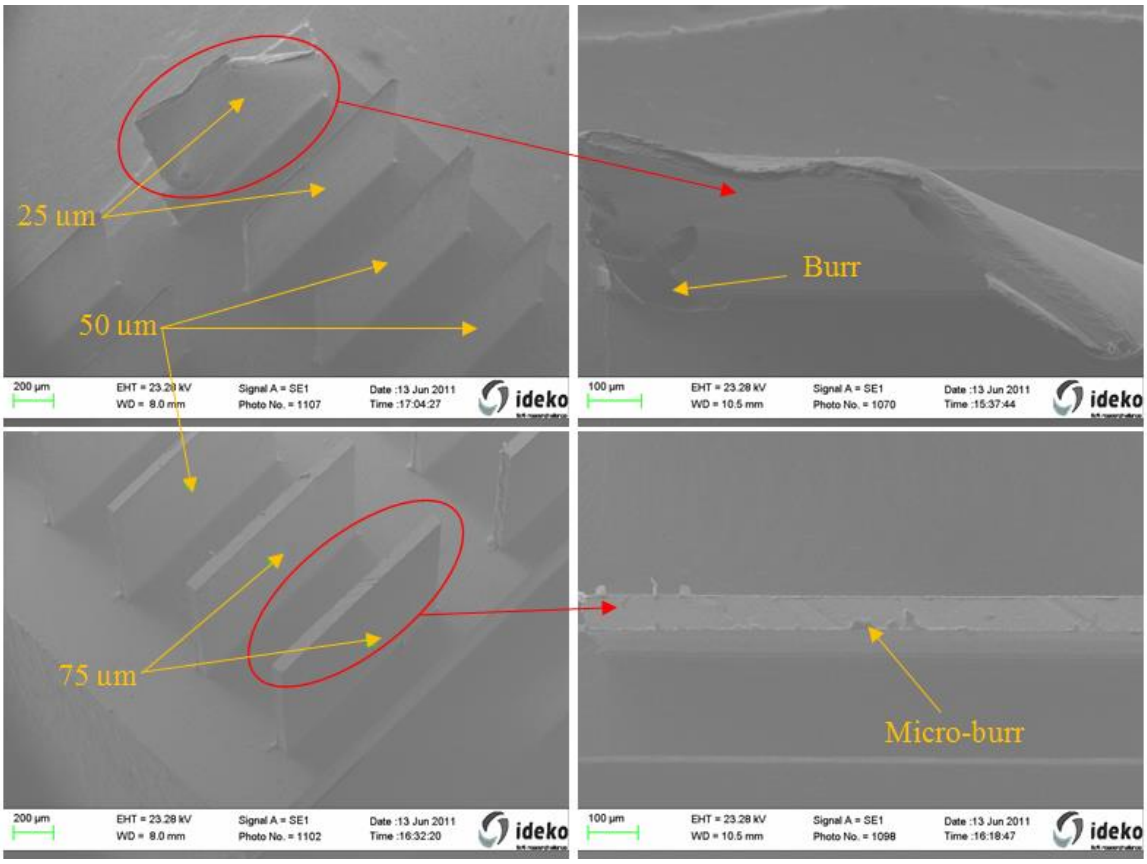

Figure 7.14: SEM images of the thin-wall array.

4. Micro-Milling of Micro-Needle Arrays

Micro-needles are new medical devices with the same purpose of classic hypodermic needles but fabricated on micro-scale often in the form of arrays in various materials. These devices aim to replace the hypodermic needles and consist of a patch with micro-sized needles. These patches generally do not induce pain since these micro-sized needles penetrate into the skin small enough and do not reach pain receptors and they can be applied without the help of a health professional (Henry et al. 1998). The basic premise of painless micro-needles patches is to design micro-needles so small (a length between 0.5-1.5 mm and the diameter should about 100-200 μm) that they cannot reach the dermis layer of human skin and do not agitate pain receptors (Maton et al. 1993). Considering this design requirement and desired shape, micro-needles can be fabricated in metals, silicon or silicon dioxide, polymers and glass. Micro-needles also offer a broad range of advantages when compared with traditional hypodermic needles.

In order to achieve painless and damage-free operation on skin for drug injection and blood extraction, research in transdermal micro-needle array is progressively developed. Several different types of micro-needles e.g. solid (straight, bent, filtered) and hollow have been fabricated. Solid needles could be used to increase drug diffusion rate by using a drug patch. Hollow needles which include tapered and beveled tips allow delivery of microliter quantities of drugs to specific locations in human body. Furthermore, small enough micro-needles could even provide drug administration to individual cells and also open possibilities for stem cell research (Hilt & Peppas 2005). The first micro-needle arrays reported in the literature were etched into a silicon wafer and developed for intracellular delivery in vitro by Hashmi et al. (Hashmi et al. 1995).

These needles were inserted into cells and nematodes to increase molecular uptake and gene transfection. Henry et al. (Henry et al. 1998) conducted studies to determine the feasibility of using micro-needles to improve transdermal drug delivery. An array of solid micro-needles was embedded in cadaver skin, which caused skin permeability to a small model compound. Kaushik et al. (Kaushik et al. 2001) carried out a small trial to determine if micro-needles are perceived as painless by human subjects. Other studies have also reported that micro-needles can be applied to human subjects in a painless manner (Mikszta et al. 2002). One of the problems reported in literature was the breakage of metal needles inside the skin since metal micro-needles were not elastic but rather brittle. Biodegradable polymer micro-needles have recently been introduced and fabricated. The advantage of biodegradable polymer needles is that they can be cost-effectively produced and not to pose a problem of breakage in the skin due to biocompatibility and biodegradability (Park et al. 2005, Smart & Subramanian 2000). Moreover micro-needles out of dissolving polymer that was mixed with a freeze-dried vaccine were proposed (Lee et al. 2008). In addition, coated encapsulated molecules within micro-needles can dissolve in the skin and leave no bio-hazardous waste thereafter (Gill & Prausnitz 2007). Fabrication of biodegradable polymer micro-needles with sharp, beveled or tapered tips is possible by using masking and etching micro-electro-mechanical-systems (MEMS) processing techniques or within an in situ lens-based lithographic technique. Metallic micro-needles are also produced through electro-deposition and glass micro-needles are fabricated using glass drawn micropipette techniques as reported in literature (Henry et al. 1998). Multi-layer structures for polymeric micro-needles are also proposed (Kuo & Chou 2004). This technique can

fabricate hollow micro-needles with sharp tips and the dimensions of 50 µm and length of 600 µm.

This literature review shows that micro-needles can be fabricated in different ways, with different shapes, materials, dimensions and for different purposes. Very small micro-needles could provide highly targeted drug administration to individual cells. These are capable of very accurate dosing, complex release patterns, local delivery and biological drug stability enhancement by storing in a micro volume that can be precisely controlled. This work aims to investigate the feasibility of directly fabricating micro-needle arrays based patch prototype using micro-milling of polymeric materials.

4.1 Micro-needle array design

There are a number of design parameters for the micro-needle array. These include a basic shape of an individual micro-needle, the height, the base diameter (conical shape) or the base dimension (square based pyramidal shape), horizontal and vertical spaces, and linear or circular array type. The micro-needle shape is defined by considering biomedical needs and the limitation in micro-milling. The micro-needle array based patch has to be made of biocompatible polymer, the needle height must be between h=0.6 and 1.5 mm with sizable base dimension for drug storage and the needle tips have to be sharp enough to penetrate easily through the skin but not break inside the skin. The micro-milling process limits are related specifically to these criteria i.e. sharpness and resistance of the tip. Therefore, it was possible to obtain a specific design for micro-needle arrays shown in Figure 7.15 with the geometrical parameters listed in Table 7.6.

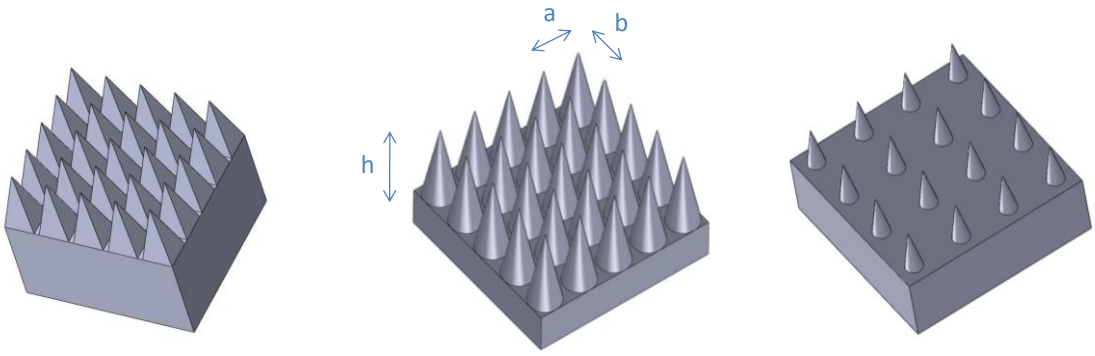

(a) Pyramidal (b) Conical (c) Dwarf-conical

Figure 7.15: Micro-needle array designs and geometrical parameters.

Table 7.6: Design parameters for the micro-needle arrays.

Variable	Description	Value
Shape	Pyramid, cone	-
h	Needle height	0.6 - 1.5 mm
d	Base diameter or dimension	0.3 - 0.7 mm
a	Horizontal space	0.5 - 2 mm
b	Vertical space	0.5 - 2 mm
Array	Linear, Circular	-

4.2 Experimental work

Due to their low thermal conductivity (k), polymers can exhibit thermal softening in micro-milling. Hence, a polymer that offers a high melting temperature (T_m) and good strength (UTS) is suitable for micro-need array fabrication using micro-milling process (see Table 7.7). Among those polymers, polymethyl methacrylate (PMMA) has been selected as prototype material due to its favorable thermal and mechanical properties.

Table 7.7: Thermal and mechanical properties of some polymers.

Polymer	T_m[°C]	k [W/m-K]	*UTS* [MPa]
PMMA	230	0.187 - 0.216	50-80
ABS	105	0.128 - 0.200	40-60
PEEK	343	0.240 - 0.300	90-100
PC	300	0.195 - 0.21	65-75

An experimental set-up for micro-milling of polymers has been prepared as shown in Figure 7.16. In this experimental set-up, a 3-axis positioning stage driven by a computer numerical control (CNC) system that accepts standard part programming codes (G codes) was utilized. An electrically driven precision spindle (NSK ASTRO-E800) with ceramic bearings and with a spindle speed of up to 80 krpm was employed. An engraving type micro-tool with a straight cutting edge was installed to the spindle using a precision collet for tool overhanging distance of about 15 mm. A rectangular PMMA based acrylic workpiece was clamped on the fixture mounted by using a precision mini-vise on the positioning stage table of this in-house developed versatile micro-milling machine. The workpiece surface was segmented by using a larger diameter flat-end mill to the desired size for the micro-needle array base. In addition, an air cooling system was employed by using a nozzle to cool down the temperature in the polymer being processes and also to blow polymeric chips and debris away.

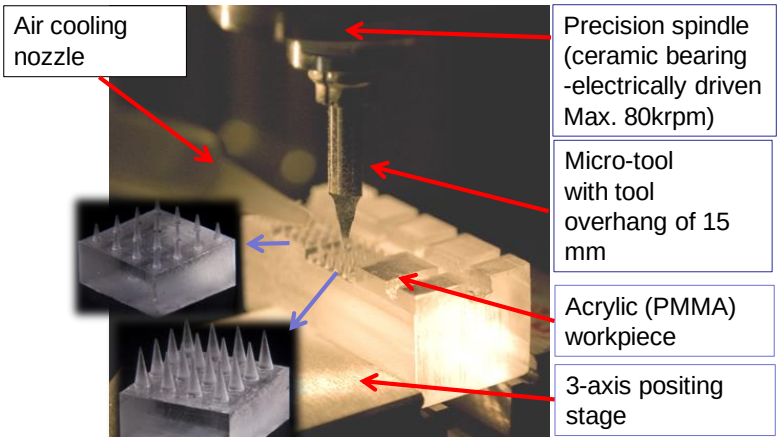

Figure 7.16: Experimental set-up for micro-milling of PMMA polymer.

As mentioned before, a single flute straight cutting edge tungsten carbide engraving type tool was selected as the micro-milling tool. This tool enabled fabrication of micro-needle features as a negative geometry of the tool tip after the material removal process. The characteristics of the tool geometry and geometrical parameters are given in Table 7.8. The tool tip had a flat bottom with a width of 0.298 mm. That assured creating a distance between the base features of the individual micro-needles. Depending on the axial depth of cut (a_p) taken during the micro-milling, this distance between the micro-needles within an array can be controlled using geometric parameters *a* and *b*.

Table 7.8: Geometrical parameters for the engraving type micro-tool.

Shank diameter	3.1750 mm (1/8 inches)
Tip width	0.2980 mm
Tip length	7.4000 mm
Cutter angle	22.0013°
Cutting length	2.7420 mm
Overall tool length	57.4000 mm
Aspect Ratio l/d	24.8322

A CAD model for the micro-needle array was developed to realize the overall geometry and understand some challenges in machining these geometries using the micro-milling process. Furthermore this model was utilized as a reference to generate toolpaths and related CNC part programming.

4.2.1 Fabrication of pyramidal micro-needle arrays

The micro-needle array that consists of a basic pyramid shape with a square base was designed as *pyramidal micro-needle array* and fabricated in PMMA polymer. The toolpath strategy that was utilized for this geometry is shown in Figure 7.17. This strategy consisted of a zig-zag toolpath with a stepover distance (essentially the distance between the centers of individual micro-needles) on the longitudinal direction followed by the same zig-zag toolpath in the transversal direction. The needles fabricated were h=2 mm-tall, the base was a square with 0.7775 mm side length, and the micro-needle tips were a=b=0.9075 mm apart from each other. In this case the array has 25 individual micro-needles arranged in 5 rows and 5 columns (5x5). Therefore the workpiece has overall dimensions of 5.426mm x 5.426mm x 5mm including the base. Figure 7.17 shows the different steps during the experiment and the resultant profiles, where the green star and the red star are the starting and the ending points on the same z-level toolpath. The tool reaches to a deeper z-level as the color used for the toolpath in Figure 7.17 turns from “yellow” to “red”.

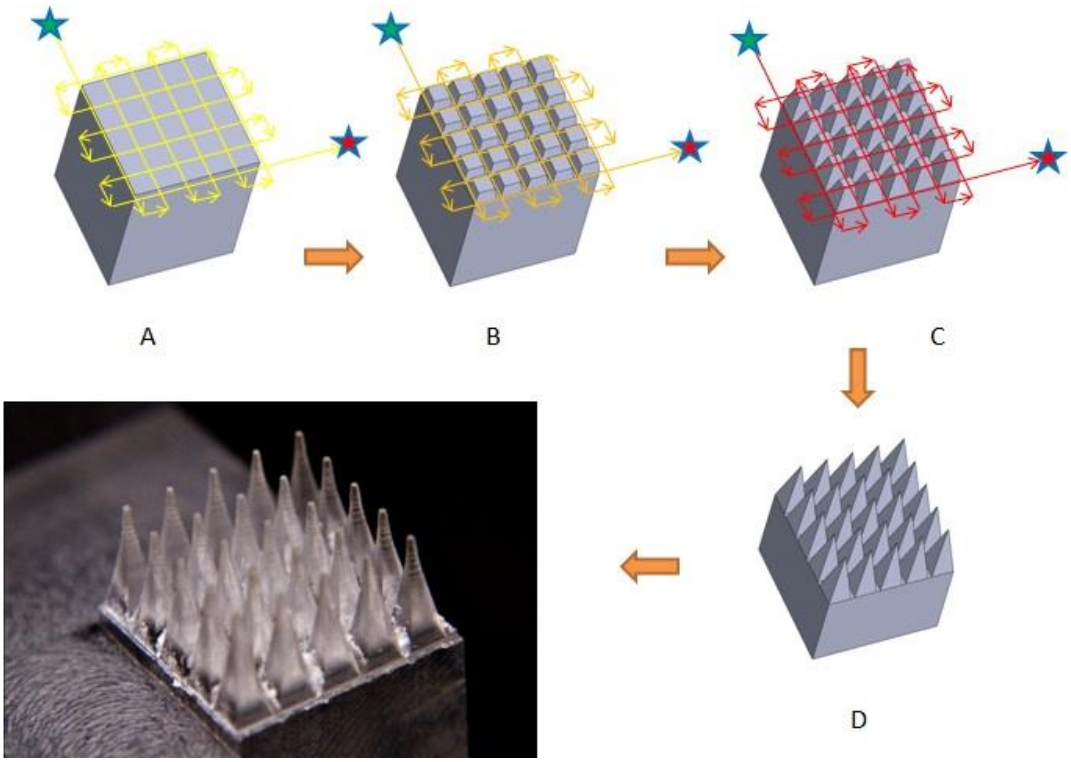

Figure 7.17: Toolpath strategy for the pyramidal micro-needle array.

This approach was found to be problematic after the experiment. The tips of the pyramidal shape micro-needles were not sharp enough because of bending occurred during the last several passes of the micro-milling toolpath. The situation was improved by modifying the toolpath strategy and the micro-needle geometry. In order to avoid the aforementioned problem, a new toolpath strategy ("S" type toolpaths) as shown in Figure 7.18 was adopted. In this case, micro-needle tips were sharper but some of them were broken during the last few passes of the micro-milling toolpath. All the dimensions were kept the same as in the previous experiment.

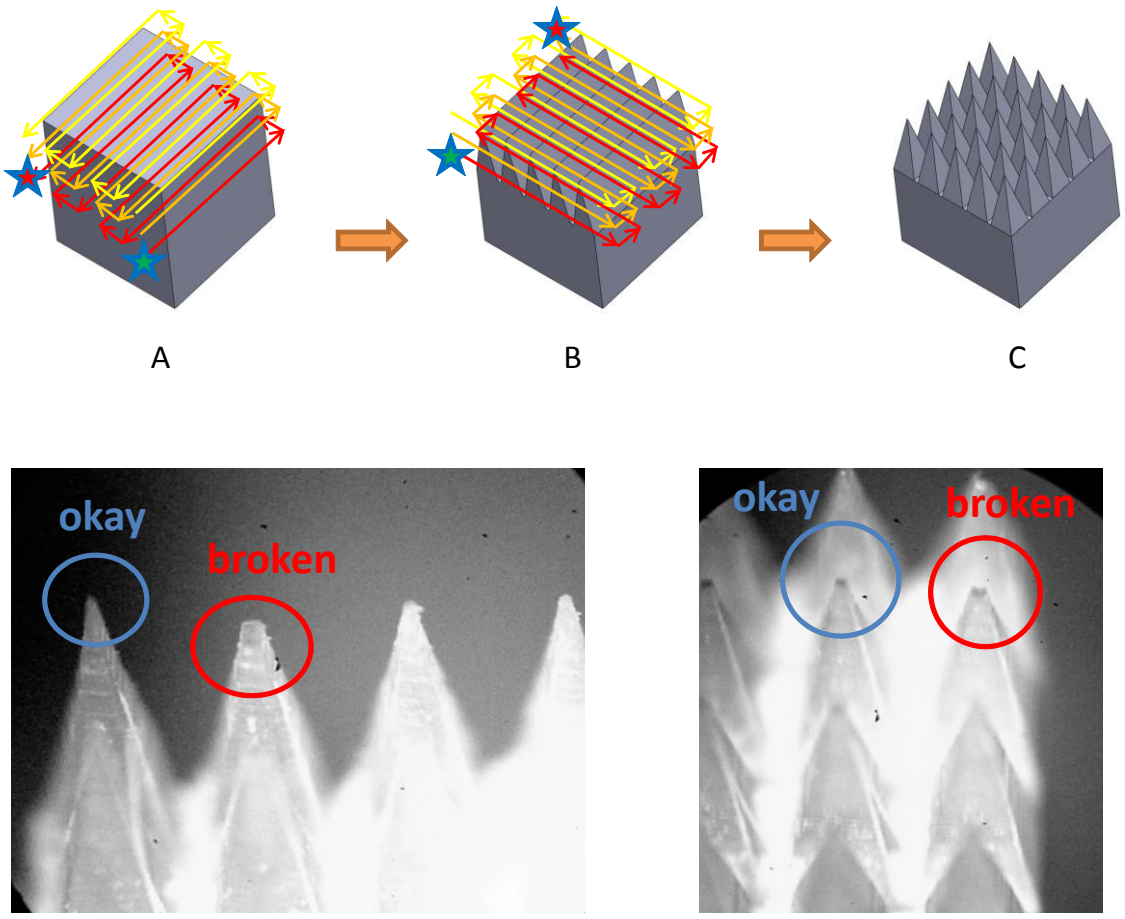

Figure 7.18: Improved toolpath strategy for pyramidal micro-needle arrays with close-up views of the individual micro-needles fabricated.

4.2.2 Fabrication of conical micro-needle arrays

The micro-needle array that consists of a basic conical shape with a circular base was also designed as *conical micro-needle array* and fabricated in PMMA polymer. This prototype provided a new shape for the needles and, related to this, a new tool path strategy was generated. These micro-needles were cone-shaped and arranged in 5 rows and 5 columns (5x5) amounting to a total of 25 micro-needles on the array as shown in Figure 7.19. The cone-shaped micro-needles were h=2 mm-tall and the base radius was

0.382mm. The workpiece had dimensions of 5.426mm x 5.426mm x 5 mm including the base. The toolpath strategy adopted for the conical micro-needle array is shown in Figure 7.19. Same z-level increment of a_p=0.1 mm was used. As it can be seen in Figure 7.19, the cone-shaped micro-needles are sharper and well-shaped than the pyramidal ones but also in this case micro-needle tips were deflected during the last few passes of the micro-milling operation.

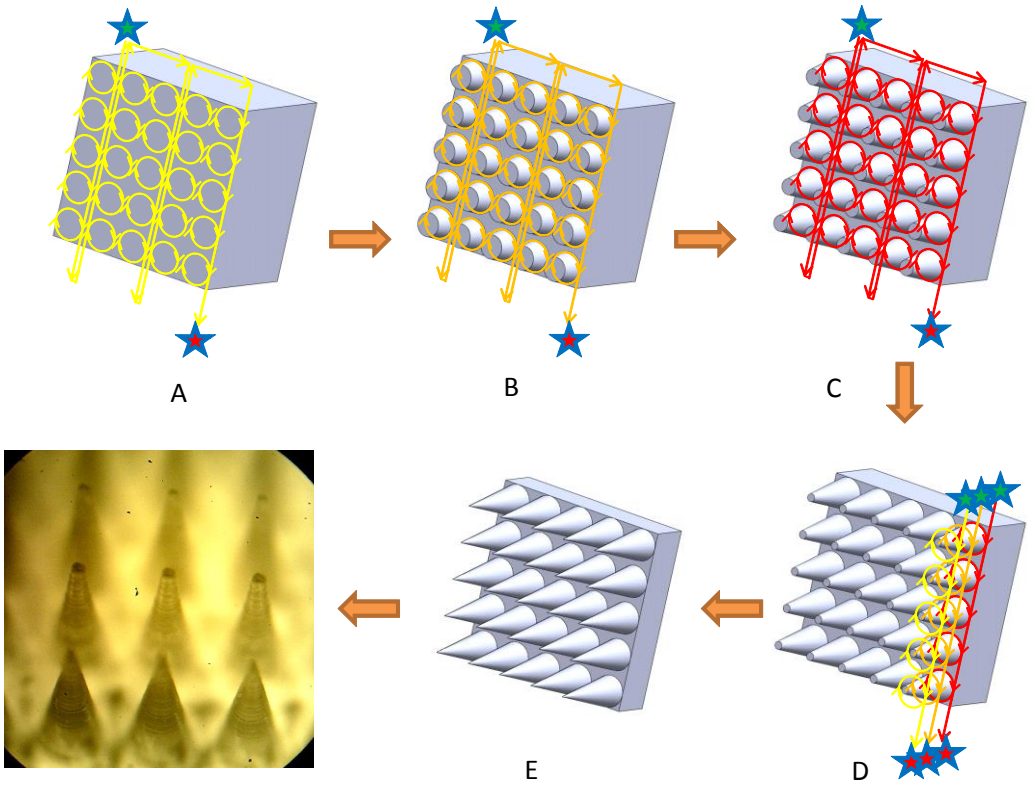

Figure 7.19: Toolpath strategy for the conical micro-needle array.

To improve the micro-need tip strength and reduce the aspect ratio, a *dwarf conical micro-needle array* design was introduced and a different toolpath strategy was adopted. In this case, the micro-needle array was designed with a larger space between each micro-needle and with shorter needle heights (see Figure 7.20). This prototype has a

total of 16 micro-needles placed in 4 rows and 4 columns (4x4). The needles were only h=1 mm tall in order to obtain higher stiffness and lower tip deflection. The base radius of micro-needles was 0.180 mm and the distance between the tips was a=b=1.420 mm. The tool path strategy was changing at every z-level increment (a_p=0.1 mm). The idea was to start micro-milling the tips of the needles in order to obtain sharper tips and not letting them to be tall and thin (slender) to avoid deflections. In the generated toolpaths, the radius of the circular movement to obtain the cones was increased at every z-level increment. Before starting with this step, a roughing operation was performed to avoid breaking the micro-tool and overheating/melting/smearing problems. The roughing operation was performed using a flat end-milling tool with the toolpath strategy (step A) given in Figure 7.20.

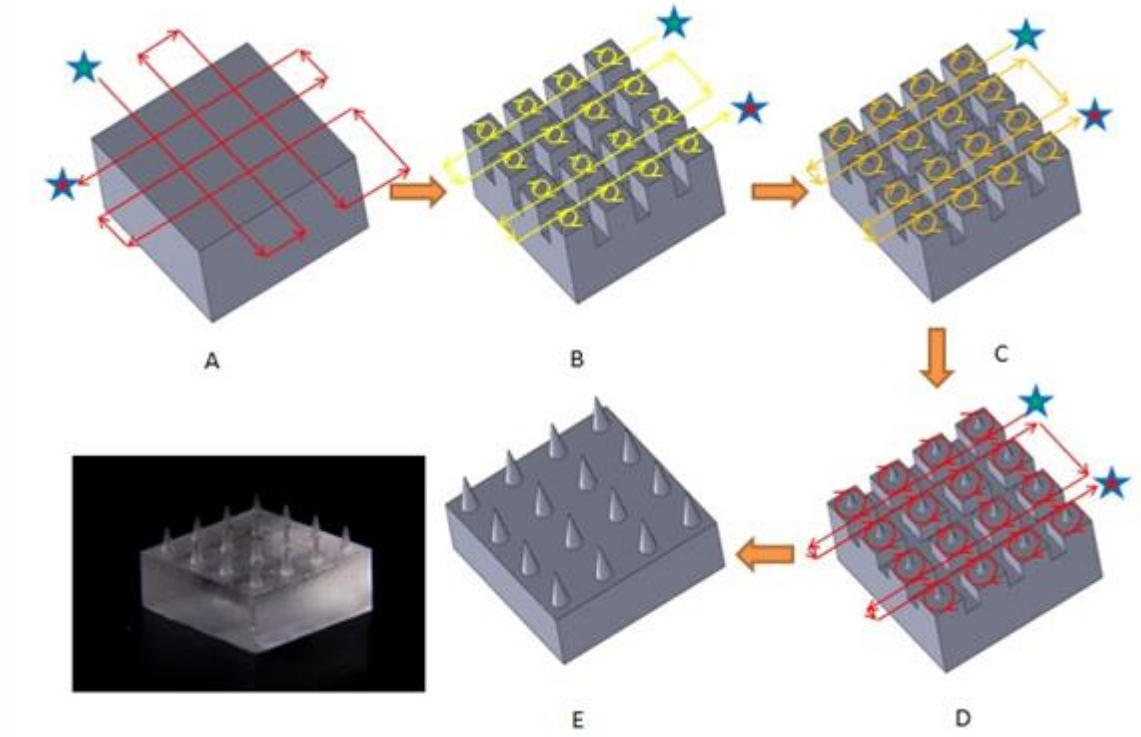

Figure 7.20: Toolpath strategy for the dwarf conical micro-needle array.

4.3 Experimental results

As it can be seen from the toolpath strategies described here, these different micro-needle array prototypes result in different total processing times. Beginning with the first prototype the processing times are increased due to a longer toolpath design. The quality of the prototype was increased in every experiment, starting from the first attempt (a good shape was obtained but burr formation and chip melting has occurred concurrently), until the last prototype fabricated which was completely burr-free and composed of the shapes desired for the micro-needle array (see Figure 7.21).

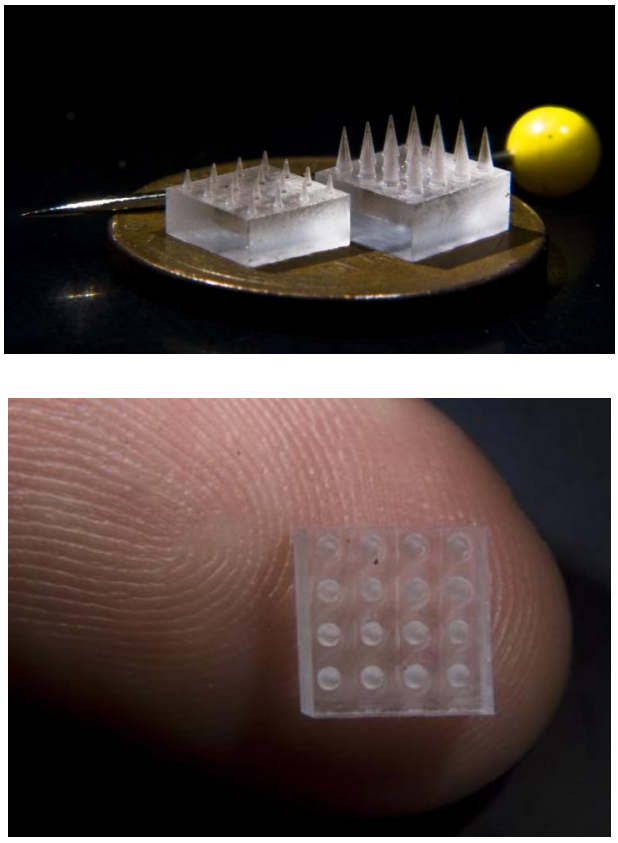

Figure 7.21: Fabricated conical micro-needle arrays.

4.4 Conclusions

In this study, micro-needle array based patch prototypes were developed using micro-milling technology. Beginning with a simple idea, the prototype was improved in shape, toolpath strategy, dimensions, and micro-milling conditions in order to obtain the most satisfactory micro-needles patch prototype. The problems experienced during these experiments were mainly related to the tiny dimensions of the needles and the micro-machining of the PMMA polymer, specially the heat generation problem. These problems were solved by modifying machining strategies, toolpaths and micro-milling process parameters.

CHAPTER 8

CONTRIBUTIONS AND FUTURE WORK

The overall content of this dissertation focuses on the investigations of micro-end milling process. The research work includes modeling and optimization of micro-end milling process, performance studies for cBN coated WC/Co micro-end mill, FE modeling and simulation of micro-end milling process, micro-end milling applications and toolpath strategies, derivation of a predictive model for tool life and development of a decision support system. Main contributions of this study can be listed as follows:

1. Sensor-assisted monitoring and optimization of process parameters (Chapter 2)
    - This study pointed out the feasibility of using acoustic emission (AE) signal to monitor the process conditions and resultant surface generation in micro-end milling. It has been shown that the AE signal waveform responds precisely to most changes in process parameters and surface conditions (Thepsonthi & Özel 2010).
    - The developed multi-objective process optimization scheme based on the response surface methodology (RSM) and multi-objective particle swarm optimization (MOPSO) has proven to be useful in supporting the decision making in micro-end milling process. The concept of this method can be generalized and utilized for use in many applications (Thepsonthi & Özel 2011, 2012).
2. Micro-end milling with uncoated and cBN coated tools (Chapter 3)

- The advantages and disadvantages of using cBN coated WC/Co micro-end mill have been studied and reported. The major advantage of cBN coated tool is the improvement of tool life. However, the drawback of using cBN coated tool is that it increases top-burr formation (Özel et al. 2011a, 2011b).
- The optimal machining condition for micro-end milling of Ti-6Al-4V using both uncoated and cBN coated tools was reported. The multi-objective optimization was performed. Also, the influences of process parameters were extensively discussed. This can be used as a guideline for industry in selecting proper process parameters that yield to desired outcomes (Özel et al. 2011a, 2011b).

3. Finite element modeling and process simulations (Chapter 4)
    - The study has shown that 2-D FE modeling and process simulations can be utilized to support the experimental study of cBN coated WC/Co micro-end mill. The 2-D FE model also proved to be accurate in predicting the tool wear rate in micro-end milling (Thepsonthi & Özel 2012, 2013a).
    - This work illustrated advantages and disadvantages of using elasto-viscoplastic material assumption over viscoplastic material assumption in FE modeling and process simulation of micro-end milling of Ti-6Al-4V. The results showed that the elasto-viscoplastic model provided an accurate chip formation while taking enormously more computation time (Thepsonthi & Özel 2013b).
4. 3-D finite element modeling and simulation of micro-end milling (Chapter 5)

- Micro-end milling is an oblique cutting process. To be able to capture the physical behavior of the process, the 3-D FE simulation is necessary. However, the 3-D FE simulation for micro-end milling has never been developed before. In this study, the 3-D FE model was developed and used in predicting the micro-end milling performance. In addition, a comparison of 3-D and 2-D FE process simulation was conducted (Thepsonthi & Özel 2013c).
- The investigations of micro-end milling process under the influence of tool wear were conducted using the developed 3-D FE simulations. The result revealed the significant impact of tool wear in reducing the process performance.

5. Process optimization and decision support for high performance micro-milling of Ti-6Al-4V alloys
    - In this study, tool wear and tool life models were developed based on the data obtained from 2-D FE process simulations (Thepsonthi & Özel 2014).
    - Instead of making decision based on experience or trial-and-error, this study provided a guideline for developing a decision support system for process optimization in micro-end milling of Ti-6Al-4V. Based on the experimental results, significant improvements in terms of process performance can be achieved when using the set of process parameters obtained from decision support system (Thepsonthi & Özel 2014).
6. Micro-end milling applications and toolpath strategy investigations (Chapter 7)
    - Micro-machining of micro thin wall is very challenging. It requires a good control over process parameters and toolpath strategy. In this work, the

optimization of process parameters and toolpath strategy for micro-end milling of micro thin wall was conducted. The result was a successful fabrication of micro thin walls down to 25 μm (Agirre et al. 2012).

- The new medical device, micro-needles, which can painlessly pierce through the human skin, was introduced to the medical world. In this work, the polymeric prototypes of micro-needle arrays were designed and fabricated using micro-end milling process with an engraving tool. The quality of the fabricated micro-needles array was satisfactory proving the feasibility of using micro-end milling to fabricate the micro-needles (Thepsonthi et al. 2012c)

Based on aforementioned contributions of this dissertation, some possible future directions can be listed as follows.

1. Based on the findings in Chapter 2, the pattern of Acoustic Emission (AE) signal can be related to the workpiece surface generation. Thus, the AE signal which has been used in on-line monitoring of tool condition can also be used in monitoring of surface generation. The development of an on-line monitoring system which can monitor both tool condition and surface generation simultaneously would be very beneficial for micro-machining.
2. The use of 3-D FE models to simulate micro-end milling process in this work has proven to be successful. Cutting forces, cutting temperature, tool wear and chip formation can be obtained from the simulation. However, burr formation and surface generation still cannot be obtained using the developed 3-D FE model. The further development of 3-D FE process simulation should focus on including the capability of predicting burr formation and surface generation. If this can be achieved, the 3-D

FE process simulation can be used to replace the physical experiments which are costly and time consuming.

3. The developed FE models in this study were based on the assumption that material is homogeneous and isotropic which might not be very accurate for the case of micro-machining process. The further improvement in material model could be done by considering the micro-structure of material. This improvement may make the FE simulations become more realistic.
4. The decision support system for high performance micro-end milling which was discussed in Chapter 6 can be improved by adding other constraints into the optimization scheme. Cutting temperature is one of the interesting constraints in micro-machining especially for micro-machining of polymers. Since, heat has significantly impact on chip and burr formation, controlling of cutting temperature may improve the process performance.
5. In this study, data were obtained from two main sources, experiments and FE simulations. However, it is possible to obtain some data using mechanistic models. Based on the literature, some mechanistic models have already been developed for prediction of cutting forces and surface roughness in micro-end milling.
6. Beside Particle Swarm Optimization (PSO), other optimization techniques such as Genetic Algorithm (GA) and Simulated Annealing (SA) can also be implemented and compared.
7. The FE simulation in micro-end milling can be expanded to the study of surface integrity such as residual stress, microstructure alteration, micro-hardness change, etc.

BIBLIOGRAPHY

Afazov, S. M., Ratchev, S. M. & Segal, J. "Modelling and Simulation of Micro-Milling Cutting Forces." *Journal of Materials Processing Technology* 210.15 (2010): 2154-2162.

Afazov, S. M., Ratchev, S. M. & Segal, J. "Prediction and Experimental Validation of Micro-Milling Cutting Forces of AISI H13 Steel at Hardness between 35 and 60 HRC." *The International Journal of Advanced Manufacturing Technology* 62.9-12 (2012): 887-899.

Agirre A., Thepsonthi T. & Özel T. "Micro-Milling of Metallic Thin-Wall Features with Applications in Micro-Heat Sinks." *Proceedings of the 9th International Conference on High Speed Machining*, March 7-8 (2012) San Sebastian, Spain.

Ai, C., Sun, Y., He, G., Ze, X., Li, W. & Mao, K. "The Milling Tool Wear Monitoring using the Acoustic Spectrum." *The International Journal of Advanced Manufacturing Technology* 61.5-8 (2012): 457-463.

Ali, M. Y., Mohamed, A. R., Khan, A. A., Asfana, B., Lutfi, M. & Fahmi, M. I. "Empirical Modelling of Vibration in Micro End Milling of PMMA." *World Applied Science Journal* 21 (2013): 73-78.

Alting, L., Kimura, F., Hansen, H. N. & Bissacco, G. "Micro Engineering." *CIRP Annals - Manufacturing Technology* 52.2 (2003): 635-657.

Alvarez-Benitez, J. E., Everson, R. M., & Fieldsend, J. E. "A MOPSO algorithm based exclusively on pareto dominance concepts." *Evolutionary Multi-Criterion Optimization*, (2005): 459-473.

Annoni, M., Petro, S., Semeraro, Q., & Solito, R. "Process parameters effect on cutting forces and geometrical quality in thin wall micromilling." *Proceeding of NAMRI/SME 41* (2013).

Aramcharoen, A. & Mativenga, P. T. "Size Effect and Tool Geometry in Micromilling of Tool Steel." *Precision Engineering* 33.4 (2009): 402-407.

Aramcharoen, A., Mativenga, P. T., Yang, S., Cooke, K. E. & Teer, D. G. "Evaluation and Selection of Hard Coatings for Micro Milling of Hardened Tool Steel." *International Journal of Machine Tools and Manufacture* 48.14 (2008): 1578-1584.

Arrazola, P.J., Özel, T., Umbrello, D., Davies, M., & Jawahir, I.S. "Recent Advances in Modelling of Metal Machining Processes," *CIRP Annals- Manufacturing Technology*, 62/2 (2013): 695-718.

Armarego, E. & Brown, R. "On the Size Effect in Metal Cutting." *The International Journal of Production Research* 1.3 (1961): 75-99.

Aurich, J. C., Dornfeld, D., Arrazola, P. J., Franke, V., Leitz, L. & Min, S. "Burrs-Analysis, Control and Removal." *CIRP Annals - Manufacturing Technology* 58.2 (2009): 519-542.

Bang Y., Lee K. & Oh S. "5-Axis Micro Milling Machine for Machining Micro Parts." *The International Journal of Advanced Manufacturing Technology* 25.9-10 (2005): 888-894.

Basuray P. K., Misra B. K. & Lal G. K. "Transition from Ploughing to Cutting during Machining with Blunt Tools." *Wear* 43.3 (1977): 341-349.

Beggan, C., Woulfe, M., Young, P. & Byrne, G. "Using Acoustic Emission to Predict Surface Quality." *The International Journal of Advanced Manufacturing Technology* 15.10 (1999): 737-742.

Bhaskaran J., Murugan M., Balashanmugam N. & Chellamalai M. "Monitoring of Hard Turning using Acoustic Emission Signal." *Journal of Mechanical Science and Technology* 26.2 (2012): 609-615.

Biermann D., Steiner M. & Krebs, E. "Investigation of Different Hard Coatings for Micromilling of Austenitic Stainless Steel." *Procedia CIRP* 7.0 (2013): 246-251.

Bissacco G., Hansen H. N. & De Chiffre L. "Micromilling of Hardened Tool Steel for Mould Making Applications." *Journal of Materials Processing Technology* 167.2–3 (2005): 201-207.

Bissacco G., Hansen, H. N. & Slunsky J. "Modelling the Cutting Edge Radius Size Effect for Force Prediction in Micro Milling." *CIRP Annals - Manufacturing Technology* 57.1 (2008): 113-116.

Blum C., & Li X. "Swarm intelligence in optimization." *Swarm intelligence* Springer (2008): 43-85

Calamaz M., Coupard D. & Girot F. "A New Material Model for 2D Numerical Simulation of Serrated Chip Formation when Machining Titanium Alloy Ti–6Al–4V." *International Journal of Machine Tools and Manufacture* 48.3-4 (2008): 275-288.

Cardoso P. & Davim J. P. "Optimization of Surface Roughness in Micromilling." *Materials and Manufacturing Processes* 25.10 (2010): 1115-1119.

Chae J., Park S. S. & Freiheit T. "Investigation of Micro-Cutting Operations." *International Journal of Machine Tools and Manufacture* 46.3-4 (2006): 313-332.

Che-Haron C. H. & Jawaid A. "The Effect of Machining on Surface Integrity of Titanium Alloy Ti-6% Al-4% V." *Journal of Materials Processing Technology* 166.2 (2005): 188-192.

Chen M. J., Ni H. B., Wang Z. J. & Jiang Y. "Research on the Modeling of Burr Formation Process in Micro-Ball End Milling Operation on Ti-6Al-4V." *The International Journal of Advanced Manufacturing Technology* 62.9-12 (2012): 901-912.

Chern G., Wu Y. E., Cheng J. & Yao J. "Study on Burr Formation in Micro-Machining using Micro-Tools Fabricated by Micro-EDM." *Precision Engineering* 31.2 (2007): 122-129.

Ciurana J., Arias G. & Ozel T. "Neural Network Modeling and Particle Swarm Optimization (PSO) of Process Parameters in Pulsed Laser Micromachining of Hardened AISI H13 Steel." *Materials and Manufacturing Processes* 24.3 (2009): 358-368.

Dhanorker A. & Özel T. "Meso/Micro Scale Milling for Micro-Manufacturing." *International Journal of Mechatronics and Manufacturing Systems* 1.1 (2008): 23-42.

Ding H., Shen N. & Shin Y. C. "Experimental Evaluation and Modeling Analysis of Micromilling of Hardened H13 Tool Steels." *Journal of Manufacturing Science and Engineering* 133.4 (2011): 041007.

Diniz A. E., Liu J. J. & Dornfeld D. A. "Correlating Tool Life, Tool Wear and Surface Roughness by Monitoring Acoustic Emission in Finish Turning." *Wear* 152.2 (1992): 395-407.

Dolinšek S. & Kopač J. "Acoustic Emission Signals for Tool Wear Identification." *Wear* 225–229, Part 1 (1999): 295-303.

Dornfeld D., Min S. & Takeuchi Y. "Recent Advances in Mechanical Micromachining." *CIRP Annals - Manufacturing Technology* 55.2 (2006): 745-768.

Filiz S., Xie L., Weiss L. E. & Ozdoganlar O. B. "Micromilling of Microbarbs for Medical Implants." *International Journal of Machine Tools and Manufacture* 48.3-4 (2008): 459-472.

Fleischer J. & Kotschenreuther J. "The Manufacturing of Micro Molds by Conventional and Energy-Assisted Processes." *The International Journal of Advanced Manufacturing Technology* 33.1-2 (2007): 75-85.

Friedrich C. R. & Vasile, M. J. "Development of the Micromilling Process for High-Aspect-Ratio Microstructures." *Journal of Microelectromechanical Systems* 5.1 (1996): 33-38.

Friedrich C. R. "Micromechanical Machining of High Aspect Ratio Prototypes." *Microsystem Technologies* 8.4-5 (2002): 343-347.

Friedrich C. R., Coane P. J. & Vasile M. J. "Micromilling Development and Applications for Microfabrication." *Microelectronic Engineering* 35.1-4 (1997): 367-372.

Gente A., Hoffmeister H. & Evans C. J. "Chip Formation in Machining Ti6Al4V at Extremely High Cutting Speeds." *CIRP Annals - Manufacturing Technology* 50.1 (2001): 49-52.

Gill H. S. & Prausnitz M. R. "Coated Microneedles for Transdermal Delivery." *Journal of Controlled Release* 117.2 (2007): 227-237.

Govekar E., Gradišek J. & Grabec I. "Analysis of Acoustic Emission Signals and Monitoring of Machining Processes." *Ultrasonics* 38.1-8 (2000): 598-603.

Guo Y. B. & Ammula S. C. "Real-Time Acoustic Emission Monitoring for Surface Damage in Hard Machining." *International Journal of Machine Tools and Manufacture* 45.14 (2005): 1622-1627.

Guo Y. B., Wen Q. & Woodbury K. A. "Dynamic material behavior modeling using internal state variable plasticity and its application in hard machining simulations."*ASME Journal of Manufacturing Science and Engineering* 128 (2006): 749–756

Hashimura M., Hassamontr J. & Dornfeld D. A. "Effect of in-Plane Exit Angle and Rake Angles on Burr Height and Thickness in Face Milling Operation." *Journal of Manufacturing Science and Engineering* 121.1 (1999): 13-19.

Hashmi S., Ling P., Hashmi G., Reed M., Gaugler R. & Trimmer W. "Genetic Transformation of Nematodes using Arrays of Micromechanical Piercing Structures." *BioTechniques* 19.5 (1995): 766-770.

Heaney P. J., Sumant A. V., Torres C. D., Carpick R. W. & Pfefferkorn F. E. "Diamond Coatings for Micro End Mills: Enabling the Dry Machining of Aluminum at the Micro-Scale." *Diamond and Related Materials* 17.3 (2008): 223-233.

Henry S., McAllister, D. V., Allen M. G. & Prausnitz M. R. "Microfabricated Microneedles: A Novel Approach to Transdermal Drug Delivery." *Journal of Pharmaceutical Sciences,* 87 (1998): 922-925.

Hilt J. Z. & Peppas N. A. “Microfabricated Drug Delivery Devices.” *International Journal of Pharmaceutics* 306.1–2 (2005): 15-23.

Ikawa N., Shimada S., Tanaka H. & Ohmori G. “An Atomistic Analysis of Nanometric Chip Removal as Affected by Tool-Work Interaction in Diamond Turning.” *CIRP Annals - Manufacturing Technology* 40.1 (1991): 551-554.

Inasaki I. “Application of Acoustic Emission Sensor for Monitoring Machining Processes.” *Ultrasonics* 36.1-5 (1998): 273-281.

Jemielniak K. & Otman O. “Tool Failure Detection Based on Analysis of Acoustic Emission Signals.” *Journal of Materials Processing Technology* 76.1-3 (1998): 192-197.

Jemielniak K. “Some Aspects of Acoustic Emission Signal Pre-Processing.” *Journal of Materials Processing Technology* 109.3 (2001): 242-247.

Jiang C., Li H. L. & Cao H. Y. “Experiment on Surface Roughness and Acoustic Emission Signal in Infeed Period of Cylindrical Plunge Grinding.” *Advanced Materials Research* 690 (2013): 2442-2445.

Jin X. & Altintas Y. “Prediction of Micro-Milling Forces with Finite Element Method.” *Journal of Materials Processing Technology* 212.3 (2012): 542-552.

Johnson, G. R., & Cook, W. H. (1983, April). “A constitutive model and data for metals subjected to large strains, high strain rates and high temperatures.” *Proceedings of the 7th International Symposium on Ballistics* 21 (1983): 541-547, The Hague, Netherlands: International Ballistics Committee.

Kakinuma Y., Yasuda N. & Aoyama T. “Micromachining of Soft Polymer Material Applying Cryogenic Cooling.” *Journal of Advanced Mechanical Design, Systems, and Manufacturing* 2.4 (2008): 560-569.

Karpat Y. & Özel T. “Multi-Objective Optimization for Turning Processes using Neural Network Modeling and Dynamic-Neighborhood Particle Swarm Optimization.” *The International Journal of Advanced Manufacturing Technology* 35.3-4 (2007): 234-247.

Kaushik S., Hord A. H., Denson D. D., McAllister D. V., Smitra S., Allen M. G., et al. “Lack of Pain Associated with Microfabricated Microneedles.” *Anesthesia & Analgesia* 92.2 (2001): 502-504.

Kaya B., Oysu C., Ertunc H. M. & Ocak H. “A Support Vector Machine-Based Online Tool Condition Monitoring for Milling using Sensor Fusion and a Genetic Algorithm.” *Proceedings of the Institution of Mechanical Engineers, Part B: Journal of Engineering Manufacture* 226.11 (2012): 1808-1818.

Kennedy J. & Eberhart R. “Particle swarm optimization.” *Proceeding of IEEE International Conference on Neural Networks* 4 (1995): 1942-1948.

Kim J. & Kim D. S. “Theoretical Analysis of Micro-Cutting Characteristics in Ultra-Precision Machining.” *Journal of Materials Processing Technology* 49.3-4 (1995): 387-398.

Ko S. & Dornfeld D. A. “A Study on Burr Formation Mechanism.” *Journal of Engineering Materials and Technology* 113.1 (1991): 75-87.

Komanduri R. & Von Turkovich B. F. “New Observations on the Mechanism of Chip Formation when Machining Titanium Alloys.” *Wear* 69.2 (1981): 179-188.

Komatsu T., Yoshino T., Matsumura T. & Torizuka S. "Effect of Crystal Grain Size in Stainless Steel on Cutting Process in Micromilling." *Procedia CIRP* 1.0 (2012): 150-155.

König W., Kutzner K. & Schehl U. "Tool Monitoring of Small Drills with Acoustic Emission." *International Journal of Machine Tools and Manufacture* 32.4 (1992): 487-493.

Kosaraju S., Anne V. & Popuri B. "Online Tool Condition Monitoring in Turning Titanium (Grade 5) using Acoustic Emission: Modeling." *The International Journal of Advanced Manufacturing Technology* (2012): 1-8.

Kuo S. & Chou Y. "Novel Polymer Microneedle Arrays and PDMS Micromolding." *Tamkang Journal of Science and Engineer* 7.2 (2004): 95-98.

Kuram E. & Ozcelik B. "Multi-Objective Optimization using Taguchi Based Grey Relational Analysis for Micro-Milling of Al 7075 Material with Ball Nose End Mill." *Measurement* 46.6 (2013): 1849-1864.

Llanos I., Agirre A., Urreta H., Thepsonthi T. & Özel T., "Micromilling High Aspect Ratio Features Using Tungsten Carbide Tools", *Proceedings of the Institution of Mechanical Engineers, Part B: Journal of Engineering Manufacture*, (2014): 0954405414522214

Lee D. E., Hwang I., Valente C. M. O., Oliveira J. F. G. & Dornfeld D. A. "Precision Manufacturing Process Monitoring with Acoustic Emission." *International Journal of Machine Tools and Manufacture* 46.2 (2006): 176-188.

Lee J. W., Park J. & Prausnitz M. R. "Dissolving Microneedles for Transdermal Drug Delivery." *Biomaterials* 29.13 (2008): 2113-2124.

Leem C. S. & Dornfeld D. A. "Design and Implementation of Sensor-Based Tool-Wear Monitoring Systems." *Mechanical Systems and Signal Processing* 10.4 (1996): 439-458.

Li P., Zdebski, D., Langen H., Hoogstrate A., Oosterling J., Schmidt R. M., et al. "Micromilling of Thin Ribs with High Aspect Ratios." *Journal of Micromechanics and Microengineering* 20.11 (2010): 115013.

Li X. "A Brief Review: Acoustic Emission Method for Tool Wear Monitoring during Turning." *International Journal of Machine Tools and Manufacture* 42.2 (2002): 157-165.

Liu X., DeVor R. E. & Kapoor S. G. "Model-Based Analysis of the Surface Generation in Microendmilling-Part I: Model Development." *Journal of Manufacturing Science and Engineering* 129.3 (2006a): 453-460.

Liu X., DeVor R. E. & Kapoor S. G. "Model-Based Analysis of the Surface Generation in Microendmilling-Part II: Experimental Validation and Analysis." *Journal of Manufacturing Science and Engineering* 129.3 (2006b): 461-469.

Liu X., DeVor R. E., Kapoor S. & Ehmann K. "The Mechanics of Machining at the Microscale: Assessment of the Current State of the Science." *Journal of Manufacturing Science and Engineering* 126.4 (2004): 666-678.

Lu, C. "Study on Prediction of Surface Quality in Machining Process." *Journal of Materials Processing Technology* 205.1-3 (2008): 439-450.

Mackerle J. "Finite Element Analysis and Simulation of Machining: An Addendum: A Bibliography (1996–2002)." *International Journal of Machine Tools and Manufacture* 43.1 (2003): 103-114.

Mackerle J. “Finite Element Analysis and Simulation of Machining: An Addendum: A Bibliography (1996–2002).” *International Journal of Machine Tools and Manufacture* 43.1 (2003): 103-114.

Mackerle J. “Finite-Element Analysis and Simulation of Machining: A Bibliography (1976-1996).” *Journal of Materials Processing Technology* 86.1-3 (1998): 17-44.

Malekian M., Park S. S. & Jun M. B. G. “Tool Wear Monitoring of Micro-Milling Operations.” *Journal of Materials Processing Technology* 209.10 (2009): 4903-4914.

Mamalis A., Horvath M., Branis A. & Manolakos D. “Finite Element Simulation of Chip Formation in Orthogonal Metal Cutting.” *Journal of Materials Processing Technology* 110.1 (2001): 19-27.

Masuzawa T. “State of the Art of Micromachining.” *CIRP Annals - Manufacturing Technology* 49.2 (2000): 473-488.

Maton A., Hopkins J., McLaughlin C.W., Johnson S., Warner M.Q., LaHart D. & Wright J.D. “Human Biology and Health.” (1993) Englewood Cliffs, New Jersey, USA

Mendes R., Kennedy J. & Neves J. “The Fully Informed Particle Swarm: Simpler Maybe Better.” *IEEE Transactions on Evolutionary Computation* 8.3 (2004): 204-210.

Mikszta J. A., Alarcon J. B., Brittingham J. M., Sutter D. E., Pettis R. J. & Harvey N. G. “Improved Genetic Immunization Via Micromechanical Disruption of Skin-Barrier Function and Targeted Epidermal Delivery.” *Nature Medicine* 8.4 (2002): 415-419.

Molinari A., Musquar C. & Sutter G. “Adiabatic Shear Banding in High Speed Machining of Ti-6Al-4V: Experiments and Modeling.” *International Journal of Plasticity* 18.4 (2002): 443-459.

Montgomery D. C. “Design and Analysis of Experiment.” John Wiley & Sons (2005) Hoboken, New Jersey, USA.

Myers R. H., & Anderson-Cook C. M. “Response surface methodology: Process and product optimization using designed experiments” John Wiley & Sons (2009) Hoboken, New Jersey, USA.

Nakayama K. & Tamura K. “Size Effect in Metal-Cutting Force.” *Journal of Engineering for Industry* 90 (1968): 119.

Narayanaswami R. & Dornfeld D. “Burr Minimization in Face Milling: A Geometric Approach.” *Journal of Manufacturing Science and Engineering* 119.2 (1997): 170-177.

Neugebauer R., Ben-Hanan U., Ihlenfeldt S., Wabner M. & Stoll A. “Acoustic Emission as a Tool for Identifying Drill Position in Fiber-Reinforced Plastic and Aluminum Stacks.” *International Journal of Machine Tools and Manufacture* 57.0 (2012): 20-26.

Özel T. & Altan T. “Process Simulation using Finite Element Method - Prediction of Cutting Forces, Tool Stresses and Temperatures in High-Speed Flat End Milling.” *International Journal of Machine Tools and Manufacture* 40.5 (2000): 713-738.

Özel T. & Liu X. “Investigations on Mechanics-Based Process Planning of Micro-End Milling in Machining Mold Cavities.” *Material and Manufacturing Process* 24 (2009): 1274-1281.

Özel T. & Zeren E. “Finite Element Modeling the Influence of Edge Roundness on the Stress and Temperature Fields Induced by High-Speed Machining.” *The International Journal of Advanced Manufacturing Technology* 35.3-4 (2007): 255-267.

Özel T., Sima M., Srivastava A. K. & Kaftanoglu B. “Investigations on the Effects of Multi-Layered Coated Inserts in Machining Ti–6Al–4V Alloy with Experiments and Finite Element Simulations.” *CIRP Annals - Manufacturing Technology* 59.1 (2010): 77-82.

Özel T., Thepsonthi T., Ulutan D. & Kaftanoğlu B. “Experiments and Finite Element Simulations on Micro-Milling of Ti-6Al-4V Alloy with Uncoated and cBN coated Micro-Tools.” *CIRP Annals- Manufacturing Technology* 60.2 (2011a): 85-88.

Özel T., Thepsonthi T., Ulutan D. & Kaftanoğlu B. “Micro-Milling of Ti-6Al-4V Alloy with Uncoated and cBN coated Micro-Tools,” *Proceedings of the 6th International Conference and Exhibition on Design and Production of Machines and Dies/Molds*, June 23-26 (2011b) Ankara, Turkey.

Park J., Allen M. G. & Prausnitz M. R. “Biodegradable Polymer Microneedles: Fabrication, Mechanics and Transdermal Drug Delivery.” *Journal of Controlled Release* 104.1 (2005): 51-66.

Prickett P. W. & Johns C. “An Overview of Approaches to End Milling Tool Monitoring.” *International Journal of Machine Tools and Manufacture* 39.1 (1999): 105-122.

Rahman M., Senthil Kumar A. & Prakash J. R. S. “Micro Milling of Pure Copper.” *Journal of Materials Processing Technology* 116.1 (2001): 39-43.

Rainelli A., Stratz R., Schweizer K. & Hauser P. C. “Miniature Flow-Injection Analysis Manifold Created by Micromilling.” *Talanta* 61.5 (2003): 659-665.

Ravindra H. V., Srinivasa Y. G. & Krishnamurthy R. “Acoustic Emission for Tool Condition Monitoring in Metal Cutting.” *Wear* 212.1 (1997): 78-84.

Razali A. R. & Qin Y. “A Review on Micro-Manufacturing, Micro-Forming and their Key Issues.” *Procedia Engineering* 53.0 (2013): 665-672.

Saedon J. B., Soo S. L., Aspinwall D. K., Barnacle A. & Saad N. H. “Prediction and Optimization of Tool Life in Micromilling AISI D2 (62 HRC) Hardened Steel.” *Procedia Engineering* 41.0 (2012): 1674-1683.

Saptaji K., Subbiah S. & Dhupia J. S. “Effect of Side Edge Angle and Effective Rake Angle on Top Burrs in Micro-Milling.” *Precision Engineering* 36.3 (2012): 444-450.

Schueler G., Engmann J., Marx T., Haberland R., & Aurich J. “Burr formation and surface characteristics in micro-end milling of titanium alloys.” *Burrs-analysis, control and removal* Springer (2010): 129-138

Shaw M. C. “The Size Effect in Metal Cutting.” *Sadhana* 28.5 (2003): 875-896.

Sima M. & Özel T. “Modified Material Constitutive Models for Serrated Chip Formation Simulations and Experimental Validation in Machining of Titanium Alloy Ti–6Al–4V.” *International Journal of Machine Tools and Manufacture* 50.11 (2010): 943-960.

Simoneau A., Ng E. & Elbestawi M. A. "Chip Formation during Microscale Cutting of a Medium Carbon Steel." *International Journal of Machine Tools and Manufacture* 46.5 (2006): 467-481.

Smart W. H. & Subramanian K. "The use of Silicon Microfabrication Technology in Painless Blood Glucose Monitoring." *Diabetes Technology & Therapeutics* 2.4 (2000): 549-559.

Son S. M., Lim H. S. & Ahn J. H. "Effects of the Friction Coefficient on the Minimum Cutting Thickness in Micro Cutting." *International Journal of Machine Tools and Manufacture* 45.4-5 (2005): 529-535.

Suzuki H., Moriwaki T., Yamamoto Y. & Goto Y. "Precision Cutting of Aspherical Ceramic Molds with Micro PCD Milling Tool." *CIRP Annals - Manufacturing Technology* 56.1 (2007): 131-134.

Taniguchi N. "Current Status in, and Future Trends of, Ultraprecision Machining and Ultrafine Materials Processing." *CIRP Annals - Manufacturing Technology* 32.2 (1983): 573-582.

Tansel I., Rodriguez O., Trujillo M., Paz E. & Li W. "Micro-End-milling—I. Wear and Breakage." *International Journal of Machine Tools and Manufacture* 38.12 (1998a): 1419-1436.

Tansel I., Trujillo M., Nedbouyan A., Velez C., Bao W., Arkan T. T., et al. "Micro-End-milling—III. Wear Estimation and Tool Breakage Detection using Acoustic Emission Signals." *International Journal of Machine Tools and Manufacture* 38.12 (1998b): 1449-1466.

Tay A., Stevenson M. & Davis G. D. V. "Using the Finite Element Method to Determine Temperature Distributions in Orthogonal Machining." *Proceedings of the Institution of Mechanical Engineers* 188.1 (1974): 627-638.

Thepsonthi T. & Özel T. "Sensor-Assisted Monitoring and Optimization of Process Parameters in Micro-end Milling of Ti-6Al- 4V Titanium Alloy." *The Fifth International Conference on Micromanufacturing (ICOMM/4M 2010),* April 5-8 (2010) Madison, Wisconsin, US.

Thepsonthi T. & Özel T. "Statistically Based Process Optimization for Improved Surface Quality in Micro-end Milling of Ti-6Al- 4V Titanium Alloy." *Proceedings of the 39th North American Manufacturing Research Conference* June 13-17 (2011) Oregon State University, Corvallis, Oregon,US.

Thepsonthi T. & Özel T. "Finite Element Modeling and Simulation of Micro-Milling." *Proceedings of the 40th North American Manufacturing Research Conference (NAMRC)* June 4-8 (2012a) University of Notre Dame, Indiana, US.

Thepsonthi T. & Özel T. "Multi-Objective Process Optimization for Micro-end Milling of Ti-6Al- 4V Titanium Alloy." *International Journal of Advanced Manufacturing Technology* 63 (2012b): 903-914.

Thepsonthi T., Milesi N. & Özel T., "Design and Prototyping of Micro-Needle Arrays for Drug Delivery Using Customized Tool-Based Micro-Milling Process." *Proceedings of the the First International Conference on Design and Processes for Medical Devices,* May 2-4 (2012c) Brescia, Italy.

Thepsonthi T. & Özel T. "Experimental and Finite Element Simulation Based Investigations on Micro-Milling Ti-6Al-4V Titanium Alloy: Effects of cBN

Coating on Tool Wear." *Journal of Materials Processing Technology* 213 (2013a): 532-542.

Thepsonthi T. & Özel T. "Finite Element Simulation of Micro-End Milling Titanium Alloy: Comparison of Viscoplastic and Elasto-ViscoPlastic Models." *Proceedings of the 41st North American Manufacturing Research Conference* June 10-14 (2013b) Madison, Wisconsin, US.

Thepsonthi T. & Özel T., "3-D Finite Element Simulation of Micro-Milling Ti-6Al-4V Titanium Alloy" *Proceedings of 7th International Conference and Exhibition on Design and Production of Machines and Dies/Molds*, June 20-23, (2013c), Antalya, Turkey.

Thepsonthi T. & Özel T., "An Integrated Toolpath and Process Parameter Optimization for High Performance Micro-Milling Process" *Proceedings of the 42nd North American Manufacturing Research Conference,* June 13-14, (2014), University of Michigan—Ann Arbor, Ann Arbor, Michigan.

Ucun İ, Aslantas, K. & Bedir F. "An Experimental Investigation of the Effect of Coating Material on Tool Wear in Micro Milling of Inconel 718 Super Alloy." *Wear* 300.1-2 (2013): 8-19.

Umbrello D. "Finite Element Simulation of Conventional and High Speed Machining of Ti6Al4V Alloy." *Journal of Materials Processing Technology* 196.1 (2008): 79-87.

Usui E., Kitagawa T. & Shirakashi T. "Analytical Prediction of Three Dimensional Cutting Process—Part 3: Cutting Temperature and Crater Wear of Carbide Tool." *Journal of Engineering for Industry* 100.2 (1978): 236-243.

Vazquez E., Ciurana J., Rodriguez C. A., Thepsonthi T. & Özel T. "Swarm Intelligent Selection and Optimization of Machining System Parameters for Microchannel Fabrication in Medical Devices." *Materials and Manufacturing Processes* 26.3 (2011): 403-414.

Vogler M. P., DeVor R. E. & Kapoor S. G. "On the Modeling and Analysis of Machining Performance in Micro-Endmilling, Part I: Surface Generation." *Journal of Manufacturing Science and Engineering* 126 (2004): 685-694.

Wang J., Gong Y., Abba G., Antoine J. & Shi J. "Chip Formation Analysis in Micromilling Operation." *The International Journal of Advanced Manufacturing Technology* 45.5-6 (2009): 430-447.

Weule H., Hüntrup V. & Tritschler H. "Micro-Cutting of Steel to Meet New Requirements in Miniaturization." *CIRP Annals - Manufacturing Technology* 50.1 (2001): 61-64.

Woon K. S., Rahman M., Fang F. Z., Neo K. S. & Liu K. "Investigations of Tool Edge Radius Effect in Micromachining: A FEM Simulation Approach." *Journal of Materials Processing Technology* 195.1–3 (2008): 204-211.

Yen Y., Jain A. & Altan T. "A Finite Element Analysis of Orthogonal Machining using Different Tool Edge Geometries." *Journal of Materials Processing Technology* 146.1 (2004): 72-81.

Yen Y., Jain A. & Altan T. "A Finite Element Analysis of Orthogonal Machining using Different Tool Edge Geometries." *Journal of Materials Processing Technology* 146.1 (2004): 72-81.

Yuan Z. J., Zhou M. & Dong S. “Effect of Diamond Tool Sharpness on Minimum Cutting Thickness and Cutting Surface Integrity in Ultraprecision Machining.” *Journal of Materials Processing Technology* 62.4 (1996): 327-330.